Université de Lille

Doctoral school: Science of Matter, Radiation and Environment
Discipline: Optics and Lasers, Physical Chemistry, Atmosphere

Dissertation

Physico-chemical characterization of size-selected internal combustion engine nanoparticles and original method for measuring adsorption energies on carbonaceous surfaces by laser mass spectrometry

by

Dumitru Duca

Thesis submitted in partial fulfillment of the requirements for the degree of
Doctor of Philosophy of the University of Lille
Defended on September 17th, 2020 in front of the defense committee composed of:

Jury president:	Prof. Marc DOUAY	Université de Lille
Reviewers:	Dr. Christine JOBLIN	CNRS, Université de Toulouse
	Prof. Ralf ZIMMERMANN	Universität Rostock
Examiners:	Dr. Sylvain PICAUD	CNRS, Université de Franche-Comté
	Prof. Marcus RIEKER	Horiba Europe
	Prof. Céline TOUBIN	Université de Lille
Invited members:	Prof. Christoph HAISCH	Technische Universität München
	Dr. Sébastien LEGENDRE	Horiba Scientific
Thesis directors:	Dr. Claire PIRIM	Université de Lille
	Prof. Cristian FOCSA	Université de Lille

Laboratoire de Physique des Lasers Atomes et Molécules
Université de Lille, France

© 2020 Tous droits réservés.

This page is intentionally left blank

© 2020 Tous droits réservés.

Université de Lille

Ecole Doctorale: Sciences de la Matière, du Rayonnement et de l'Environnement
Discipline: Optique et lasers, Physicochimie, Atmosphère

Thèse de doctorat

Caractérisation physico-chimique de nanoparticules sélectionnées en taille émises par moteur à combustion interne et méthode originale pour la mesure des énergies d'adsorption sur surfaces carbonées par spectrométrie de masse laser

présentée par

Dumitru Duca

pour obtenir le grade de docteur de l'Université de Lille
soutenue le 17 septembre 2020

Composition du jury:

Président du jury:	Prof. Marc DOUAY	Université de Lille
Rapporteurs:	Dr. Christine JOBLIN	CNRS, Université de Toulouse
	Prof. Ralf ZIMMERMANN	Universität Rostock
Examinateurs:	Dr. Sylvain PICAUD	CNRS, Université de Franche-Comté
	Prof. Marcus RIEKER	Horiba Europe
	Prof. Céline TOUBIN	Université de Lille
Membres invités:	Prof. Christoph HAISCH	Technische Universität München
	Dr. Sébastien LEGENDRE	Horiba Scientific
Directeurs du thèse:	Dr. Claire PIRIM	Université de Lille
	Prof. Cristian FOCSA	Université de Lille

Laboratoire de Physique des Lasers Atomes et Molécules
Université de Lille, France

© 2020 Tous droits réservés.

This page is intentionally left blank

© 2020 Tous droits réservés.

Caractérisation physico-chimique de nanoparticules sélectionnées en taille émises par moteur à combustion interne et méthode originale pour la mesure des énergies d'adsorption sur surfaces carbonées par spectrométrie de masse laser

Résumé

Les émissions à l'échelle mondiale de particules carbonées fines et ultra-fines présentent un risque bien connu pour la santé et soulèvent des préoccupations environnementales importantes. Bien que les niveaux ambiants de particules carbonées aient été considérablement réduits au cours des dernières décennies par les restrictions successives des normes d'émission, leurs rejets dans l'atmosphère continuent de représenter l'une des principales sources de particules dans les zones urbaines. Les émissions de particules ultra-fines (suie) générées par les moteurs essence à combustion interne modernes sont au centre des préoccupations puisque les plus petites d'entre elles ne sont actuellement pas concernées par les règlementations sur les émissions automobiles qui se limitent aux particules de taille supérieure à 23 nm. Les effets potentiels sur l'environnement et la santé de ces émissions ultra-fines ne sont pas encore complètement compris en raison de l'absence de caractérisation expérimentale de ces nanoparticules carbonées.

La caractérisation physico-chimique détaillée de particules sélectionnées en taille émises par un moteur essence à combustion interne a été réalisée dans ce travail pour fournir des informations cruciales au bon développement de nouvelles technologies pour la détection et la mesure des particules de taille inférieure à 23 nm. Ces analyses ont été réalisées dans le cadre du projet H2020 PEMS4Nano qui vise à développer une technologie de mesure robuste, fiable et reproductible de particules ultrafines atteignant une taille aussi petite que 10 nm émises sur banc de test et en conditions réelles de conduite. Les caractérisations chimiques de ces particules sélectionnées en taille ont été réalisées par spectrométrie de masse (par exemple de type désorption ionisation laser, L2MS), qui révèle au niveau moléculaire des informations essentielles sur les classes chimiques des composés les constituant telles que les organosulfates, les hydrocarbures oxygénés, les hydrocarbures azotés, les métaux ou les hydrocarbures aromatiques polycycliques. La morphologie des particules émises a été sondée avec des techniques de microscopie à force atomique, microscopie électronique en transmission et à balayage. La spectroscopie Raman exaltée par effet de pointe a été également appliquée pour la première fois à des particules de combustion inférieures à 10 nm pour recueillir des informations sur leur nanostructure.

La composition chimique de suface et la nature de l'interaction entre les adsorbats et la surface (chimi/physi-sorption) régissent la réactivité des particules dans l'environnement et leurs effets nocifs sur la santé humaine. Afin de mieux comprendre ces interactions et prédire leurs impacts, il est nécessaire de pouvoir déterminer les énergies d'adsorption des composés chimiques présents à la surface des particules. Dans ce but a été développée et validée dans ce travail une nouvelle méthode basée sur le phénomène de désorption induite par laser pour déduire l'énergie d'adsorption d'espèces chimiques sur différents types de surfaces carbonées à partir de spectres de masse L2MS. Cette procédure expérimentale a été développée pour être rapide, résolue spatialement, sensible aux molécules de surface, et, supplémentée par un modèle théorique décrivant le phénomène de désorption, permet de déterminer l'énergie d'adsorption sur une grande variété d'échantillons. La preuve de concept de la méthode a été fournie par son application à des systèmes chimiques de complexité grandissante, montrant son énorme potentiel pour l'étude d'échantillons de terrain complexes.

Mots-clés: spectrométrie de masse laser, caractérisation physico-chimique, aérosols générés par la combustion, moteur à combustion interne, surfaces carbonées, nanoparticules

© 2020 Tous droits réservés. lilliad.univ-lille.fr

Physico-chemical characterization of size-selected internal combustion engine nanoparticles and original method for measuring adsorption energies on carbonaceous surfaces by laser mass spectrometry

Abstract

The extensive global emissions of fine and ultra-fine carbon-based particulates present a well-known health risk and raise significant environmental concern. Although the ambient particulate matter levels have been significantly reduced in the past decades by the successive tightening of emission standards, transport emission of carbonaceous particles continues to represent one of the main sources of particulates in urban areas. A major concern is now raised by the ultra-fine particle (soot) emissions of modern internal combustion engines. A large portion of these emissions are not covered by existing vehicle emission regulations that only limit the number of particles larger than 23 nm. The potential environmental and health effects of ultra-fine vehicle emissions are still not entirely understood due to the lack of experimental characterization of such carbonaceous nanoparticles.

Detailed physico-chemical characterizations of size-selected particulate matter emitted by an internal combustion gasoline engine (ICE) were carried out in this work to support the development process of measurement technologies for sub-23 nm particles. These analyses were performed in the framework of the H2020 PEMS4Nano project which aims to develop robust, reliable, and reproducible measurement technology for particles down to 10 nm for both chassis dyno and real driving emissions. Chemical characterizations of the ICE size-selected particles were performed using mass spectrometry, such as laser desorption/ionization mass spectrometry, L2MS, which gives access to detailed molecular information on the chemical classes of critical interest such as organosulphates, oxygenated hydrocarbons, nitrogenated hydrocarbons, metals, or polycyclic aromatic hydrocarbons. The morphology of the emitted particles was probed with atomic force microscopy and transmission and scanning electron microscopies. Tip-Enhanced Raman Spectroscopy was applied for the first time to sub-10 nm combustion-generated particles to gather information on their nanostructure.

The reactivity of particles is mainly driven by the surface chemical composition and by the strength of the interaction between the adsorbates and the surface (physi- /chemisorption), therefore, to truly understand and predict the impact of soot emissions, the adsorption energies of chemical compounds present on their surface must be also determined. In this regard, a novel laser-based method for determining the adsorption energy of chemical species on various carbonaceous surfaces was developed and validated. This involved the development of a fast, spatially resolved, surface-sensitive experimental procedure and a theoretical model that allows us to determine the adsorption energy of chemical species adsorbed on a wide variety of samples. The proof of concept of this method has been demonstrated on several surrogate carbonaceous systems of varying complexity which demonstrated the great potential of the method for the future analyses of field collected samples.

Keywords: laser mass spectrometry, physico-chemical characterization, combustion-generated aerosols, internal combustion engine, carbonaceous surface, nanoparticles

© 2020 Tous droits réservés. lilliad.univ-lille.fr

Acknowledgements

A PhD thesis is not an individual experience, rather it takes place in a social context and involves multiple people, whom I would like to thank sincerely. This thesis would not have been possible without the Erasmus+ scholarship I received for my second year of Master studies, which allowed me to enrol in the International Master "Atmospheric Environment" program at the University of Lille. During that year, I had the opportunity to perform my MSc research internship in the PhLAM laboratory and more specifically in the ANATRAC group. This first contact with research activities at the University of Lille determined me to continue my studies with a PhD thesis in the same group. I would like to express my deepest gratitude to all PhLAM laboratory members, especially technical and administrative staff, its Director Prof. Marc Douay, and to all ANATRAC research group members for the excellent work environment they provided during these years. This work would not have been possible without the financial support I received from the H2020 PEMS4Nano project and for that I would like to thank all its members (especially its coordinator Prof. Marcus Rieker) for their continuous support and the very exciting scientific exchanges we had during the three years of the project.

I would like to express my deepest gratitude to my supervisors, Prof. Cristian Focsa and Dr. Claire Pirim, for their invaluable guidance throughout this research. They taught me the methodology to carry out experimental research, to carefully analyze and interpret the collected data and to present the results in a clear and sound manner. Their guidance helped me during the whole duration of this research and the writing of this thesis, therefore I am also grateful for all the time they spent revising the manuscript.

Every result in this thesis was accomplished with the help and support of fellow labmates and collaborators. I very much appreciate the support I received from Dr. Jennifer Noble, Dr. Marin Vojkovic, Dr. Cornelia Irimiea, Dr. Alessandro Faccinetto, and Dr. Yvain Carpentier. Their help with instrumentation and data analysis along with their continuous encouragements significantly facilitated my work and contributed to an unforgettable PhD. I also thank Bénédicte Calimet and Marc Le Parquier from CERLA for their assistance, especially with the laser systems. I would like to thank Dr. Nicolas Nuns for his help during the SIMS experiments, Dr. Ahmed Addad for his assistance with TEM measurements, and Dr. Torsten Reinhardt for helping with the SEM analyses. AFM/TERS studies would not have been possible without the contribution of Dr. Sébastien Legendre and Dr. Ophélie Lancry from Horiba Scientific, for which I am grateful. A big thank you to Dr. Dimitris Papanastasiou, Dr. Alexander Lekkas and Dr. John Orfanopoulos from Fasmatech S&T for their continuous assistance with the installation and optimization of the new high-resolution mass spectrometer. Special thanks go to Prof. Cristian Preda for long discussions on statistical data treatment methods.

I also want to thank everyone who participated with me in the sampling campaigns. I am grateful to Roman Grzeszik and Andreas Manz from Robert Bosch GmbH for their help with the test engine, to Dr. Christopher Betrancourt and Dr. Pascale Desgroux for their assistance during sampling as well as interesting scientific discussions. I thank Dr. Adam Boies and Dr. Mostafiz Rahman from University of Cambridge for their stimulating conversations during long sampling sessions. I also thank Dr. Torsten Tritscher from TSI for his support with the NanoMOUDI impactor.

I am deeply honored and would like to express my gratitude to all the members of the

© 2020 Tous droits réservés. lilliad.univ-lille.fr

defense committee for accepting to evaluate this PhD work: Dr. Christine Joblin, Prof. Ralf Zimmermann, Dr. Sylvain Picaud, Prof. Marcus Rieker, Prof. Céline Toubin, Prof. Marc Douay, Prof. Christoph Haish and Dr. Sébastien Legendre. A special thank to Dr. Christine Joblin and Prof. Ralf Zimmermann for accepting to review the manuscript (I thank also Prof. Zimmermann for the opportunity to visit his laboratory at the University of Rostock and for the interesting discussions we had on this occasion with members of his research group).

Last but not the least, I would like to thank my family and friends for supporting me throughout these years of research.

© 2020 Tous droits réservés.

lilliad.univ-lille.fr

Table of Contents

Table of Contents v

List of Acronyms vii

List of Figures ix

List of Tables xx

1 Introduction 1
- 1.1 Atmospheric aerosols . . . 1
  - 1.1.1 Impact of aerosols on climate . . . 1
  - 1.1.2 Impact of aerosols on human health . . . 3
- 1.2 Combustion-generated carbonaceous aerosols . . . 4
  - 1.2.1 On-road vehicle emissions . . . 6
  - 1.2.2 Reactivity of carbonaceous aerosols . . . 9
- 1.3 Context of the study . . . 10
- 1.4 Structure of the manuscript . . . 11

2 Materials and Methods 13
- 2.1 Collection / synthesis of samples . . . 13
  - 2.1.1 Internal combustion engine emissions . . . 13
    - 2.1.1.1 Test engine and sampling line . . . 15
    - 2.1.1.2 Sampling of polydisperse particles and gas phase . . . 18
    - 2.1.1.3 Collection of size-selected particles down to 10 nm . . . 20
  - 2.1.2 Preparation of "surrogate soot" samples . . . 22
- 2.2 Characterization techniques . . . 24
  - 2.2.1 Structural and morphological analysis . . . 24
    - 2.2.1.1 Scanning and Transmission Electron Microscopy . . . 24
    - 2.2.1.2 Atomic Force Microscopy / Tip Enhanced Raman Spectroscopy . . . 25
    - 2.2.1.3 Micro-Raman spectroscopy . . . 25
  - 2.2.2 Chemical characterization . . . 26
    - 2.2.2.1 Secondary Ion Mass Spectrometry . . . 26
    - 2.2.2.2 Two-Step Laser Mass Spectrometry (L2MS) . . . 28
    - 2.2.2.3 High-Resolution Two-Step Laser Mass Spectrometer (HR-L2MS) . . . 35
- 2.3 Data processing methodology . . . 49
  - 2.3.1 Assignment of mass peaks . . . 50
  - 2.3.2 Statistical procedures . . . 51
    - 2.3.2.1 Principal Component Analysis . . . 52
    - 2.3.2.2 Hierarchical Clustering Analysis . . . 55
    - 2.3.2.3 Volcano plot . . . 57
- 2.4 Conclusion . . . 58

© 2020 Tous droits réservés. lilliad.univ-lille.fr

3 Size-selective characterization of ultra-fine particles emitted by an internal combustion engine 59
3.1 Introduction . . . 59
3.2 Morphology and structure characterization . . . 60
3.2.1 SEM analyses . . . 61
3.2.2 TEM analyses . . . 62
3.2.3 AFM/TERS analyses . . . 65
3.3 Chemical characterization . . . 68
3.3.1 Evolution of the chemical composition with particle size . . . 69
3.3.1.1 "Worn out" engine regime . . . 69
3.3.1.2 Fuel injection system malfunction simulation . . . 74
3.3.2 Evolution of the chemical composition with engine regime . . . 81
3.3.3 Influence of the catalytic stripper on the chemical composition 84
3.3.3.1 Polydisperse particles . . . 85
3.3.3.2 Size-selected particles . . . 93
3.3.4 Conclusion . . . 101

4 A novel laser-based method to measure the adsorption energy on carbonaceous surfaces 103
4.1 Introduction . . . 103
4.2 Previous works . . . 105
4.3 Experimental considerations . . . 106
4.3.1 Experimental approaches . . . 106
4.3.2 Detected molecules . . . 107
4.3.3 Sample (surface) evolution upon irradiation . . . 109
4.4 Theoretical framework . . . 110
4.4.1 Thermal desorption of physisorbed species . . . 112
4.4.1.1 "Effective temperature" desorption model . . . 113
4.4.1.2 Transient laser-induced heating . . . 115
4.4.1.3 Transient temperature desorption model . . . 118
4.4.2 Data fitting process . . . 121
4.4.2.1 Markov chains Monte Carlo fitting . . . 121
4.4.2.2 Retrieving the average values and error bars of fitted parameters . . . 122
4.5 Results on various systems . . . 124
4.5.1 Adsorption energy measurements on surrogate soot systems . 125
4.5.1.1 Pyrene/activated carbon system . . . 125
4.5.1.2 Binary system: Pyrene and Coronene adsorbed on activated carbon . . . 127
4.5.1.3 Desorption of heavy metals: Pb / activated carbon . 129
4.5.2 Effect of the adsorbent: from activated carbon to graphite surfaces . . . 130
4.6 Toward studying complex soot samples . . . 132
4.7 Conclusion . . . 135

5 Conclusions and perspectives 137

Bibliography 168

© 2020 Tous droits réservés. lilliad.univ-lille.fr

List of acronyms

AAC	–	aerodynamic aerosol classifier
AFM	–	atomic force microscopy
AFR	–	air/fuel ratio
AMS	–	aerosol mass spectrometry
ANOVA	–	analysis of variance
BC	–	black carbon
CI	–	compression ignition
CNT	–	carbon nanotubes
CPMA	–	centrifugal particle mass analyser
CS	–	catalytic stripper
DMA	–	differential mobility analyser
DSC	–	differential scanning calorimetry
EC	–	elemental carbon
EGR	–	exhaust gas recirculation
EI	–	electron ionization
ERF	–	effective radiative forcing
ET	–	evaporative tube
FWHM	–	full width at half maximum
G-20	–	group of twenty world's larges economies
GDI	–	gasoline direct injection engine
HC	–	hydrocarbon compounds
HCA	–	hierarchical clustering analysis
HCPC	–	hierarchical clustering on principal components
HR-L2MS	–	high-resolution laser desorption / laser ionization / time of flight mass spectrometry
HR-TEM	–	high-resolution transmission electron microscope
IC	–	internal combustion
ICE	–	internal combustion engine
IMEP	–	indicated mean effective pressure
ITC	–	isothermal titration calorimetry
L2MS	–	laser desorption / laser ionization / time of flight mass spectrometry
LITD	–	laser-induced thermal desorption
MCP	–	microchannel plate
MS	–	mass spectrometry
MPI	–	multi-photon ionization
NAS	–	nanoscale aerosol sampler
NMHC	–	non-methane hydrocarbon content
OC	–	organic carbon
PAH	–	polycyclic aromatic hydrocarbon
PC	–	principal component
PCA	–	principal component analysis

© 2020 Tous droits réservés.

lilliad.univ-lille.fr

PF	–	particle filter
PM	–	particulate matter
PMP	–	particle measuring program
PN	–	particle number
QFF	–	quartz fiber filter
R2PI	–	resonant two-photon ionization
RDE	–	real driving emissions
REMPI	–	resonance enhanced multi-photon ionization
RF	–	radio frequency
SCAC	–	single-crystal adsorption calorimetry
SEM	–	scanning electron microscopy
SI	–	spark ignition
SIMS	–	secondary ion mass spectrometry
STEM	–	scanning/transmission electron microscopy
TIC	–	total ion counts
TEM	–	transmission electron microscope
TERS	–	tip-enhanced Raman spectrometry
THC	–	total hydrocarbon content
ToF	–	time-of-flight
TPD	–	temperature-programmed desorption
UV	–	ultraviolet
VPR	–	volatile particle remover
VUV	–	vacuum ultraviolet
WHO	–	World Health Organization

© 2020 Tous droits réservés.

lilliad.univ-lille.fr

List of Figures

1.1 Summary of the radiative forcing in 2011 relative to 1750 shown for various emitted components, reproduced from The Climate Change report. 2
1.2 Schematic diagram representing deposition of particles with different sizes in the lungs due to various mechanisms. The diagram shows that smaller particles deposit primarily in the lower airways. 4
1.3 Structure of Diesel soot particles obtained by Ishiguro et al. (1997) via High Resolution Transmission Electron Microscopy. 5
1.4 Diagram showing the fuel/air equivalence ratio and temperature ranges for soot and NO_x formation and the regions associated with conventional Diesel, spark ignition, homogeneous charge compression-ignition (HCCI), and Diesel low-temperature combustion (LTC) engines. 7
1.5 Annual CO and NO_x emissions from different sectors. 8

2.1 Schematic representation of the sampling line used for engine monitoring and particle collection. The sampling of combustion byproducts for the chemical analysis (with NanoMOUDI and two-filter system) can be done with or without a catalytic stripper (represented by the dashed lines). 17
2.2 (a) The custom-built catalytic stripper employed for the removal of organic species from the engine exhaust, (b) size-dependent penetration efficiency plot provided by the manufacturer of the catalytic stripper (University of Cambridge). 18
2.3 Schematic representation of the two-filter sampling system used for the separation and collection of the particulate matter and gas phase from the engine exhaust. A set of collected filters (front and back) is also shown. 18
2.4 A "contrast plot" illustrating the partitioning of organic species emitted by a miniCAST (Combustion Aerosol Standard) soot generator between the front and back filters. 19
2.5 The electrode of the NAS with three substrates attached (with copper tape): one gold-coated silicon wafer and two TEM grids. 21
2.6 (a) Stepper motor impaction stage diagram of the NanoMOUDI, reproduced from the MOUDI II impactor catalogue (TSI). (b) Image of the aluminum foil substrate with deposited soot particles (18–32 nm). 22
2.7 Size distribution of particle emitted by the single-cylinder engine in two operation regimes and recorded by the EEPS. 22
2.8 (a) Block diagram of the surrogate soot preparation process, (b) UV-Vis extinction spectra of the original stock and filtrated solution of pyrene. The reduction in extinction is due to the adsorption of pyrene onto activated carbon particles. 23

© 2020 Tous droits réservés. lilliad.univ-lille.fr

2.9 Comparison between mass spectra of soot particles obtained with L2MS at different ionization wavelengths and SIMS. Different desorption and ionization mechanisms result in significantly different mass spectra, indicating that different chemical species have been targeted. For instance, the ionization of laser-desorbed species with a laser pulse at 266 nm results in a high signal from PAHs, while ionization at 118 nm will lead to preferential detection of aliphatic compounds. 27

2.10 (a) A photo of the ToF-SIMS[5] instrument and its main parts: load-lock chamber, analysis chamber, Bi_3^+ primary ion source, and ToF-MS mass analyzer. (b) SIMS working principle. 28

2.11 (a) The three stages involved in the L2MS technique: i) Laser Desorption – the sample is irradiated by a nanosecond laser pulse (green) which promotes the ejection of molecules; ii) Laser Ionization (purple) – the ejected molecules are ionized by the second ns laser pulse (UV); iii) Mass Spectrometry (red) – the obtained ions are extracted and mass-separated in a ToF-MS. (b) Schematic representation of the Jordan Tof L2MS set-up. 29

2.12 Desorption laser beam optical path for the lower resolution L2MS setup. All distances are given in centimeters. The transverse beam profile at the sample surface is illustrated in the inset. 30

2.13 Top view of the lower resolution ToF-MS analysis chamber. 31

2.14 Photo-ionization mechanisms of hydrocarbon compounds for some commonly used laser wavelengths (266 nm, 157 nm, and 118 nm were available in our laboratory). Ionization energies for selected classes of molecules as a function of their carbon number. 32

2.15 266 nm laser beam path. 33

2.16 (a) Schematic of the analysis chamber (side view): representation of the desorption (532 nm) and ionization (118 nm) configurationexperimental arrangement. (b) Ionization beam path at 118 nm. 34

2.17 Path of ions in the ToF-MS, from their generation to detection. . . . 35

2.18 Pictures of the high-resolution L2MS instrument (Fasmatech S&T). . 36

2.19 3D model of the octapole ion trap showing the ion source optics, the differentially pumped ion trap enclosure, the electrical connections (at the top) for applying RF and DC signals to the ion trap segments, the transfer hexapole and the ToF-MS analyzer. 36

2.20 (a) Schematic representation of the inlet apertured electrodes (top view, all dimensions in mm). (b) 3D visualization of the Laser Desorption/Ionization source. 37

2.21 Desorption laser beam optical path for the high-resolution L2MS instrument. All distances are given in centimeters. Note that relative dimensions of the presented objects are not to scale. 38

2.22 Ionization laser beam optical path for the high-resolution L2MS instrument. All distances are given in centimeters. Note that relative dimensions of the presented objects are not to scale. 38

2.23 3D model of the octapole ion trap assembly. 39

2.24 Schematic diagram of the injection lenses (**L1**, **L2**), the segmented PCB RF octapole ion trap, **L3** transfer lens and RF hexapole transfer ion guide (bottom panel). DC voltages applied across the segments of the octapole trap are (top panel). All dimensions are given in mm. 40

© 2020 Tous droits réservés. lilliad.univ-lille.fr

2.25 Ion trajectories for m/z values corresponding to cesium-iodide ions over a wide mass range extending from m/z=133 to m/z=1952. (a) Ion guide combining octapolar and quadrupolar fields and (b) ion guide with quadrupolar field only. The normalized equipotentials in the octapolar and quadrupolar field configuration are also shown. (c) Translational cooling for two ions traversing the ion guide. (d) Simulated transmission efficiency for two modes of operation shown in (a) and (b). Note that the simulations were performed on an ion guide containing 8 segments, however, the results for 7 segments are similar. The simulations were provided by Fasmatech S&T. 41
2.26 Synchronization between the different steps of the analysis. First, He gas is introduced into the ion trap. The desorption and ionization of molecules follows. The produced ions are introduced into the ion trap and are stored in the S6 segment for 25 ms. The ion packet is then transferred to the S7 segment for axial compression by changing the DC voltage of the S7 segment (Table 2.5). Finally, the ions are transmitted via a hexapole and pulse accelerated into the ToF-MS for mass measurements. 42
2.27 Schematic representation of the ion path (orange dashed line) inside the HR-L2MS and the evolution of the ion packet shape (blue elipse) during its passage through the instrument. 43
2.28 (a) Reference mass spectrum obtained from single-window mass spectra using equation 2.2. (b) An example of a single-window mass spectrum is shown in green along with the corresponding transmission window. Note that the red line "transmission window envelope" is shown here only as an illustration, the calculation of the exact shape is discussed below. 45
2.29 Position and shape of seven chosen windows (solid lines) and the resulted overall transmission function (red dashed line). 46
2.30 Comparison between the reference spectrum (left) and the one obtained from seven transmission-windows (right). 47
2.31 Illustration of the electronic jitter influence on six time-of-flight spectra recorded from the same sample in the same experimental conditions. The average time of flight and jitter-induced offset is shown for a single peak (blue). 48
2.32 Time-of-flight spectra aligned after jitter-induced offset correction. Note that the peaks in the insets are different from those in Figure 2.31. 49
2.33 Example of mass peaks recorded with the HR-L2MS instrument, showcasing high accuracy and mass resolution. 49
2.34 Comparison of sample coverage for the 100–180 nm (a) and 10–18 nm (b) size bins. 50
2.35 (a) Example of a mass defect plot obtained from the SIMS mass spectrum of soot particles collected from a laboratory flame and illustrating its capacity to separate chemical species based on their corresponding molecular class. Ions with a low H/C ratio (black dots) are mainly attributed to fragment ions, high H/C ions to unsaturated hydrocarbons and low-mass PAHs (red dots), while high-mass ions (green dots) are assigned to PAHs and oxygen-containing hydrocarbons.The size of displayed markers is proportional to the corresponding peak integrated area. (b) Mass defect plot obtained from L2MS mass spectrum of soot collected from a standard soot generator (miniCAST) showing the alignment of homologous compounds. . . . 52

© 2020 Tous droits réservés. lilliad.univ-lille.fr

2.36 Example of a loadings plot showing the contribution of each mass peak to first (a) and second (b) principal components. The contribution of hydrocarbon and oxygenated species are shown in different colors. Based on the loadings plot, the physical meaning of each principal component can be determined. 54
2.37 Example of a typical scree plot showing the contribution of each principal component and the cumulative contribution of all PCs to the explained variance. The trend line of the component contribution is shown in black with the "elbow" point highlighted. For this particular scree plot, only the first two principal components are located before the "elbow" and, therefore, contain the majority of the meaningful data. 55
2.38 Example of a score plot showing the projection of the data on the first two principal components. On such a projection, observations can be easily grouped into three distinct clusters (C1, C2, and C3). . 55
2.39 (a) Example of hierarchical clustering dendogram. Two main clusters can be seen (red and green) and each can be further subdivided into another two clusters. Four different clusters will be formed if an Euclidian distance of 2.0 is chosen to cut the dendogram (black dashed line). (b) Example of a hierarchical clustering heat-map. HCA was performed on both observations (samples, columns) and variables (chemical species, rows) as indicated by two dendograms. The relative correlation between a certain observation and variable is represented by the color of each cell. 56
2.40 Example of a volcano plot illustrating the three main regions: points with either a small fold change or statistical significance – grey markers, points with high contribution to the first sample with a high statistical significance – green markers, and points with high contribution to the second sample with a high statistical significance – red markers. 58

3.1 SEM images of size-selected particles (size bin centered at 18 nm) collected on Si wafers with a NAS in NH2000 (a) and NM2000 (b) engine regimes. 61
3.2 SEM images of particles collected on a Si wafer in the OM2000 regime (size bin centered at 18 nm). Needle or tube shape particles have been detected (red rectangles). 62
3.3 TEM images of size-selected NH2000 (2000RPM, high load) particles collected with a combination of DMA and NAS on a SiN wafer (a and b) and NanoMoudi on a carbon Lacey TEM grid (c). A possible shape of the particle/aggregate is also shown. 63
3.4 High magnification TEM images of two $NH2000_{10-18}$ (2000RPM, high load, 10–18 nm size bin collected on a carbon Lacey TEM grid) particles. A high variability in particle nanostructure is observed, as illustrated by the different length and tortuosity of the carbon fringes. 63
3.5 Comparison between high resolution TEM images of a soot particle obtained in the NH2000 engine regime taken before (left panel) and after (right panel) electron irradiation in STEM mode. 64
3.6 Examples of high-resolution TEM images of the same particle taken at different tilt angles of the sample holder. The relative tilt angle of the sample holder is indicated for each image. 65
3.7 Comparison between the high resolution TEM images of a soot particle and its corresponding snapshots of the reconstructed 3D model taken from the same perspective. 66

© 2020 Tous droits réservés. lilliad.univ-lille.fr

3.8 AFM and TERS study of nanoparticles collected in the NH2000 engine regime (optimal conditions, high load) on gold coated Si wafers. Topography image (1.2 x1.2 μm^2) (a), TERS mapping (G band only) of zone I, particles 1 and 2 (b), and zone II, particles 3 and 4 (c), topographic cross-sections of particles 1 and 2 (d). 67

3.9 Five-band fitting model applied to the TERS spectra of particles 2 (a), 3 (b), and 4 (c). Spectra were fitted using tools available in Labspec 6 software (Horiba Scientific). 67

3.10 L2MS spectra of four samples (particle size 18-180 nm) obtained in the OM2000 engine conditions (optimal operation, medium load). The analyses were performed with an ionization wavelength λ_i=266 nm to target aromatic compounds. 70

3.11 Mass spectra of the four samples (particle size 18 – 180 nm) obtained in the OM2000 engine conditions. The analyses were performed with an ionization wavelength λ_i=118 nm which has a high sensitivity for aliphatic compounds. 70

3.12 Contribution of different species to PC1 and PC2 for size-selected particles collected in the OM2000 engine regime. Ionization at 266 nm (left) and 118 nm (right). 73

3.13 Size separation of combustion-generated particles obtained in the OM2000 engine regime (optimal operation with addition of oil, medium load) by means of principal component analysis, with ionization wavelengths of λ_i=266 nm (a), or λ_i=118 nm (b). 74

3.14 Positive polarity SIMS spectra of samples obtained in the FM2000 engine regime (fuel system malfunction) and a blank aluminum foil used for reference. Mass spectra were acquired in the range m/z 0 – 600 but only the highest intensity m/z 0 – 300 range is displayed here. 75

3.15 Negative polarity SIMS spectra of samples obtained in the FM2000 engine regime (fuel system malfunction) and a blank aluminum foil used for reference. Mass spectra were acquired in the range m/z 0 – 600 but only the highest intensity m/z 0 – 300 range is displayed here. 75

3.16 Size discrimination of FM2000 particles based on the PCA of positive (a) and negative (b) SIMS spectra. The blue and green arrows indicate the main trends in various classes of compounds extracted from the loadings plots (Figure 3.17). 78

3.17 Contribution of different species to PC1 and PC2 for size-selected particles collected in the FM2000 engine regime. Left panel - positive SIMS polarity, right panel - negative SIMS polarity. 79

3.18 Separation of size-selected particulates obtained in the FM2000 (fuel system malfunction) engine regime by the hierarchical clustering analysis based on positive polarity SIMS spectra. 80

3.19 Integrated peak areas of positive and negative SIMS fragment ions of interest normalized to the total ion count (TIC) for particles produced in the FM2000 engine regime (low air/fuel ratio). The error bars represent the standard deviation among all analyzed zones of the same sample. 81

© 2020 Tous droits réservés. lilliad.univ-lille.fr

3.20 (a) Mass defect plot obtained from positive polarity SIMS mass spectrum of the $OM2000_{100-180}$ sample (addition of oil, medium load, 2000RPM). Four different chemical classes are highlighted: oxygenated species (blue), aliphatic fragment (red), aromatic species (green), and hopanes/n-alkanes (purple). To improve the readability, the marker size was kept constant. (b) A zoomed in portion of the mass defect plot showing the alignment of homologous chemical compounds. The size of the markers is proportional to the corresponding peak integrated area. Molecular formulas of homologous species are displayed. 82

3.21 Score plots of PCA performed on SIMS data (positive polarity) revealing sample separation according to (a) engine regime and (b) main source of particles. The blue and green arrows indicate the main trends in various classes of compounds extracted from the loadings plots (Figure 3.22). 83

3.22 Loading plots of PC1 and PC2 components corresponding to the PCA analysis displayed in Figure 3.21. (a) Separation of engine regimes. (b) Separation of main source of particles. 83

3.23 Mass spectra of $NH2000_{FF/BF}$ and $NH2000CS_{FF/BF}$ samples (polydisperse particles and gas phase collected with and without the catalytic stripper) obtained with HR-L2MS ($\lambda_d = 532\,\text{nm}$, $\lambda_i = 266\,\text{nm}$). The desorption and ionization fluences were optimized for a maximum signal of unfragmented molecules. The displayed mass spectra correspond to an average of four spectra obtained in different zones of the same sample. 85

3.24 (a) Score plot of the first two principal components for polydisperse soot (**pp**) and gas phase (**gp**) samples ($NH2000_{FF/BF}$ and $NH2000CS_{FF/BF}$). Ellipses highlight different sampling regimes (with and without the CS) and are for visual purposes only. The meaning of each principal component, derived from its loadings plot (Figure 3.25), is illustrated with arrows. (b) Hierarchical clustering analysis performed on the results of PCA (first five components, HCPC). The obtained clusters are displayed on the score plot of the first two principal components. The same color code as in (a) is used here. 87

3.25 Loadings plots for the first two principal components obtained from the mass spectra of polydisperse particles and gas phase sampled with and without the catalytic stripper ($NH2000_{FF/BF}$ and $NH2000CS_{FF/BF}$): PC1 - upper panel, PC2 - lower panel. 88

3.26 Two-way hierarchical clustering heat-map for ions of $NH2000_{FF}$ and $NH2000CS_{FF}$ samples. The correlation between masses in individual samples is expressed as relative value and represented by the cell color. Several zones on the heatmap that determine the separation between samples are highlighted. For instance, the separation between cluster 4 (magenta) and the rest of the samples (cluster 1 (red), 2 (blue), and 3 (green)) is primarily determined by the different contribution of OC-related (e.g. aromatic species) and EC-related (C_n^+) species. . . 89

© 2020 Tous droits réservés. lilliad.univ-lille.fr

3.27 Volcano plots showing the "differential expression" of detected chemical species on different samples. Coloured markers are associated with compounds that have, at the same time, a high statistical significance and fold change, while grey points correspond to chemical species that have either a low statistical significance or fold change, and thus do not contribute to the separation between two spectra. (a) Comparison between the particulate and gas phase sampled without the catalytic stripper ($NH2000_{FF}$ and $NH2000_{BF}$), (b) Comparison between the chemical composition of the particulate phase sampled with and without the catalytic stripper ($NH2000_{FF}$ and $NH2000CS_{FF}$), (c) Influence of the catalytic stripper on the chemical composition of the gas phase ($NH2000_{BF}$ and $NH2000CS_{BF}$). 91

3.28 Loadings plots for the first two principal components obtained from the mass spectra of polydisperse particles and gas phase samples collected with and without the catalytic stripper in two different engine regimes (NH1200 and NH2000, Table 2.3): PC1 – upper panel, PC2 – lower panel. 92

3.29 Score plot of the first two principal components for the polydisperse soot particles and gas phase samples obtained with and without the catalytic stripper in two different engine regimes (NH1200 and NH2000, Table 2.3). The arrow indicate the meaning of the principal component derived from the corresponding loadings plot (Figure 3.28a). 92

3.30 Volcano plots showing the "differential expression" of chemical species between: (a) the particulate phase (front filters) collected in different engine regimes without the catalytic stripper ($NH2000_{FF}$ and $NH1200_{FF}$), (b) the particulate phase collected in different engine regimes with the catalytic stripper ($NH2000CS_{FF}$ and $NH1200CS_{FF}$). Coloured markers are associated with compounds that have, at the same time, a high statistical significance and fold change, while grey points correspond to chemical species that have either a low statistical significance or fold change, and thus do not contribute to the separation between two spectra. 93

3.31 Mass spectra of size-selected particles produced in the NH2000 engine regime and sampled with (red line – NH2000CS) and without (blue line – NH2000) the catalytic stripper. The labels indicate the NanoMOUDI size-bin that was used to collect the size-selected particles. All displayed spectra have been obtained by averaging the signal recorded in 4 different zones of each sample. 95

3.32 (a) Score plot of the first two principal components obtained from mass spectra of size-selected particles collected with and without catalytic stripper (NH2000 and NH2000CS, Table 2.3). The arrows show the meaning of the principal components derived from their loadings. (b) HCPC performed on the first five principal components (explaining more than 82% of the variance). The biggest clusters correspond to: small particles collected with the catalytic stripper ($NH2000CS_{10-18}$ and $NH2000CS_{18-32}$) – black markers, small particles collected without the catalytic stripper ($NH2000_{10-18}$, $NH2000_{18-32}$, and $NH2000_{32-56}$) – green markers, and bigger particles collected in both regimes – red markers. 95

3.33 Loadings plots of the first two principal components obtained from the mass spectra of size-selected particles collected with and without the catalytic stripper (NH2000 and NH2000CS). 96

© 2020 Tous droits réservés. lilliad.univ-lille.fr

3.34 Schematic representation of the experimental setup used for simultaneous online volatile mass fraction measurements and particle sampling. The on-line particle characterization was performed with a series of Aerodynamic Aerosol Classifier (AAC), differential mobility analyser (DMA), optional catalytic stripper (CS) and subsequent centrifugal particle mass analyser (CPMA) followed by a condensation particle counter (CPC). 97

3.35 Variation of the volatile mass fraction with the particle size obtained from online aerodynamic-mass-mobility measurements (A. Boies, University of Cambridge). 97

3.36 (a) Score plot of the first two principal components obtained from mass spectra of size-selected particles collected with and without catalytic stripper (NH2000 and NH2000CS) with datapoints corresponding to the smallest particles (10 – 18 nm) highlighted. (b) Volcano plot for the smallest analyzed particles ($NH2000_{10-18}$ and $NH2000CS_{10-18}$) showing the "differentially expressed" species that result in the separation by PCA of the two samples, Figure 3.32. Coloured markers are associated with compounds that have, at the same time, a high statistical significance and fold change, while grey points correspond to chemical species that have either a low statistical significance or fold change, and thus do not contribute to the separation between two spectra. 98

3.37 Mass spectra of size-selected particles produced in the NH1200 engine regime and sampled with (red line – NH1200CS) and without (blue line – NH1200) the catalytic stripper. 99

3.38 Score plot of the first two principal components obtained from the mass spectra of size-selected particles collected in the NH1200 and NH2000 engine regimes without (a) and with (b) catalytic stripper. The arrows indicate the meaning of principal components obtained from their corresponding loadings. 100

3.39 Loadings plots of the first two principal components obtained from mass spectra of size-selected particles collected in the NH1200 and NH2000 regimes with the catalytic stripper. 100

4.1 (a) Schematic representation of the "signal decay" approach: adsorbate coverage evolution upon successive laser irradiation (at constant fluence, F_0) of the same spot on the sample surface. (b) Recorded mass spectra corresponding to two distinct desorption laser pulses (left – 1st pulse, right – 13th pulse). (c) Signal (pyrene) recorded by the mass spectrometer for the first 15 laser pulses successively applied on the same spot of a pyrene / activated carbon sample. (d) Schematic representation of the "fluence curve" approach – different zones of the sample irradiated with single laser pulses of various fluences. (e) Recorded "fluence curve". 108

© 2020 Tous droits réservés. lilliad.univ-lille.fr

4.2 Schematic representation of the laser desorption / laser ionization / ToF-MS experimental arrangement. The desorption laser beam (green) with a top-hat transverse beam profile forms a 700μm spot on the sample surface. The desorbed neutral molecules form a "plume" (dark yellow) which propagates from the sample surface (z axis) toward the ionization region situated in between the extraction electrodes of the Time-Of-Flight (TOF) mass spectrometer. A pulsed UV ionization laser beam (purple, y axis) intersects the desorption plume 100 μs after the desorption beam hits the surface. The obtained ions are then extracted and accelerated (x axis) toward a 1-meter long reflectron TOF mass spectrometer (see Section 2.2.2.2). 109

4.3 Temperature variation of physical parameters used for temperature profile calculations sourced from the literature: the density of graphite and activated carbon (*ac*), specific heat capacity of graphite and *ac*, and thermal conductivity of graphite and air. 118

4.4 Temperature profiles calculated for activated carbon (blue lines) and graphite (green lines) obtained for F_{des} = 32 mJ cm^{-2}: (a) temporal variation of the temperature in the center of the irradiated spot T(x=0, y=0, z=0, t), (b) temperature depth profile in the center of the sample at t=5.5 ns, T(x=0, y=0, z, t=5.5 ns). The temporal profile of the desorption laser is plotted for comparison (red dashed line). 119

4.5 (a) Comparison between temporal evolution of the desorption rate for pyrene molecules desorbing from activated carbon and graphite (with an initial surface coverage of 10^{-3} monolayers) induced by adsorption of an identical laser pulse. (b) Temporal evolution of the desorption rate of pyrene from activated carbon for successive laser pulses. The temporal laser profile is shown for comparison (red dashed line). . . . 120

4.6 (a) Example of a Markov chain obtained during fitting of experimental data with equation (4.11). The convergence of the fit is depicted with a red dashed line. The last portion of the chain (orange line) is used to determine the posterior distribution of the fitted parameter (b). The distribution is then used to identify the most probable value and variance of the determined parameter. 122

4.7 Symbols: pyrene molecule signal recorded in the same experimental conditions ($F_{des} = 32\ mJ\,cm^{-2}$) from four different zones (A, B, C, D) of the same pyrene / activated carbon sample (homogeneous coverage). Solid lines: most probable (mode) fits returned by the Bayesian posterior distribution for each individual dataset. Dashed line: effective temperature model decay curve generated with average parameter values. 124

4.8 (a) Experimental signal decay recorded for pyrene desorbing from activated carbon ($F_{des} = 32\,mJ\,cm^{-2}$, four zone average data points) along with the fits with the "effective temperature" (red dashed line) and transient (green dashed line) models. The fits correspond to the mode of the Bayesian posterior distribution of E_{ads}. (b) Bayesian posterior distribution retrieved with the "effective temperature" (top) and transient temperature model (bottom). Shaded areas represent the 95% credibility intervals of E_{ads}. 125

© 2020 Tous droits réservés. lilliad.univ-lille.fr

4.9 (a) Steady-state model fitted to the "fluence curve" recorded for pyrene desorbing from activated carbon. Each data-point is the average of the signal obtained in four different zones of the same sample, irradiated with the same fluence. (b) Posterior distribution of adsorption energy retrieved with the "effective temperature" model. The most probable fit (mode of the distribution) is plotted (dashed line) in (a). 127

4.10 (a) Symbols: four-zone averaged experimental data for pyrene (blue) and coronene (purple) desorbed in the same experimental conditions ($F_{des} = 43\,mJ\,cm^{-2}$) from the same (pyrene+coronene) / activated carbon sample (homogeneous coverage). Dashed lines: effective temperature model decay curves calculated with average parameter values from Table 4.3. Solid lines: transient temperature model decay curves calculated with average parameter values from Table 4.3. (b) Symbols: average experimental data for pyrene (blue) and coronene (purple) desorbed from multiple zones of the same (pyrene+coronene) / activated carbon sample (homogeneous coverage) for a range of desorption fluence values. Dashed lines: effective temperature model fluence curves calculated with average parameter values from Table 4.4. 128

4.11 Pb^+ isotopes (m/z 204–208) detected by 532 nm laser desorption of the lead/activated carbon prepared sample / 266 nm laser ionization of the ejecta / time-of-flight mass spectrometry. 129

4.12 (a) Symbols: four-zone averaged experimental data for lead desorbed in the same experimental conditions ($F_{des} = 104\,mJ \cdot cm^{-2}$) from the same lead/activated carbon sample (homogeneous coverage). Dashed lines: decay curves calculated with average parameter values from Table 4.3. (b) Symbols: average experimental data for lead desorbed in the same experimental conditions from multiple zones of the same lead/activated carbon sample (homogeneous coverage). Dashed line: effective temperature model fluence curve calculated with average parameter values from Table 4.4. 130

4.13 Experimental datapoints (four-zone average) recorded with the "signal decay" approach for pyrene desorbing from (a) graphite sheet ($F_{des} = 50\,mJ\,cm^{-2}$) and (b) HOPG ($F_{des} = 61 mJ\,cm^{-2}$). Steady-state (red dashed line) and transient (green dashed line) decay curves calculated with parameters from Table 4.3. 131

4.14 Comparison between Raman spectra of three different carbonaceous samples used in adsorption energy studies: activated carbon, graphite sheet, and HOPG. Spectra were deconvoluted into two bands: D and G. 132

4.15 Laboratory flame byproducts deposited on a Ti wafer with a home-built impactor (top left) and Raman/fluorescence spectra recorded on various zones of the sample. The sampling technique enables the separation of the two phases present in combustion byproducts: particulate and gas phase. The sample contains three different concentric regions: center – corresponds to soot particles and gas phase condensed on their surface, first light circle – gas phase (condensable gas) adsorbed on Ti wafer, and the second, darker circle – a mixture of the two phases containing a lower amount of soot particles. Raman spectra of each zone of the sample (bottom panel) illustrate a significantly different response. 134

4.16 Signal decays corresponding to different zones (soot, condensed gas phase, and soot+gas phase) of the sample shown in Figure 4.15. . . . 134

© 2020 Tous droits réservés. lilliad.univ-lille.fr

5.1 Top panel – 3D representation of the new ion source installed on the HR-L2MS instrument that combines laser desorption and laser ionization with optical microscopy. Bottom panel – Internal layout of the new ion source illustrating the relative position of optical microscopy elements. The sample, positioned horizontally on a motorized platform, is irradiated at normal incidence by a desorption laser beam, focused on its surface with the Cassegrain objective (the same objective as used for microscopy). The ionization laser intercepts the expanding plume in an orthogonal direction. The ions are then guided into the inlet of the ion source, described in Section 2.2.2.3. 141

© 2020 Tous droits réservés.

lilliad.univ-lille.fr

List of Tables

1.1 Overview of historic and current European Union emission standards for passenger cars. 9

2.1 List of studied engine regimes. The Indicated Mean Effective Pressure (IMEP, bar) indicates the load applied to the engine. 15
2.2 Engine specifications (b/aTDC – before/after Top Dead Center) . . . 16
2.3 List of samples collected in different engine regimes and with different sampling techniques. 20
2.4 List of the samples synthesized for adsorption energy measurements (Chapter 4). 23
2.5 DC voltages applied to various electrodes and octapole segments. Octapole segments (S_{1-7}) and transfer lens (L_3) can be switched between two voltage levels (**Voltage 1** and **Voltage 2**) to axially move the position of a potential well and trap the ion packet, Figure 2.24(top panel). 40

3.1 Deconvolution of the TERS spectra for particles 2, 3, and 4. 68
3.2 List of molecular and atomic species, along with their exact mass, detected by (low-resolution) L2MS with two different ionization wavelengths. Only the most intense peaks are shown. 71
3.3 List of molecular and atomic species, with their exact mass, detected with SIMS in positive polarity. The mass assignment accuracy is better than 20 ppm for all listed peaks. Peaks that have been associated with the substrate are not shown. 76
3.4 List of molecular and atomic species, with their exact mass, detected with SIMS in negative polarity. The mass assignment accuracy is better than 20 ppm for all listed peaks. Peaks that have been associated with the substrate are not shown. 77

4.1 Typical characteristics of adsorption processes. 111
4.2 B parameters calculated from (Equation 4.5) for activated carbon particles and graphite, along with physical parameters sourced from the literature (references in brackets) and used in the calculation. . . 114
4.3 Main parameters derived with the "signal decay" experimental approach with the steady-state and transient models. Mean values and error bars are computed using the procedure described in Section 4.4.2. 126

4.4 Estimated adsorption energy (E_{ads}) and B parameter for 3 species desorbing from distinct environments. Values of E_{ads} were retrieved using the fluence curve experimental approach, mathematically described by the "effective temperature" model. The reported values represent the average parameters computed with the procedure described in Section 4.4.2. 127

© 2020 Tous droits réservés. lilliad.univ-lille.fr

Chapter 1

Introduction

1.1 Atmospheric aerosols

Atmospheric aerosols are suspensions of liquid, solid, or mixed particles in the air. The particle size may span more than four orders of magnitude (from nanometer to tens of microns) and the bulk/surface chemical composition exhibit a huge variety, reflecting diverse origins and atmospheric processing. Understanding the sources, properties, and evolution of these particles in the atmosphere is one of the major challenges in environmental research today.

Atmospheric aerosols are commonly categorized based on their formation pathway as being either primary or secondary [1]. Primary aerosols are emitted in the atmosphere as particles (solid or liquid) by processes such as bulk-to-particle conversion (*e.g.* wind blown dust from arid regions), liquid-to-particle conversion (*e.g.* sea-salt aerosols), emissions of pollen and spores by vegetation, combustion processes (*e.g.* carbon particles emitted during wild fires), and volcanic eruptions (*e.g.* volcanic ash). In contrast, secondary aerosols are formed in the atmosphere by chemical reactions from precursor substances (gases) by gas-to-particle conversion. Common examples of secondary aerosols in the atmosphere are sulphates, nitrates, and secondary organic aerosols. In addition, aerosols can be classified based on their natural or anthropogenic source. Some aerosols have mainly natural origins (*e.g.* dust, sea salt, volcanic ash, and volcanic sulphates), while others result, at least partly, from human activities (*e.g.* carbonaceous particles, ammonium sulphate, and ammonium nitrate). The concentration of anthropogenic aerosols in the atmosphere significantly increased from the start of the industrial revolution [1]. Since most of the natural aerosols have relatively large dimensions (*e.g.* mineral dust and sea salt), they account for the largest aerosol mass in the atmosphere (2200 – 24000 Tg/yr). Anthropogenic aerosols, on the other hand, exhibit on average a smaller size and thus show a lower global mass emission rate (320 – 640 Tg/yr) [2].

1.1.1 Impact of aerosols on climate

The estimated contribution of aerosols and various gases to the radiative forcing of the climate (*i.e.* the perturbation to the global energy balance due to a change in the climate system) is presented in Figure 1.1. Even though aerosols have a small mass or volume fraction and a relatively short atmospheric lifetime, ranging from a few days to a few weeks (in contrast to greenhouse gases with lifetimes up to a

© 2020 Tous droits réservés. lilliad.univ-lille.fr

Thèse de Dumitru Duca, Université de Lille, 2020

century or more), they can still contribute significantly to the radiative forcing, and thus influence the weather and climate. Aerosols interact both directly and indirectly with the Earth's radiation budget and climate. As a direct effect, the aerosols scatter and absorb radiation from the Sun, referred to as direct radiative forcing. A large concentration of inorganic aerosols will tend to scatter sunlight back into space (*e.g.* sulfate, nitrate aerosols), hereby preventing the direct radiation from reaching the surface which induces cooling of the Earth–atmosphere system. Such an increase in the reflected solar radiation at the top of the atmosphere is nearly identical to the reduction in the solar radiation at the surface. While the direct radiation is prevented from reaching the surface, more scattered light is available which can affect the photosynthesis process, and thus improve plant productivity. Carbonaceous aerosols (*e.g.* black carbon) absorb and scatter solar radiation. Their presence in the atmosphere results in the absorption of both direct solar radiation and the one reflected from the surface. Therefore, black carbon aerosols have primarily a heating effect on the atmosphere with an estimated radiative forcing of +0.65 [+0.25 – +1.09] $W\,m^2$ [1, 3], representing approximately one third of that of CO_2.

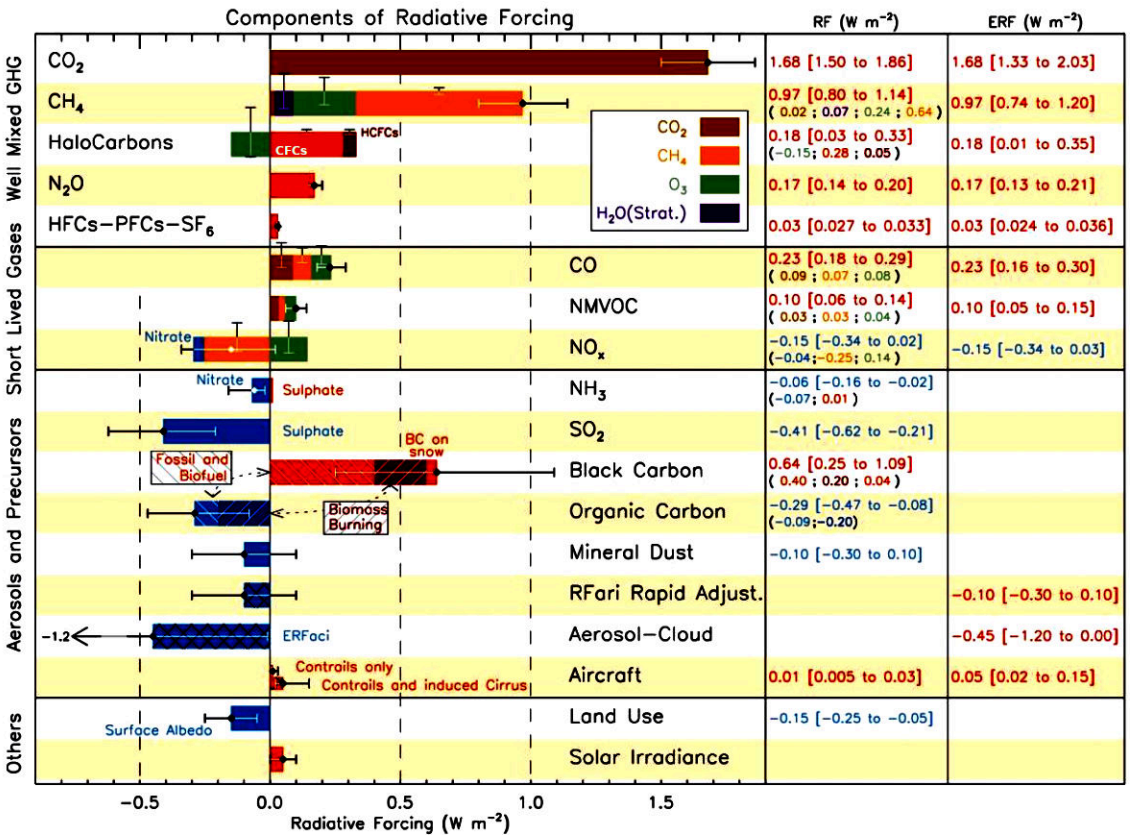

Figure 1.1 *Summary of the radiative forcing in 2011 relative to 1750 shown for various emitted components, reproduced from The Climate Change report [1]. Horizontal bars correspond to the overall uncertainty of a group while the vertical bars show the error associated with individual components. CFC = chlorofluorocarbons, HCFC = hydrochlorofluorocarbons, HFC = hydrofluorocarbons, PFC = perfluorocarbons, NMVOC = Non-Methane Volatile Organic Compounds, BC = black carbon, ERF – effective radiative forcing.*

As an indirect effect, aerosols in the lower atmosphere can modify the size of cloud particles, changing how clouds reflect and absorb solar radiation, and thus

© 2020 Tous droits réservés.

lilliad.univ-lille.fr

Thèse de Dumitru Duca, Université de Lille, 2020

modify the Earth's energy budget (indirect radiative forcing). Cloud droplets require an initial "seed" to start the condensation of water which is provided by aerosols. Changes in aerosol characteristics can therefore lead to changes in cloud properties. For example, the sulfate aerosols (coming primarily from anthropogenic sources) can cause the augmentation in the number of cloud droplets while also reducing their size. The resulting clouds reflect more sunlight than they would have reflected without the presence of these aerosols. In addition to making the clouds more reflective, it is also believed that such clouds have a longer atmospheric lifetime [4]. Since some aerosols can have a cooling effect, they were proposed as a means of mitigating global warming caused by large emissions of greenhouse gases (geo-engineering), either by using them near the Earth's surface to increase cloud formation, or by injecting them into the stratosphere to reflect the incoming solar radiation [5]. However, the impacts of such schemes are complex and uncertain.

1.1.2 Impact of aerosols on human health

In addition to their effects on climate, aerosols have also an impact on human health. Clean air is considered a basic human requirement, therefore air pollution (with gases and aerosols) has become a serious worldwide problem. According to a recent World Health Organization (WHO) report [6], approximately 7 million people die every year from air pollution-related illnesses, such as stroke and heart diseases, respiratory illness, and cancer, a number that significantly increased over time [7]. On a global scale, air pollution is the second leading risk factor together with tobacco smoking, surpassed only by high blood pressure. The size of particulate matter (PM) determines how the human body deals with the pollutant. Particles larger than 100 μm are usually too large to be inhaled. Aerosols with a diameter ranging from 10 to 100 μm usually get processed by the in-built defence mechanisms of the body – mucus membranes in the respiratory system [8, 9]. Particles between 1 and 10 μm (coarse mode) are most frequently deposited in the nose, pharynx and larynx while aerosols smaller than 1 μm in size (fine mode) have a high chance of penetrating deep into the lungs, reaching bronchioles and alveoli [8, 9], Figure 1.2. Coarse-mode particles are dominated by inorganic species, such as minerals and sea salt. Fine and coarse aerosols can also contain some minor components that might be relevant in defining aerosol sources and toxicological properties, such as black carbon (BC), transition metals, and aromatic or halogenated organic species [10]. The presence of additional chemical species on the surface of aerosols, for instance polycyclic aromatic hydrocarbons (PAH) present on the surface of combustion-generated particles with many of them exhibiting a carcinogenic/mutagenic potential [11–13], considerably increases the health impact of aerosols, extending their effects beyond the lungs [14]. In fact, the presence of combustion-derived nanoparticles (ultra-fine mode, $<0.1\,\mu$m) has been detected in the frontal cortex of autopsy brain samples [15], urine of healthy children [16], and even in the fetal side of the placenta [17]. If transported to the fetus, these particles, as surface carriers for potentially toxic species, could significantly affect fetal health and development [17].

Since there is a close, quantitative relationship between exposure to high concentrations of small particulates and increased mortality, air quality regulations have been introduced as a measure of protecting the general population from exposure to high levels of particulates. Fine and ultra-fine aerosols have health impacts

© 2020 Tous droits réservés.
lilliad.univ-lille.fr

Thèse de Dumitru Duca, Université de Lille, 2020

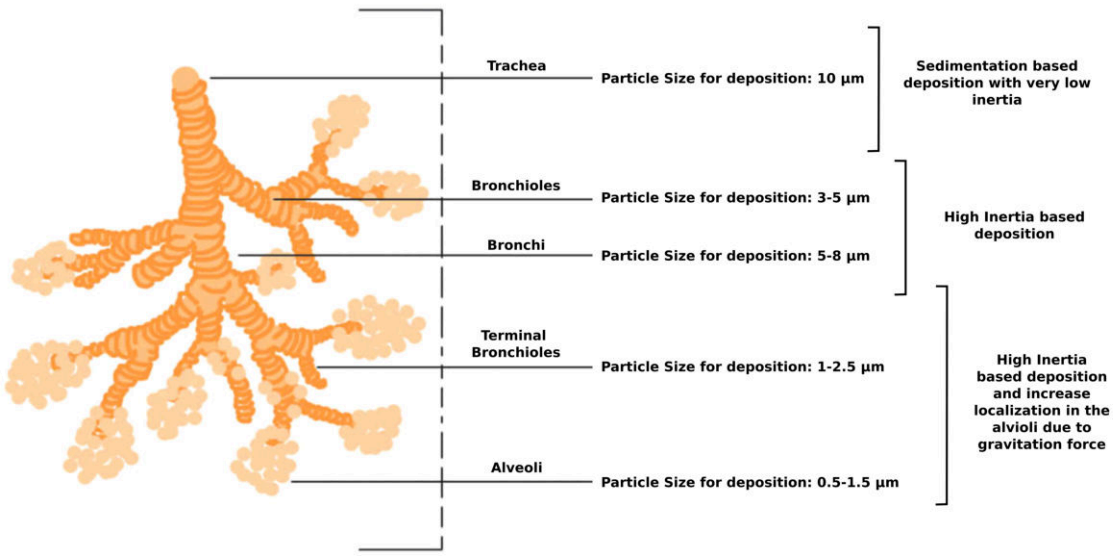

Figure 1.2 *Schematic diagram representing deposition of particles with different sizes in the lungs due to various mechanisms. The diagram shows that smaller particles deposit primarily in the lower airways. Reproduced from Sankhe et al. [9].*

even at very low concentrations and therefore the guidelines proposed by WHO aim to achieve the lowest possible PM concentration [7]: 10 μg/m^3 annual mean and 25 μg/m^3 24-hour mean for particulate matter smaller than 2.5μm ($PM_{2.5}$), and 20 μg/m^3 annual mean and 50 μg/m^3 24-hour mean for coarse particulate matter ($< 10\,\mu$m, PM_{10}). It is estimated that reducing the annual average concentration of fine particles from levels common in many developing cities ($\sim$ 35 μg/m^3) to the WHO guideline level (10 μg/m^3) could potentially reduce the number of pollution-related deaths by 15%.

1.2 Combustion-generated carbonaceous aerosols

One of the major components of fine particulate matter is soot – carbonaceous particles emitted as unwanted byproducts from virtually every combustion process, from laboratory burners to internal combustion engines and forest fires. Depending on the source, soot particles usually have different structures, compositions, and absorption properties.

Soot formation is a complex process consisting of several rapid and successive mechanisms that are significantly impacted by combustion physical and chemical parameters. This process is a constantly studied aspect of combustion, not only because of its significance for internal combustion engine (ICE) development, but also for its environment implications, as soot particles exhibit a positive radiative forcing and represent an important source of atmospheric carbon. Under ideal conditions the combustion of hydrocarbons leads to the production of mainly carbon dioxide and water. Ideal conditions can correspond to stoichiometric composition of the combustible mixture, *i.e.* the content of the oxidizer such as oxygen is sufficient to completely oxidize all the present fuel. In practice, combustion conditions deviate locally from ideality. If the locally present oxidizer is not sufficient to react with all

© 2020 Tous droits réservés.

lilliad.univ-lille.fr

Thèse de Dumitru Duca, Université de Lille, 2020

the hydrocarbon fuel, in addition to CO_2 and H_2O, other products of incomplete combustion, such as carbon monoxide (CO), nitrogen oxides (NO_x), hydrocarbons (C_nH_m) and soot appear. Properties of soot particles that are emitted by a given combustor (*e.g.* ICE, laboratory flame) are determined by multiple factors, such as the time available for the soot formation and oxidation, and mixing between fuel-rich parcels and oxidizer. Their size spans the nanometer to micrometer range [18, 19], with morphologies going from simple spherical shape (*i.e.* primary particles) to complex fractal aggregates. Their nano-structure can be finely characterized using High Resolution Transmission Electron Microscopy (HR-TEM) [20–23], which shows that "young" soot particles (with a diameter smaller than 10 nm) typically have a disordered structure, consisting of short and curved carbon layers [20]. These small particles are thought to be formed from fast coalescence of precursor particles that act as nuclei for the condensation of gas phase species [24–27]. The nuclei might be formed by collision of polycyclic aromatic hydrocarbon (PAH) clusters [25, 28]. Furthermore, primary soot particles exhibit a core-shell structure with two different levels: a less structured inner core, potentially containing multiple nuclei [20], and a micro-crystalline outer shell, Figure 1.3. The inner core of the primary particle corresponds to the first nuclei produced during soot inception. The outer shell is composed of graphitized layers of carbon (crystallites) that are aligned parallel to the surface [29]. We notice however that the soot nucleation process is still a matter of intense debate and the scenario described here above is only a tentative one [30–33]. On the other hand, mature soot particles typically consist of many spherical primary particles, most of them having a diameter between 15 and 50 nm, combined in necklace-like agglomerates [34–36].

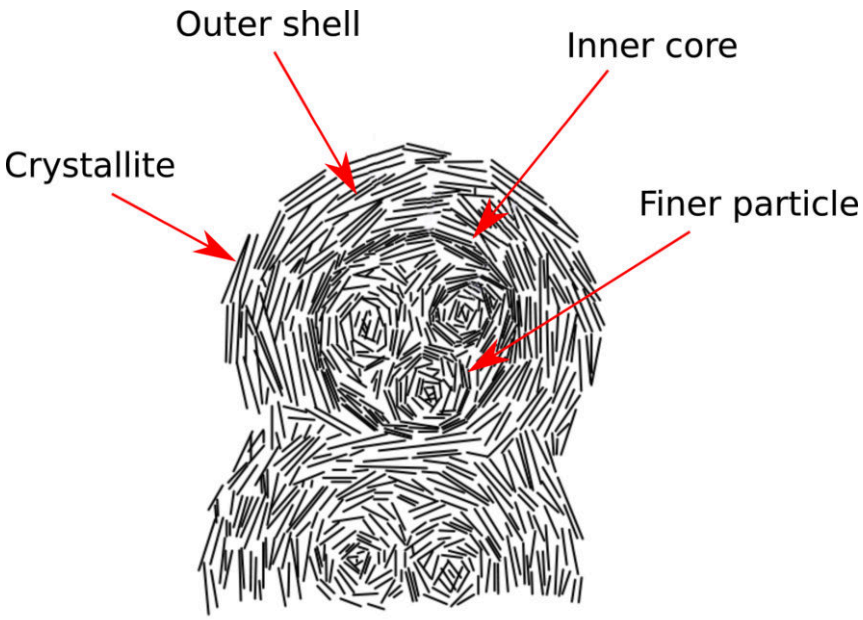

Figure 1.3 *Structure of Diesel soot particles obtained by Ishiguro et al. [20] via High Resolution Transmission Electron Microscopy.*

© 2020 Tous droits réservés.

lilliad.univ-lille.fr

Thèse de Dumitru Duca, Université de Lille, 2020

1.2.1 On-road vehicle emissions

Transport plays an important role in the modern industrial society. The transportation sector constitutes a major segment in many developed economies, with a total of over a billion motor vehicles worldwide. Traffic constitutes one of the major sources of combustion-generated carbonaceous aerosols (*i.e.* soot). Due to the large variability of on-road vehicles, traffic related PM emissions, including non-combustion sources *e.g.* brake, tire-wear, can have a size distribution ranging from coarse-mode to fine-mode particles [37], and is often dominated by combustion-generated submicron particles.

The main source of transport power over the past century has been represented by internal combustion engines. The ICEs are to date the most fuel-efficient engines for transportation purposes, due to their relatively high compression ratios and lack of throttling-related losses [38]. There are two types of ICEs: spark-ignition (SI) engines and compression ignition (CI) engines (*e.g.* Diesel engines)[39, 40]. In an SI engine, fuel and air are premixed, compressed, and ignited by a spark close to the end of the compression cycle, which results in an expanding turbulent flame. In a CI engine the fuel is not fully premixed with air, the combustion is initiated by auto-ignition of the fuel vapors as it mixes and reacts with oxygen inside the cylinder. Currently, the passenger car sector is dominated by SI engines operating on gasoline, while the commercial on-road vehicle fleet is mostly powered by CI engines using diesel fuel.

The emissions of ICEs strongly depend on their operation regime as it impacts the in-cylinder combustion conditions (*e.g.* fuel/air equivalence ratio, combustion temperature). This can be illustrated by the fuel/air equivalence ratio (ϕ) – temperature diagram presented in Figure 1.4 [38, 41]. The diagram shows contour plots of the ϕ-temperature combinations at which the formation of NO_x and soot occurs. As can be seen, a trade-off between the NO_x and PM production occurs. NO_x levels can be minimized if the in-cylinder temperature and oxygen content is decreased, however, this reduces the oxidation of soot particles, thus increasing their emitted mass and number. Low engine emissions (for both gases and particulates) can be achieved only by combining traditional emission reduction techniques (*e.g.* exhaust gas recirculation (EGR) used to lower the combustion temperature) with exhaust after-treatment systems, such as particle filters (PF) and catalytic strippers (CS) that only recently have been introduced on a large scale.

Changes in engine design are being driven by consumer demand for performance, drivability and affordability, as well as by legislative requirements aimed at promoting energy efficiency, energy security, and environmental protection. The emission of such compounds as nitrogen oxides (NO_x), unburned hydrocarbons (HC), carbon monoxide (CO), and particulate matter (PM) are being historically regulated. The air quality has been significantly improved in the past decades through the successive tightening of emission standards. Since the first passenger and heavy duty emissions directive (1970 and 1988 respectively), there has been an overall reduction of emissions on the order of 90% for CO, unburned hydrocarbons, NO_x, and particulates [42, 43]. These improvements are illustrated in the Figure 1.5. An overview of the past and current European emission standards for passenger cars and adopted by 17 out of 20 members of the G-20 countries (accounting for 90% of global vehicle sales [44]), is presented in Table 1.1.

Over the last 40 years, the method of regulating the PM emissions was based on

© 2020 Tous droits réservés.
lilliad.univ-lille.fr

Thèse de Dumitru Duca, Université de Lille, 2020

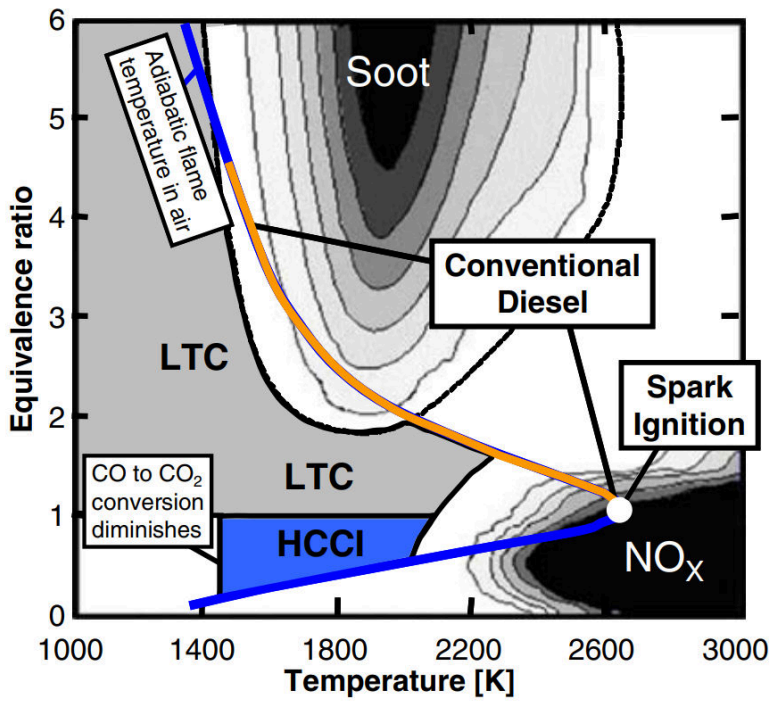

Figure 1.4 *Diagram showing the fuel/air equivalence ratio temperature ranges for soot and NO_x formation and the regions associated with conventional Diesel, spark ignition, homogeneous charge compression-ignition (HCCI), and Diesel low-temperature combustion (LTC) engines. Reproduced from Dec et al. [38].*

the gravimetric quantification of the PM mass collected by filters. With the introduction of Diesel Particulate Filters (DPFs) at the beginning of 2000s, the limit of detection of such a method was no longer sensitive enough to record PM concentrations. On the initiative of several European Union member states to develop a more sensitive and precise measurement methodology than PM mass measurement, the Particle Measurement Program (PMP) was launched in 2001 [45–47]. In 2007 PMP proposed the Solid Particle Number (SPN) measurement method that was based on the counting of solid particles < 23 nm. This measurement method was integrated into the European Union emission control legislation for light-duty vehicles in 2009. The new approach required the introduction of new definitions, most importantly that of a "solid" particle (which does not evaporate upon heating to 350°C). Along with emission standards, the introduction of a number of on-board computer diagnostics was mandated together with a compulsory "road-worthiness" test which ensures low emission levels throughout the lifetime of a vehicle.

In order to obtain an actual decrease in emissions and thus contribute to the reduction of air pollution in urban areas, a test cycle that reflects realistic driving conditions has to be used. In an effort to guarantee that the emissions of certified vehicles are in line with current limits during real driving conditions, a new and robust test procedure was introduced in September 2017. A single, laboratory-based test was replaced by two procedures: Worldwide Harmonized Light Vehicle Test Procedure (WLTP), performed under laboratory conditions, and the Real Driving Emissions test (RDE), thus narrowing the gap between the theoretical (emitted under ideal conditions) and the actual on-the-road emissions. The RDE test complements the laboratory procedure as it is conducted on the road with a Portable

© 2020 Tous droits réservés.

lilliad.univ-lille.fr

Thèse de Dumitru Duca, Université de Lille, 2020

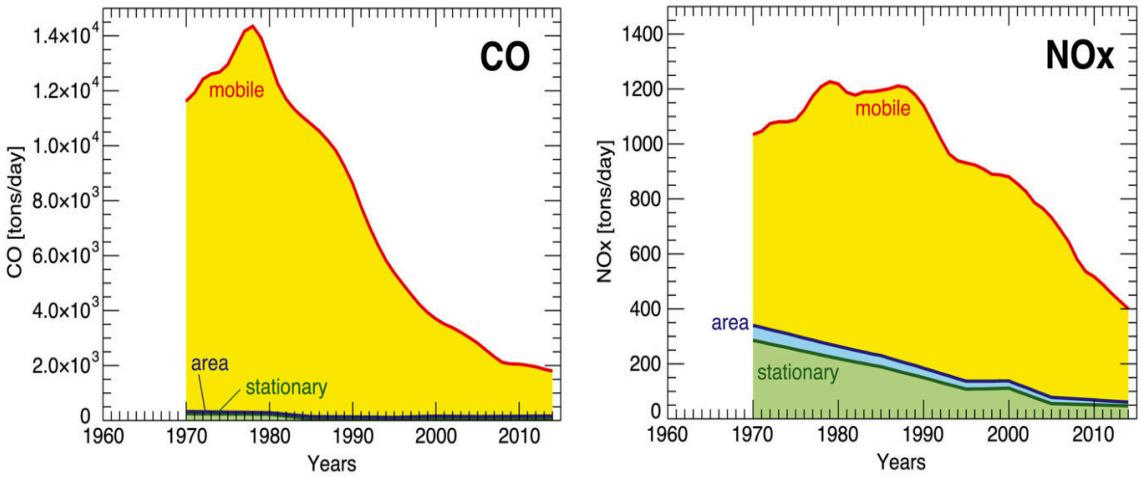

Figure 1.5 *Annual evolution of CO and NO_x emissions (day average) from different sectors. Emissions from transportation (mobile sources) are shown in red/yellow. Adapted from [48].*

Emissions Measurement System (PEMS). RDE test includes driving on urban, rural roads, and highways under a set of realistic conditions (*e.g.* uphill/downhill driving) and also capturing high-emission transitory regimes.

Major improvements in engine technology and the use of alternative fuels over the last few years have helped contain the environmental harm caused by PM emissions [49]. While NO_x and hydrocarbons emissions have been reduced along with the mass and number of emitted particles, one of the downsides has been the shift in the particle diameter toward smaller sizes (lower than 100 nm [50]), thus likely contributing to air pollution in urban areas, and becoming a greater public health issue [51–54]. Therefore, information about the particle number (PN) of ultrafine particles is becoming more and more valuable for vehicle certification. The current certification procedures have a cut-off size of 23 nm for measuring PN. However, sub-23 nm particles have recently attracted a lot of attention for mainly two reasons. First, sub-23 nm particles can be produced, and sometimes in large concentrations, by both Diesel and gasoline direct injection (GDI) engines (*e.g.* Giechaskiel et al.[55]). Second, the harmfulness of the particles has been shown to correlate better with surface area than with mass [56, 57], which becomes important for ultrafine particles even though their residence time in the atmosphere is shorter. It has been estimated that the percentage of sub-23 nm solid particles, which are not measured by current certification procedures, could reach 30–40% of the total PN for vehicles equipped with a GDI, and even higher levels when alternative fuels are employed [58]. Therefore, the critical lack of certification procedures for the measurement of ultrafine ($<$ 23 nm) particulate matter emissions should be addressed. Current efforts [59–61] focus on establishing solid scientific grounds to allow lowering the 23 nm limit to 10 nm, with the aims of providing robust particle number measurement methodology and associated instrumentation. PN measurements below this limit, although possible in principle (at least in well-controlled laboratory conditions), are challenging to implement as nanometer-size particles raise important sampling, measurement, and quantification issues, which can result in undesired biases and artifacts [62, 63].

© 2020 Tous droits réservés.

lilliad.univ-lille.fr

Thèse de Dumitru Duca, Université de Lille, 2020

Table 1.1 *Overview of historic and current European Union emission standards for passenger cars.*

Tier	Date		CO	THC	NMHC	NO_x	THC+NO_x	Particle mass	Particle number
	Approval	First Registration	[g/km]	[g/km]	[g/km]	[g/km]	[g/km]	[g/km]	[#/km]
Gasoline vehicles									
Euro 1	July 1992	January 1993	2.72	-	-	-	0.97	-	-
Euro 2	January 1996	January 1997	2.2	-	-	-	0.5	-	-
Euro 3	January 2000	January 2001	2.3	0.20	-	0.15	-	-	-
Euro 4	January 2005	January 2006	1.0	0.10	-	0.08	-	-	-
Euro 5a	September 2009	January 2011	1.0	0.10	0.068	0.060	-	0.005*	-
Euro 5b	September 2011	January 2013	1.0	0.10	0.068	0.060	-	0.0045*	-
Euro 6b	September 2014	September 2015	1.0	0.10	0.068	0.060	-	0.0045*	$6{\cdot}10^{11}$**
Euro 6c	-	September 2018	1.0	0.10	0.068	0.060	-	0.0045*	$6{\cdot}10^{11}$
Euro 6d-Temp	September 2017	September 2019	1.0	0.10	0.068	0.060	-	0.0045*	$6{\cdot}10^{11}$
Euro 6d	January 2020	January 2021	1.0	0.10	0.068	0.060	-	0.0045*	$6{\cdot}10^{11}$
Diesel vehicles									
Euro 1	July 1992	January 1993	2.72	-	-	-	0.97	0.14	-
Euro 2	January 1996	January 1997	1.0	-	-	-	0.7	0.08	-
Euro 3	January 2000	January 2001	0.66	-	-	0.50	0.56	0.05	-
Euro 4	January 2005	January 2006	0.50	-	-	0.25	0.30	0.025	-
Euro 5a	September 2009	January 2011	0.50	-	-	0.180	0.230	0.005	-
Euro 5b	September 2011	January 2013	0.50	-	-	0.180	0.230	0.0045	$6{\cdot}10^{11}$
Euro 6b	September 2014	September 2015	0.50	-	-	0.080	0.170	0.0045	$6{\cdot}10^{11}$
Euro 6c	-	September 2018	0.50	-	-	0.080	0.170	0.0045	$6{\cdot}10^{11}$
Euro 6d-Temp	September 2017	September 2019	0.50	-	-	0.080	0.170	0.0045	$6{\cdot}10^{11}$
Euro 6d	January 2020	January 2021	0.50	-	-	0.080	0.170	0.0045	$6{\cdot}10^{11}$

*Norms apply only to vehicles with direct injection engines

** $6{\cdot}10^{12}$ #/km within the first three years from Euro 6b effective dates

THC – total hydrocarbon, NMHC – non-methane hydrocarbons

1.2.2 Reactivity of carbonaceous aerosols

Aerosols can also act as favorable surfaces for chemical reactions to take place on (heterogeneous chemistry). The most significant of these reactions are those that lead to the destruction of stratospheric ozone. During winter in the polar regions, aerosols grow to form polar stratospheric clouds. Chemical reactions take place on the large surface areas of these cloud particles leading to the formation of significant amounts of reactive chlorine and, ultimately, to the destruction of ozone in the stratosphere. Evidence showing changes in the stratospheric ozone concentrations occurring after major volcanic eruptions have been gathered over the years (*e.g.* Mount Pinatubo, 1991).

Several studies have also examined the atmospheric role of reactions taking place on the surface of soot particles [64–68]. Some works suggested that reduction reactions involving soot surfaces may have an impact on the chemistry of stratosphere and troposphere. For instance, it was determined that the amount of ozone lost on soot particles may be non-negligible in a polluted boundary layer with a high mass concentration of particles [66]. Additionally, the reduction of HNO_3 to NO on black carbon has been proposed as a mechanism to explain the previously observed discrepancy between the calculated and measured NO_x/NO_y ratios in the troposphere [67]. Further, it has been shown that NO_2 reaction with soot in the atmosphere may be responsible for observed $HONO$ levels in the troposphere [69].

Due to its irregular agglomerate structure, carbonaceous aerosols are characterized by a large specific surface area, which leads to a high adsorptive capacity. This,

© 2020 Tous droits réservés. lilliad.univ-lille.fr

Thèse de Dumitru Duca, Université de Lille, 2020

in turn, increases the potential of such aerosol to act as surface carriers for a variety of chemical compounds such as PAHs and can lead to a long-range transport of toxic species adsorbed on the surface of these materials. PAHs, exhibiting carcinogenic and mutagenic potentials and present on the surface of soot particles may react with atmospheric oxidants to form nitrated or oxygenated derivatives [70]. Such derivatives can act as direct mutagens, believed to be more toxic than the parent PAH [71], and thus increase the danger of combustion-generated particles.

In this context, the study of the interaction between various chemical species and carbonaceous surfaces has a great importance. The identification of the adsorption mechanism on carbonaceous surfaces and its associated adsorption energy is beneficial for several reasons. First, it can provide necessary information to better understand, and potentially minimize, the health and climate impact of carbonaceous aerosols. Second, it can help design better carbon-based materials for industrial use, for instance materials designed for adsorptive fixation of organics/toxins in the gas and liquid phases for treating wastewaters and emission gases [72–75]. And finally, it can offer some insights into the complex and still only partially understood soot formation mechanism. This is possible since adsorption energies define whether the surface species (adsorbates) are chemisorbed or physisorbed, and therefore if the surface molecular compounds result from surface chemistry (remnants of the soot formation) or physical condensation [76].

1.3 Context of the study

The studies performed during this PhD thesis were carried out in the ANATRAC (Trace Analysis) research group from the PhLAM laboratory (UMR 8523 – Physique des Lasers, Atomes et Molécules) at the University of Lille. The ANATRAC group has developed highly-sensitive and selective laser-based mass spectrometry techniques. These techniques were optimized to specifically probe the chemical composition of combustion by-products [77–79]. The high sensitivity and selectivity toward specific classes of compounds make these techniques an extremely valuable analytical tool that can be adapted to various samples. In addition to laser-based techniques, a shared-use secondary ion mass spectrometer (SIMS) instrument, available at the Regional Platform of Surface Analysis (UCCS – Unité de Catalyse et Chimie du Solide, University of Lille) was also used in this study.
This thesis is separated into two main parts that have different objectives:

- The collection and physico-chemical characterization of size-selected soot particles emitted by a single cylinder gasoline engine.

- Fundamental adsorption studies of various chemical species on carbonaceous surfaces. This includes the development and validation of a novel laser-based method for determining the adsorption energy of adsorbed compounds.

The first part of this study was carried out in the framework of the H2020 PEMS4Nano project (`www.pems4nano.eu`) funded by the European Union's Horizon 2020 research and innovation programme under Grant Agreement no. 724145. It involved researchers and staff from nine organizations in five countries: Horiba Automotive Test Systems (DE), Robert Bosch GmbH (DE), CMCL Inovations (UK), TSI (DE),

© 2020 Tous droits réservés.
lilliad.univ-lille.fr

Thèse de Dumitru Duca, Université de Lille, 2020

University of Cambridge (UK), University of Lille (FR), IDIADA (ES), Horiba Scientific (FR), and Uniresearch (NL). The aim of this project was to develop a robust, reliable and reproducible particle emission monitoring system (PEMS) for both chassis dyno and real-driving conditions compliant with possible future particle number regulations (*i.e.* able to reliably count particles with a size down to 10 nm). The development of such a system required extensive knowledge of the physico-chemical properties of emitted particles, obtained by their thorough experimental characterization (morphology, structure, chemical composition, volatility, and reactivity as a function of their size). Four particle sampling campaigns were organized during this project at the engine test-bench provided by Robert Bosch GmbH (Renningen, Germany). My work focused on the collection of size-selected and polydisperse soot particles from the single cylinder test engine in a number of different engine regimes and their subsequent physico-chemical analysis. I performed comprehensive surface chemical characterization of the collected particles and conducted structural and morphological analyses of size-selected particles.

The second part of the thesis involved studies of more fundamental nature, with the ultimate objective being the development of a laser-based technique for measuring the adsorption energies of various compounds adsorbed on carbonaceous surfaces. The technique is to be applied to heterogeneous samples and thus can be used, for instance, for the study of soot reactivity. This involved the development of a theoretical model that links the adsorption energy of a compound with physical quantities that can be easily measured by laser-based mass spectrometry techniques available in the research group (*e.g.* signal recorded by the mass spectrometer upon irradiation of the sample with a pulsed laser). The model was supplemented by a mathematical apparatus that allows fitting of the experimental data with the theoretical model and adsorption energy retrieval. The developed method was subsequently validated on multiple standardized samples, involving various chemical species, as well as carbonaceous surfaces with varying structures.

1.4 Structure of the manuscript

The dissertation is structured in five chapters. The current (first) chapter presents the practical and scientific context of the work conducted during my PhD thesis. The impact of aerosol emissions on climate and human health is briefly reminded. The importance of carbonaceous aerosols, in particular produced by on-road vehicles, is introduced along with an overview of the past and current emission regulations meant to limit the particle pollution of the atmosphere. Finally, this part introduces the significance of the present study with regards to the current global pollution situation.

The second chapter presents all the experimental techniques / set-ups employed in this work. The chapter is subdivided into three sections describing: i) the collection (for combustion-generated carbonaceous particles) and synthesis (for laboratory-obtained standards) of samples, ii) the analytical techniques employed for their characterization, including mass spectrometry and microscopy techniques, and iii) the data-treatment methodology used for interpretation of experimental data.

The third chapter is dedicated to the characterization of both size-selected and polydisperse soot particles collected from a gasoline single cylinder engine (PEMS4-

© 2020 Tous droits réservés.
lilliad.univ-lille.fr

Thèse de Dumitru Duca, Université de Lille, 2020

Nano project). Particles collected in several different engine regimes were studied. The complementary information obtained with laser- and ion-based mass spectrometric techniques allowed the detection of a large variety of chemical species. Advanced statistical methods were used to interpret mass spectrometry data and identify size-related trends in the chemical composition of soot particles, as well as discriminate them according to the engine regimes where they were produced. The study of emissions collected from a simulated engine malfunction allowed the identification of chemical markers associated with different engine failure modes. The chapter ends with the study on the influence of a catalytic stripper, complying with European Union regulations, on the surface chemical composition of combustion emissions.

The development of an original laser-based method for the adsorption energy measurements is the subject of the fourth chapter. First, the derivation of the theoretical model describing laser-induced thermal desorption is detailed, followed by its experimental validation. The validation was performed with laboratory-obtained "surrogate soot" samples, having a known structure and chemical composition. A number of different adsorbate-adsorbent systems have been tested while comparing the results obtained from the newly developed method with literature values. The chapter ends with a discussion about the extension of the method toward field collected combustion-generated particles.

The fifth and final chapter summarizes the main results of my work, proposing several general conclusions and future perspectives. The work will be continued in both areas covered by this dissertation, specifically, in the physico-chemical characterization of combustion-generated particles, which also includes instrumental development, enhancing the capabilities of the mass spectrometric analytical technique, as well as in providing further refinement of the laser-based adsorption energy measurement method, through the launch of two new PhD theses.

© 2020 Tous droits réservés.
lilliad.univ-lille.fr

Chapter 2

Materials and Methods

This chapter provides a description of the experimental equipment used to generate, collect, and characterize several types of soot samples. Various analytical techniques were utilized to provide detailed information about the chemical composition (mass spectrometry techniques) and structure (microscopy and Raman) of the analyzed samples.

2.1 Collection / synthesis of samples

Two different types of soot samples were analyzed in this work. Samples were either produced by an internal combustion engine (ICE) or synthesized in the laboratory from standard carbon surfaces and known PAH molecules. The former were produced from the indirect control of a combustion-based source, whereas the latter were produced under controlled laboratory conditions with known carbon structure, surface chemical composition, and adsorbate concentration. The collection or synthesis of these distinct sets of samples served two different purposes: while ICE soot samples were produced to mimic combustion emissions generated by motorized traffic (Chapter 3), laboratory "surrogate soot" samples were utilized to develop a new methodology allowing the retrieval of the adsorption energy of molecules physisorbed on carbon surfaces (Chapter 4).

2.1.1 Internal combustion engine emissions

Engine soot samples were collected during four sampling/measurement campaigns that were organized in the framework of the PEMS4Nano project (see Chapter 3) and took place at the engine test-bench (Robert Bosch GmbH, Renningen, Germany). The goal of these campaigns was to collect combustion generated particles for a subsequent offline analysis, allowing to build an extensive database containing detailed physico-chemical characterization of ICE emitted particles. The purpose of the database was to serve as input to a theoretical approach (Model Guided Application, MGA) developed by CMCL Innovations (Cambridge, United Kingdom) and aiming to model particle formation in the engine, as well as particle dynamics in the exhaust system and sampling line, thus contributing to the development of a precise and reliable particle measuring system for automotive certifications. In order to obtain a comprehensive database, a variety of engine regimes had to be tested, thus simulating multiple operating conditions that are often encountered during real

© 2020 Tous droits réservés. lilliad.univ-lille.fr

Thèse de Dumitru Duca, Université de Lille, 2020

driving conditions. In order to exclude the possible impact of variables such as traffic and weather on engine emissions, a stationary test engine was used as stable and reliable source of soot particles. The advantage is that it can be easily tuned to operate in conditions equivalent to the ones encountered on the road.

Since the collection of material for offline analysis can be lengthy (up to 12 hours) the tested engine regimes must be carefully chosen to collect particles carrying the maximum amount of physico-chemical information within the time frame of the sampling campaign (typically one to two weeks). Two different variables related to the test engine were extensively studied: i) the engine working point, which includes different air/fuel ratios, applied loads and speeds, and ii) the influence of the mechanical state of the engine (*i.e.* the impact of various malfunctions). Additionally, the influence of a catalytic stripper on the chemical composition of emitted particles was investigated. A catalytic stripper (CS) is often used in vehicle exhaust after-treatment systems to remove hydrocarbons and sulfuric acid from the engine exhaust [80] and hence contributes to the reduction of emitted PM [81]. All the studied operating regimes along with their description are listed in Table 2.1.

The air-fuel ratio (AFR) of a well maintained spark ignition engine varies within the range 12:1 (rich) to 20:1 (lean) and depends on the condition of the engine (temperature, speed, load, fuel, etc.). The air-fuel ratio is usually represented by an equivalence factor – *lambda* corresponding to the ratio between the actual AFR and the ideal/stoichiometric ratio for the given fuel (*e.g.* 14.7:1 for EURO5 gasoline):

$$\lambda = \frac{AFR_{actual}}{AFR_{ideal}} \tag{2.1}$$

Modern internal combustion engines operate primarily around the stoichiometric ratio (lambda value close to unity). The deviation from $\lambda = 1$ depends on the tune of the engine as it can be optimized either for maximum power (slightly rich combustion, $\lambda \sim 0.9$) or best fuel economy (slightly lean combustion, $\lambda \sim 1.05$) [82]. A λ value of one is also preferable since most gas after-treatment systems are designed to have the highest efficiency when the engine operates in a narrow band around the regime with the stoichiometric mixture.

Two different air/fuel ratios were tested, one corresponding to an engine operating regime defined as optimal by the engine control unit (ECU, $\lambda \approx 1$, balanced regime compromising between power and fuel consumption) and a rich air-fuel mixture set point ($\lambda = 0.75$). Such a low λ value (for the given engine speed and torque) cannot occur during normal engine operation and is used instead to simulate a fault in the engine fuel injection system.

Sampling with an excess of lubricating oil in the combustion chamber was also performed. This was achieved by reducing the oil draining rate of the cylinder head, effectively raising the oil level above the valve guides and causing a small leakage of lubricant oil into the cylinder. Such a leakage simulates a common failure of the valve stem seals. These two engine regimes, simulating different malfunctions, were studied alongside conditions corresponding to normal engine operation with the intention to gather information about the contribution of the two main hydrocarbon sources (fuel and lubricant oil) to the chemical composition of engine exhaust, in particular soot particles. Such information will later help identify the main source of organic species contributing to size-selected particles emitted by a "healthy" engine.

The load applied to the engine is expressed in terms of Indicated Mean Effective

© 2020 Tous droits réservés.
lilliad.univ-lille.fr

Thèse de Dumitru Duca, Université de Lille, 2020

Table 2.1 *List of studied engine regimes. The Indicated Mean Effective Pressure (IMEP, bar) indicates the load applied to the engine.*

Designation	Speed, RPM	IMEP, bar	λ	Description
NM2000	2000	6	1.01	Normal operation regime
NH2000	2000	12	1.01	Normal operation regime
NH2000CS	2000	12	1.01	Normal operation regime, with CS
NH1200	1200	10	1.01	Normal operation regime
NH1200CS	1200	10	1.01	Normal operation regime, with CS
FM2000	2000	6	0.75	Fuel system malfunction
OM2000	2000	6	1.01	Oil system malfunction

Pressure (IMEP) – a uniform pressure that would be required throughout the power stroke of the engine to do the same amount of work as it is done by the pressure obtained from the fuel combustion. A "high load" (Table 2.1) corresponds to the highest load that could be applied to the engine (preserving its speed and λ value) that does not induce engine knock – abnormal combustion of one or more pockets of air-fuel mixture (outside of the normal combustion front)[83]. "Medium load" is the load equal to the average value between the IMEP of a free-running engine at the same rotational speed (no load applied) and the maximum possible IMEP (*i.e.* "high load").

Generated particles were collected for a subsequent off-line characterization, performed with multiple analytical techniques (Section 2.2). Since each characterization technique has a unique set of requirements for the sample (*e.g.* substrate material, coverage), multiple samples (different sampling times, substrate materials) were collected for each tested engine regime. Engine specifications and associated experimental setup utilized for combustion byproduct monitoring and collection are described in further details in the following section.

2.1.1.1 Test engine and sampling line

A single cylinder test engine was used in this work to generate particulate matter in the regimes listed in Table 2.1. The cylinder is similar to what is implemented on the Mercedes-Benz M272 V6 engine. A single cylinder engine is preferred over a multi-cylinder one to avoid any slight variations of combustion conditions between different cylinders and thus make the operating conditions more controllable.

In addition to liquid fuel (gasoline), the engine was set with an auxiliary injection port dedicated to gaseous fuels, which was used to prepare the engine before the production of soot particles intended for off-line characterization. Specifically, methane gas (at 6 bar injection pressure) was supplied to the engine. Its combustion served as a conditioning step used to warm up all engine components (*e.g.* exhaust port) and eliminate the possibility of contamination with particles left from the last engine run. After the cleaning procedure, with an average duration of 10–15 minutes, the engine was switched to liquid fuel operation, Euro Stage V E5 Gasoline: CEC-RF-02-08 E5, supplied by a two-piston dosing pump equipped with a pressure regulator compensating for pressure oscillations. The fuel was injected in the cylin-

© 2020 Tous droits réservés.
lilliad.univ-lille.fr

Thèse de Dumitru Duca, Université de Lille, 2020

der with a solenoid-type high-pressure fuel injector with six spray holes. The engine was equipped with pressure and temperature probes/sensors, monitoring the engine at the intake, exhaust port, and in-cylinder. The engine control and data sampling were done using LabVIEW [84]. The temperature of the engine coolant and that of the lubricating oil were maintained at 80°C during sampling of the combustion byproducts. Detailed engine and fuel specifications are indicated in Table 2.2.

Table 2.2 *Engine specifications (b/aTDC – before/after Top Dead Center)*

Specification		**Value**
Fuel		Euro Stage V E5 Gasoline (CEC-RF-02-08 E5)
Lubricant		Agip SIGMA, 10W-40
Cylinder head		Pentroof type
Compression ratio		12.5:1
Bore		82 mm
Stroke		85 mm
Stroke volume		449 cm^3
Fuel direct injection system		Central mounted generic six-hole injector
Fuel injection pressure		150 bars
Spark plug location		Exhaust side
Intake valve timing:	Open	334° bTDC
	Close	166° bTDC
Exhaust valve timing:	Open	154° aTDC
	Close	330° aTDC

As described in the introduction, combustion byproducts include gases of different nature and carbonaceous particles exhibiting distinct characteristics (*e.g.* stucture, size, composition or adsorption properties) all depending on the combustion conditions. In order to best characterize these emissions, it is necessary to account as much as possible for the different physical state of the molecules released in the exhaust and their specificity, especially regarding their size. For instance, one can wonder whether the smallest particles carry the same chemical information as the largest ones. To address these concerns (particulate matter versus gas phase and polydisperse versus size-selected particles), experimental solutions have been designed and implemented (two-filter system [85]) or integrated (*e.g.* Nano-Differential Mobility Sizer) to the home-built sampling line connected to the test engine (Figure 2.1, details given further below). However, each analytical technique employed here to reveal fundamental information about the particles' morphology and structure (Section 3.2) or chemical composition (Section 2.2.2) is subjected to a specific set of requirements regarding sample coverage (from individual particles to homogeneous coverage) and nature of substrates (*e.g.* copper grids, silicon wafers). Therefore, the analytical information that will be possible to extract from the collected samples will depend on the compatibility between these requirements and the collection scheme employed. Figure 2.1 illustrates the analytical and collection strategy put into operation.

A partial flow was taken from the exhaust duct, approximately 5 cm after the exhaust port and was then supplied via an 8 cm long transfer line to a DEKATI

© 2020 Tous droits réservés.
lilliad.univ-lille.fr

Thèse de Dumitru Duca, Université de Lille, 2020

FPS 4000 (Fine Particle Sampler) two-stage dilution system that prevented the condensation of volatile particles. The temperature of the primary dilution stage (hot dilution stage) was set to 180°C. The diluted exhaust was then cooled down to 35°C in the second, cold dilution stage. The overall dilution ratio of the DEKATI FPS 4000 was 1:30 (1:3 and 1:10 for the hot and cold dilution stages, respectively). After the diluter, the engine exhaust was split into three branches. The first branch consisted of a series of two instruments placed one after another to first, remove the volatile particles from the exhaust through the action of a home-built thermodenuder (350°C, dilution rate of 1:10), and second, monitor engine stability and particle production during sampling using an Engine Exhaust Particle Sizer (EEPS, TSI, model 3090). The second branch was used to collect size-selected particles for structural and morphological studies with a combination of a Nano-Differential Mobility Sizer (Nano-DMA, TSI, model 3085) and a Nanometer Aerosol Sampler (NAS, TSI, model 3089). Finally, the third branch further divides into two lines where the collection of size-selected particles was conducted with a NanoMOUDI II cascade impactor (TSI/MSP, model 125R), while the gas and polydisperse particle phases were sampled with a custom-built two-filter separation and collection system [85]. A detailed description of the sampling equipment and procedures used to collect size-selected and polydisperse particles will be presented in the following sections.

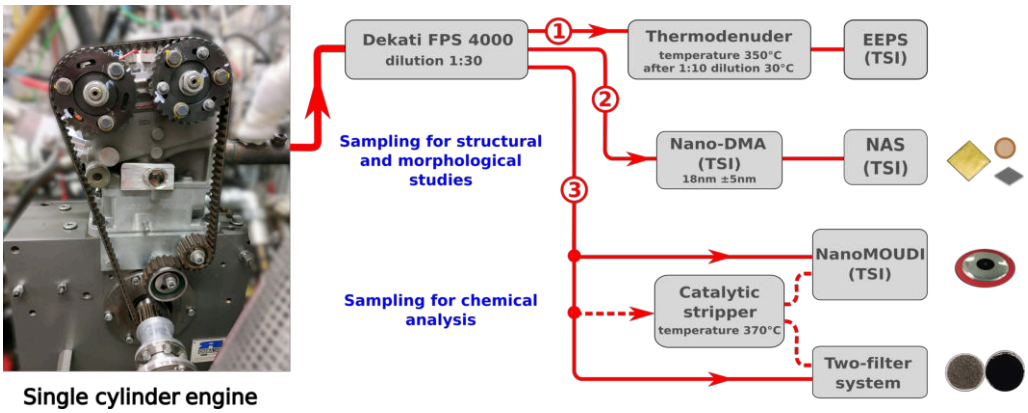

Figure 2.1 *Schematic representation of the sampling line used for engine monitoring and particle collection. The sampling of combustion byproducts for the chemical analysis (with NanoMOUDI and two-filter system) can be done with or without a catalytic stripper (represented by the dashed lines).*

A catalytic stripper (Figure 2.2) can be placed on the third sampling branch before the sampling equipment (either NanoMoudi or the two-filter system) in order to investigate its impact on the properties of particles sampled in different engine regimes. The CS was built by the University of Cambridge (A. Boies group) in a similar fashion to the commercially-available models (Catalytic Instruments). The coating was commercially available precious metal loading (100—300 g/ft^3) with an alumina wash coat. The CS was calibrated and monitored with a temperature controller to ensure that the centerline temperature of the aerosol flow achieves 350°C prior to entering the catalytic monolith contained within the device. The catalytic stripper performance in terms of hydrocarbon removal was tested to be >99% for 30 nm tetracontane ($C_{40}H_{82}$) particles at a concentration of >10^4 cm^{-3}. The particle penetration was >60% for 10 nm particles and the entire system residence time was 1–2 s.

© 2020 Tous droits réservés.

lilliad.univ-lille.fr

Thèse de Dumitru Duca, Université de Lille, 2020

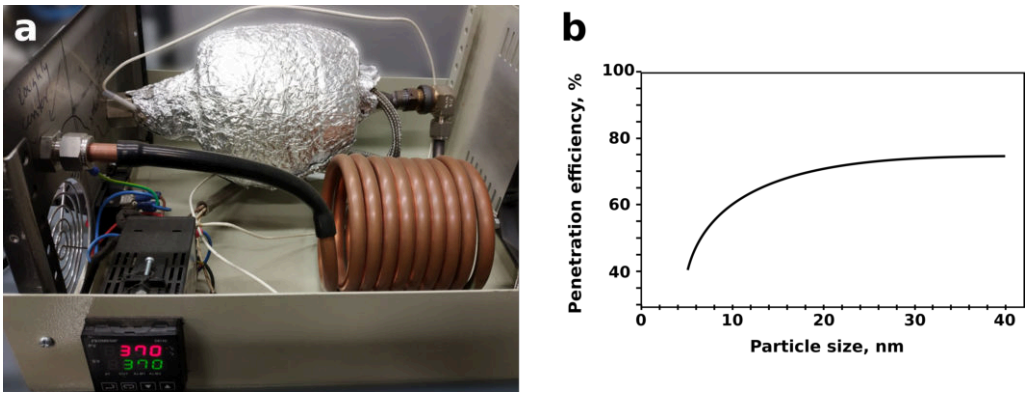

Figure 2.2 *(a) The custom-built catalytic stripper employed for the removal of organic species from the engine exhaust, (b) size-dependent penetration efficiency plot provided by the manufacturer of the catalytic stripper (University of Cambridge).*

2.1.1.2 Sampling of polydisperse particles and gas phase

Polydisperse soot particles and the gas phase were collected only for chemical characterization. To separate and collect both the particulate (polydisperse particles) and gas phases present in the engine exhaust, an original two-filter sampling system [85, 86] was used. The separation between two phases enabled an in-depth chemical characterization of both particle-bound species and the ones present in the gas phase. The new sampling system is comprised of two quartz fiber filters (QFF, Pall Tissuquartz QAT-UP 2500) placed one after the other, Figure 2.3. The front filter (FF) is used to retain the particulate matter entering the system, without size-selection, while letting through the gas phase (*i.e.* volatile organic components, NO_x, CO). The back filter (BF), placed 3.5 cm downstream of the front one and covered with a thin layer of activated black carbon particles (Pureblack 100 Carbon, Columbian Chemicals Company, specific surface 80–150 m^2g^{-1}) is used to adsorb the organic fraction from the gas phase that passed through the front filter.

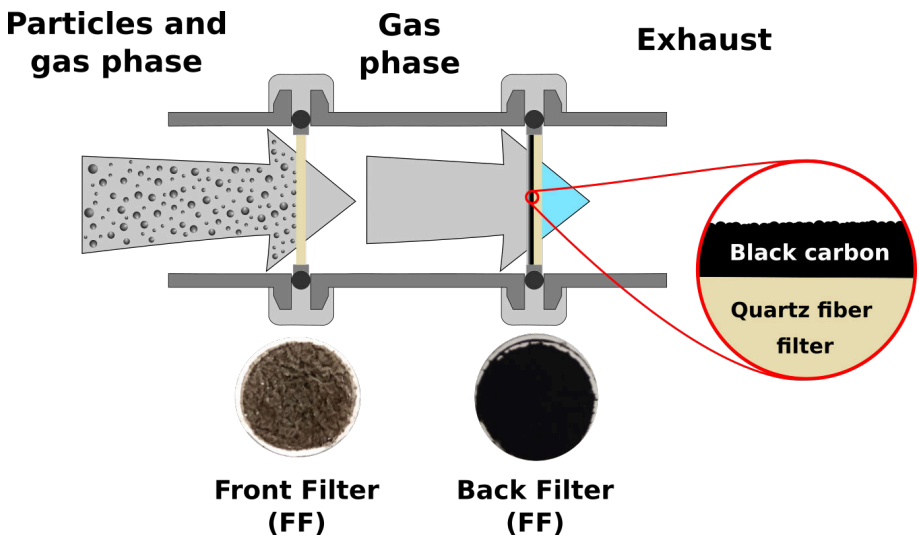

Figure 2.3 *Schematic representation of the two-filter sampling system used for the separation and collection of the particulate matter and gas phase from the engine exhaust. A set of collected filters (front and back) is also shown.*

© 2020 Tous droits réservés.

lilliad.univ-lille.fr

Thèse de Dumitru Duca, Université de Lille, 2020

The efficiency of the system to separate the gas and particulate phases present in combustion emissions was previously tested with the exhaust of laboratory flames and standardized soot generators [85, 86]. The front filter, retaining the particulate phase, shows a high contribution from semi- and non-volatile compounds while the back filter, corresponding to the adsorbed gas phase, is characterized by a much higher abundance of volatile species, as can be seen in Figure 2.4.

Before sampling, both front and back filters were heated in an oven at 200°C for at least 16 hours to remove pre-adsorbed species. For collection of exhaust, the two-filter system was placed on the third sampling branch connected either directly to the DEKATI diluter or the catalytic stripper, Figure 2.1. The sampling of polydisperse soot particles and gas phase was performed in several engine regimes, yielding eight different samples, Table 2.3. The collection of combustion byproducts was performed for 10 minutes (with and without CS) per engine set-point, a period long enough to obtain a uniform coverage of the front filter, Figure 2.3. In addition to the collected samples, a pair of blank filters (a clean QFF for the the FF and a carbon covered QFF for the BF) were prepared, later to be used as reference samples during the chemical characterization. The blank filters were stored and managed in a similar way to other collected samples.

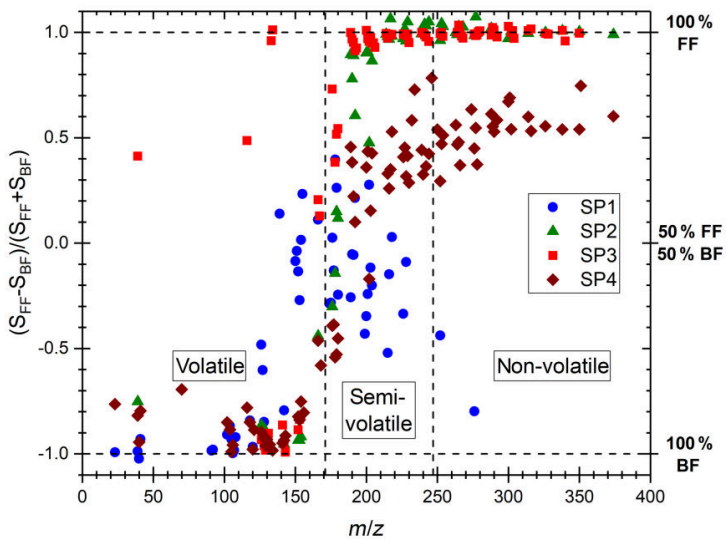

Figure 2.4 *A "contrast plot" illustrating the partitioning of organic species emitted by a miniCAST (Combustion Aerosol Standard) soot generator between the front and back filters. Results obtained in four different regimes (SP1–4) are shown here.* S_{FF} *and* S_{BF} *represent the signal of a chemical compound recorded with a Two-Step Laser Mass Spectrometer on the front and back filters, respectively. Values on the y axis correspond to the partitioning of the species between the filters: -1 indicates that the species are all found on the back filter, +1 that they are all found on the front filter, and 0 that they are equally partitioned on both filters. One can see that low mass species (volatile) are predominantly present on the back filter while higher mass compounds (non-volatile) are mainly found on the front filter. Reproduced from Ngo et al. [85].*

Since a multitude of samples were obtained, each one corresponding to a different engine regime as well as sampling method, a notation scheme that provides a short summary of all the necessary information about the sample was employed (< *engine regime* >< *description* >):

© 2020 Tous droits réservés.

lilliad.univ-lille.fr

Thèse de Dumitru Duca, Université de Lille, 2020

$$\mathbf{NH2000CS_{FF}} = \overbrace{\underbrace{\mathbf{N}}_{\text{normal op.}}\mathbf{H}}^{\text{high load}}\underbrace{\mathbf{2000}}_{\text{2000RPM}}\overbrace{\mathbf{CS}}^{\text{cat. stripper}}\underbrace{\mathbf{FF}}_{\text{front filter}}$$

Table 2.3 *List of samples collected in different engine regimes and with different sampling techniques.*

Designation	Engine regime	Sampling method	Substrate
$NM2000_{NAS}$	NM2000	NAS	Si wafer, TEM grid
$NM2000_{<size-bin>}$		NanoMOUDI	Al foils
$NH2000_{NAS}$	NH2000	NAS	Si wafer, TEM grid
$NH2000_{FF/BF}$		Two-filter system	QFF
$NH2000_{<size-bin>}$		NanoMOUDI	Al foils
$NH2000CS_{FF/BF}$	NH2000CS	Two-filter system + CS	QFF
$NH2000CS_{<size-bin>}$		NanoMOUDI + CS	Al foils
$NH1200_{FF/BF}$	NH1200	Two-filter system	QFF
$NH1200_{<size-bin>}$		NanoMOUDI	Al foils
$NH1200CS_{FF/BF}$	NH1200CS	Two-filter system + CS	QFF
$NH1200CS_{<size-bin>}$		NanoMOUDI + CS	Al foils
$FM2000_{<size-bin>}$	FM2000	NanoMOUDI	Al foils
$OM2000_{NAS}$	OM2000	NAS	Si wafer, TEM grid
$OM2000_{<size-bin>}$		NanoMOUDI	Al foils

2.1.1.3 Collection of size-selected particles down to 10 nm

In order to expose the variation of physico-chemical properties of soot particles with their dimensions, size-selected particles were sampled in various engine regimes. These particles were collected for subsequent structural, morphological and chemical investigations and, therefore, two different sampling methods were employed: one for sampling particles for microscopy analysis, and the other for chemical characterization.

Sampling of size-selected particles in a single narrow size range (18±5 nm) was performed with a combination of a Nano Differential Mobility Analyser (Nano-DMA, TSI, model 3085) and a Nanometer Aerosol Sampler (NAS, TSI, model 3089), the latter allowing size separation based on the electrostatic mobility of particles. Substrates intended for structural and morphological analysis using TEM encompassed SiN wafers (3.0x3.0 mm^2 Silicon Frame with 0.5x0.5mm^2, 10 nm thick Silicon Nitride membrane, Norcada) and TEM grids (lacey carbon films on copper grids, AgarScientific, AGS166H), while for SEM and AFM measurements the substrates were Si and Au coated Si wafers. The sample substrates were fixed to the electrode of the NAS as shown in Figure 2.5, ensuring a good electrical connection between the two. The particles charged by the Nano-DMA enter the electric field created between the ground chamber and the NAS electrode whereby they are directed towards the substrate and ultimately impinge on the surface. The sampler runs at a fixed flow rate and voltage for the entire sampling period. The collection time was adjusted

© 2020 Tous droits réservés. lilliad.univ-lille.fr

Thèse de Dumitru Duca, Université de Lille, 2020

based on the engine regime, according to the number of particles in the sampled size bin as reported by EEPS, and varied between 30 minutes and 1 hour.

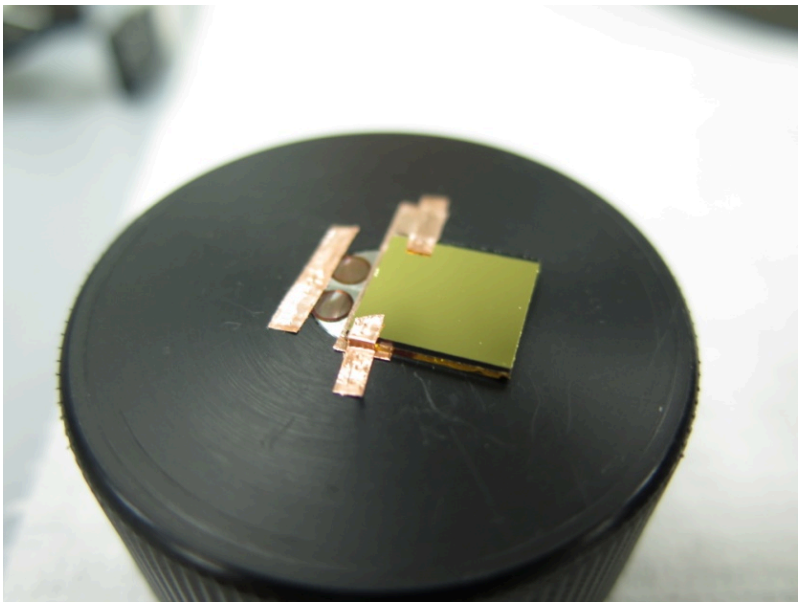

Figure 2.5 *The electrode of the NAS with three substrates attached (with copper tape): one gold-coated silicon wafer and two TEM grids.*

The collection of size-selected particles for chemical analysis was performed using a NanoMOUDI II (TSI/MSP, model 125R) 13 stage cascade impactor. It combines aerodynamic design and micro-orifice nozzles to reduce jet velocity, pressure drop, particle bounce and re-entrainment. NanoMOUDI works on the principle of inertial impaction [87]. At each stage, jets of particle-laden air exiting from nozzles impinge on an impaction plate. Particles larger than the cut-off size of the stage cross the air streamlines and are collected on the impaction plate. Smaller particles, with less inertia, do not cross the streamlines and can reach the next stage where the nozzles are smaller, the air velocity through them is higher and finer particles are collected. This principle continues through the cascade impactor. The NanoMOUDI has 13 stages with nominal cut-off sizes of 10000, 5600, 3200, 1800, 1000, 560, 320, 180, 100, 56, 32, 18, and 10 nm. The design of a stage, consisting of nozzle plate and impaction plate with substrate for deposition, is shown in Figure 2.6. Each impaction stage has embedded stepper motors used to rotate the collecting substrate for a uniform deposition, Figure 2.6b.

The NanoMOUDI was attached by a stainless steel line to either the Dekati FPS dilution stage or the catalytic stripper, Figure 2.1 . Al foils were chosen as substrates for the 13 impaction stages. To avoid any cross contamination that would skew the results of the chemical analysis, no coating was applied to the substrates prior to the sampling. The sampling time was adjusted depending on the engine regime in order to obtain sufficient particle coverage on the last impaction stage (10–18 nm) and varied from 6 to 12 hours. We remind that the focus of the project was the study of ultra-fine particles, specifically with sub-23 nm size. However, in order to derive meaningful trends in the chemical composition of particulate emissions, particles collected on stages with cut-off sizes up to 560 nm were analyzed, a size-range encompassing the majority of particles emitted by the engine (as illustrated by the size distribution recorded by the EEPS, Figure 2.7). All the samples associated

© 2020 Tous droits réservés. lilliad.univ-lille.fr

Thèse de Dumitru Duca, Université de Lille, 2020

with size-selected particles and collected from different engine regimes are listed in Table 2.3. In addition to samples containing size-selected particles, a blank Al foil and a QFF filter was prepared and stored in the same conditions as other samples, later to be used as reference samples during the chemical analysis.

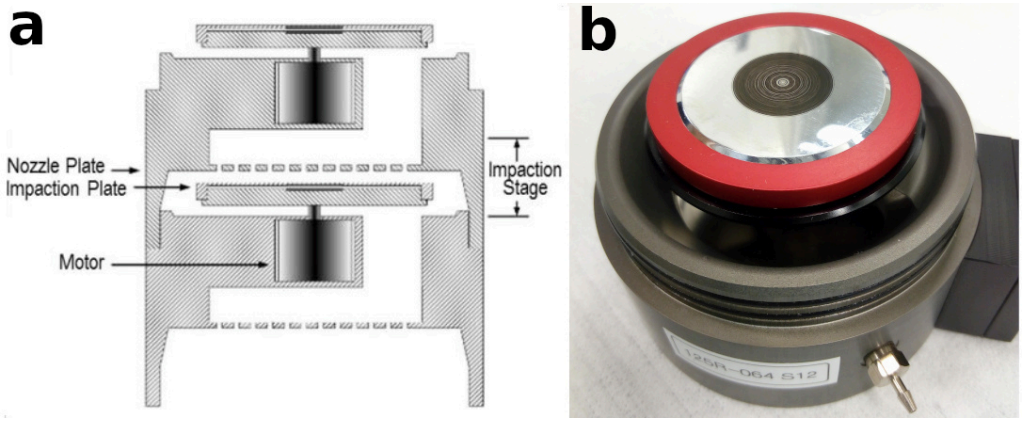

Figure 2.6 *(a) stepper motor impaction stage diagram of the NanoMOUDI, reproduced from the MOUDI II impactor catalogue (TSI)[88]. (b) Image of the aluminum foil substrate with deposited soot particles (18–32 nm size bin).*

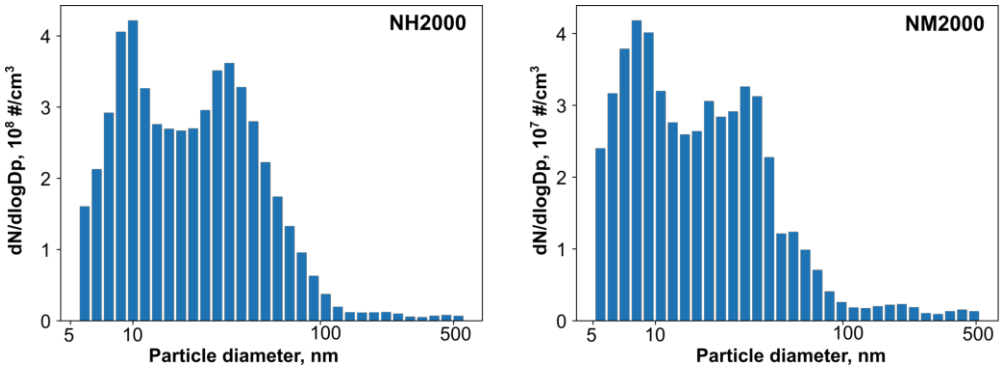

Figure 2.7 *Size distribution of particle emitted by the single-cylinder engine in two operation regimes and recorded by the EEPS.*

2.1.2 Preparation of "surrogate soot" samples

In the previous section the collection of ICE soot particles was described. Physicochemical characteristics of such particles (e.g. specific surface, porosity, chemical composition), in addition to being linked to the combustion conditions they originate from, show high variability with the size, as will be demonstrated in Chapter 3. The development and validation of a method for adsorption energy determination, described in Chapter 4, requires well characterized samples with constant properties. For these reasons, laboratory-synthesized "surrogate soot" was used, as it has a known and controllable surface chemical composition, while mimicking the structure of soot particles emitted by a real combustor.

Surrogate soot samples containing adsorbed PAHs or an inorganic salt were prepared in the laboratory following the protocol described by Faccinetto et al. (2015) [78]. Polycyclic aromatic hydrocarbons (pyrene and coronene, Sigma Aldrich, 98%

© 2020 Tous droits réservés.

lilliad.univ-lille.fr

Thèse de Dumitru Duca, Université de Lille, 2020

purity) were dissolved into dichloromethane forming solutions of known concentrations, which were subsequently mixed with activated carbon particles (Pureblack 100 Carbon, average particle diameter 80 nm, specific surface area 80–150 m^2g^{-1}). The mixture was then magnetically stirred for 2 hours, followed by vacuum filtration of the suspended powder onto a quartz fiber filter (Pall Tissuquartz QAT-UP 2500), forming a sub-millimeter thick soot layer on its surface. The amount of analyte left in the filtered solution was determined from UV-Vis extinction measurements [78], Figure 2.8, and enabled the calculation of the adsorbate surface concentration, Table 2.4 . A similar protocol (with the exception of the solvent - ultra-pure deionized water, Purelab Option-Q) was used to prepare surrogate soot samples containing lead, sourced from $PbCl_2$ salt (Sigma Aldrich, 98% purity).

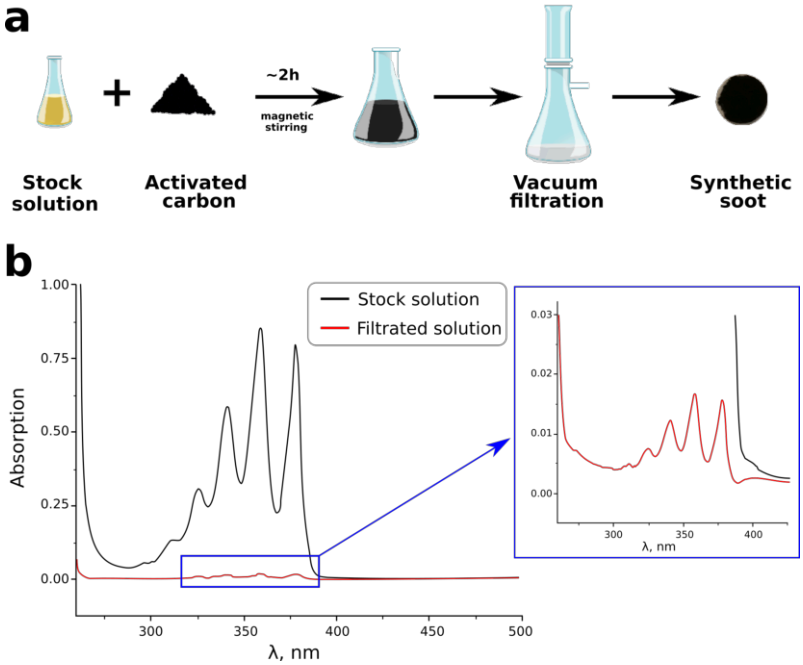

Figure 2.8 *(a) Block diagram of the surrogate soot preparation process, (b) UV-Vis extinction spectra of the original stock and filtrated solution of pyrene. The reduction in extinction is due to the adsorption of pyrene onto activated carbon particles.*

Table 2.4 *List of the samples synthesized for adsorption energy measurements (Chapter 4). The surface coverage (in mono-layers, ML) was determined from UV-Vis extinction measurements following the method presented in Faccinetto et al. [78].*

Nr.	Adsorbent/adsorbate system	Adsorbent	θ, ML
1.	Pyrene / activated carbon	Pyrene	$2 \cdot 10^{-3}$
2.	(Pyrene + Coronene) / activated carbon	Pyrene	$8 \cdot 10^{-3}$
		Coronene	$1.2 \cdot 10^{-3}$
3.	Pyrene / graphite sheet	Pyrene	$\leq 10^{-3}$
4.	Pyrene / HOPG	Pyrene	$\leq 10^{-3}$
5.	Pb / activated carbon	Pb	$\leq 10^{-3}$

© 2020 Tous droits réservés.

lilliad.univ-lille.fr

Thèse de Dumitru Duca, Université de Lille, 2020

In addition to samples based on activated carbon particles, other adsorbents have also been used. Specifically, samples based on (mm-thick) graphite sheet and HOPG (highly-oriented pyrolitic graphite) substrates were prepared and used to determine the variation of the adsorption energy with the structure of the substrate. The sample preparation procedure for these adsorbents is similar to the preparation of surrogate soot with the exclusion of the vacuum filtration step. Graphite (Alfa Aesar, graphite foil) and HOPG (Sigma Aldrich) exhibit significantly lower specific surface areas compared to activated carbon. The resulting adsorbate surface concentration is therefore at the limit of detection of the spectrophotometric method [78]. For this reason, only upper limits of the coverage ($\sim 10^{-3}$ ML) are provided in Table 2.4. The low coverages obtained for all sample ensures that no lateral interaction between adsorbate molecules is present. Moreover, due to the preparation protocol, the coverage can be considered homogeneous across the surface of all samples. A detailed characterization of the surrogate soot samples will be presented in Chapter 4.

2.2 Characterization techniques

Carbonaceous samples, collected either from an ICE or synthesized in the laboratory, were characterized with multiple off-line analytical techniques in order to investigate their physico-chemical properties. The structure and morphology of particles were studied with microscopy techniques (SEM (Scanning Electron Microscopy), TEM (Transmission Electron Microscopy), AFM/TERS (Atomic Force Microscopy / Tip Enhanced Raman Spectroscopy)) and Raman spectroscopy, while the chemical composition was probed using mass spectrometric techniques (Two-Step Laser Mass Spectrometry (L2MS) and Secondary Ion Mass Spectrometry (SIMS)). Note that the level of technical details provided for each analytical technique depends on the extensiveness of its utilization in this work.

2.2.1 Structural and morphological analysis

Structural and morphological studies were performed on samples containing size-selected particles collected with a combination of NAS and Nano-DMA (Section 2.1.1.3). The analysis was performed on duplicate samples, collected in the same engine regime but on different substrates, to avoid any cross-contamination or sample alteration, the latter possibly induced by the analytical technique. Since the samples were collected in the same conditions (in terms of engine regime and sampling method), the results obtained with different analyzing techniques are complementary.

2.2.1.1 Scanning and Transmission Electron Microscopy

Two types of electron microscopes were used for morphology studies: scanning- and transmission-based. The SEM used here was a Merlin Zeiss REM Supra 35VP instrument available at Robert Bosch GmbH analytical center (Renningen, Germany). The instrument features a spatial resolution of 1 nm and high detection efficiency. Images of the sample are produced by scanning the surface with a focused beam of electrons. The electrons interact with atoms in the sample, producing signals

© 2020 Tous droits réservés.
lilliad.univ-lille.fr

Thèse de Dumitru Duca, Université de Lille, 2020

that contain information about the surface topography and composition. Since the analyzed samples contained primarily ultra-fine particles, a low accelerating voltage (1kV) has been chosen. This decreased the size of the interaction volume, improved the spatial resolution, and decreased the impact of the electron beam on studied particles. Additionally, it enabled the study of ultra-fine combustion-generated particles without the need of applying a conductive coating. As SEM studies could be performed during the sampling campaign, the results were used to determine the sample surface coverage and adjust, if needed, the sampling time for other samples.

The TEM Tecnai G^2 microscope, available at the Platform for Materials and Transformations Analysis (Unité Matériaux et Transformations (UMET), University of Lille), was used for transmission-based morphology studies of particles. A beam of electrons at 20 kV is used to characterize the structure and certain properties of the solid material at the atomic scale. In the bright field mode, only the direct beam is allowed to pass through the sample, and the image is created from the weakening of the beam from its interaction with the material present on the sample. Thus, the thickest regions or areas containing heavy atoms will have the highest contrast. A high spatial resolution (1.9 Å) allows to study the structure of even the smallest particles. Moreover, by recording series of images of the same particle/aggregate obtained for different tilt angles of the sample holder it is also possible to create the 3D model of the particle, in other words, to reconstruct its shape (3D tomography) (Chapter 3).

2.2.1.2 Atomic Force Microscopy / Tip Enhanced Raman Spectroscopy

A NanoRaman system combining an atomic force microscope (AFM) with a Raman spectrometer (Xplora Nano, Horiba Scientific, Villeneuve d'Ascq, France) was used for AFM imaging and tip-enhanced Raman measurements. The topography of the sample was retrieved by "touching" the surface with a special mechanical probe (tip). High-resolution cantilever-based tips (Hi'Res C14/Cr-Au, μmasch, typical 1 nm-radius) were used for high lateral resolution. TERS measurements, in which the enhancement of Raman scattering occurs only at the point of a near atomically sharp tip, were performed in a reflection configuration allowing the use of an 100x objective lens (NA 0.7) with a 60° angle. The incident laser (633 nm, p-polarized) is focused through the objective onto the apex of the cantilever-based silver TERS probe (Ag coated OMNI TERS probe). The collection of the back-scattered signal is performed through the same objective. The reliable stability of the whole system allows the laser-tip alignment and accurate XYZ position to be maintained during the TERS map acquisition (at least 1 hour).

2.2.1.3 Micro-Raman spectroscopy

Raman spectroscopy is a spectroscopic technique used to determine vibrational modes of molecules, thus providing their structural fingerprint. This technique relies on the inelastic scattering of photons (Raman scattering), resulting in an energy shift. The shift in energy gives information about the vibrational modes present in the analyzed system and thus can inform on the molecular composition and structure of different samples. Consequently, Raman spectroscopy is frequently employed for characterization of carbon allotropes: the structural changes in graphitic carbon

© 2020 Tous droits réservés.
lilliad.univ-lille.fr

Thèse de Dumitru Duca, Université de Lille, 2020

materials [89], the determination of diameter and chirality of single-wall carbon nanotubes [90], and the structural characterization of graphene [91].

Activated carbon particles and graphite surfaces have been analyzed with a Raman spectrometer (Renishaw InVia Reflex) coupled with a confocal BFXM Olympus microscope (micro-Raman) available in our laboratory. The spectra were obtained by irradiation with a 514.5 nm laser with a maximum power at sample of 2 mW. The laser power was reduced from the nominal value (150 mW) to avoid sample alteration. Using a lens with 20x magnification (N.A. 0.5), the laser was focused on the surface of the sample to a spot of $\sim 3.0\,\mu$m diameter (irradiance max = 0.116 MW/cm^2). The spectrometer was calibrated using the Stokes Raman signal of pure Si (520 cm^{-1}). All the spectra were obtained with an extended scan (500–2200 cm^{-1}) using a 1800 grooves/mm diffraction grating, which gives a spectral resolution of about 4 cm^{-1}.

2.2.2 Chemical characterization

The chemical characterization of collected or synthesized samples was performed using mass spectrometry – an analytical technique used to identify unknown compounds within a sample, thus helping identify its chemical composition. Due to its sensitivity and versatility, mass spectrometry is quickly becoming the preferred analytical technique in numerous fields [92–94]. The general principle of mass spectrometry is to create gas-phase ions, separate them in space or time based on their mass to charge ratio (m/z) and then measure their relative abundances (intensities).

Combustion generated particles contain a multitude of chemical species associated with different chemical classes such as hydrocarbon species (including PAHs and aliphatic compounds), metal and sulfur-containing species that generally have a substantially different ionization potential. Exploring the complexity of such convoluted systems requires the use of several analytical techniques employing different desorption and ionization mechanisms, Figure 2.9. As mass spectra obtained with different desorption/ionization mechanisms provide information only about a fraction of chemical species, to obtain a detailed and complete chemical characterization of a sample, the information extracted from mass spectra obtained with different techniques must be combined.

In order to cover the majority of species present on the surface of the collected combustion generated particles, two mass spectrometric techniques were used in this study: i) L2MS which was implemented and developed in our laboratory and ii) ToF-SIMS, employing a commercial shared-use instrument available at the Regional Platform of Surface Analysis (UCCS, University of Lille). The operating principle and experimental conditions in which these two techniques were used are described below. Samples collected for chemical characterization had a relatively large size which allowed them to be divided into several equivalent portions, each analyzed on a different instrument.

2.2.2.1 Secondary Ion Mass Spectrometry

Secondary Ion Mass Spectrometry (SIMS) is a widely used technique for material characterization demonstrating high sensitivity to most elements in the periodic table. The use of this technique proved to be of high interest in several fields (*e.g.* material science, bioscience) and led to the emergence of several commercial versions

© 2020 Tous droits réservés.
lilliad.univ-lille.fr

Thèse de Dumitru Duca, Université de Lille, 2020

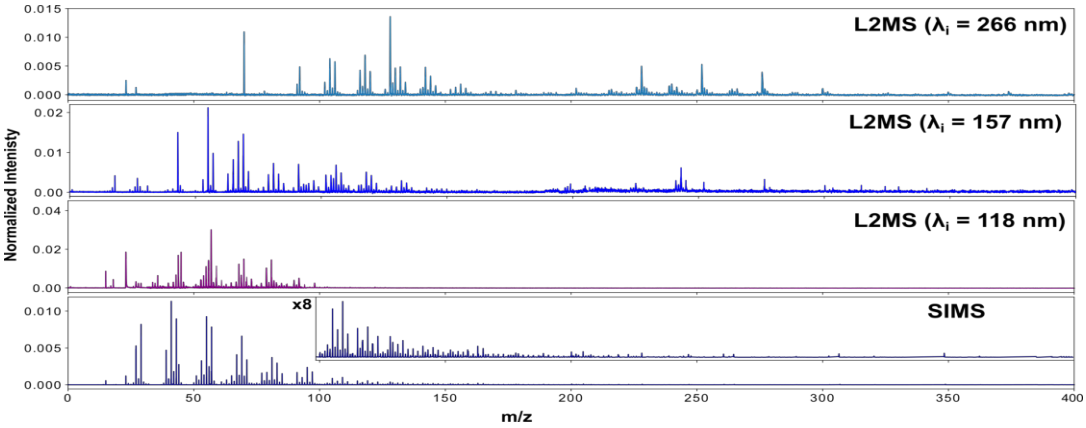

Figure 2.9 *Comparison between mass spectra of soot particles obtained with L2MS at different ionization wavelengths and SIMS. Different desorption and ionization mechanisms result in significantly different mass spectra, indicating that different chemical species have been targeted. For instance, the ionization of laser-desorbed species with a laser pulse at 266 nm results in a high signal from PAHs, while ionization at 118 nm will lead to preferential detection of aliphatic compounds.*

of the instrument. In this technique, secondary ions are ejected (sputtered) from the sample surface by primary-ion bombardment in a ultrahigh vacuum (UHV) environment. These secondary ions are individually detected and recorded as a function of their mass-to-charge ratio. The high sensitivity attainable by individual ion detection, and the high depth resolution are the principal attributes of SIMS.

A TOF.SIMS[5] instrument (ION-TOF GmbH) available at the Regional Platform of Surface Analysis was used in this study, Figure 2.10. For this instrument, the sample is attached to a sample holder and introduced through a load-lock into the analysis chamber with a residual pressure of 10^{-9} mbar. The sample is placed on a mobile stage where it can be visualised with an optical camera, thus allowing to select the zone for the analysis.

SIMS can be operated in two working modes: static and dynamic. In the static mode, where the sample surface remains relatively undisturbed, the majority of secondary ions originate from the top one or two monolayers of the sample. The ion dose is limited to a level at which every primary ion should always hit a fresh area of the sample. This mode is devoted to the surface molecular analysis. In dynamic mode, selected secondary-ion intensities are monitored as a function of sputtering time, yielding a depth concentration profile. Depth resolution is typically in the 5–20 nm range. This mode is primarily used for the depth distribution analysis of trace elements.

This work focuses mainly on the surface chemical composition and therefore only the static mode was employed. A mass spectrum obtained in this mode reveals characteristic molecular fragmentation patterns that help identify the surface chemical composition of the sample. Bi_3^+ was chosen as primary ion source, over such sources as Cs^+ and O_2^+, since it has a high ionization efficiency for organic species and a lower fragmentation probability of parent molecules. The energy of primary ions (Bi_3^+) was set to 25 keV with a current intensity of 0.29 pA. The primary ion source was forming a pulsed, tightly focused ion beam (50 nm diameter at the sample surface) with a pulse length of ∼1 ns which was rastered over a 500 μm x 500 μm zone. The penetration depth of the primary ions was typically 1-3 nm. Upon

© 2020 Tous droits réservés. lilliad.univ-lille.fr

Thèse de Dumitru Duca, Université de Lille, 2020

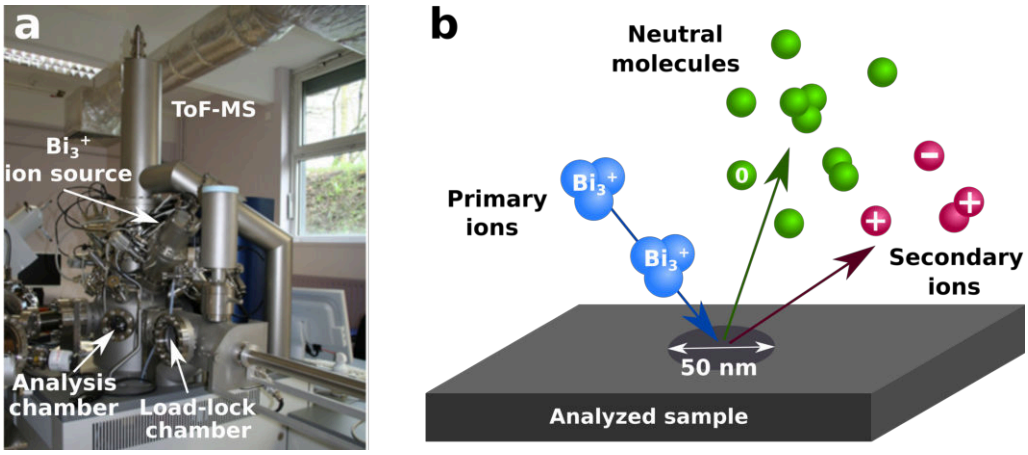

Figure 2.10 *(a) A photo of the ToF-SIMS[5] instrument and its main parts: load-lock chamber, analysis chamber, Bi_3^+ primary ion source, and ToF-MS mass analyzer. (b) SIMS working principle.*

bombardment, the energy of primary ions is transferred to the atoms of the sample. The energy transfer initiates a cascade of collisions between the atoms of the solid accompanied by the emission of atoms and molecules (*sputtering*), a small fraction of which is ionized (*i.e.* secondary ions), Figure 2.10. Both positive and negative ions can be analyzed thus providing complementary information about the surface chemical composition. Secondary ions are then extracted from the sputtered region and guided to the mass analyzer – a Time-of-Flight Mass Spectrometer (V-mode, average resolution m/Δm ∼ 4000–6000). The signal recorded at the detector can be either averaged over all measured pixels (128x128 pixels) to produce one spectrum, or extracted for each pixel which allows the mapping of measured species on the sample surface. The obtained spectrum was calibrated using several known secondary ions (at least four ions evenly distributed across the whole mass range). For this technique, the mass resolution depends not only on the instrumental parameters (*e.g.* primary ion pulse length) [95] but also on the sample itself. Specifically, low surface roughness is required in order to obtain high mass resolution.

2.2.2.2 Two-Step Laser Mass Spectrometry (L2MS)

The Two-Step Laser Mass Spectrometry (L2MS) technique is based on the coupling of Laser Desorption (LD), Laser Ionization (LI), and Time-of-Flight Mass Spectrometry (ToF-MS), Figure 2.11. This laser-based technique has been developed and extensively used by the ANATRAC group to characterize the chemical composition of combustion byproducts for more than 15 years [78, 79, 96–103]. The main advantages of L2MS are its high sensitivity and selectivity with regards to specific classes of compounds. Two different L2MS instruments were used in this study. The first one (Jordan TOF Products) is limited to a mass resolution of m/Δm ∼ 1000, while the second one can reach a mass resolution of about 15 000 (HR-L2MS, Fasmatech S&T). The second, high-resolution spectrometer was installed and optimized at the laboratory during this thesis. The operational principle of the L2MS technique will be first presented on the lower resolution L2MS instrument, then a detail description of the second instrument (HR-L2MS), highlighting the features allowing it to reach a much higher mass resolution, will be given.

© 2020 Tous droits réservés.

lilliad.univ-lille.fr

Thèse de Dumitru Duca, Université de Lille, 2020

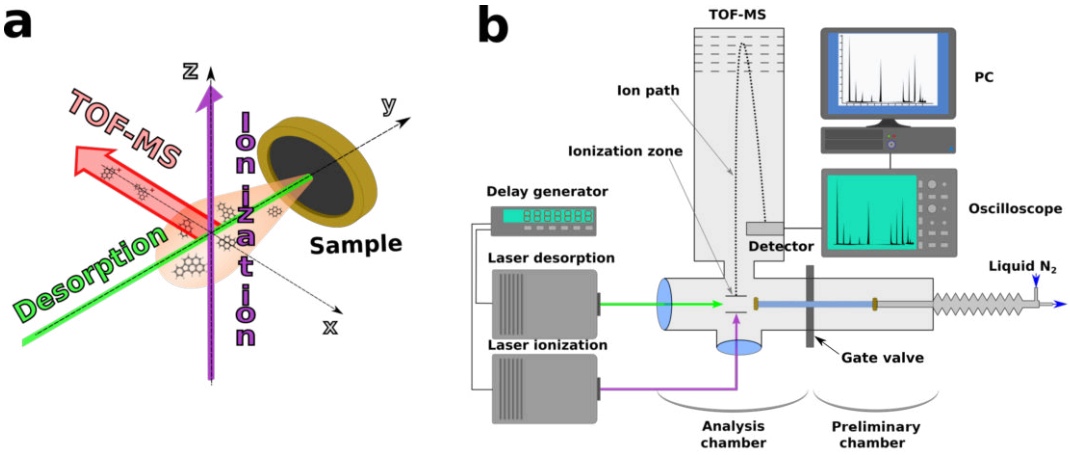

Figure 2.11 *(a) The three stages involved in the L2MS technique: i) Laser Desorption – the sample is irradiated by a nanosecond laser pulse (green) which promotes the ejection of molecules; ii) Laser Ionization (purple) – the ejected molecules are ionized by the second ns laser pulse (UV); iii) Mass Spectrometry (red) – the obtained ions are extracted and mass-separated in a ToF-MS. (b) Schematic representation of the Jordan Tof L2MS set-up.*

During L2MS analyses with the lower resolution instrument (Jordan TOF), the sample is placed on a temperature-controlled sample holder in the preliminary (sample introduction) chamber, Figure 2.11. The preliminary chamber is connected to the main analysis chamber (with residual pressure of 10^{-9} mbar) through a gate-valve. The sample holder incorporates a liquid nitrogen circulation loop intended to cool down the sample and thus prevent the sublimation of volatile species in the vacuum. The sample is only cooled down after the pressure in the preliminary chamber reaches 10^{-1} mbar. The temperature of the sample is monitored with a resistance temperature detector (RTD, PT100) and reaches -100°C during the analysis. After the sample reaches a low temperature and the residual pressure in the preliminary chamber goes down to 10^{-7} mbar the separation gate valve between the two chambers is opened and the sample is transferred into the analysis zone. The analysis of the sample starts with the step in which the molecules present on the surface are transferred from the condensed to the gas phase – laser desorption.

Laser Desorption

During the desorption process, the energy of a pulsed laser beam is used to transfer molecules/atoms from the sample surface into the gas phase. The absorption of the laser light induces localized heating of the sample leading to the ejection of neutral species. Typically, only a small fraction of the first monolayer is affected by the desorption process [104] transferring into the gas phase molecular species adsorbed/condensed on the surface without breaking the much stronger chemical bonds responsible for the structure of the sample (*e.g* of soot particles) [105]. The main criterion that separates this process from other, more destructive ablation phenomena [106, 107] (*e.g.* phase explosion, hydrodynamic sputtering, photomechanical spallation) is the laser fluence (*i.e.* pulse energy per unit of irradiated area) which is relatively low in the case of desorption. This parameter has to be carefully controlled in order to avoid extensive molecular fragmentation. Besides the laser fluence, the

© 2020 Tous droits réservés.

lilliad.univ-lille.fr

Thèse de Dumitru Duca, Université de Lille, 2020

desorption process is also influenced by the properties of the sample such as the optical absorption coefficient, thermodynamic properties, etc. Since only species present on the surface are desorbed and subsequently analyzed, L2MS can be qualified as a surface-sensitive analytical technique, comparable in limit of detection (10^{-6} monolayers) with static-mode secondary ion mass spectrometry (SIMS, Section 2.2.2.1), but with much lower analyte fragmentation [78].

For the carbonaceous samples studied here, the laser energy is primarily absorbed by the (black) carbon substrate [78, 105]. For this reason, the 2nd harmonic of the Nd:YAG laser (532 nm) was used for desorption (Continuum Minilite II laser, 4 ns pulse duration, 10 Hz repetition rate). A *quasi* top-hat transverse profile (∼0.7 mm diameter, measured with a Gentec Beamage-4M beam profiler) was used to ensure that the desorption of species present in the irradiated zone occurs in similar conditions. The optical path followed by the desorption laser beam is schematized in Figure 2.12. The quasi top-hat transverse intensity profile was obtained from the laser output beam by first enlarging it with a beam expander, built around a set of convergent (F= 250 mm) and divergent (F= –50 mm) lenses, and then selecting the quasi-flat central region (∼5%) of the beam with an adjustable diaphragm, which is further image relayed onto the sample surface using a convergent lens. The desorption laser beam enters the analysis chamber through a quartz window, crosses the mass spectrometer ionization/extraction region and irradiates the sample surface at normal incidence, Figure 2.13. The laser fluences on the sample surface used in this configuration were in the range 10–150 mJ/cm^2 for the majority of the samples. The optimal fluence values were individually determined for each sample as to obtain the highest possible analyte signal for the unfragmented analyte.

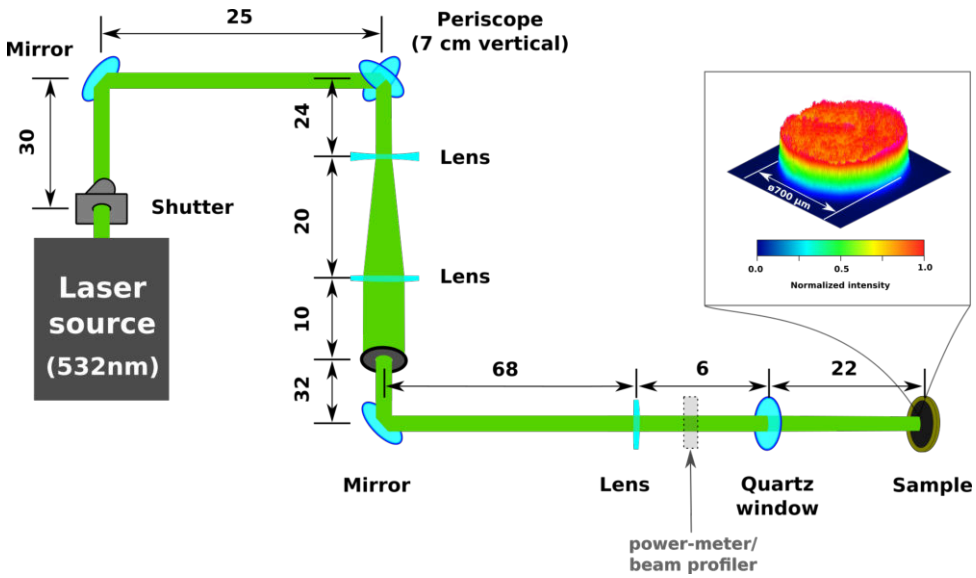

Figure 2.12 *Desorption laser beam optical path for the lower resolution L2MS setup. All distances are given in centimeters. The transverse beam profile at the sample surface is illustrated in the inset.*

The species ejected from the surface of the sample form a desorption plume rapidly expanding into the vacuum, with species having velocities of hundreds of m/s [108]. Given the low desorption fluence, the desorption plume consists predominantly of neutral molecules, and, therefore, an additional ionization step is required before the compounds can be mass analyzed.

© 2020 Tous droits réservés.

lilliad.univ-lille.fr

Thèse de Dumitru Duca, Université de Lille, 2020

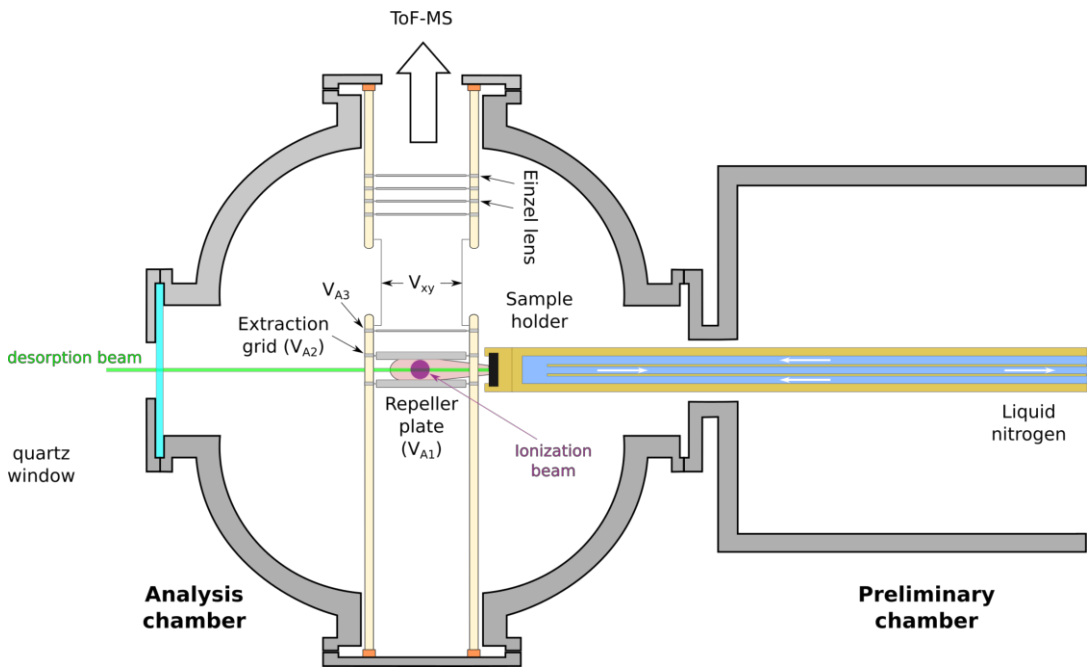

Figure 2.13 *Top view of the lower resolution ToF-MS analysis chamber.*

Laser Ionization

The ionization of desorbed species can be performed in several ways. Since the molecules present in the desorption plume can fragment upon ionization, the choice of a hard ionization method (*i.e.* ionization leading with high probability to the fragmentation of the parent molecule) can considerably reduce the amount of information that can be extracted from a complex mass spectrum (interpretation of a spectrum featuring a large number of fragments is more complex). Electron impact (EI) is a widely used method for ionizing species in the gas phase. However, this ionization technique, due to high electron energies, can induce extensive fragmentation which makes it less suitable for studying relatively large organic molecules. Photo-ionization is a good alternative [92]. Since the energy of the photon can be tuned to match the ionization potential of molecules belonging to a certain chemical class, the fragmentation can be minimized and even avoided.

Based on the energy of used photons, molecules can be photo-ionized via different mechanisms [109], Figure 2.14, employing single or several photons (of the same or different energy). If the energy of one photon is higher than the ionization potential of a given molecule, Single Photon Ionization (SPI) will take place. The probability of photo-ionization is given by the photo-ionization cross-section which depends on the energy of the photon and the target molecule. A main concern of this study was the detection of PAHs, motivated by their high toxicity and importance in the soot formation mechanism. Most of these molecules (with masses in the range 128 – 300 amu) have ionization potentials in the range of 6 to 9 eV, and therefore their ionization would require a vacuum UV (VUV, $\lambda < 180\,\text{nm}$) photon source, which can be difficult to implement in practice. As an alternative, several photons with a smaller energy can be used to ionize a molecule/atom with their combined energy – Multi-Photon Ionization (MPI). The probability of this ionization mechanism rapidly decreases with the number of required photons. Upon the absorption of the first photon, the molecule transitions from its ground state to

© 2020 Tous droits réservés.
lilliad.univ-lille.fr

Thèse de Dumitru Duca, Université de Lille, 2020

an excited state, which can be either a virtual or a real excited level. Additional photons are absorbed until the ionization potential is reached. Resonance-enhanced multi-photon ionization (REMPI) is a special case of MPI where a resonant single or multiple photon absorption to a real excited intermediate state is followed by the absorption of another photon that ionizes the molecule/atom. Since a real excited state is involved, with a much (orders of magnitude) longer life-time compared to a virtual state, the ionization efficiency of the resonant mechanism (REMPI) is significantly higher than the one obtained for the non-resonant multi-photon process. Coupled with mass spectrometry, the REMPI mechanism allows to selectively analyze the resonant species with very high sensitivity.

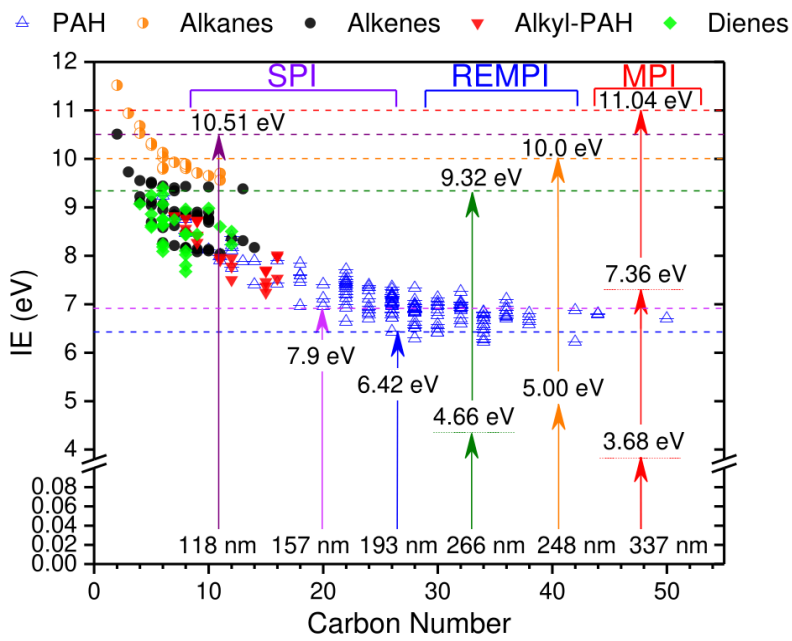

Figure 2.14 *Photo-ionization mechanisms [109] of hydrocarbon compounds for some commonly used laser wavelengths (266 nm, 157 nm, and 118 nm were available in our laboratory). Ionization energies for selected classes of molecules as a function of their carbon number. SPI – single photon ionization, REMPI – Resonance Enhanced Multi-Photon Ionization, MPI – Multi-Photon Ionization.*

The majority of PAH species exhibit strong absorption in the UV at wavelengths around 266 nm [110] and therefore can be ionized via a Resonant Two-Photon Ionization (R2PI) mechanism with the 4th harmonic of the Nd:YAG laser (266 nm, 4 ns pulse duration, Continuum Powerlite). At the same time, other compounds that are often found in combustion byproducts (*e.g.* aliphatic species) can have a higher ionization potential, thus requiring the non-resonant absorption of three photons of 4.66 eV ($\lambda = 266$ nm). This process is very inefficient and results in a poor sensitivity for aliphatic species. An SPI mechanism with a wavelength of 118 nm was used to study these species. The use of different ionization mechanisms allows complementary data about the surface chemical composition of the sample to be obtained, including information about aromatic and aliphatic compounds.

Figure 2.15a illustrates the optical path of the 266 nm laser beam used to achieve the efficient ionization of most aromatic species. The laser was set to the maximum output energy in order to obtain the highest stability. The fluence used for the ionization was then adjusted using an attenuator (Altechna 6ATT). The laser beam

© 2020 Tous droits réservés.

lilliad.univ-lille.fr

Thèse de Dumitru Duca, Université de Lille, 2020

intercepts orthogonally (on the vertical axis) the horizontally expanding desorption plume in the space between the repeller and extraction electrodes of the mass spectrometer (Figure 2.15, 2.13). Such a configuration leads to a loosely focused laser beam in the ionization region, with a diameter of ∼0.5 mm. The diameter of the laser beam could be adjusted by moving the position of the UV lens along the vertical axis (Figure 2.15a). The ionization fluence was adjusted for each sample in order to obtain the maximum signal intensity and minimize the fragmentation rate (< 40 mJ/cm^2).

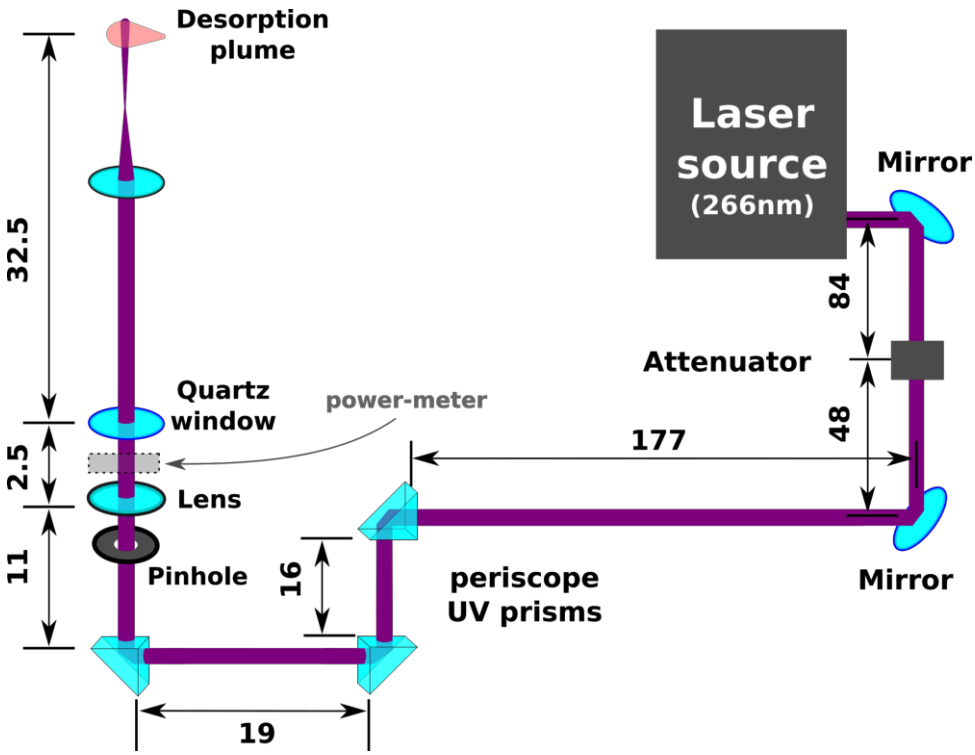

Figure 2.15 *266 nm laser beam path.*

A coherent source (developed in our laboratory) emitting 118 nm VUV radiation was employed for the study of aliphatic compounds. Xenon gas was used as a nonlinear medium to generate the third harmonic of the 355 nm pump laser resulting from a four-wave mixing process [85, 111] and equivalent to the ninth harmonic of the Nd:YAG laser (118.2 nm, 10.49 eV). The Xe cell (p= 10–15 Torr) was attached directly to the analysis chamber of the spectrometer through a MgF_2 window in order to avoid the absorption of the generated VUV radiation in the air, Figure 2.16 The pump laser beam (Continuum Surelite III, 355 nm, ∼40mJ, 3-5 ns, 10 Hz) was focused in the center of the cell by the same UV lens used in case of 266 nm ionization (in a different position). The 118 nm source is then focused by a MgF_2 lens inside the extraction zone of the mass spectrometer. The residual 355 nm radiation is also propagating towards the ionization region, but cannot induce ionization due to a large beam diameter (low fluence), Figure 2.16. Since the direct measurement of the generated 118 nm pulse energy was not possible, the conversion process was optimized by monitoring the relative ionization efficiency of acetone (ionization potential 9.69 eV, 127.9 nm) injected in the ionization chamber at the pressure of 4–5·10^{-8}mbar.

When using separate steps for desorption and ionization it is necessary to define

© 2020 Tous droits réservés.
lilliad.univ-lille.fr

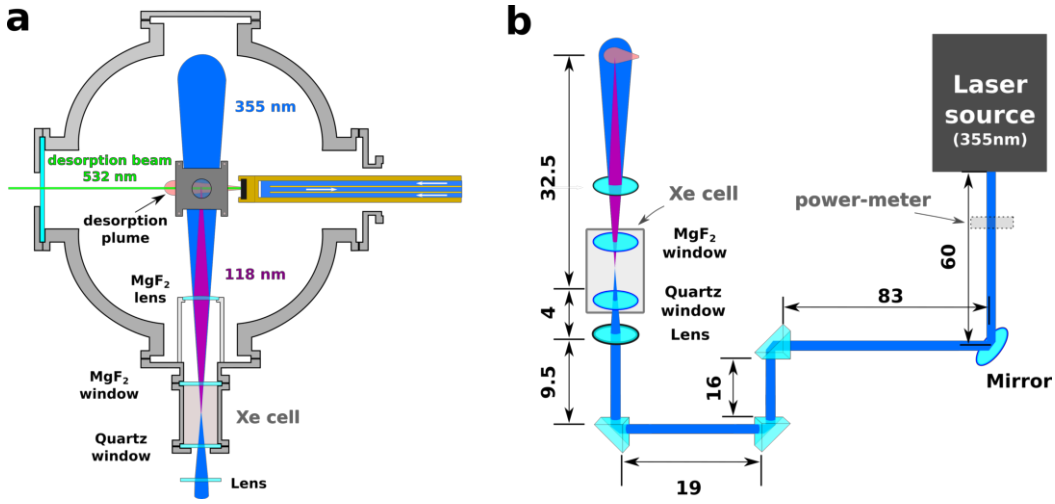

Figure 2.16 *(a) Schematic of the analysis chamber (side view): representation of the desorption (532 nm) and ionization (118 nm) configurationexperimental arrangement. (b) Ionization beam path at 118 nm.*

a time delay between the two laser pulses. Typical desorption plume velocities are in the order of hundreds of m/s (for the used desorption fluences), thus a time delay of up to hundreds of μs will be needed for the molecules to travel the distance between the sample surface and the ionization beam ($\sim$ 30 mm). In this study, a time delay of 100 μs, obtained with a delay/pulse generator(Stanford Research System, Inc, model DG-535), was used to obtain the highest signal for analytes in a wide mass range.

Time-of-Flight Mass Spectrometer

After the ionization step, the generated ions are mass analyzed in a reflectron Time-of-Flight Mass Spectrometer (Jordan TOF Products, Figure 2.17) where the mass-to-charge ratio (m/z) of the ions is determined from time measurements. Ions are accelerated by a static electric field created between two plates that define the ionization region: the repeller plate (V_{A1} $\sim$3000 V) and the extraction grid (V_{A2} $\sim$2400 V). The ions are accelerated toward the extraction grid, cross the V_{A3} (ground potential), pass through deflection plates (V_{XY} $\sim$100 V), an Einzel lens and enter the free-flight (drift) region where no electric field is applied. The kinetic energy distribution in the direction of the ion flight was corrected with a two-stage reflectron [112] (V_{R1} $\sim$1700 V, V_{R2} $\sim$2700 V). The reflectron is using an electric field to change the trajectory of the ions by first slowing them down and then re-accelerating them toward the detector. This effectively compresses the ion packets of the same mass to charge ratio (m/z) and improves the mass resolution. An additional advantage to the reflectron equipped TOF-MS is the increased flight distance (approximately double the length of the ToF-MS flight tube) which further increases the mass resolution. The velocity of the ion depends on its m/z ratio (since the same energy was communicated to all the ions by the accelerating electric field), *i.e.* heavier ions will reach a lower final speed. The time that the ions require to reach the detector, placed at a known distance, is measured. This time will depend on the velocity of the ion, and therefore is a measure of its mass-to-charge ratio. When the ions arrive at the detecter placed at the spatial focal plane with respect to the extraction from

© 2020 Tous droits réservés.
lilliad.univ-lille.fr

Thèse de Dumitru Duca, Université de Lille, 2020

the ion source, they impact the MCP assembly (two microchannel plates, chevron mounted, V_{D1} ∼-1320 V, V_{D2} ∼-720 V, V_{D3} ∼-120 V) and produce electrons (∼10^6 electrons for one impacting ion) generating a measurable current on the anode. The current is then recorded with a digital oscilloscope (LeCroy Waverunner 6200A) at a time resolution of 2 ns/point and transferred to a PC for further treatment.

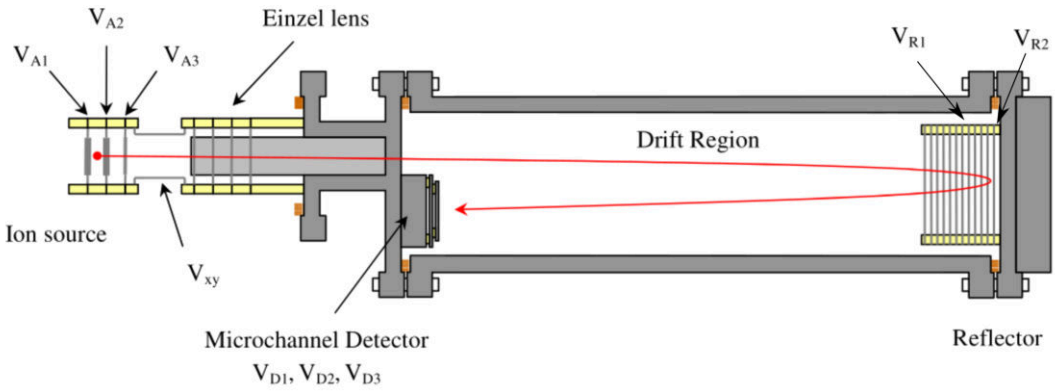

Figure 2.17 *Path of ions in the Jordan ToF-MS, from their generation to detection. Reproduced from [105].*

2.2.2.3 High-Resolution Two-Step Laser Mass Spectrometer (HR-L2MS)

During this thesis, a new custom-built L2MS instrument (Fasmatech S&T) was implemented and used for chemical characterization of samples, Figure 2.18. The instrument features a much higher resolving power (m/Δm ∼ 15000) which allows for a better discrimination between ions with the same nominal mass. Since the instrument was put into operation and optimized during this thesis, its operational principle, optimization, and associated methodology will be thoroughly described. The unique feature of the HR-L2MS instrument is the presence of a differentially pumped segmented PCB (printed circuit board) octapole ion trap, Figure 2.19, driven by rectangular RF waveforms for efficient ion storage across a wide mass range. The ions that are stored in the ion trap are cooled down through collisions with *He* atoms, injected in the ion trap by a fast solenoid valve, and significantly improving the mass resolution. This mass spectrometer is similar to the one used in the group of Christine Joblin at University of Toulouse [113, 114].

The experimental setup is comprised of three main parts that will be described in detail in the following sections (Figure 2.19):

- Laser Desorption/Ionization source.
- A segmented PCB octapole ion trap that allows trapping and isolating either all or ions of a certain mass (*e.g.* for cooling purposes).
- An orthogonal ToF-MS equipped with a two-stage reflectron and a fast MCP detector.

© 2020 Tous droits réservés.
lilliad.univ-lille.fr

Thèse de Dumitru Duca, Université de Lille, 2020

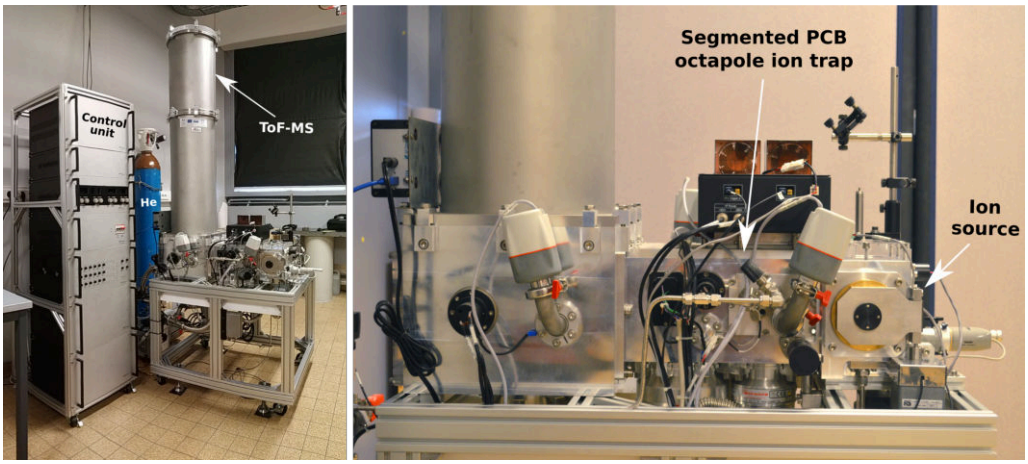

Figure 2.18 *Pictures of the high-resolution L2MS instrument (Fasmatech S&T).*

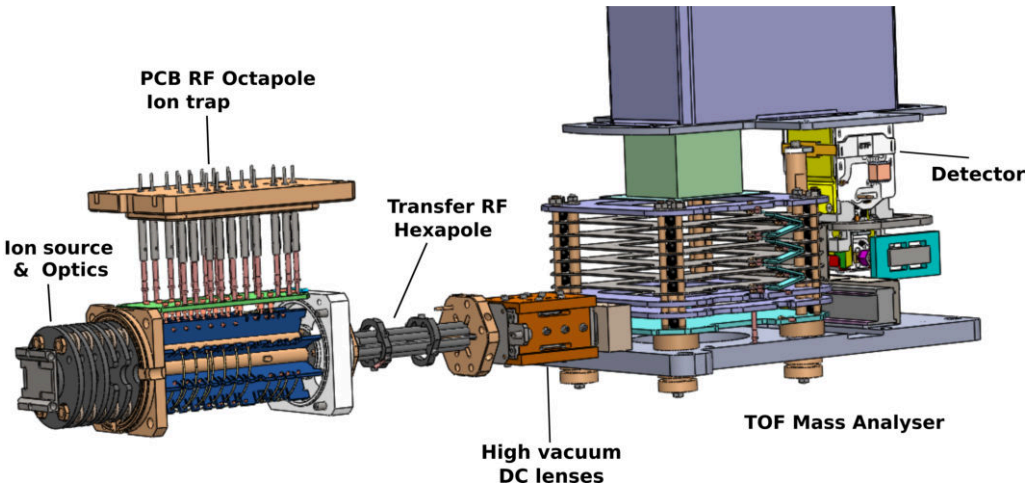

Figure 2.19 *3D model of the octapole ion trap showing the ion source optics, the differentially pumped ion trap enclosure, the electrical connections (at the top) for applying RF and DC signals to the ion trap segments, the transfer hexapole and the ToF-MS analyzer.*

Laser Desorption/Ionization source

Similar to the previously described instrument, the compounds adsorbed/condensed on the surface of the sample are transferred into the gas phase and later ionized using a sequence of two laser pulses. The sample is introduced in the Laser Desorption/Ionization source (analysis zone, p = 10^{-6} mbar) via a small preparation chamber and mounted vertically on a 2-axis motorized holding arm which positions the sample in front of a set of inlet apertured electrodes, Figure 2.20. In order to avoid charge accumulation on the surface of insulating samples that can perturb the ion plume propagation, a metallic electrode, biased at the same DC potential as the first inlet aperture electrode, is placed on top of the sample, Figure 2.20. The inlet electrodes have cut-outs allowing the passage of the desorption laser beam and the visualization of the sample with a digital camera. The combination of the motorized holding arm and real-time visualization enables an easy and fast selection of the sample region for the analysis.

The desorption of species present on the surface of the sample was performed with the 2nd harmonic of a Nd:YAG laser (λ_d = 532 nm, Quantel Brilliant). The

© 2020 Tous droits réservés.
lilliad.univ-lille.fr

Thèse de Dumitru Duca, Université de Lille, 2020

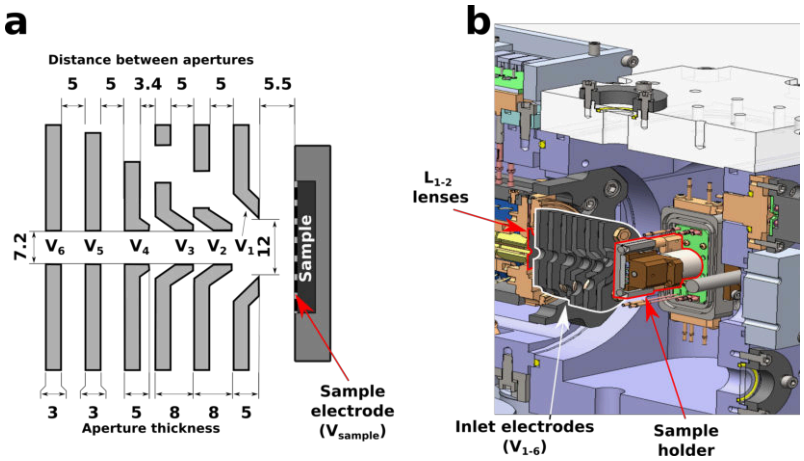

Figure 2.20 *(a) Schematic representation of the inlet apertured electrodes (top view, all dimensions in mm). (b) 3D visualization of the Laser Desorption/Ionization source.*

optical path followed by the desorption laser beam is illustrated in Figure 2.21. The laser beam profile was shaped into a quasi top-hat by a combination of a beam expander built around a set of convergent (F=200mm) and divergent (F=-150mm) lenses, and a diaphragm. The energy of the laser pulse was adjusted with a home-made attenuator based on a variable transmission quartz disk mounted on a stepper motor. The laser pulse was then imaged on the sample surface (30° incidence angle) using a convergent lens, Figure 2.21. In such a configuration, the laser beam was forming a slightly elliptical spot on the surface of the sample with an area of 0.06 mm^2. The desorption fluence was adjusted for each analyzed sample as to obtain the maximum signal intensity while also minimizing the fragmentation rate and never exceeded 30 mJ/cm^2 for the samples analyzed in Chapter 3.

After the desorption step, the molecules that have been transferred into the gas phase are photo-ionized. The ionization was performed with 266 nm photons (4th harmonic of Nd:YAG laser, Quantel Briliant). The optical path followed by the ionization laser is schematized in Figure 2.22. Since the distance between the sample and the input apertures of the spectrometer is relatively small (5.5 mm), in order for the ionization laser beam to intercept the expanding desorption plume without irradiating the sample or the apertures, it was shaped into a light-sheet (10x2 mm^2) with the help of a rectangular slit. Similar to the desorption step, the ionization fluence was adjusted for each sample. Fluences up to 40 mJ/cm^2 were used, as fragmentation of the aromatic species at higher values was observed.

Compared to the previously described instrument, the distance between the sample and the ionization region is much smaller and thus a shorter time delay between the two laser pulses (desorption and ionization) has to be used. The optimal time delay was determined from mass spectrometric measurements performed on a sample containing a standard reference material NIST1650b (Diesel particulate matter, Sigma-Aldrich). Both desorption and ionization fluences were kept constant throughout the measurements. From the evolution of the signal with the time delay between desorption and ionization laser pulses it was determined that a delay of 9 μs yields the highest signal for molecules within a wide mass range (<400 amu).

© 2020 Tous droits réservés. lilliad.univ-lille.fr

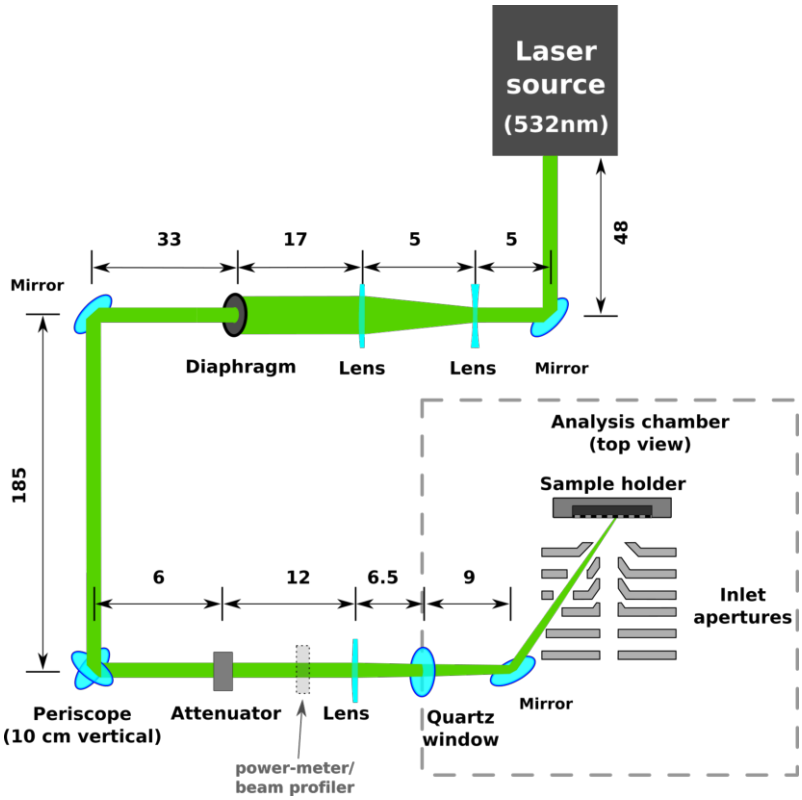

Figure 2.21 *Desorption laser beam optical path for the high-resolution L2MS instrument. All distances are given in centimeters. Note that relative dimensions of the presented objects are not to scale.*

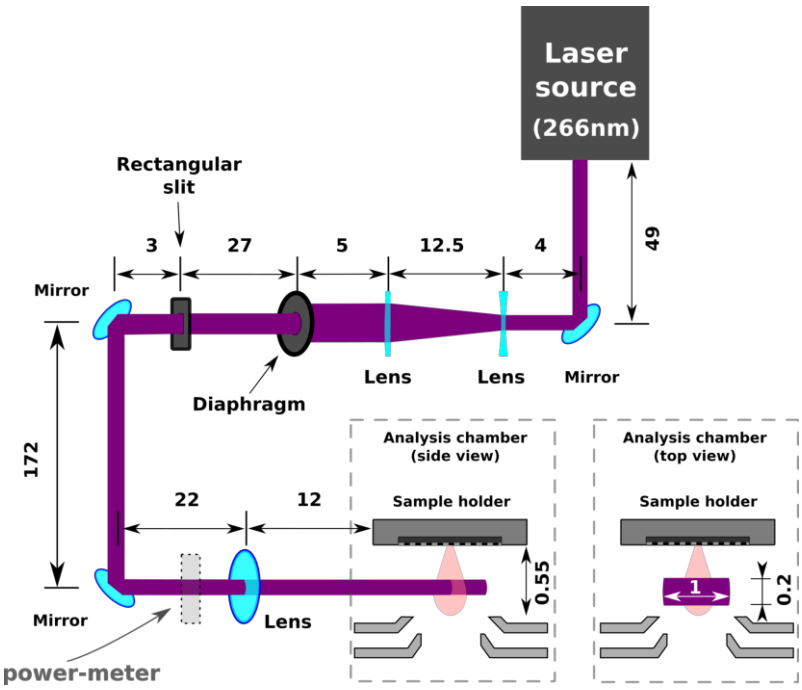

Figure 2.22 *Ionization laser beam optical path for the high-resolution L2MS instrument. All distances are given in centimeters. Note that relative dimensions of the presented objects are not to scale.*

© 2020 Tous droits réservés.
lilliad.univ-lille.fr

Thèse de Dumitru Duca, Université de Lille, 2020

Typical ion path

Once the molecules are ionized, they are extracted from the ionization region by a set of input aperture electrodes, Figure 2.20, that guide the ions into the segmented PCB octapole, Figure 2.23. The potential applied to each electrode, listed in Table 2.5, was determined from ion simulations as to maximize the transmission of the inlet while also obtaining a homogeneous ion cloud. Moreover, the axial energy of the ions has to be minimized before they enter the segmented octapole in order to reduce the probability of their fragmentation (collision induced dissociation, CID). In the configuration used in the experiments, Table 2.5, the axial energy of the ions entering the segmented octapole ion trap was 21 eV higher (from the acceleration by the inlet apertures) than their initial axial kinetic energy.

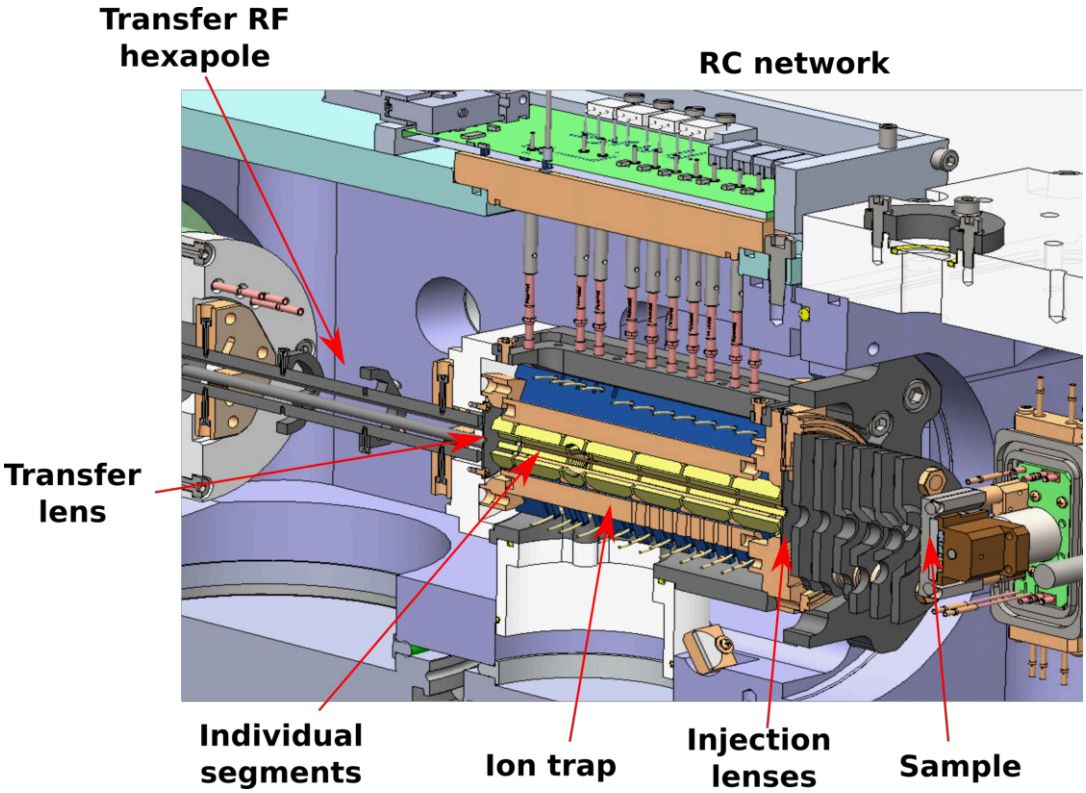

Figure 2.23 *3D model of the octapole ion trap assembly.*

The ion trap is composed of 7 independent segments enclosed in a differentially pumped vacuum compartment, Figure 2.23. Each segment contains a pair of insulating rings (PEEK) radially slotted to position eight electrodes, matched together using high precision machining. The segments are then compressed together using a PEEK flange at the entrance and a stainless steel ring at opposite ends, Figure 2.23. The geometry of the ion trap is presented in Figure 2.24. The PEEK flange is also used for positioning the DC lens electrodes (**L1** and **L2**) at the entrance of the ion trap. Pumping is applied through a gap between the two bottom PCBs. A closed structure of the ion trap is required in order to confine the gas that can be introduced in the assembly by a pulsed solenoid valve. A PCB RC network mounted on top of the ion guide assembly delivers the RF and DC signals to all segments. Signal distribution to all electrodes is achieved via phosphor bronze spring-loaded connectors. The ion trap is driven by a pair of opposite phase rectangular RF wave-

© 2020 Tous droits réservés.

lilliad.univ-lille.fr

Thèse de Dumitru Duca, Université de Lille, 2020

forms at 1.8 MHz with the amplitude of 170 V, resulting in a good transmission for ions with m/z larger than 40 (transmission of lower mass ions can be improved by changing the RF frequency and amplitude).

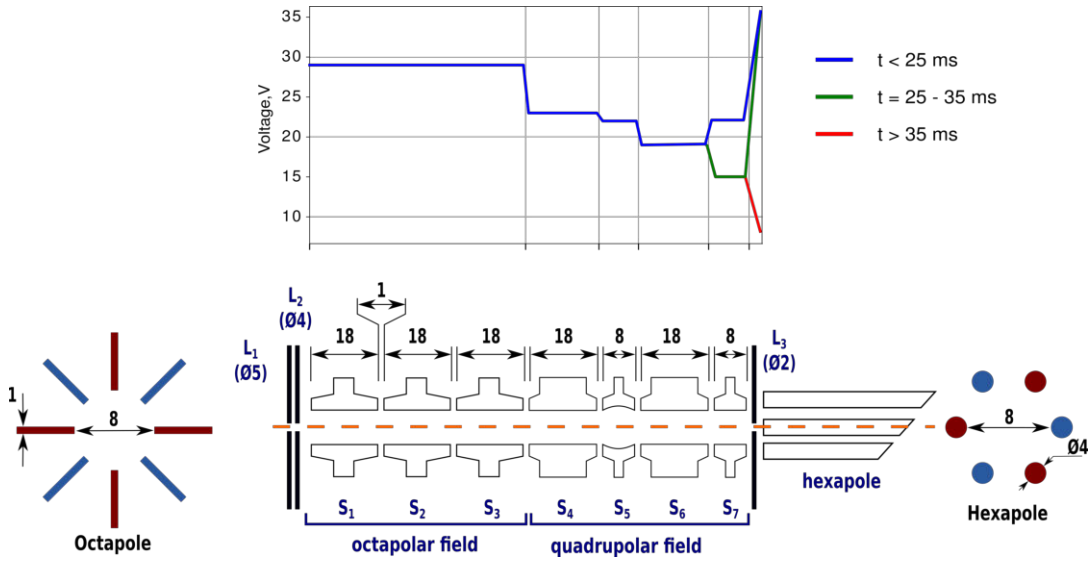

Figure 2.24 *Schematic diagram of the injection lenses (**L1**, **L2**), the segmented PCB RF octapole ion trap, **L3** transfer lens and RF hexapole transfer ion guide (bottom panel). DC voltages applied across the segments of the octapole trap are (top panel). All dimensions are given in mm.*

Table 2.5 *DC voltages applied to various electrodes and octapole segments. Octapole segments (S_{1-7}) and transfer lens (L_3) can be switched between two voltage levels (**Voltage 1** and **Voltage 2**) to axially move the position of a potential well and trap the ion packet, Figure 2.24(top panel).*

Electrode	Voltage, V	Electrode	Voltage 1, V	Voltage 2, V
V_{sample}	+50	S_{1-3}	+29	
V_1	+50	S_4	+23	
V_2	-3500	S_5	+22	
V_3	-700	S_6	+19	
V_4	-370	S_7	+22	+15
V_5	-3500	L_3	+35	+8
V_6	-700			
L_1	+20			
L_2	-30			

After the extraction from the ionization region, ions are injected through the inlet lenses **L1** and **L2** into the ion trap and are confined radially by an RF octapole field created in the first three segments (**S1-S3**), Figure 2.24. The RF field is then changed to a quadrupole configuration in the remaining segments (**S4-S7**). Axial control of the ions is accomplished by DC voltages applied independently and dynamically to each segment, Table 2.5. A hybrid field configuration was chosen in

© 2020 Tous droits réservés.

lilliad.univ-lille.fr

Thèse de Dumitru Duca, Université de Lille, 2020

order to maximize the transmission efficiency for ions in a wide mass range. The octapolar field is used in the first part of the ion guide as it is particularly useful for capturing ions from diffusive jet flows originating from narrow pressure limiting apertures. At the same time, the quadrupolar field, established toward the exit, is useful for radial compression of the ion packet. Simulations of ion trajectories show that significant losses are observed for the case when a uniform quadrupolar field distribution is used, Figure 2.25. Such a low transmission efficiency is partly attributed to the narrow phase-space acceptance at the entrance of the ion guide. Therefore, a hybrid field (octapolar and quadrupolar) provides improved transmission for heavier ions and also high transmission through narrow apertures (transfer lens, **L3**) due to the high radial compression of the ion packet in the quadrupolar part of the ion guide, Figure 2.25.

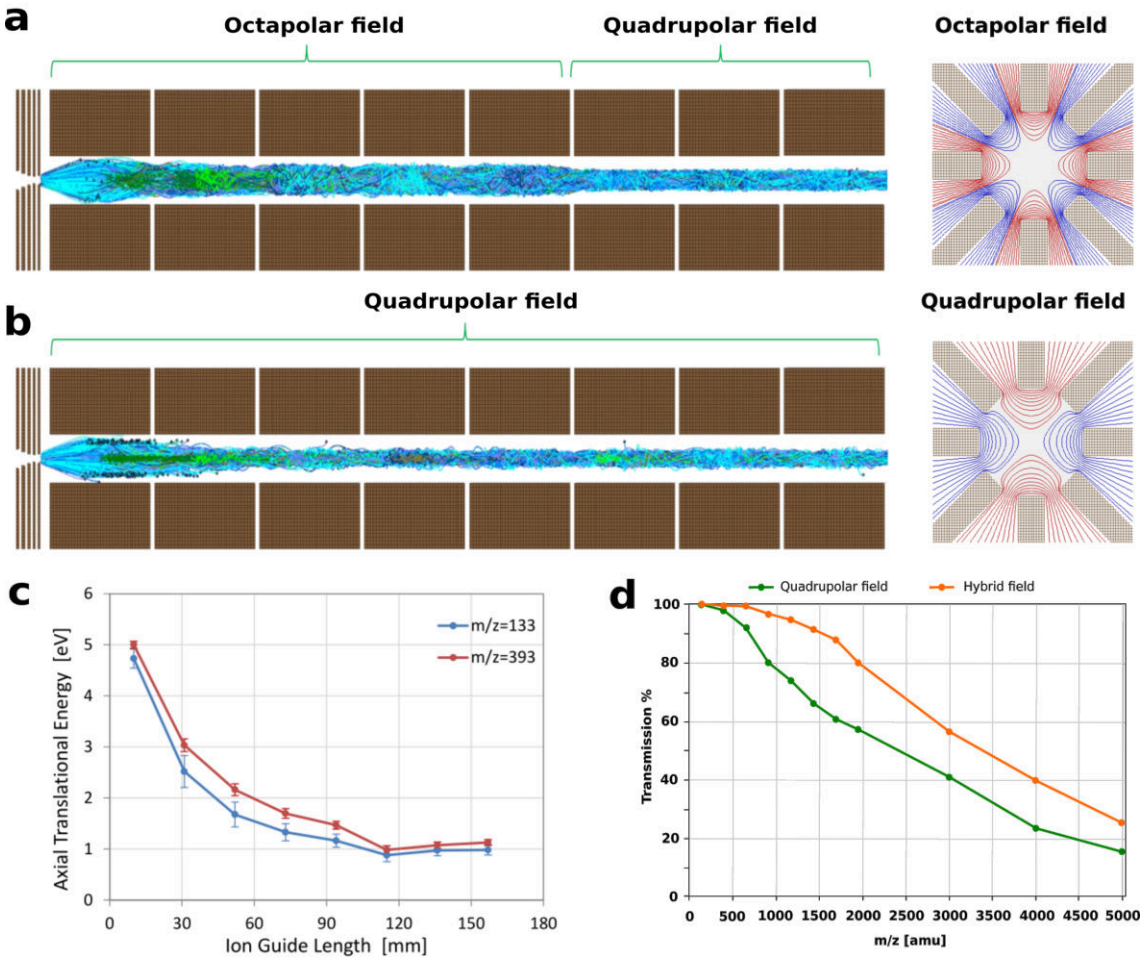

Figure 2.25 *Ion trajectories for m/z values corresponding to cesium-iodide ions over a wide mass range extending from m/z=133 to m/z=1952. (a) Ion guide combining octapolar and quadrupolar fields and (b) ion guide with quadrupolar field only. The normalized equipotentials in the octapolar and quadrupolar field configuration are also shown. (c) Translational cooling for two ions traversing the ion guide. (d) Simulated transmission efficiency for two modes of operation shown in (a) and (b). Note that the simulations were performed on an ion guide containing 8 segments, however, the results for 7 segments are similar. The simulations were provided by Fasmatech S&T.*

The loss of heavy ions at the entrance of the quadrupolar field (**S4-S7**) is minimized by reducing the ion translation energy via collisions with buffer gas molecules

© 2020 Tous droits réservés.

lilliad.univ-lille.fr

Thèse de Dumitru Duca, Université de Lille, 2020

occurring in the octapolar part of the ion guide. The injection of the gas is synchronized with the arrival of ions. Heavy gasses such as argon, krypton, xenon, nitrogen and methane can be used as buffer gasses during collision-induced dissociation studies, however, since the main objective in this particular configuration is the thermalization of ions, a lighter gas (He) should be used instead [115, 116]. After gas injection into the ion trap, the pressure slowly increases and reaches its maximum value of $\sim 5 \cdot 10^{-2}$ mbar after ~3–4 ms [115, 116]. Therefore, the injection of He has to occur before the desorption laser pulse. The synchronization between the gas introduction and the two laser pulses (desorption and ionization) is illustrated in Figure 2.26.

The position of the ions in the ion trap is controlled by DC voltages applied across the segments, Figure 2.24, thus making possible the trapping of the ion packet in any of the seven segments. In the current configuration, the thermalization of ions, started in the first segments, continues in the segment **S6** for 25 ms (Figure 2.24 blue line) with a larger axial dimensions. The ions are then transferred into the **S7** segment by lowering the applied DC voltage, *i.e.* moving the edge of the potential well to the lens **L3**, Figure 2.24 green line. The **S7** segment is much shorter which leads to the axial compression of the ion packet. The ions are stored in the S7 segment for another 10 ms and are then transported to a RF hexapole ion guide, Figure 2.24 red line. The hexapole conveys the ion packet through a series of high vacuum DC lenses shaping the ion beam in the lateral direction into the extraction region of the mass analyzer. Ions are then finally pulsed orthogonally into the ToF-MS flight tube equipped with a two-stage reflectron, Figure 2.27. The voltage of the inner flight tube is set to -8320V and the pressure is maintained at 10^{-7} mbar. Similarly to the previously described instrument, an MCP-based detector is used here. The arrival of ions to the detector is monitored with a digitizer and transferred to a PC with a custom-built software.

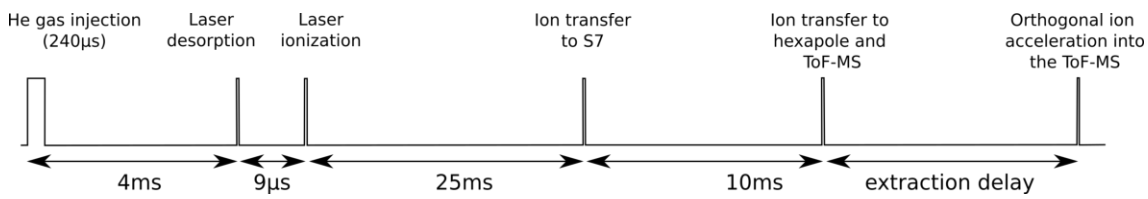

Figure 2.26 *Synchronization between the different steps of the analysis. First, He gas is introduced into the ion trap. The desorption and ionization of molecules follows. The produced ions are introduced into the ion trap and are stored in the S6 segment for 25 ms. The ion packet is then transferred to the S7 segment for axial compression by changing the DC voltage of the S7 segment (Table 2.5). Finally, the ions are transmitted via a hexapole and pulse accelerated into the ToF-MS for mass measurements.*

The procedure of transferring the ions to the ToF-MS can be seen as the first step in separating them based on their mass to charge ratio [117]. Once the ion packet arrives at the extraction region of the ToF-MS, it is extended compared to its initial length (8 mm), with the final dimension dependent on the mass range of the ions (Figure 2.27). Therefore, in order to obtain a full mass spectrum, several portions of the ion packet are individually mass analyzed in the ToF-MS. Individual portions of the ion packet ("mass windows") are selected based on the time delay between the ion ejection from the ion trap (the switch between **Voltage 1** and **Voltage 2** for **L3**

© 2020 Tous droits réservés.
lilliad.univ-lille.fr

Thèse de Dumitru Duca, Université de Lille, 2020

aperture, Table 2.5) and the start of ion acceleration into the ToF-MS, Figure 2.26. The signal obtained for all "mass windows" selected in this way are then combined into a single mass spectrum. The procedure of determining the optimal number of mass windows and their time delay is detailed in the next section.

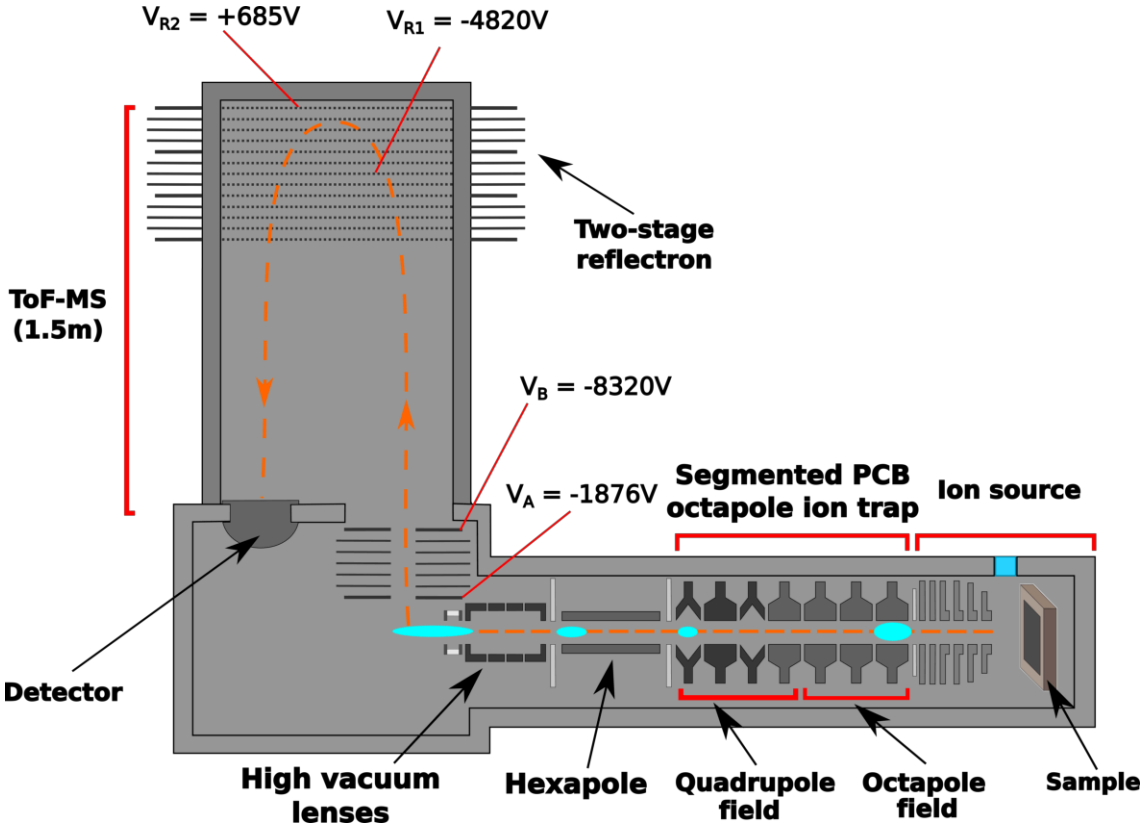

Figure 2.27 *Schematic representation of the ion path (orange dashed line) inside the HR-L2MS and the evolution of the ion packet shape (blue elipse) during its passage through the instrument.*

Transmission function measurements

The mass spectrum recorded for a given sample is obtained from the combination of a series of single-shot spectra (spectra obtained after a single desorption laser shot) recorded for different extraction delays (*i.e.* different mass windows that are accelerated into the orthogonal ToF-MS (Figure 2.27). Therefore, it is extremely important to choose a set of mass windows (*i.e.* time delays) that result in a relatively constant transmission for the ions in the mass range of interest. Moreover, the smallest possible number of windows should be used as to reduce the total analysis time and minimize the number of required desorption pulses. The latter is essential when analysing either small samples (since each desorption shot should be taken on a new, pristine spot on the sample) or inhomogeneous samples (*e.g.* minerals, fossils). The information about the shape of the transmission function for the instrument is of great importance – a low transmission for certain masses can lead to compounds not being detected and, therefore, skew the result of the analysis. The edges of a mass window are not sharp, therefore, a number of ions with masses covered by the extremities of the windows can have a rather low transmission. Accounting for the

© 2020 Tous droits réservés.

lilliad.univ-lille.fr

Thèse de Dumitru Duca, Université de Lille, 2020

edges of the transmission window can be difficult and can only be done if the overall transmission function (for a given set of mass windows) is known.

The optimal number of mass windows and their positions (*i.e.* time delay) was determined using an experimentally-based approach. In this case, it is essential to have a constant and repeatable source of ions throughout all the measurements. Since the ions are generated via desorption and subsequent ionization of the chemical species present on the surface of a sample, it is important to choose a specimen with homogeneous surface chemical composition thus allowing us to always perform measurements on a pristine zone of the sample. Moreover, the surface concentration of species should be significantly higher than the limit of detection of the setup. In this case, it will be possible to detect species even when the transmission for their corresponding mass will be lower (*i.e.* the mass of the compound is associated with the extremities of the transmission window). The exact chemical composition of the sample is less important as long as a multitude of species can be easily desorbed and ionized at the utilized desorption/ionization wavelengths. It is also essential to choose a sample that contains a large number of species, covering a wide mass range, preferably species/fragments that are detected at almost every integer mass. A standard reference material for Diesel particulate matter (NIST1650b), was found to be a suitable sample for transmission measurements. Its chemical composition consists primarily of polycyclic aromatic hydrocarbons (PAHs) and nitro-substituted PAHs (nitro-PAHs) that are commonly found in Diesel particulate matter and similar matrices. The sample was found appropriate since it contains species that can be easily ionized with the used technique, resulting in a mass spectrum with peaks up to 400 m/z with an acceptable signal to noise ratio. In order to obtain sufficient data points allowing to determine the width and shape of transmission windows, mass spectra were recorded for a multitude of window positions (*i.e.* time delays) for the mass range that contained detectable ions. Each spectrum was summed over 25 laser shots taken for different positions on the sample (in order to have a constant surface concentration of analytes) – a number of shots found to be sufficient to obtain a high enough signal even for peaks located in the extremities of transmission windows. Note that the transmission of the instrument was studied here only for ions with m/z lower than 400, a limit determined entirely by the utilized sample. A sample containing chemical species with a higher molecular mass will be required for the study of the transmission above 400 m/z (*e.g.* fullerene sample).

To be able to determine the shape of transmission windows and its variation with the position (*i.e.* time delay) a reference spectrum should be first determined – a mass spectrum characteristic of the ion source and not influenced by the transmission of the instrument. This information has to be obtained on the same instrument in order to account for efficiencies of desorption, ionization, extraction and detection. Therefore, the reference spectrum can be seen as a full mass spectrum of the analyzed sample obtained with the same instrument with a transmission window covering the whole mass region of interest. A single transmission window is expected to have a plateau in the center, corresponding to the maximum transmission efficiency, surrounded by edges with a lower and decreasing transmission. In this case, if a multitude of mass spectra are recorded (each one for a different mass window that cover the whole mass region of interest) for each mass peak there will be at least one mass spectrum (associated with a single mass window) in which the plateau

© 2020 Tous droits réservés.
lilliad.univ-lille.fr

Thèse de Dumitru Duca, Université de Lille, 2020

of the transmission window will be centered on the mass peak, Figure 2.28. The intensity of the signal for these compounds should be only affected by the constant (mass independent) transmission losses, and therefore can be used to construct the reference mass spectrum. The intensity of a mass peak in the reference spectrum is equal to its plateau value (*i.e.* the highest value of the given peak within all the mass spectra obtained for different transmission window positions, corresponding to different extraction delays), Figure 2.28.

$$I_i^{reference} = \max_{j=1}^{n} I_{ij}^{single\,window} \tag{2.2}$$

where i is the index of the detected mass peak and j is the index of the individual spectrum associated with one mass window.

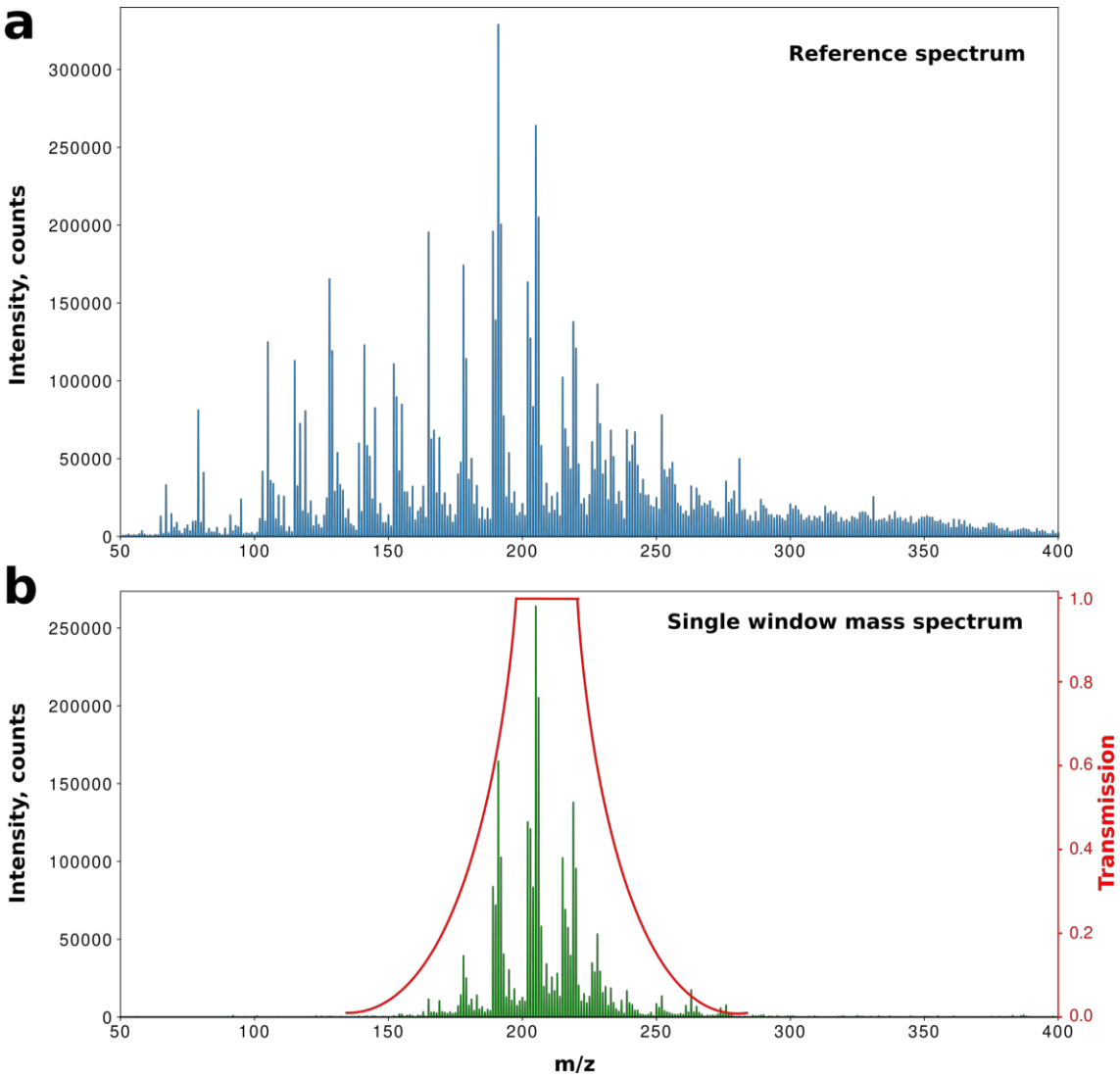

Figure 2.28 *(a) Reference mass spectrum obtained from single-window mass spectra using equation 2.2. (b) An example of a single-window mass spectrum is shown in green along with the corresponding transmission window. Note that the red line "transmission window envelope" is shown here only as an illustration, the calculation of the exact shape is discussed below.*

© 2020 Tous droits réservés.

lilliad.univ-lille.fr

Thèse de Dumitru Duca, Université de Lille, 2020

We calculate the transmission function of each mass window by comparing its corresponding single-window spectrum to the reference one with the help of the following formula:

$$T_j = \frac{I_j^{single\,window}}{I_j^{reference}} \tag{2.3}$$

where j is the index of the single-window spectrum corresponding to a certain transmission window position.

Once the transmission function has been calculated for a set of window positions (*i.e.* time delays), the optimal combination of windows, resulting in a relatively uniform transmission throughout the whole mass region of interest, can be determined. As mentioned above, in order to get a precise shape of transmission windows, the ion source should be stable. However, due to a multitude of factors that determine the output of the ion source (laser fluence, small variations in the surface concentration for hundreds of components), the output of the source cannot be considered constant. For that reason, the obtained transmission functions are somewhat noisy at the edges. Therefore, a smoothing filter (Low-Pass Filter, LPF) was applied to the extremities of the calculated transmission windows. Due to the filtering, the shape of transmission window edges will be less precise. Nevertheless, the derived shape should be sufficiently exact to determine optimal window positions as to obtain a relatively constant transmission function up to 400 m/z. The optimal positions for the windows, as well as their optimal number, is considered the combination of n windows that leads to a total transmission function with the least under/overestimation, Figure 2.29.

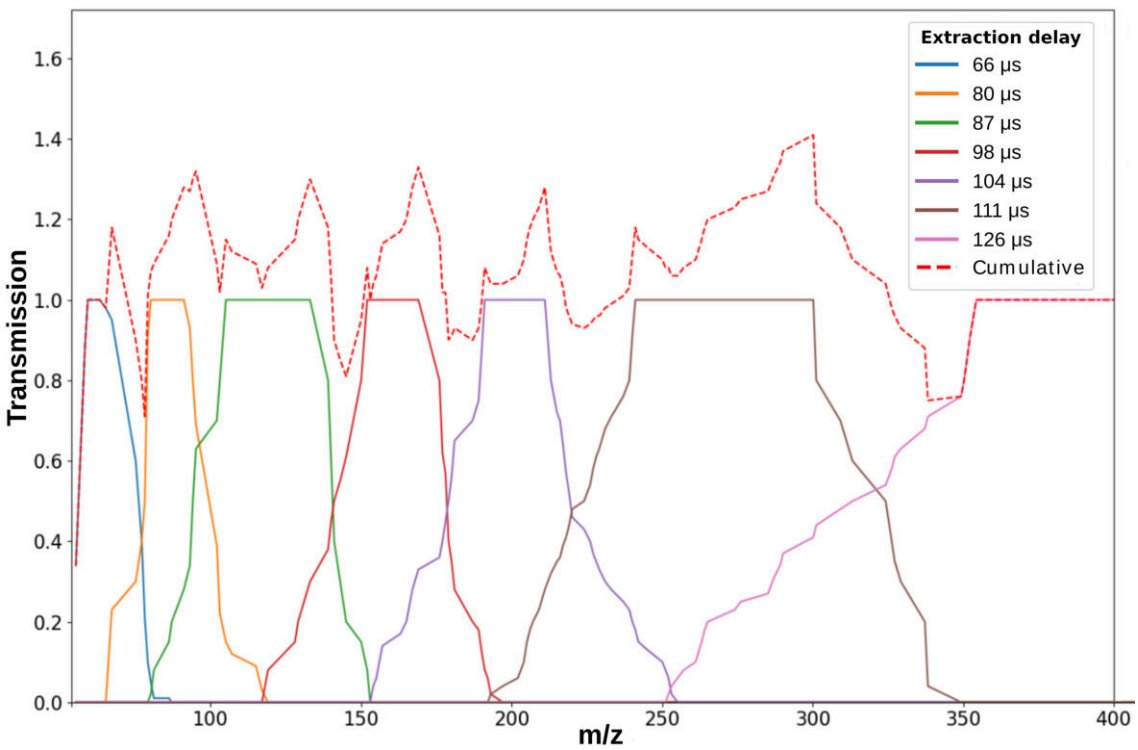

Figure 2.29 *Position and shape of seven chosen windows (solid lines) and the resulted overall transmission function (red dashed line).*

© 2020 Tous droits réservés.

lilliad.univ-lille.fr

Thèse de Dumitru Duca, Université de Lille, 2020

Due to a complicated shape of window edges, it is not possible to find the positions resulting in a perfectly flat transmission function (T = const). However, such a perfectly flat transmission may not be necessary. A transmission function that allows the instrument to detect compounds with a relatively low detection limit should be sufficient for any type of mass spectrometric analysis: qualitative and quantitative. For the qualitative analysis, the detection of a compound is more significant than the absolute intensity of its corresponding peak. In contrast, quantitative analysis is based entirely on the absolute signal intensity of the studied compound. However, such an analysis requires a calibration with a standardized ion source, therefore, as long as the transmission function remains the same during the calibration procedure and analysis, the variations in transmission efficiency are taken into account by the calibration function. Once the number and position of transmission-windows have been established, one can construct the spectrum for the whole mass range by summing the signal obtained only with the chosen transmission-windows. The comparison between the reference spectrum (obtained from over 70 spectra recorded for various transmission-window positions) and the one obtained from the combination of only seven selected windows is presented in Figure 2.30. With the exception of some minor differences in the intensity of several mass peaks, both spectra look very similar. The above-mentioned dissimilarities are a result of the non-constant transmission function. As long as the same transmission windows are used during the analysis of one or several samples, the small differences should not affect the outcome of the analysis.

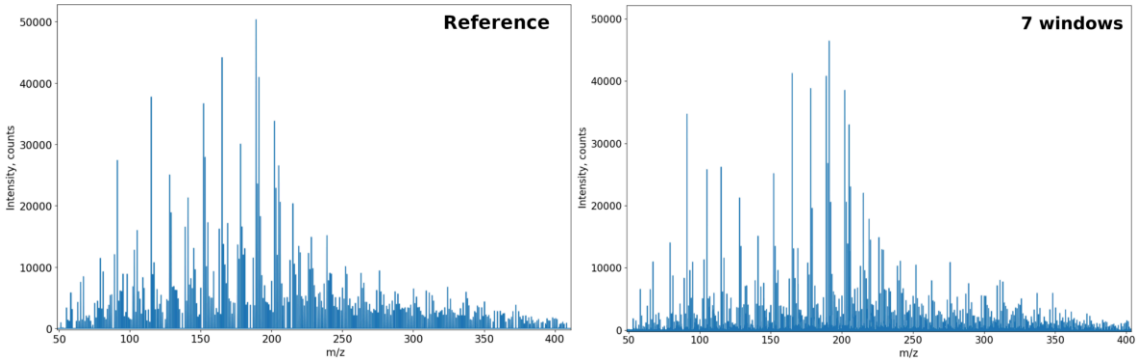

Figure 2.30 *Comparison between the reference spectrum (left) and the one obtained from seven transmission-windows (right).*

Mass calibration

A ToF mass spectrum is composed of a series of peaks that correspond to the ion impacts on the detector. The relationship between the m/z ratio of an ion and the time it needs to arrive at the detector is quadratic:

$$m/z = A(t - t_0)^2 \tag{2.4}$$

where A and t_0 are parameters that only depend on the experimental conditions. Once the masses for at least two peaks are known, A and t_0 constants are calculated and the spectrum can be calibrated. In case of a soft ionization, all ions are usually singly-charged, therefore the m/z axis of the calibrated spectrum will be numerically equal to the mass of the ion in atomic mass units. Equation 2.4, however, cannot

© 2020 Tous droits réservés.
lilliad.univ-lille.fr

Thèse de Dumitru Duca, Université de Lille, 2020

be used for high accuracy calibration of mass spectra obtained with HR-L2MS since it assumes a null intercept. For HR-L2MS, the "0" point on the time-of-flight spectrum corresponds to the start of ion acceleration, specifically to the emission of the corresponding TTL signal by the control unit of the spectrometer. Taking into account the small time delay between the emission of the control signal and the actual acceleration of the ions requires the addition of a small negative intercept, t_1, to the equation 2.4. For that reason, mass calibration of spectra obtained with HR-L2MS are performed with a 2nd degree polynomial where the free term can be written as $At_0^2 + t_1$.

The accuracy and mass resolution of the recorded (and calibrated) spectrum can be affected by the electronic jitter – small fluctuations in the voltage of the accelerating electrodes causing a linear shift of the recorded spectrum. This is particularly notable for high-resolution time-of-flight spectra where the jitter-induced shift is comparable with the FWHM of mass peaks, reaching ~ 1 ns for m/z = 202, Figure 2.31. A mass spectrum is usually obtained by either averaging or summing several (tens or hundreds) of single shot mass spectra that are all affected by the jitter. Not taking into account the jitter will lead to an artificial increase in peak width and decrease of the mass resolution. Moreover, a single mass spectrum in the 50 to 400 m/z mass region is constructed from spectra corresponding to 7 different transmission-windows, each one carrying a different jitter component. In this case, the presence of the jitter will result in a much lower mass accuracy after the calibration.

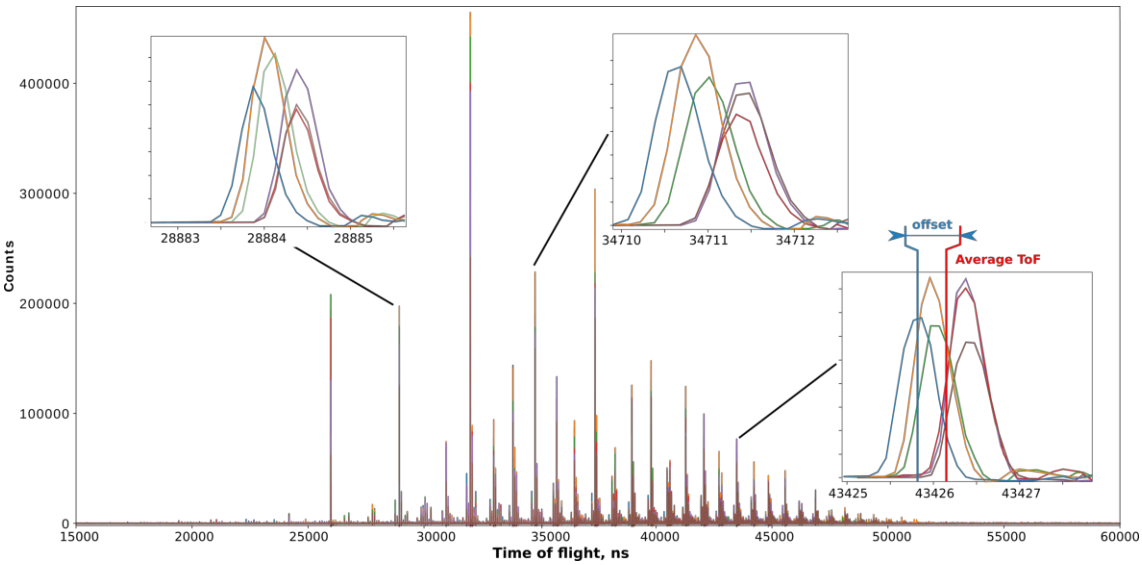

Figure 2.31 *Illustration of the electronic jitter influence on six time-of-flight spectra recorded from the same sample in the same experimental conditions. The average time of flight and jitter-induced offset is shown for a single peak (blue).*

In order to obtain both high accuracy and mass resolution, the shift induced by the electronic jitter must be eliminated before the calibration, effectively aligning all the spectra. The alignment can be only performed on raw output of the spectrometer – a collection of single-shot mass spectra, recorded after each desorption laser pulse, instead of a single, summed or averaged spectrum. A Python script was developed for this purpose and uses ten different peaks to align recorded ToF spectra. For each peak, a jitter-induced offset is calculated in relation to the average ToF value

© 2020 Tous droits réservés.

lilliad.univ-lille.fr

Thèse de Dumitru Duca, Université de Lille, 2020

determined across all recorded spectra, as illustrated on Figure 2.31. The offsets obtained for all the selected peaks in a given ToF spectrum are then averaged and result in a mean value for the jitter-induced shift. These individual offsets are then applied to all the spectra, effectively aligning each detected peak to its corresponding mean ToF value, Figure 2.32. The insets in Figure 2.32 represent mass peaks which were not used to calculate the jitter-induced offset and their perfect alignment (once offset-corrected) proves the high efficiency of the procedure described above. A sum (or average) of all the spectra is then computed resulting in a spectrum that can be easily calibrated with a 2nd degree polynomial function. Mass spectra processed in this way feature an accuracy better than 10 ppm and a mass resolution over 15 000, Figure 2.33.

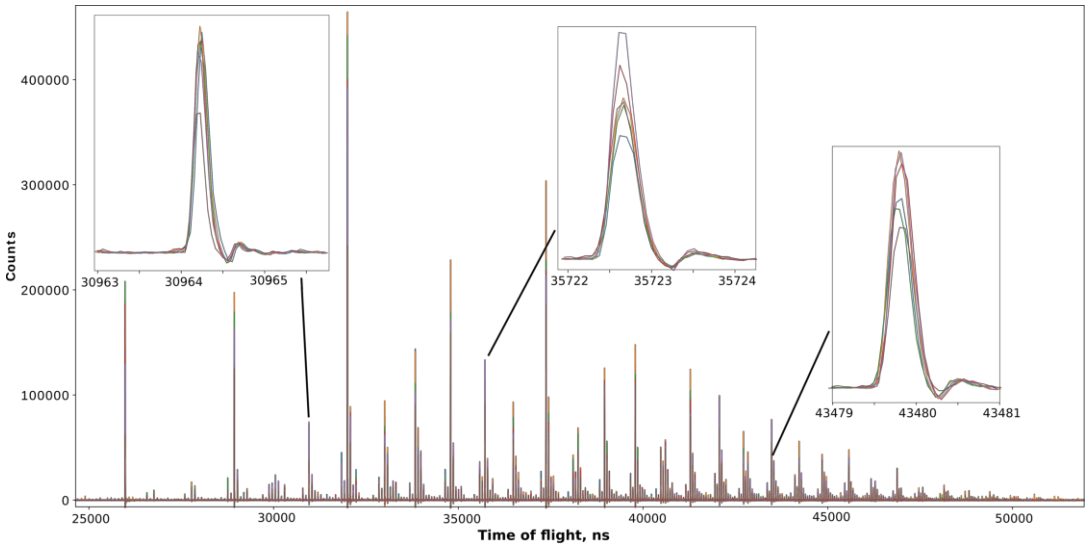

Figure 2.32 *Time-of-flight spectra aligned after jitter-induced offset correction. Note that the peaks in the insets are different from those in Figure 2.31.*

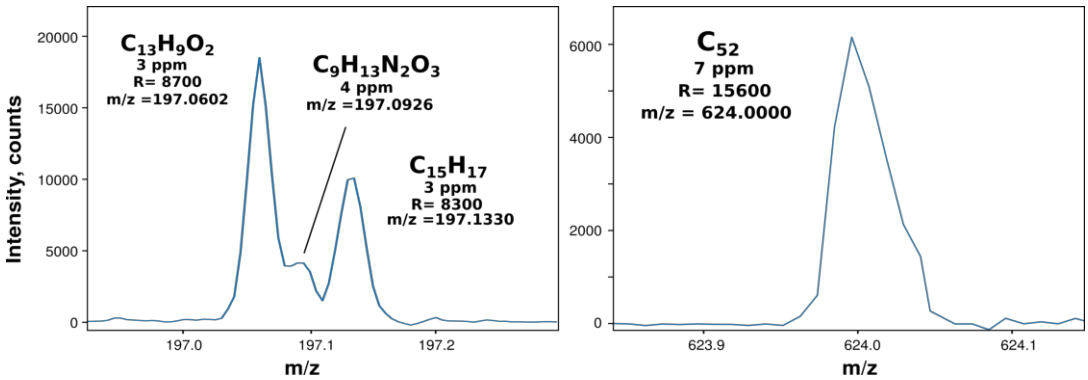

Figure 2.33 *Example of mass peaks recorded with the HR-L2MS instrument, showcasing high accuracy and mass resolution.*

2.3 Data processing methodology

Since the samples intended for offline chemical characterization were collected in different engine regimes, with a different particle production rate and size distribu-

© 2020 Tous droits réservés.

lilliad.univ-lille.fr

Thèse de Dumitru Duca, Université de Lille, 2020

tion, their coverage was not identical. Samples made-up of the smallest ultra-fine particles usually contain a much lower amount of material (Figure 2.34), which may further complicate the analysis. As a result, a comparison between mass spectra of different size-bin samples needs to take into account the variation in the analyzed particle mass. Therefore, to extract the maximum amount of information from mass spectra of size-selected soot particles, including trends in the chemical composition (*i.e.* size-dependent chemical composition), a data treatment methodology, developed in our laboratory and tailored to the specific nature of combustion generated particles mass spectra, was used [30, 99, 102]. All mass spectrometric data are analyzed using a two-step approach: i) assignment of chemical formulas to mass peaks based on the mass defect analysis, and ii) a subsequent statistical analysis using advanced multivariate tools.

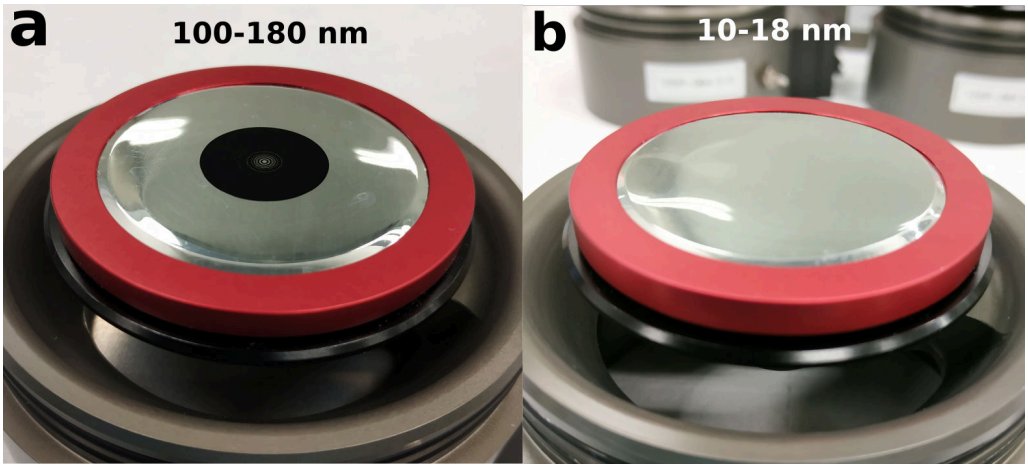

Figure 2.34 *Comparison of sample coverage for the 100–180 nm (a) and 10–18 nm (b) size bins.*

2.3.1 Assignment of mass peaks

Mass spectra of combustion generated particles are very complex, containing a large number of mass peaks. Although statistical analyses extracting important trends and patterns can be performed without identifying all the present species, peak identification is essential for interpretation of the obtained results. The mass defect analysis was used here for identification and assignment of molecular formulas to unknown mass peaks, and thus for defining a working peak list.

The slight difference in the nuclear binding energy of every nuclide gives rise to different exact masses. Therefore, different atoms, molecules or ions with the same nominal (integer) mass have unique exact masses. The mass defect (Δm) is defined as the difference between the exact and the nominal mass of an atom, molecule or ion and is a unique value linked to its composition. For that reason, mass defect analysis represents a powerful tool for identification of unknown species even in complex mass spectra [102, 118–120]. For instance, the exact mass of Carbon ^{12}C is $m_{exact} = 12.000000$ u and that of hydrogen H is $m_{exact} = 1.007825$ u, resulting in a null mass defect for carbon ($\Delta m_C = 0$ u) and a positive one for hydrogen ($\Delta m_H = +0.007825$ u). As a result, two hydrocarbons with different number of carbon atoms, but the same number of hydrogen atoms have the same mass defect. At the

© 2020 Tous droits réservés.
lilliad.univ-lille.fr

Thèse de Dumitru Duca, Université de Lille, 2020

same time, species with an identical number of carbons but a different hydrogen count have a positive mass defect, proportional to the number of hydrogen atoms (*e.g.* $\Delta m_{C_{10}H_8}$ = +0.062600 u). Since the mass defect of an oxygen atom is negative (Δm_O = -0.005085 u), oxygenated chemical species have lower mass defects values compared to hydrocarbons with the same nominal masses.

A typical mass defect plot (Figure 2.35) merges into one graph important information extracted from the raw mass spectra: the nominal mass of each detected peak (x-axis), its mass defect (y-axis), and its relative intensity (dot size). The advantages of these plots are twofold: first, they can be used to simplify the visualization of complex mass spectra, and second, homologous series of peaks line up, and thus complex patterns which can be used to identify unknown compounds may be highlighted. Such a representation enables the association of mass peaks to molecular classes such as aliphatic (arranged on a line with a relatively large positive slope due to the higher number of hydrogen atoms present in the molecule) and aromatic compounds (with a smaller slope as a result of a lower number of hydrogen atoms per carbon atom), Figure 2.35a. Therefore, the identification of several species belonging to the same series (found on a straight line) can help assign chemical formulas to other homologous compounds [102, 120], Figure 2.35b. This is especially helpful for species with high molecular masses, where the attribution of a chemical formula can be complicated.

The assignment of chemical formulas to mass peaks requires a mass resolution sufficient to separate chemical species with the same nominal mass. For instance, while a resolution of around 5000 is sufficient to completely separate $C_{14}H_{10}^+$ (m_{exact} = 178.078250 u) and $C_{13}H_6O^+$ (m_{exact} = 178.041865 u), for closely spaced ions (*e.g.* $C_{32}H_{14}^+$, 398.109550 u and $C_{25}H_{18}O_5^+$, 398.115425 u), the required resolution can easily increase up to 10^5 or even higher. As the m/z increases, the number of combinations of different elements resulting in the same nominal massH grows very fast [30]. Nevertheless, a lower mass resolution spectrum can provide important information about a sample. In particular, when studying combustion emissions sampled from a laboratory flame, C, H, and O are the major contributors to the total mass of soot, and therefore the mass analysis of peaks with a high signal-to-noise ratio (SNR) can be reasonably limited to $C_mH_nO_p^+$ ions. In the case of ICE emissions, elements associated with fuel (*e.g.* Na, K), lubricant (*e.g.* Ca), and wear of engine components (*e.g.* Al) can also be found, however, with a much smaller contribution. Identification of a mass peak within 5 ppm accuracy, often assumed as being "certain" [121], in this work is possible up to m/z 150–200. Additional information about the samples and experimental conditions can extend this range up to m/z 500–550, for instance by ruling out elements that should not be present in large quantities on the analyzed samples. In this work, mass defect analysis was applied to all mass spectrometry data obtained from L2MS and SIMS in order to assign chemical formulas to all detected peaks.

2.3.2 Statistical procedures

The choice of the appropriate technique for the analysis of mass spectrometric data is dictated by the structure of the mass spectrometric database. The latter is typically composed of a number of mass spectra each containing up to thousands of peaks. Statistical tools, such as multivariate analysis, can be used in this case to reduce the

© 2020 Tous droits réservés.
lilliad.univ-lille.fr

Thèse de Dumitru Duca, Université de Lille, 2020

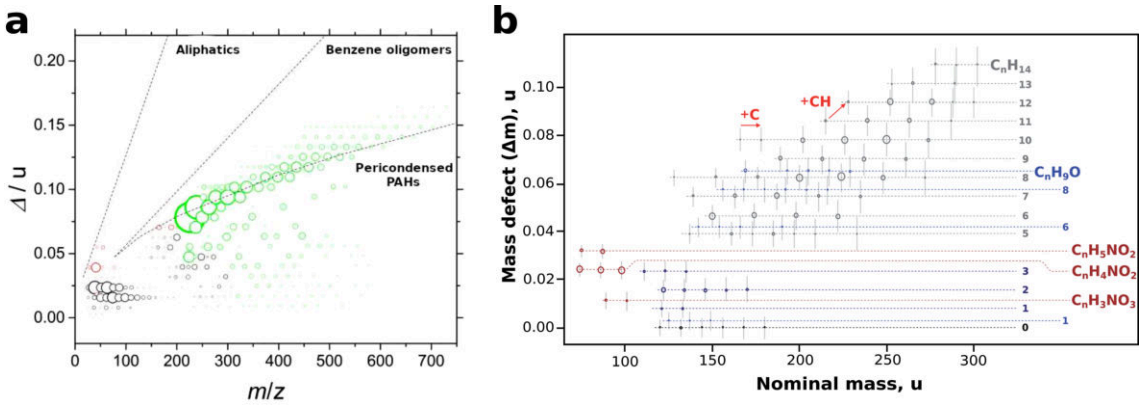

Figure 2.35 *(a) Example of a mass defect plot obtained from the SIMS mass spectrum of soot particles collected from a laboratory flame and illustrating its capacity to separate chemical species based on their corresponding molecular class. Ions with a low H/C ratio (black dots) are mainly attributed to fragment ions, high H/C ions to unsaturated hydrocarbons and low-mass PAHs (red dots), while high-mass ions (green dots) are assigned to PAHs and oxygen-containing hydrocarbons.The size of displayed markers is proportional to the corresponding peak integrated area. Reproduced from Irimiea et al. [30]. (b) Mass defect plot obtained from L2MS mass spectrum of soot collected from a standard soot generator (miniCAST) showing the alignment of homologous compounds. Reproduced from Duca et al. [102].*

dimensionality of the data and organize it into several clusters containing similar spectra or mass peaks. In this section, statistical techniques that have been adopted by our group for the analysis of mass spectrometric data, allowing us to identify convoluted patterns and extract hidden relationships, are described.

2.3.2.1 Principal Component Analysis

Principal Component Analysis (PCA) is a dimensionality-reduction method that is often used to minimize the number of dimensions of the used mass spectrometric database (*i.e.* a large set of observations, analyzed samples, described by several dependent and inter-correlated variables, mass peaks). The algorithm extracts the important information from the input data and expresses it as a set of summary indices called principal components. A transformed data set still contains the majority of the initial information, but, due to a lower dimensionality, can be more easily visualized. Moreover, a smaller data set also facilitates the identification of trends, jumps, clusters and outliers.

Principal components, determined by this algorithm, are new variables constructed from linear combinations of the initial ones. Geometrically speaking, principal components represent the orthogonal directions of the data in the multidimensional space that explain a maximal amount of variance (*i.e.* the lines that capture most information in the data). The relationship between variance and information is as follows: the larger is the variance along a given direction (the larger is the dispersion between data points), the more information it contains. Therefore, principal components can be seen as new axes that provide the best angle to visualize and evaluate the data, so that the differences between the observations are more apparent [122]. As a consequence, transformed data can be used to classify samples, reveal trends/patterns in large databases [123], and is often used to improve the

© 2020 Tous droits réservés. lilliad.univ-lille.fr

Thèse de Dumitru Duca, Université de Lille, 2020

readability of complex data [124].

PCA is quite sensitive regarding the variances of initial variables. Specifically, if there are large differences between the ranges of initial variables, those with larger ranges will dominate over the ones with small ranges, inadvertently leading to biased results. Moreover, the absolute signal intensity of detected compounds depends on a variety of factors such as sample coverage, substrate, desorption/ionization fluence, and thus all mas spectrometry data must be first normalized. A commonly accepted approach is the normalization to the total or partial ion count (TIC) [120, 125, 126]. The latter is used when several compounds, unrelated to the sample (*e.g.* compounds that are related to the substrate), have a rather high signal intensity. All mass peaks that have a signal-to-noise ratio higher than 3 are considered and then area integrated. The variance of the integrated peaks, usually, has a *L-shape* distribution, caused by a big difference in signal intensities of mass peaks, which is unacceptable for any statistical analysis techniques (within the normality-assuming statistics) [127]. Using a *L-shape* distribution with normality-assuming statistical tools will lead to an overestimated contribution from high intensity mass peaks, effectively "hiding" other patterns. Data scaling is commonly used to change the distribution from a *L-shape* to a *normal* one, however not all scaling techniques can be applied to mass spectrometric data as the majority of them are usually considered very "aggressive". For instance the Standard Scaling approach transforms the data such that its distribution will have a mean value of zero and a variance of 1 [128]. This effectively removes all the information about the covariance between different mass peaks and therefore will lead to a loss of information and should not be used with this particular data set. Another, more suitable method for converting the data to a bell-shaped distribution is by calculating the decimal logarithm of the data set, a procedure that preserves all the information about the covariance between mass peaks.

Principal components are calculated using the covariance matrix of initial variables [122, 129]. The eigenvectors of this matrix represent the directions of the axes with the largest variance (*i.e.* directions of principal components). Eigenvalues are simply the coefficients attached to eigenvectors that give the amount of variance carried by each component. Given a data set X with p observations and n variables, the first principal component PC_1 is represented by the linear combination of the original variables X_1, X_2, .., X_n:

$$PC_1 = \omega_{11}X_1 + \omega_{12}X_2 + ... + \omega_{1n}X_n \tag{2.5}$$

where ω_{1j} are the elements of the first eigenvector and can be used to interpret the meaning of the principal component. Most of the time, however, the interpretation of principal components is instead performed with loadings, as their magnitude is representative of the covariances/correlations observed between the initial variables:

$$loadings = eigenvectors \cdot \sqrt{eigenvalues} \tag{2.6}$$

A loadings plot, illustrating the loading of all the initial variables (Figure 2.36), are used to identify variables (*i.e* mass peaks) that have the largest effect on each principal component. A higher loading indicate that the variable strongly influences the principal component. Moreover, the sign of the loading is also important as it shows the correlation among variables.

© 2020 Tous droits réservés.
lilliad.univ-lille.fr

Thèse de Dumitru Duca, Université de Lille, 2020

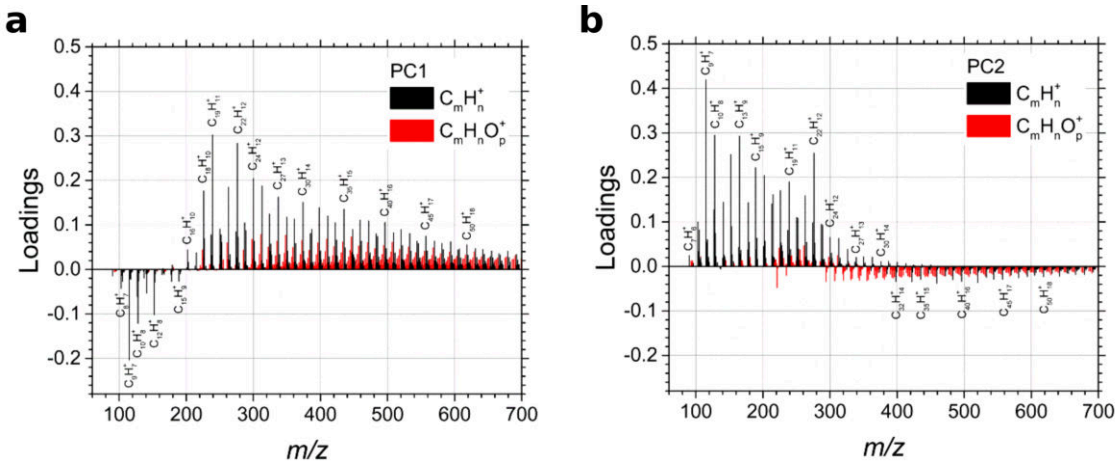

Figure 2.36 *Example of a loadings plot showing the contribution of each mass peak to the value of the first (a) and the second (b) principal components. The contribution of hydrocarbon and oxygenated species are shown in different colors. Based on the loadings plot, the physical meaning of each principal component can be determined. Reproduced from Irimiea et al. [30].*

As there are as many principal components as there are variables in the data, principal components are ranked in accordance with their significance (*i.e.* the first principal component accounts for the largest possible variance in the data set). Therefore, selecting only the first m components allows to reduce the dimensionality of the data set while still preserving the majority of the variance (*i.e.* information). It is, thus, important to properly choose the number of principal components that are considered. The eigenvalue (also called score) of each principal component measures the amount of variation it retains and can be used to determine the optimal number of components to take into account. An eigenvalue greater than 1 indicates that the corresponding principal component accounts for more variance than a single initial variable (*i.e.* one mass peak) - value commonly used as a cutoff point for the number of PCs. However, this is not very practical for datasets with a large number of variables and high redundancy, *e.g.* mass spectrometric data, as the variance retained by a single variable is very small. There is no universally established way to decide how many principal components to keep in the analysis. The choice depends on the specific field of application and the data set. Usually, for mass spectrometric data, the number of components is determined by the total variance, *i.e.* only the components that account for a certain fraction of the total variance (*e.g.* 70-80%) are considered. Another common practice in determining the optimal number of PCs is to use the *scree plot*, which represents the percentages of explained variance by each PC (proportional to its eigenvalue), ordered from the largest to the smallest, and to identify the point where the slope significantly changes. Only the components before the change point (also called "elbow") are considered [123, 130], Figure 2.37.

By projecting all the observations onto the low-dimensional (two or three dimensions) sub-space and plotting the results, it is possible to visualize the structure of the investigated data set. The coordinates of the observations (mass spectra in our case) on this plane are called scores, and hence the plotting of such a projected configuration is known as a score plot, Figure 2.38. When investigating score plots we look for clusters, outliers, and other patterns (*e.g.* gradual change in the principal component value between several observations). The combination of the score and

© 2020 Tous droits réservés.

lilliad.univ-lille.fr

Thèse de Dumitru Duca, Université de Lille, 2020

loadings plots allows to determine the contribution of initial variables (*i.e.* mass peaks) to all the observations (*i.e.* mass spectra).

2.3.2.2 Hierarchical Clustering Analysis

Clustering is an important method of uncovering information from a multivariate data set [122]. Hierarchical clustering analysis (HCA) is a multivariate procedure that identifies patterns in a data set by grouping the observations based on the distances between them. Additionally, it accounts for the total variation in the

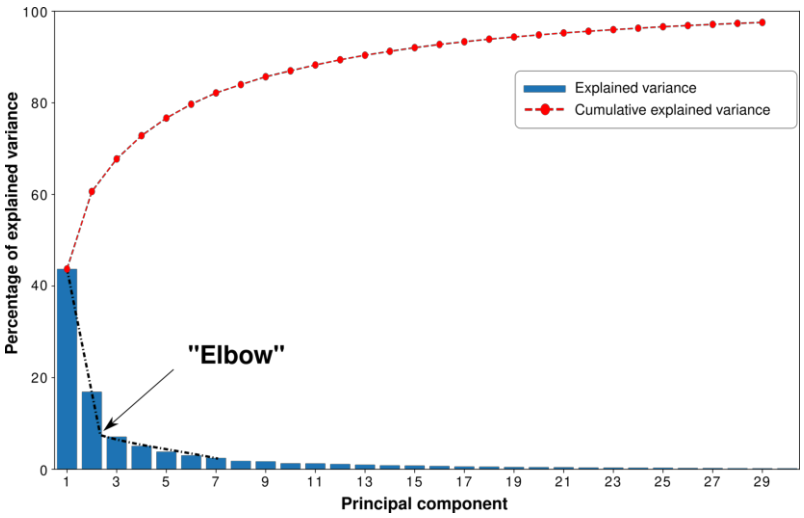

Figure 2.37 *Example of a typical scree plot showing the contribution of each principal component and the cumulative contribution of all PCs to the explained variance. The trend line of the component contribution is shown in black with the "elbow" point highlighted. For this particular scree plot, only the first two principal components are located before the "elbow" and, therefore, contain the majority of the meaningful data.*

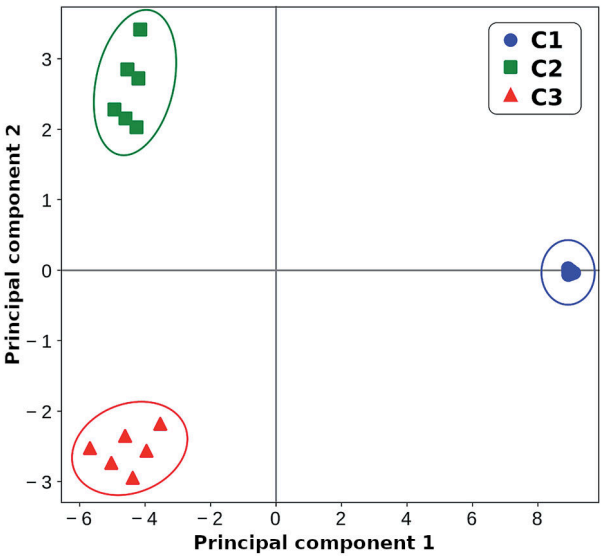

Figure 2.38 *Example of a score plot showing the projection of the observations (mass spectra) on the first two principal components. On such a projection, the observations can be easily grouped into three distinct clusters (C1, C2, and C3). Reproduced from Duca et al. [102].*

© 2020 Tous droits réservés.

lilliad.univ-lille.fr

Thèse de Dumitru Duca, Université de Lille, 2020

data set [131, 132]. This approach starts with a cluster for each observation (*e.g.* mass spectrum) or variable (*e.g.* mass peak) and then, at every step, merges the two closest ones, finishing with a single cluster. Since the dimensionality of the data is rather high, the distance between the clusters can be computed in different ways, which gives rise to various hierarchical methods [132, 133]. However, for mass spectrometric data Euclidian distances are typically used – a direct straight-line distance between two points [102, 120]:

$$d = \sqrt{\sum_{i=1}^{n} (q_i - p_i)^2} \tag{2.7}$$

where q and p are the coordinates of the two studied points for a given dimension and n is the total number of dimensions of the data set (equal to the number of variables). The main output of HCA is a dendogram, which shows the hierarchical relationship between clusters. For example, in Figure 2.39a two large clusters can be seen on the dendogram (green and red), each one consisting of even smaller ones. The number of output clusters is determined by the height (*i.e.* Euclidian distance) at which the dendogram is "cut". For instance, four different clusters will be formed if the black dashed line on the Figure 2.39a is used to cut the dendogram. The optimal distance value that yields an appropriate number of clusters depends on the analyzed data and should be individually chosen for each data set.

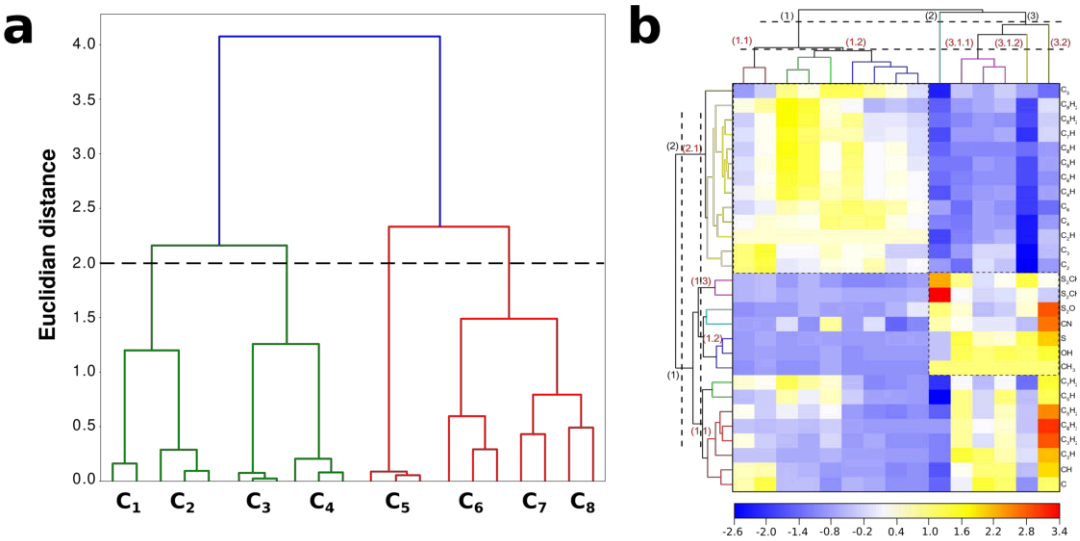

Figure 2.39 *(a) Example of hierarchical clustering dendogram. Two main clusters can be seen (red and green) and each can be further subdivided into another two clusters. Four different clusters will be formed if an Euclidian distance of 2.0 is chosen to cut the dendogram (black dashed line). (b) Example of a hierarchical clustering heat-map. HCA was performed on both observations (samples, columns) and variables (chemical species, rows) as indicated by the two dendograms on the top and left sides. The relative correlation between a certain observation and a variable is represented by the color of the corresponding cell. Adapted from Duca et al. [102].*

HCA can be applied not only to the original data set but also to principal components, technique called Hierarchical Clustering on Principal Components (HCPC). As mentioned above, large datasets of mass spectrometric data contain multiple

© 2020 Tous droits réservés.

lilliad.univ-lille.fr

Thèse de Dumitru Duca, Université de Lille, 2020

highly correlated variables that may lead to a clustering diagram which is difficult to interpret. Therefore, since principal components are not correlated, clustering performed on them is usually easier to interpret. Moreover, PCA acts as a de-noising method (a pre-processing step) that isolates the important information in the data set (in the first principal components used for HCPC) from the noise. Clustering obtained in this manner is more stable while still preserving the same tree-shape. The number of principal components to use for HCPC can be chosen with the methods that have been described above. A too small number of principal components will, however, lead to a suppression of information.

HCA and HCPC are usually applied only to the observations (*i.e* mass spectra), however, such clustering can be performed on both observations (samples) and variables (chemical species). In this case, a clustering heat-map is produced, illustrating the groups forming within the entire data set. The main advantage of a heatmap data representation is that it shows both dendograms (for observations and variables) alongside a colour-scaled illustration of the data (correlation) matrix itself, as one can see in Figure 2.39b. Each cell of the heat-map represents the correlation between a certain observation (sample) and variable (chemical compound), making the identification of highly-correlated species that determine the similarity between observations much easier.

2.3.2.3 Volcano plot

When comparing only two sample-sets (*e.g.* two samples), not all species will have a significant enough variation. For datasets characterized by a large number of variables (detected masses) and a relatively small number of observations (samples, mass spectra) it is important to choose a proper method of identifying variables that are the most different between two observations [134], *i.e.* that contribute the most to their "differential expression". The two usual methods of identifying the most different variables within a data set are the fold-change and the t-statistics, each one with its own advantages and drawbacks [134–136]. The fold-change represents the magnitude of the change in the signal of the same variable between two different observations: $FC_{1-2} = \frac{S_2}{S_1}$ (*e.g.* the signal of an organic compound measured on a sample collected with and without the catalytic stripper). The fold-change, however, does not take into account the noise often present in mass spectra, moreover, its value becomes less important with the increasing variance. Even though the t-statistics takes into account the noise, it can be less reliable for small datasets. To obtain a robust visualization of the "differential expression" of two observations (*e.g.* samples), a combination of the two methods can be used, leading to a *volcano plot*, Figure 2.40. This plot displays both fold-change (x-axis) and t-statistics (y-axis), thus combining a measure of statistical significance with the magnitude of the change.

The statistical significance is computed based on the **p** value obtained from the ANOVA model (a generalization of the t-statistics model for more than two groups) [132]. To improve the readability of the plot when the variance in the data set is rather high, the fold-change (FC) can be replaced by its logarithm ($log_2(FC)$). A volcano plot (Figure 2.40) consists of three main regions: i) the region where the data-points have either a small magnitude of change (< 1) or are not statistically significant (p-value > 0.05 or $-\log_{10}$(p-value) > 1.3) – usually displayed in grey, ii) data-points with high contribution to the first sample with a high statistical

© 2020 Tous droits réservés.
lilliad.univ-lille.fr

Thèse de Dumitru Duca, Université de Lille, 2020

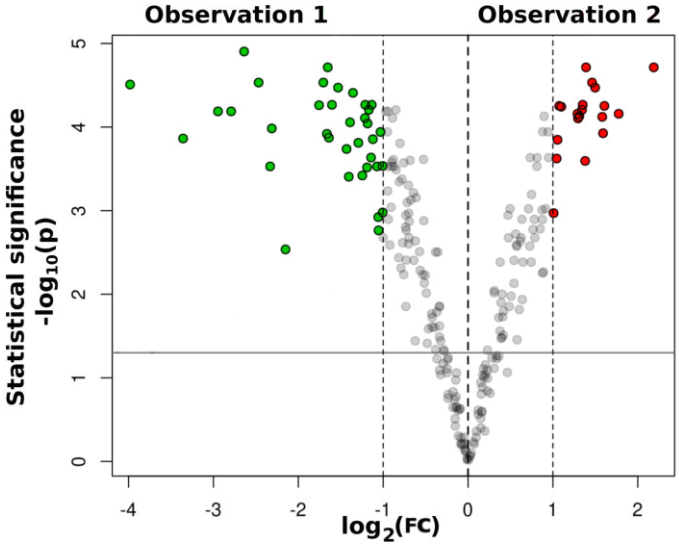

Figure 2.40 *Example of a volcano plot illustrating the three main regions: points with either a small fold change or statistical significance – grey markers, points with high contribution to the first sample with a high statistical significance – green markers, and points with high contribution to the second sample with a high statistical significance – red markers.*

significance, and iii) data-points with high contribution to the second sample with a high statistical significance. Since only the last two regions contain statistically significant information, they need to be used for making meaningful conclusions about the mass spectrometric data.

2.4 Conclusion

In this chapter, the necessary experimental and theoretical background for understanding the studies described in Chapter 3 – physico-chemical characterization of ICE emissions, and Chapter 4 – adsorption energy measurements on surrogate soot samples were presented. Some (customized) techniques or instruments, such as the newly acquired high-resolution two-step laser mass spectrometer installed at the laboratory during this thesis, were presented in more detail as to create a complete description, possibly useful for future studies. Other techniques that are either commercially available or have been thoroughly described before were presented in less detail, with necessary reference to existing literature.

© 2020 Tous droits réservés.
lilliad.univ-lille.fr

Chapter 3

Size-selective characterization of ultra-fine particles emitted by an internal combustion engine

3.1 Introduction

The road traffic constitutes one of the major sources of combustion generated carbonaceous aerosols (*i.e.* soot). Even though the air quality has been significantly improved in the past decades through the successive tightening of emission standards, particulate emissions from on-road vehicles continues to represent one of the major sources of anthropogenic ultra-fine particulate matter (PM) in urban areas [37, 55, 58, 137]. Recent improvements in engine technology resulted in a significant decrease in the total number and mass of PM emitted by on-road vehicles. This, however, also led to a shift in the particle diameter toward smaller sizes (lower than 100 nm [50]). In particular, sub-23 nm particles, produced in large concentrations by both Diesel and gasoline direct injection (GDI) engines [55], have recently attracted a lot of attention. The percentage of these particles, currently not being limited by existing emission regulations with a cut-off size of 23 nm, could reach 30–40% of the total PN for vehicles equipped with a GDI [58]. The results presented in this chapter were obtained in the framework of the European H2020 PEMS4Nano project (`www.pems4nano.eu`), with the objective of developing a robust and reliable measuring system for sub-23 nm particles, together with the associated measurement methodology and procedures. The created system and measurement procedures are meant to aid with the development process of new engine technologies and, most importantly, serve as a basis for future regulations by demonstrating both the capabilities and limitations of particle measurement technologies, especially under real driving conditions (RDE). The development of a particle measurement system capable of maintaining its precision and reliability for a wide range of engine operation conditions (*i.e.* in real driving conditions) requires extensive knowledge of physico-chemical properties of the particles emitted during the drive cycle. Therefore, we propose here an extensive experimental characterization (morphology, nanostructure, chemical composition), whose results will constitute the building blocks of an extensive database, *i.e.* the necessary foundation upon which measurement procedures and theoretical models can be built (bottom-up approach). The theoretical approach (Model-Guided Application, MGA) supplied with the physico-chemical

© 2020 Tous droits réservés. lilliad.univ-lille.fr

Thèse de Dumitru Duca, Université de Lille, 2020

data derived from our experimental characterizations was developed to predict particle formation in the engine, as well as particle dynamics in the exhaust system and sampling line. The use of MGA is advantageous since it allows the optimization of the developed procedures with respect to a wide variety of engine set points. The latter is especially important due to a multitude of regimes the engine goes through in real driving conditions, some being only transitory. One key strategic decision made while building the particle emission measuring system (PEMS) prototype was to use a catalytic stripper (CS) to remove the organic fraction from the particles emitted by the engine. The CS action on both the gas and particulate phases emitted by the engine, and, more specifically, on size-selected particles were thoroughly experimentally investigated in this work. Online measurements (performed by a research team from the University of Lille, PC2A – LII measurements, and University of Cambridge – aerodynamic–mobility–mass measurements) and collection of particulate matter intended for offline characterization (University of Lille, PhLAM and Horiba Scientific) were carried out in parallel. This chapter describes the results of the offline physico-chemical characterization of combustion byproducts (polydisperse and size-selected particles, and gas phase). More information about the sampling procedure (*i.e.* sampling line, collection methods and used substrates) can be found in Section 2.1.1.1. A multi-diagnostic approach was adopted for sample characterization, including Mass Spectrometry analysis (L2MS and SIMS, University of Lille) as well as structural/morphological characterization using microscopy techniques (SEM, Bosch; TEM, University of Lille; AFM, Horiba Scientific) and Tip Enhanced Raman Spectroscopy (Horiba Scientific). Main findings of these analyses were used as an input for the theoretical model (CMCL, Cambridge, UK) allowing its training and validation. A collaborative paper outlining the main results has been published [103] with three more being in preparation.

A single-cylinder test engine was used here as a source of combustion-generated particles, produced under different operation conditions in a controlled environment, Section 2.1.1.1. Since the collection of material for offline analysis can be lengthy (up to 12 hours, Section 2.1.1.3) the regimes must be carefully chosen in order to collect particles carrying the maximum amount of physico-chemical information within the time frame of a sampling campaign (typically one to two weeks at the engine test-bench Robert Bosch GmbH, Renningen, Germany). All the analyzed engine regimes are listed in Table 2.1. Two different variables related to the test engine were extensively studied: i) the engine working point, which includes different air/fuel ratios, applied loads and speeds, and ii) the impact of the mechanical state of the engine (*i.e.* the impact of various malfunctions). Since a multitude of samples (Table 2.3) were analyzed, each one corresponding to a different engine regime as well as sampling method, a notation scheme that provides a short summary of all the necessary information about the sample is employed (see Section 2.1.1 page 20).

3.2 Morphology and structure characterization

One of the biggest challenges in collecting and studying size-selected combustion-generated particles is avoiding their agglomeration in the sampling line. A proper sampling procedure is essential to prevent the agglomeration of small particles that can result in them being collected on a different impaction stage (with a higher cut-off size compared to their initial dimensions) and thus skewing the results of

© 2020 Tous droits réservés.
lilliad.univ-lille.fr

Thèse de Dumitru Duca, Université de Lille, 2020

the size-selected chemical analysis. In order to ensure that the experimental setup is well optimized for sampling of even small single particles, several samples of collected particulates were analyzed with SEM during the sampling campaign (Robert Bosch GmbH, Renningen, Germany). Moreover, the information obtained from SEM images (*e.g.* number of particles) was used to evaluate the surface coverage and determine the optimal collection time for samples intended for chemical characterization. This kind of "on-site" analysis, allowing to fine-tune the sampling setup, is essential to avoid the collection of unnecessary samples that, due to improper sampling, do not carry any useful information. After the sampling campaign, additional analyses were performed with TEM and AFM/TERS (University of Lille and Horiba Scientific, respectively), see Section 2.2.1, to study the structure and morphology of the collected particles.

3.2.1 SEM analyses

Particles analyzed with SEM were collected on Si wafers with a combination of a short DMA, set to pass particles with a mobility diameter of 18 nm (±5 nm), and a NAS, Section 2.1.1.3. The analysis of particles produced in engine regimes corresponding to a normal operation (NH2000 and NM2000 regimes) revealed the presence of predominantly single, spherical particles with a diameter ranging from 17 to 23 nm, Figure 3.1, which are presumably primary soot particles. This is in agreement with previous studies on the emitted particles from gasoline direct injection engines [138, 139]. The fact that single primary particles were collected on these samples and were not lost on the way due to their aggregation confirms that the experimental setup is able to minimize the aggregation of particles to an extent that should not affect the subsequent chemical analysis (*i.e.* caused by contribution of smaller and aggregated particles to a size-bin corresponding to larger dimensions).

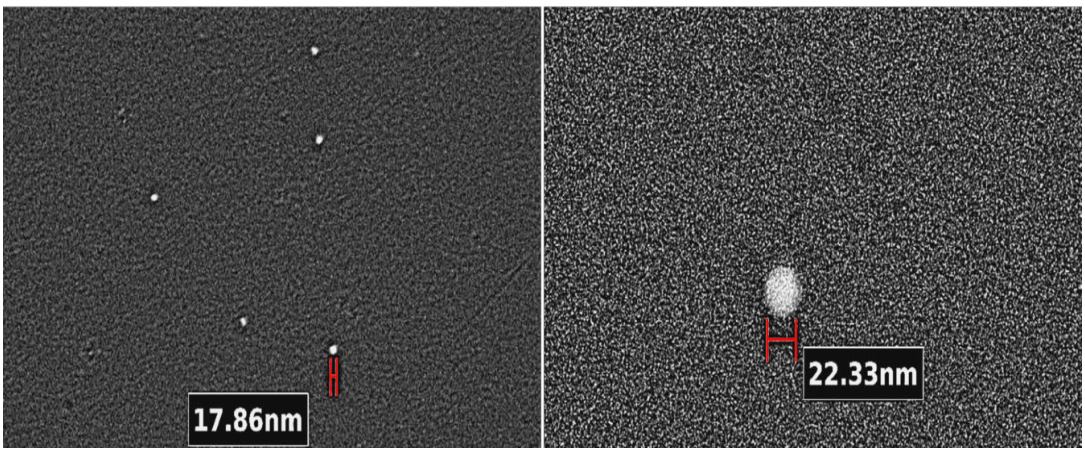

Figure 3.1 *SEM images of size-selected particles (size bin centered at 18 nm) collected on Si wafers with a NAS in NH2000 (a) and NM2000 (b) engine regimes.*

The analysis of sample OM2000 (medium load, addition of oil, Table 2.3), presented in Figure 3.2, revealed the presence of particles in a needle or tube shape with a length up to 200 nm. Particles in this shape were only detected for this regime

© 2020 Tous droits réservés.

lilliad.univ-lille.fr

Thèse de Dumitru Duca, Université de Lille, 2020

(OM2000 regime, *i.e.* only when additional oil was supplied to the combustion chamber). Carbon nanotubes (CNT) and nano-rods are known to be present in the exhaust of spark ignited engines [140, 141]. Their formation requires a hydrocarbon source, a catalyst source (*e.g.* Mb, Ni, or Fe), and a group 16 element promoter (*e.g.* S, Se, Te). Metallic seed particles can originate either from the consumption of lubricating oil or from fuel additives such as ferrocene [$Fe(C_5H_5)_2$], an iron-carrying organometallic compound that is used as an antiknock agent in gasoline fuels. The presence of the latter was confirmed by SIMS mass spectra, as will be discussed in Section 3.3. In this reaction mechanism, thermal decomposition of the iron source leads to the formation of catalyst nanoparticles, which act as catalytic surfaces for CNT/nano-rod growth once sufficient carbon is available from the decomposition of hydrocarbons. Dibenzothiophene ($C_{12}H_8S$), one of the most common forms of S in fuels, was also detected. Therefore, any CNTs/nano-rods observed on the samples could potentially be produced in the engine, rather than being contaminants.

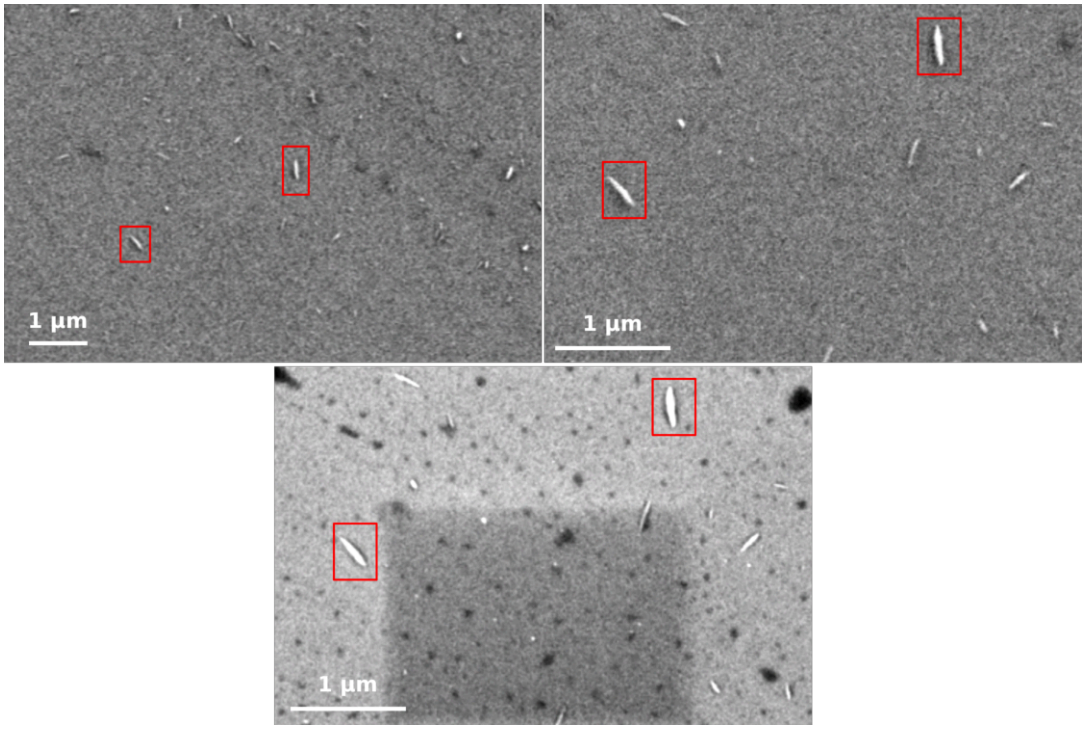

Figure 3.2 *SEM images of particles collected on a Si wafer in the OM2000 regime (size bin centered at 18 nm). Needle or tube shape particles have been detected (red rectangles).*

3.2.2 TEM analyses

The analysis of high-resolution TEM images, Figure 3.3, reveals that the size of primary particles is around 14–19 nm, however there are also solitary particles of a bigger size. These "big" particles are not very numerous (only a few were found) and can have a size of up to ∼60 nm.

High-resolution TEM analyses were performed to reveal the nanostructure of collected particles. Figure 3.4 shows patterns characteristic of nanoscale graphene layers arrangements suggesting these particles are indeed soot. However, Figure 3.4 also evidences that the particles collected under the exact same conditions (size bin

© 2020 Tous droits réservés.

lilliad.univ-lille.fr

Thèse de Dumitru Duca, Université de Lille, 2020

and engine regime) can exhibit large variation in carbon fringe length and tortuosity (the ratio of the fringe length to the straight-line distance). Long carbon fringes with a reduced tortuosity are indicative of a more graphitized soot particle while the inverse is true for the amorphous soot nanostructure [142]. Therefore, the fact that particles collected under the same conditions show different degrees of graphitization is a sign of different soot maturity (a higher degree of graphitization indicates a more mature soot), caused by different particle inception time [142, 143].

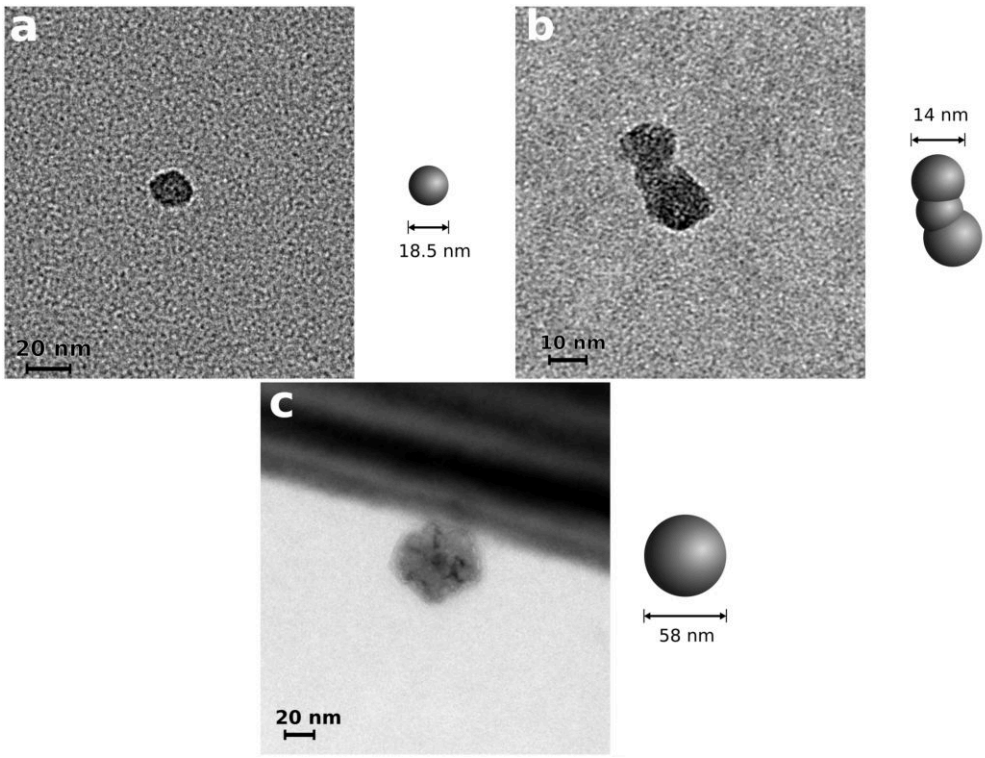

Figure 3.3 *TEM images of size-selected NH2000 (2000RPM, high load) particles collected with a combination of DMA and NAS on a SiN wafer (a and b) and NanoMoudi on a carbon Lacey TEM grid (c). A possible shape of the particle/aggregate is also shown.*

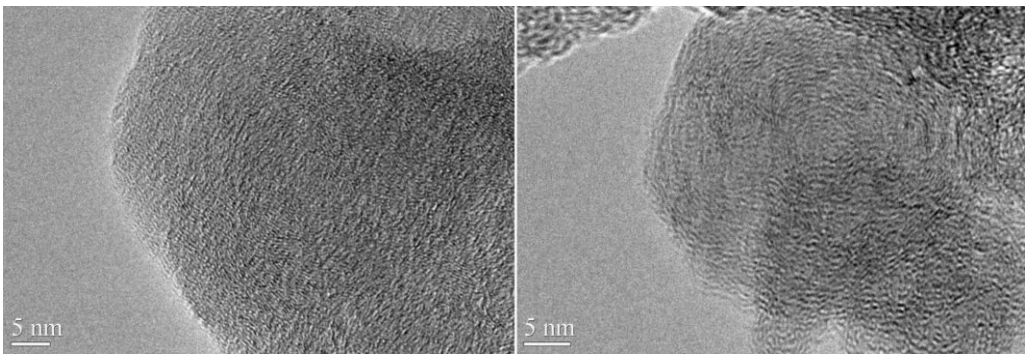

Figure 3.4 *High magnification TEM images of two NH2000$_{10-18}$ (2000RPM, high load, 10–18 nm size bin collected on a carbon Lacey TEM grid) particles. A high variability in particle nanostructure is observed, as illustrated by the different length and tortuosity of the carbon fringes.*

TEM images do not provide any information about the surface organic fraction of the analyzed particles, however its presence can be inferred from the particle

© 2020 Tous droits réservés.

lilliad.univ-lille.fr

Thèse de Dumitru Duca, Université de Lille, 2020

behavior in the vacuum and under the electron beam. To test whether particles contain a notable amount of organic compounds, the microscope was switched to the STEM mode (scanning transmission electron microscopy) in which the electron beam was focused (with a focused beam diameter of 1 nm) on a single particle. The particle was scanned for 10 minutes during which the interaction between the electron beam and the particle promotes the desorption of organic compounds. TEM images before and after irradiation of the same particle (shown with the same magnification) are displayed in Figure 3.5. One can see that the irradiation with an electron beam caused the particle to shrink, reducing its diameter by ∼10%. This reduction in size is likely due to the desorption of the surface organic fraction. In addition, while the transformation might also originate from the alteration of the carbon nanostructure, no change in either fringe length or tortuosity was observed.

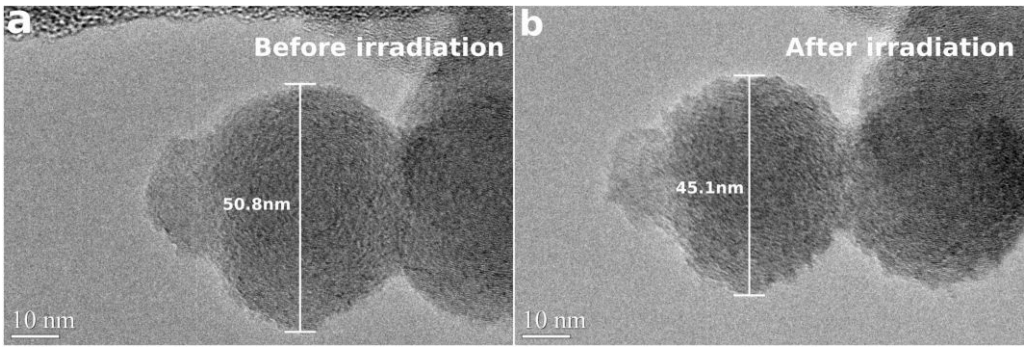

Figure 3.5 *Comparison between high resolution TEM images of a soot particle obtained in the NH2000 engine regime taken before (left panel) and after (right panel) electron irradiation in STEM mode.*

Soot aggregates can contain tens or even hundreds of primary particles (depending on their size), therefore it is rather difficult to retrieve the information about its three dimensional shape only from a "top-view" image. One of the advantages of TEM analysis is the ability to record images of the sample (in this case soot particles) for different tilt angles of the sample holder in order to recover the shape of the analysed particle. In fact, by recording a series of images of the same particle for a range of different tilt angles, one can reconstruct its three dimensional shape. This technique, while being resource and time consuming, opens the possibility to characterize the particle (*e.g.* determine the surface, volume, fractal dimension) with a much higher precision.

Not all particles can be chosen for 3D reconstruction as they should be well visible at any possible tilt angle (their view can be obstructed by other particles, sample holder or substrate material, Lacey carbon membrane in this case). The 3D reconstruction procedure started with the recording of high resolution image series of a particle/aggregate, taken under different tilt angles, Figure 3.6. More specifically, a TEM image was taken every 5° from -55° to +55° of tilt. All images were then aligned to each other in order to eliminate the spacial drift. To be able to reconstruct the shape of the particle, high contrast images are required, however, due to the amorphous nature of the substrate and soot particles the obtained contrast (between the particle and the Lacey carbon TEM grid) was rather low. A better contrast can be achieved for a particle/aggregate suspended from a side of the copper grid, however no particles were found to be attached on the grid in a way where the

© 2020 Tous droits réservés.

lilliad.univ-lille.fr

Thèse de Dumitru Duca, Université de Lille, 2020

copper would not obstruct the view at extreme tilt angles. Due to the low contrast, images containing only the outline of the particle, without the background, were used instead.

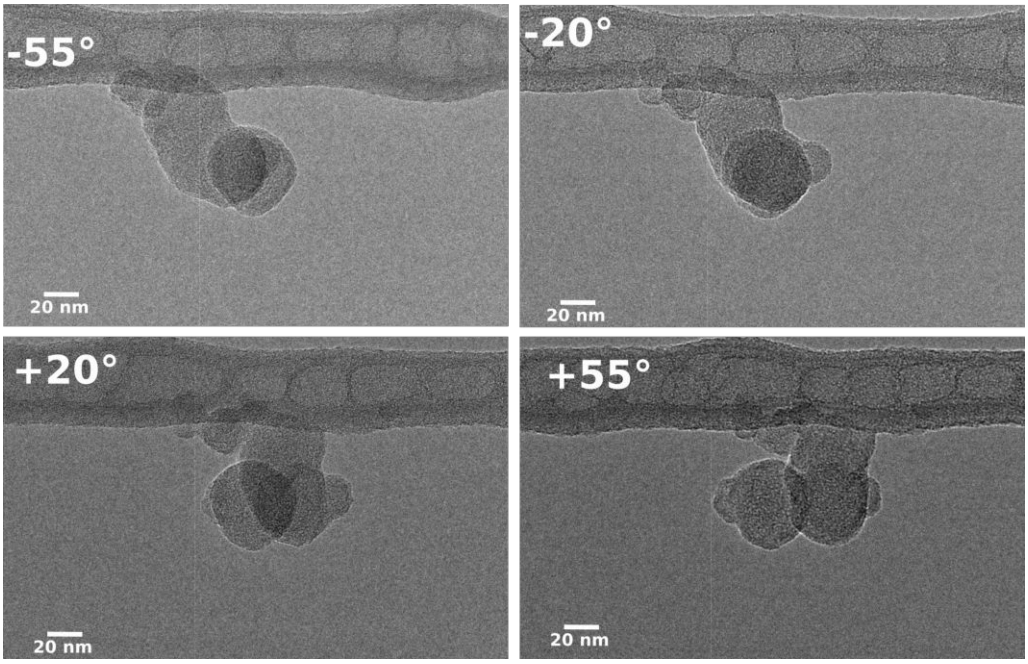

Figure 3.6 *Examples of high-resolution TEM images of the same particle taken at different tilt angles of the sample holder. The relative tilt angle of the sample holder is indicated for each image.*

The reconstruction process requires a "complete" image series - ideally with pictures taken from 0° to 360° (or from -180° to +180°) which cannot be accomplished in practice (the angles are determined by the sample holder). Therefore, the first step is to compute the projections from the missing angles by interpolation (for $\varphi \in [-55°, +55°]$) and extrapolation (for $\varphi \notin [-55°, +55°]$) of the existing data [144]. The algebraic reconstruction technique (ART) was used for the 3D reconstruction [145] as it is more adapted for the electron microscopy images. The comparison between high-resolution TEM images and the corresponding projections of the obtained 3D model are shown in Figure 3.7. We can see that the algorithm was able to reconstruct all the fine details seen on the original images of the particle, despite the relatively small number of available TEM images. Therefore, this technique can be used to obtain reliable information about the shape of soot aggregates, providing that a sufficient number of high resolution TEM images of the particle can be recorded.

3.2.3 AFM/TERS analyses

AFM analysis, performed at Horiba Scientific, Villeneuve D'Ascq (partner in the PEMS4Nano project), was used to determine the size of single particles. Moreover, we took advantage of the TERS module installed on the instrument to record Raman spectra for individual particles. The analysis was performed on samples collected in the NH2000 engine regime (optimal conditions, high load), Table 2.3. AFM measurements were carried out on a 1.2 x 1.2 μm^2 region (300 x 300 pixels), Figure

© 2020 Tous droits réservés.

lilliad.univ-lille.fr

Thèse de Dumitru Duca, Université de Lille, 2020

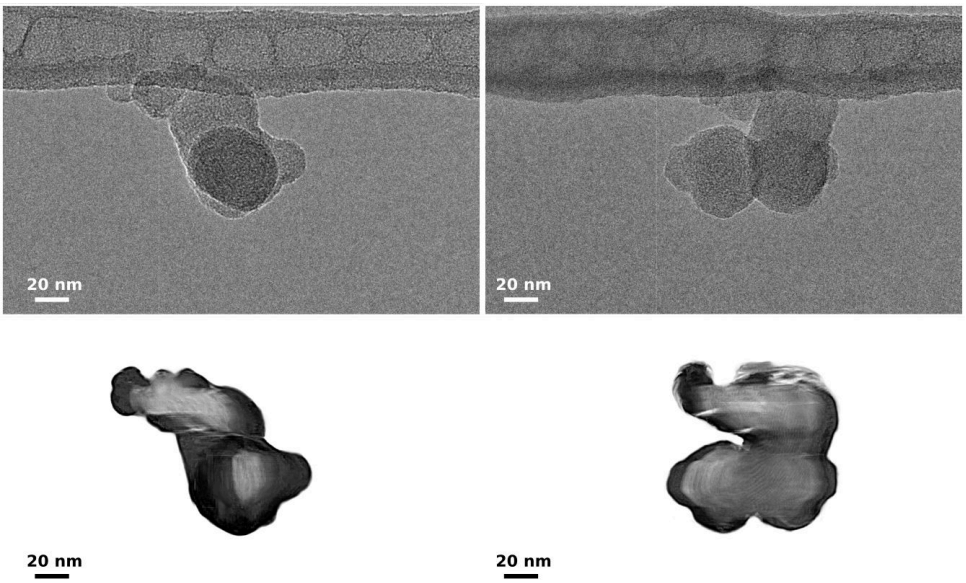

Figure 3.7 *Comparison between the high resolution TEM images of a soot particle and its corresponding snapshots of the reconstructed 3D model taken from the same perspective.*

3.8a. The heights of particles 1 and 2 shown in Figure 3.8d were determined to be 10 nm and 6 nm. The measured diameter is highly dependent on the used tip, especially when the radius of the scanned object is close to dimensions of the tip. The Full Width at Half Maximum (FWHM) of the profiles for particles 1 and 2, obtained with a sharp tip (r = 1 nm), are <48 nm and <43 nm, respectively.

Two smaller zones of the NH2000 sample have been characterized by TERS with a resolution of 7 nm/pixel (zone I) and 5 nm/pixel (zone II) and with a Raman integration time of 100 ms (one spectrum/pixel). The TERS maps of zones I and II are presented in Figure 3.8b and 3.8c, respectively. Raman spectra of carbon materials exhibit two main features whose intensities depend on the nature of the analyzed carbon material (see Figure 3.9): the G (graphite) band, derived from in-plane motion of carbon atoms (around 1580 cm^{-1}) and the D (defect) band (D1), attributed to lattice motion away from the center of the Brillouin zone (around 1270 — 1450 cm^{-1}). The TERS maps displayed in Figure 3.8b,c are obtained by integrating the G band only.

Besides TERS maps, TERS spectra were obtained for particles 2, 3, and 4 and are displayed in Figure 3.9. The three spectra exhibit very different profiles (for example, the relative intensity of the D band to the G band is higher for particle 2 and lower for particles 3 and 4) which is indicative of major structural variations between nanoparticles collected in the same engine regime and within the same size bin.

A more quantitative approach involves a five-band fitting method, often applied to Raman spectra of soot particles [21, 146], in which the G, D1, D2, and D4 bands are fitted with a Lorentzian profile, whereas the D4 band is fitted with a Gaussian profile. The fit results are presented in Figure 3.9. The spectral parameters determined by curve fitting are highly variable across the three particles (Table 3.1), confirming our first observation. For instance, the ratio of the integrated areas of D1 to those of (G+D2) bands is usually considered a good indicator of the order in the soot structure in conventional micro-Raman studies [147]. This value increases from

© 2020 Tous droits réservés.

lilliad.univ-lille.fr

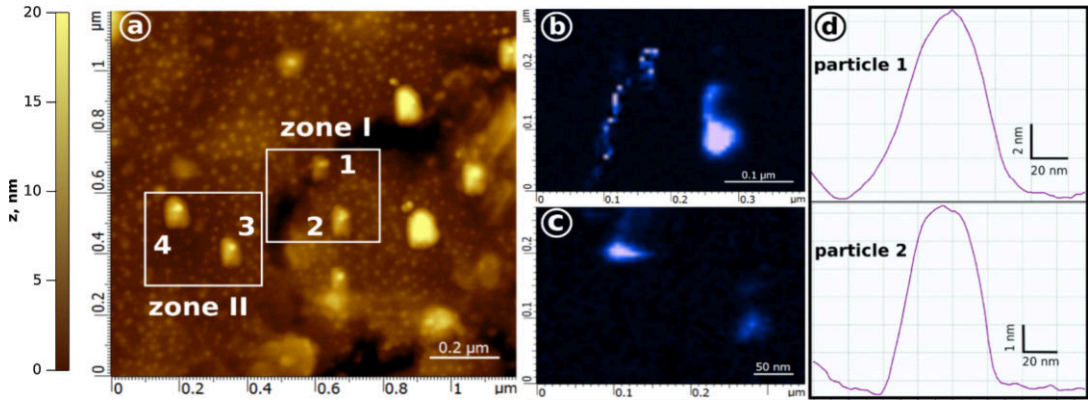

Figure 3.8 *AFM and TERS study of nanoparticles collected in the NH2000 engine regime (optimal conditions, high load) on gold coated Si wafers. Topography image (1.2 x 1.2 μm^2) (a), TERS mapping (G band only) of zone I, particles 1 and 2 (b), and zone II, particles 3 and 4 (c), topographic cross-sections of particles 1 and 2 (d).*

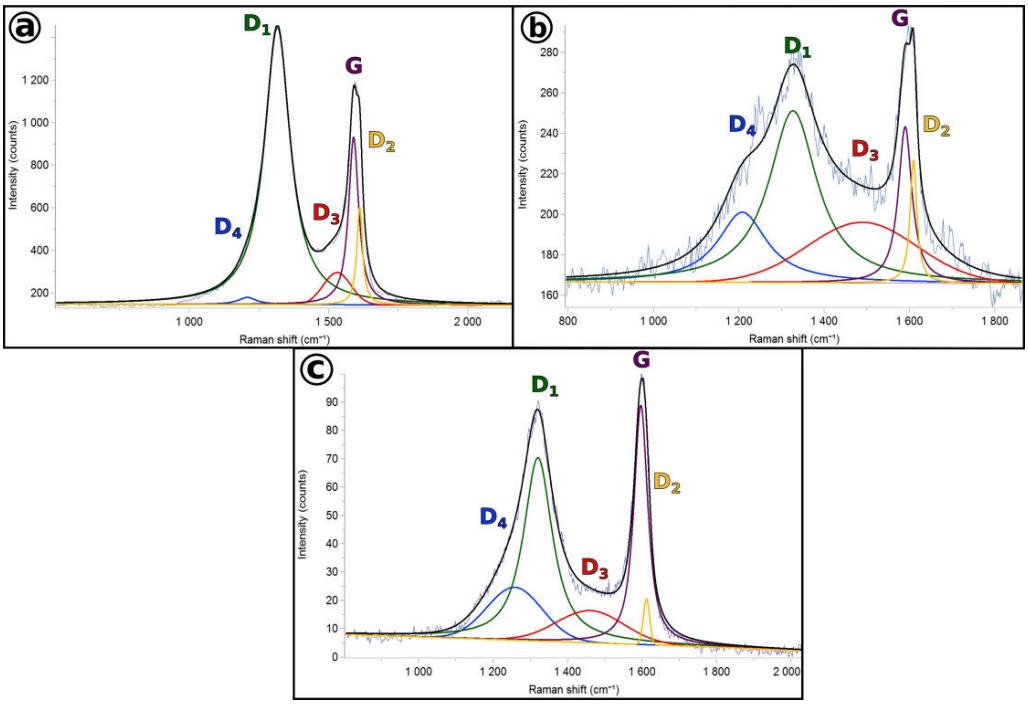

Figure 3.9 *Five-band fitting model applied to the TERS spectra of particles 2 (a), 3 (b), and 4 (c). Spectra were fitted using tools available in Labspec 6 software (Horiba Scientific).*

1.5 (particle 4) to 2.5 (particle 3) and to 3 (particle 2), suggesting that particle 2 has a much more disordered structure compared to particles 3 and 4. In addition, the presence of strong signatures at 1208 and 1278.6 cm^{-1} on the spectra of particles 3 and 4 could be an indicator of organic molecules present on the surface of the particles. However, since TERS measurements were performed here (to the best of our knowledge) for the first time on ultra-fine combustion-generated particulate matter, more research is needed to determine if the relative intensity of D and G bands can be interpreted in the same way as the ones obtained in common Raman studies.

Structural and morphological measurements described in this section revealed the diversity (in terms of nanostructure) of soot particles generated in the same

© 2020 Tous droits réservés.

lilliad.univ-lille.fr

Thèse de Dumitru Duca, Université de Lille, 2020

Table 3.1 *Deconvolution of the TERS spectra for particles 2, 3, and 4.*

Particle	Band	Position, cm^{-1}	Width, cm^{-1}
Particle 2	G	1589.7	43.4
	D1	1315.5	111.4
	D2	1611.5	24.7
	D3	1530.7	117.8
	D4	1208	80.4
Particle 3	G	1589.4	38.5
	D1	1326.8	137.1
	D2	1608.5	19
	D3	1489	304.1
	D4	1208	140
Particle 4	G	1596.6	44.6
	D1	1320.2	92.8
	D2	1611.7	20.1
	D3	1460.6	213.9
	D4	1257.8	175.1

engine regime and collected within the same size bin. This observation is especially important for the interpretation of off-line chemical characterization results, presented below (Section 3.3), which, conversely, were not obtained for individual particles but rather for a larger number of them (the number of addressed particles is determined by the diameter of the laser or ion beam used in the experiments). Therefore, the properties and trends that are derived in the next section are averaged over many (different) particles, and thus are statistically significant.

3.3 Chemical characterization

To obtain a comprehensive chemical characterization and thus provide valuable inputs for building and validating the theoretical model, combustion particles were analyzed with L2MS and SIMS. This analysis, in conjunction with the data-treatment methodology developed in our group [30, 99, 102] (Section 2.3), not only allows an extensive database featuring size-dependent molecular-level chemical composition to be built, but also unveils hidden trends and chemical dependencies that can be linked to experimental conditions used to obtain the samples (*e.g.* fuel and lubricant oil used in the engine). As the main objective of this work is the study of size-dependent chemical composition of soot particles, the following section first details the chemical composition of size-selected soot particles sampled in a variety of engine operation regimes. The obtained information is then used to discriminate particles with respect to their size and provenience (*i.e.* engine condition). Then, the chemical composition of both particulate matter (size-selected and polydisperse) and gas phase emitted by the engine was used to assess the efficiency of the catalytic stripper. And finally, the study of particulate matter sampled with and without the stripper enabled the evaluation of the surface organic fraction present on size-selected particles.

© 2020 Tous droits réservés.

lilliad.univ-lille.fr

Thèse de Dumitru Duca, Université de Lille, 2020

3.3.1 Evolution of the chemical composition with particle size

One major points to be determined is whether the chemical composition of emitted particles varies with their size. Several engine regimes were studied (Table 2.3), each one associated with a set of unique conditions defining the combustion process, and thus the chemical composition of engine emissions. A malfunction represents an extreme case of engine operation accompanied by combustion in sub-optimal conditions which leads not only to higher emissions (in terms of particle number, mass and gases) but also to a larger number of organic species present on the surface of the emitted particles. For this reason, mass spectra of particles sampled from a faulty engine contain a large number of peaks. The complexity of such spectra makes their analysis quite arduous. Mass spectra of particles sampled in the OM2000 regime (optimal conditions with an addition of oil, Table 2.3) and illustrated in Figures 3.10 and 3.11 are examples of such complex spectra. Therefore these typical spectra of size-selected particles produced in engine regimes associated with a malfunction, were preferentially chosen to demonstrate the analytical procedure followed to interpret mass spectrometry data. Note that a similar approach, adapted to the complexity of each spectrum, was applied to the analysis of all other samples. Two different engine malfunctions were studied: OM2000 – optimal conditions with an addition of oil, and FM2000 – low air/fuel ratio. These particular engine regimes were chosen as they simulate two different extreme cases of operation, equivalent to either a "worn out" engine with high oil consumption (OM2000) or a fault in the fuel system but with a normal oil consumption (FM2000), Section 2.1.1. Since both regimes feature a higher consumption of one of the two main sources of organic species emitted by the engine, fuel or oil, the study of particles generated in these regimes can help identify chemical markers associated with the aforementioned sources. Such information can further aid with the interpretation of mass spectrometric data obtained for particles emitted by a well-maintained engine, and thus should be obtained before analyzing samples collected in normal operation conditions.

3.3.1.1 "Worn out" engine regime

The analysis of samples obtained in the OM2000 regime was performed with L2MS with two different ionization wavelengths (266 nm and 118 nm, Figures 3.10 and 3.11, respectively), to selectively target either aromatic or aliphatic compounds. Several metals were detected (Na^+, K^+ and Ca^+) with both ionization wavelengths. While Na^+ and K^+ are mostly associated with fuel, they can also be present in the lubricating oil as trace elements [148–151]. In addition, the origin of Ca^+ is most likely the lubricating oil, since Ca is a component of detergent additives, widely used in modern motor oils [149, 151].

Mostly aromatic species are detected when the ionization of laser-desorbed compounds is performed at 266 nm (Figure 3.10). They are visually separated into two groups: one of lower and one of higher mass compounds. The first group gathers aromatic species with one to two aromatic rings and their alkylated derivatives (m/z 78 – 170) and is present in all sample spectra with varying relative intensities. The second group encompasses aromatic compounds with three and more rings. Volatility properties of aromatic compounds were linked before to the number of aromatic rings present in the molecule [85, 152]. Accordingly, three different volatility-related

© 2020 Tous droits réservés.

lilliad.univ-lille.fr

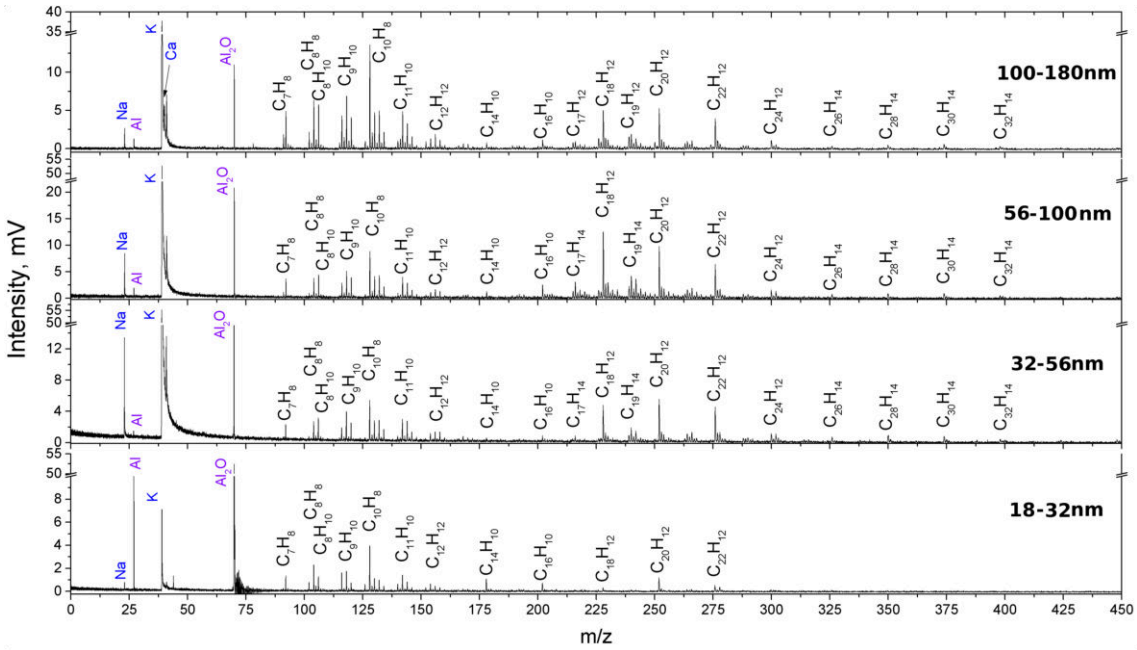

Figure 3.10 *L2MS spectra of four samples (particle size 18-180 nm) obtained in the OM2000 engine conditions (optimal operation, medium load). The analyses were performed with an ionization wavelength λ_i=266 nm to target aromatic compounds.*

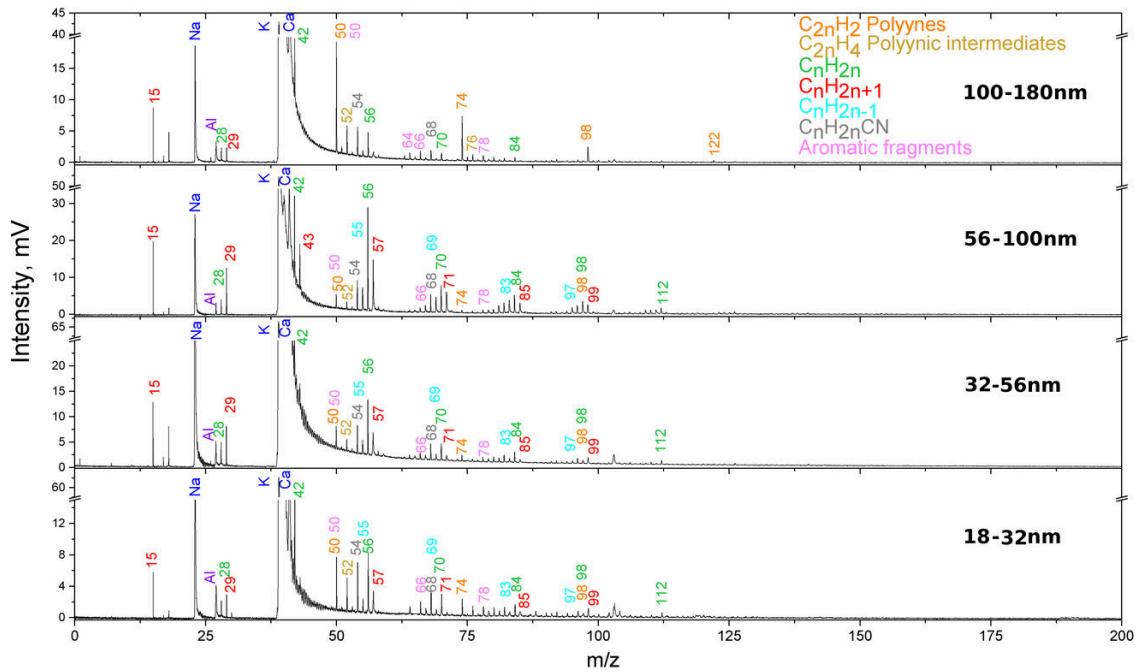

Figure 3.11 *Mass spectra of the four samples (particle size 18 – 180 nm) obtained in the OM2000 engine conditions. The analyses were performed with an ionization wavelength λ_i=118 nm which has a high sensitivity for aliphatic compounds.*

categories can be defined: volatile species – compounds consisting of two aromatic rings and mostly present in the gas phase, semi-volatiles – species made of three and four rings, and non-volatile – compounds comprising more than four rings and primarily found in the condensed phase. Consequently, the species making up the first detected group can be considered as volatile. In contrast, the second group

© 2020 Tous droits réservés.

lilliad.univ-lille.fr

Thèse de Dumitru Duca, Université de Lille, 2020

brings together semi- and non-volatile compounds. Therefore, the intensity ratio of the first to the second group is related to the overall volatility of the organic layer on the surface of particles. Species with masses between m/z 178 and 398 are detected on larger OM2000 particles (32 – 180 nm), *i.e.* on samples $OM2000_{100-180}$, $OM2000_{56-100}$, and $OM2000_{32-56}$, while for the sample $OM2000_{18-32}$ (18 – 32 nm) the highest detected mass is only m/z 278. Table 3.2 displays the most intense peaks detected in these (low-resolution) L2MS spectra.

Table 3.2 *List of molecular and atomic species, along with their exact mass, detected by (low-resolution) L2MS with two different ionization wavelengths. Only the most intense peaks are shown.*

m/z	Formula	m/z	Formula	m/z	Formula	m/z	Formula	m/z	Formula
				266nm ionization					
22.99	Na^+	120	C_{10}^+	154.078	$C_{12}H_{10}^+$	204	C_{17}^+	276.094	$C_{22}H_{12}^+$
26.982	Al^+	120.094	$C_9H_{12}^+$	156.094	$C_{12}H_{12}^+$	216.094	$C_{17}H_{12}^+$	278.11	$C_{22}H_{14}^+$
38.964	K^+	128.063	$C_{10}H_8^+$	158.11	$C_{12}H_{14}^+$	218.11	$C_{17}H_{14}^+$	300.094	$C_{24}H_{12}^+$
39.963	Ca^+	130.078	$C_{10}H_{10}^+$	166.078	$C_{13}H_{10}^+$	226.078	$C_{18}H_{10}^+$	302.11	$C_{24}H_{14}^+$
69.958	Al_2O^+	132	C_{11}^+	178.078	$C_{14}H_{10}^+$	228	C_{19}^+	326.11	$C_{26}H_{14}^+$
78.047	$C_6H_6^+$	132.094	$C_{10}H_{12}^+$	168.094	$C_{13}H_{12}^+$	228.094	$C_{18}H_{12}^+$	350.11	$C_{28}H_{14}^+$
92.063	$C_7H_8^+$	134.11	$C_{10}H_{14}^+$	168	C_{14}^+	240	C_{20}^+	374.11	$C_{30}H_{14}^+$
101.948	$Al_2O_3^+$	142.078	$C_{11}H_{10}^+$	170.11	$C_{13}H_{14}^+$	240.094	$C_{19}H_{12}^+$	398.11	$C_{32}H_{14}^+$
104.063	$C_8H_8^+$	144	C_{12}^+	178.078	$C_{14}H_{10}^+$	242.11	$C_{19}H_{14}^+$		
106.078	$C_8H_10^+$	144.094	$C_{11}H_{12}^+$	180	C_{15}^+	252.094	$C_{20}H_{12}^+$		
116.063	$C_9H_8^+$	146.11	$C_{11}H_{14}^+$	192	C_{16}^+	264.094	$C_{21}H_{12}^+$		
118.078	$C_9H_10^+$	152.063	$C_{12}H_8^+$	202.078	$C_{16}H_{10}^+$	266.11	$C_{21}H_{14}^+$		
				118nm ionization					
15.023	CH_3^+	52.031	$C_4H_4^+$	70.078	$C_5H_{10}^+$	84.094	$C_6H_{12}^+$	108.094	$C_8H_{12}^+$
22.99	Na^+	54.034	$C_2H_4CN^+$	71.086	$C_5H_{11}^+$	85.102	$C_6H_{13}^+$	110.11	$C_8H_{14}^+$
26.982	Al^+	55.055	$C_4H_7^+$	74.016	$C_6H_2^+$	95.086	$C_7H_{11}^+$	112.125	$C_8H_{16}^+$
28.031	$C_2H_4^+$	56.063	$C_4H_8^+$	76.031	$C_6H_4^+$	96.094	$C_7H_{12}^+$	122.016	$C_{10}H_2^+$
29.039	$C_2H_5^+$	57.07	$C_4H_9^+$	78.047	$C_6H_6^+$	97.102	$C_7H_{13}^+$	124.031	$C_{10}H_4^+$
38.964	K^+	66.047	$C_5H_6^+$	79.055	$C_6H_7^+$	98.016	$C_8H_2^+$	126.047	$C_{10}H_6^+$
39.963	Ca^+	67.055	$C_5H_7^+$	80.063	$C_6H_8^+$	98.11	$C_7H_{14}^+$	140.063	$C_{11}H_8^+$
42.047	$C_3H_6^+$	68.05	$C_3H_6CN^+$	82.078	$C_6H_{10}^+$	99.117	$C_7H_{15}^+$		
50.016	$C_4H_2^+$	69.07	$C_5H_9^+$	83.086	$C_6H_{11}^+$	106.078	$C_8H_{10}^+$		

The intensity ratio of species belonging to the second group to those in the first one changes from sample to sample within the OM2000 regime. For the largest particles ($OM2000_{100-180}$), as well as for the smallest ($OM2000_{18-32}$), the first group ($78 \leq m/z \leq 170$) shows higher intensity. However, for samples $OM2000_{56-100}$ and $OM2000_{32-56}$, the contribution of the second group ($m/z \geq 178$) is more prominent. Within the first group, for all samples the base peak is located at m/z 128 and the group features fairly constant peak and intensity distributions. The second aromatic group shows a distinct behavior, where the base peak is m/z 252 for samples $OM2000_{100-180}$, $OM2000_{32-56}$, and $OM2000_{18-32}$, but m/z 228 for sample OM_{56-100}. However, with the exception of the peak at m/z 228, intensity distributions change only slightly across samples. The change in relative intensity of the m/z 228 peak

© 2020 Tous droits réservés.

lilliad.univ-lille.fr

Thèse de Dumitru Duca, Université de Lille, 2020

is probably linked to a $C_{18}H_{12}^{+}$ isomer present on particles in the size range 32 – 100 nm. The fact that only species up to m/z 278 can be seen on sample $OM2000_{18-32}$ might be explained by an overall lower intensity, as this sample had the lowest coverage of deposited particles. However, it is still possible to derive the intensity ratio of species belonging to the second group to those present in the first one. A low ratio observed for this sample suggests that smaller particles contain mostly light aromatic species.

The samples also contain a variety of aliphatic species, detected with a different ionization scheme (λ_i=118nm) [153], Figure 3.11. The ion series with the formula $C_nH_{2n-1}^{+}$ is typical of cycloalkanes and alkenes while the $C_nH_{2n+1}^{+}$ series (alkyl fragments) is typical of linear or branched alkane compounds [154]. The series at m/z 67, 81, 95, and 109 (C_nH_{2n-3} fragments of bicycloalkanes) is also present, however with a very low intensity. The asymmetrical shape of the peaks is a sign of fragmentation. The fragmentation pattern is characteristic of the presence of aliphatic hydrocarbons, specifically alkanes (C_nH_{2n+2}). As alkane cations are not stable, especially if the excess internal energy is high after ionization, they can easily fragment. Since lubricating oils tend to be dominated by cycloalkanes due to the deliberate removal of n-alkanes during a de-waxing process [155], an intense signal for cycloalkanes is usually a sign of oil contribution. The main source of aliphatic compounds can be derived from the ratio of n-alkanes to cycloalkanes. The signal corresponding to alkanes is superior to that of neighboring cycloalkanes in the mass range $m/z = 67 - 71$ and 81 – 85 when the fuel is the main source of these compounds, and inferior for the lubricating oil [151, 155, 156]. Ion signals at m/z 71 and 85 are lower than those at m/z 69 and 83, suggesting that the measured exhaust particles mainly consist of unburnt lubricating oil (in case of Diesel particles this pattern would be caused by at least 95% oil and 5% fuel, while in the case of gasoline, the ratio should be higher [151, 156]). The one exception is observed for the sample $OM2000_{56-100}$ where the signal at m/z 69 is lower than that of m/z 71 (r = S_{69}/S_{71} ≈0.8), while the m/z 83 to 85 ratio is close to unity. Since the source of organic species in the exhaust includes fuel, lubricating oil, and their partially oxidized products, it is possible that marker species of fuel are primarily concentrating in the size bin associated with sample $OM2000_{56-100}$ (56 – 100 nm). Peaks at m/z 50, 64, 66 and 78 can be attributed to fragments of aromatic species. Series of highly unsaturated aliphatic compounds are present as well: $C_{2n}H_2^{+}$ and $C_{2n}H_4^{+}$. These series were attributed to polyynic fragments, known to be present in rich premixed flames and to play an important role in the formation of combustion-generated particles [157, 158].

To classify the samples and uncover differences and similarities between them, principal component analysis (PCA, Section 2.3.2.1) was used [30, 99, 102]. For both ionization schemes, the first two principal components are responsible for most (≈ 97 %) of the variation between samples (containing particles of different sizes), and therefore the number of dimensions of the original data was reduced to only two. The contribution of mass peaks to each principal component is represented by their loadings (Figure 3.12). To extract the maximum amount of information, the data obtained with different ionization wavelengths were treated separately. In case of the ionization at 266 nm, the first principal component (PC1) can be associated with the total number of different aromatic species, since it receives a high negative contribution from both alkylated and non-alkylated PAHs. The first group of aromatic compounds ($78 \leq m/z \leq 170$) shows a high positive contribution

© 2020 Tous droits réservés.

lilliad.univ-lille.fr

Thèse de Dumitru Duca, Université de Lille, 2020

to the second principal component (PC2) while the second group ($m/z \geq 178$) is related to the negative PC2 value. For the data obtained with 118 nm ionization, PC1 is linked to all detected aliphatic species and can be also seen as an indicator of the homogeneity of aliphatic signal throughout the mass spectrum. PC2 has a strong contribution from highly unsaturated hydrocarbons ($C_{2n}H_2^+$, $C_{2n}H_4^+$, positive PC2) and several aliphatic species (negative PC2), Figure 3.12. Moreover, since contributions to PC2 from $C_{2n}H_2^+$, $C_{2n}H_4^+$, and aliphatic species ($C_nH_{2n-1}^+$, $C_nH_{2n}^+$, $C_nH_{2n+1}^+$) have the opposite sign, PC2 can be seen as the partitioning of highly unsaturated hydrocarbons and aliphatic species. In addition, the fact that peaks at m/z 50, 52, 74 and 78 (fragments of aromatic species) have a high contribution to PC2 proves that these species have the same origin, which is in agreement with soot formation models [157, 158].

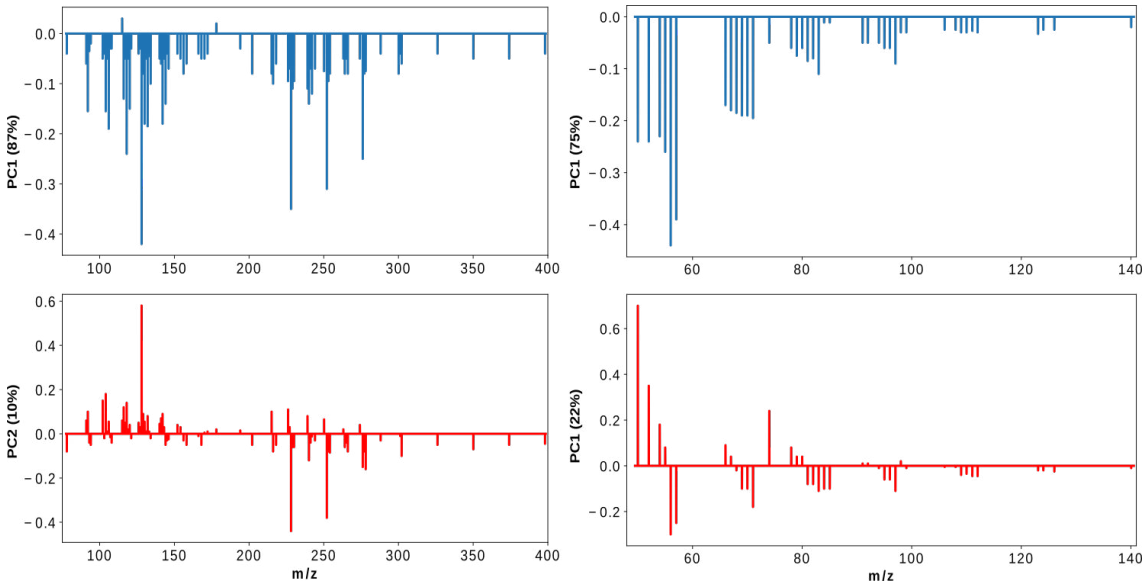

Figure 3.12 *Contribution of different species to PC1 and PC2 for size-selected particles collected in the OM2000 engine regime. Ionization at 266 nm (left) and 118 nm (right).*

Score plots for both ionization wavelengths are presented in Figure 3.13. There is a notable separation between different samples, thus demonstrating the capability of the PCA method to discriminate between samples that present, at first glance, similar mass spectra. Spectra belonging to the same size-bin samples are clustered together, proving that the sample surface is homogeneous and the reproducibility of the method is high. Sample $OM2000_{100-180}$ contains a large number of aromatic species (266 nm ionization), with a higher contribution coming from the light-weight compounds ($78 \leq m/z \leq 170$). In contrast, sample $OM2000_{56-100}$ exhibits a higher contribution from the second group of aromatic compounds ($m/z \geq 178$). Sample $OM2000_{32-56}$ seems to have fewer species, however heavier compounds ($m/z \geq 178$) still dominate. For the smallest analyzed particles, *i.e.* sample $OM2000_{18-32}$, the contribution of lighter aromatic compounds increases considerably, with only a few species detected from the second group. It appears that aromatic species with lower mass are present on all samples and are not bound to a specific particle size. In contrast, there is a clear increase in the contribution from higher mass aromatic species for $OM2000_{56-100}$ and $OM2000_{32-56}$ samples, suggesting that these compounds preferably adsorb on particles in this size range (32 – 100 nm). Sample

© 2020 Tous droits réservés.

lilliad.univ-lille.fr

$OM2000_{56-100}$ shows the most peaks coming from aliphatic species (118 nm ionization), including peaks in the mass range m/z 64 – 112 (leading to a negative value of PC1 associated with all detected aliphatic species in Figure 3.13). The smallest number of aliphatic compounds was detected on the $OM2000_{32-56}$ sample which also has a fairly inhomogeneous-looking spectrum (Figure 3.11). The contribution of highly unsaturated hydrocarbons ($C_nH_2^+$ and $C_nH_4^+$) decreases with the size of particles, being the highest for the $OM2000_{18-32}$ sample and the lowest for the $OM2000_{100-180}$ (see Figure 3.13b, PC2 values). At the same time, the contribution of other aliphatic compounds increases with the particle size.

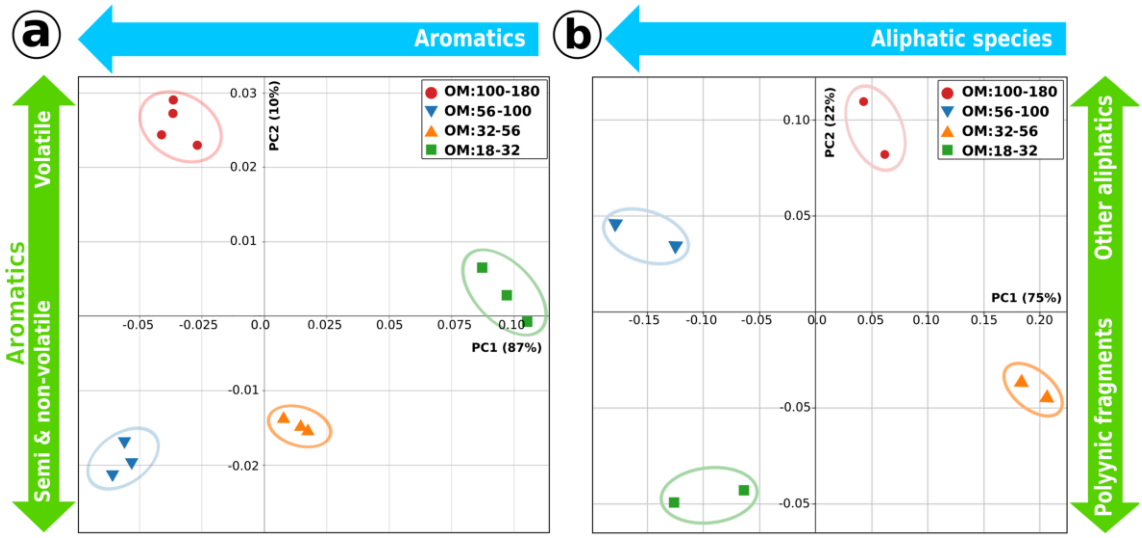

Figure 3.13 *Size separation of combustion-generated particles obtained in the OM2000 engine regime (optimal operation with addition of oil, medium load) by means of principal component analysis, with ionization wavelengths of λ_i=266 nm (a), or λ_i=118 nm (b). Based on the information extracted from the loadings plots (see text), the blue and green arrows indicate the main trends in various classes of compounds, classified as volatile, semi- and non-volatile species according to Bari et al [152].*

3.3.1.2 Fuel injection system malfunction simulation

Another engine regime that simulates a malfunction is FM2000 (low air/fuel ratio, medium load), also representing an extreme operation point, this time with a normal oil consumption. Particle emissions obtained in this engine regime are analyzed with SIMS in both positive and negative polarity (Figures 3.14 and 3.15, respectively). Chemical formulas were assigned to the most intense mass peaks in both spectra with the help of mass defect analysis (Section 2.3.1) and are listed in Tables 3.3 and 3.4. We note that metallic and metalloid ions such as Na^+, Mg^+, Al^+, Si^+, K^+, Ca^+ and Cu^+ are present in the spectra, however their intensity is higher for the blank aluminum foil, and therefore they were assumed to come from the underlying substrate rather than from the collected particles and are not displayed in the list of assigned species.

© 2020 Tous droits réservés.

Thèse de Dumitru Duca, Université de Lille, 2020

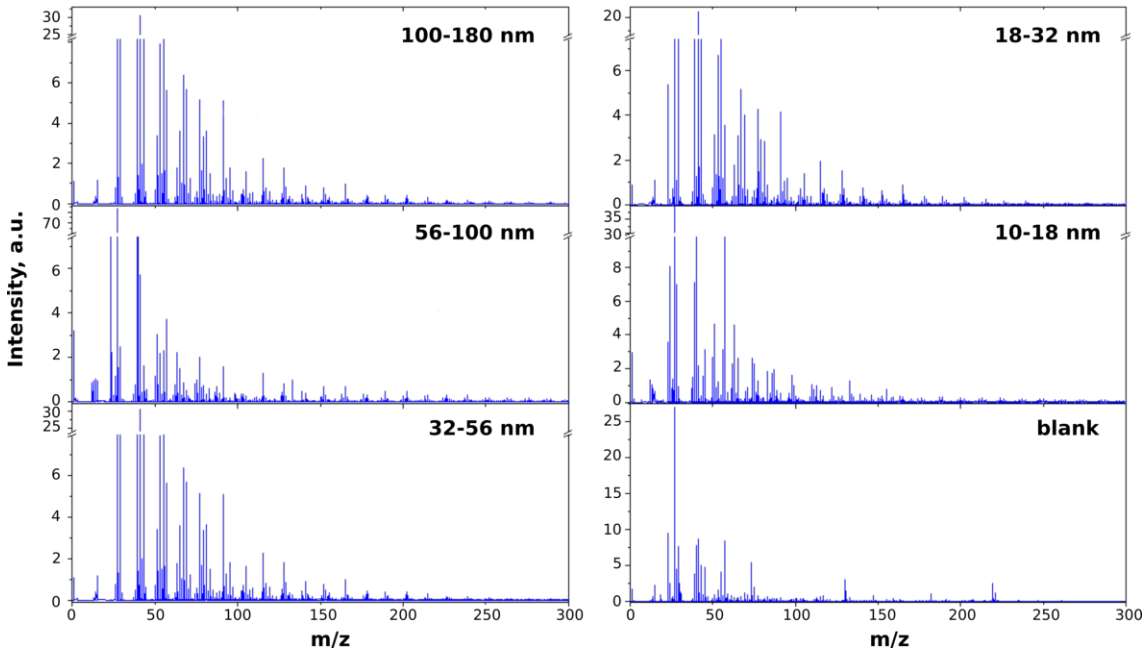

Figure 3.14 *Positive polarity SIMS spectra of samples obtained in the FM2000 engine regime (fuel system malfunction) and a blank aluminum foil used for reference. Mass spectra were acquired in the range m/z 0 – 600 but only the highest intensity m/z 0 – 300 range is displayed here.*

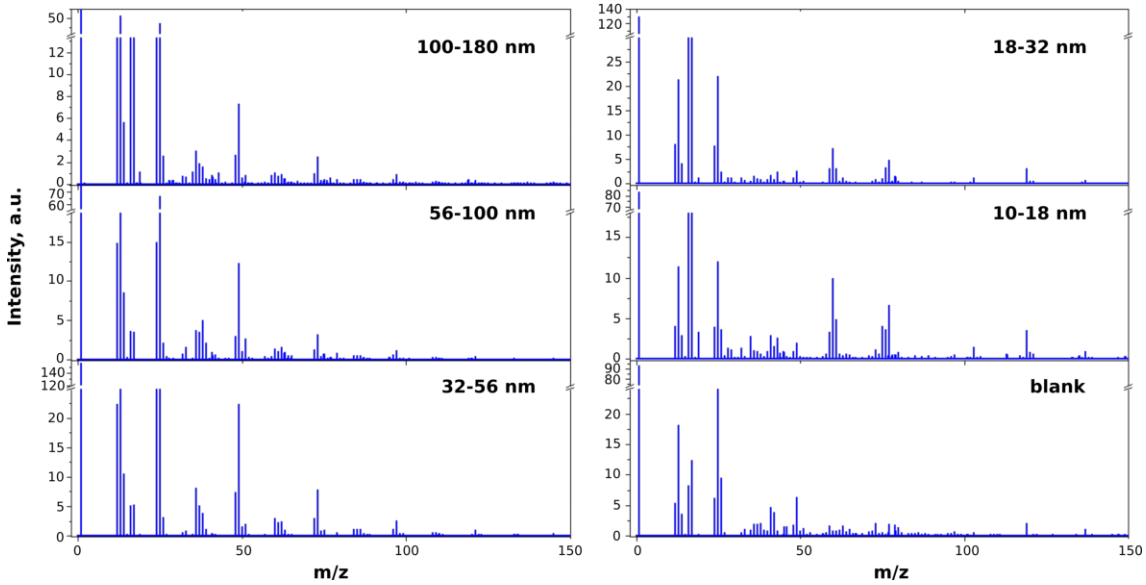

Figure 3.15 *Negative polarity SIMS spectra of samples obtained in the FM2000 engine regime (fuel system malfunction) and a blank aluminum foil used for reference. Mass spectra were acquired in the range m/z 0 – 600 but only the highest intensity m/z 0 – 300 range is displayed here.*

© 2020 Tous droits réservés.

lilliad.univ-lille.fr

Table 3.3 *List of molecular and atomic species, with their exact mass, detected with SIMS in positive polarity. The mass assignment accuracy is better than 20 ppm for all listed peaks. Peaks that have been associated with the substrate are not shown.*

m_{exact}	Formula	m_{exact}	Formula	m_{exact}	Formula	m_{exact}	Formula	m_{exact}	Formula
12	C^+	77.039	$C_6H_5^+$	158.016	$C_{13}H_2^+$	287.086	$C_{23}H_{11}^+$	396.094	$C_{32}H_{12}^+$
13.008	CH^+	78.047	$C_6H_6^+$	163.055	$C_{13}H_7^+$	289.102	$C_{23}H_{13}^+$	398.11	$C_{32}H_{14}^+$
14.016	CH_2^+	79.055	$C_6H_7^+$	164.063	$C_{13}H_8^+$	290.11	$C_{23}H_{14}^+$	399.117	$C_{32}H_{15}^+$
15.023	CH_3^+	80.063	$C_6H_8^+$	165.07	$C_{13}H_9^+$	296.026	$C_{23}H_4O^+$	400.125	$C_{32}H_{16}^+$
24	C_2^+	81.07	$C_6H_9^+$	166.078	$C_{13}H_{10}^+$	298.053	$C_{22}H_6N_2^+$	401.133	$C_{32}H_{17}^+$
26.016	$C_2H_2^+$	82.066	$C_5H_8N^+$	170.016	$C_{14}H_2^+$	300.094	$C_{24}H_{12}^+$	407.086	$C_{33}H_{11}^+$
27.023	$C_2H_3^+$	83.037	$C_4H_5NO^+$	174.047	$C_{14}H_6^+$	301.102	$C_{24}H_{13}^+$	409.102	$C_{33}H_{13}^+$
28.031	$C_2H_4^+$	85.008	C_7H^+	176.063	$C_{14}H_8^+$	302.11	$C_{24}H_{14}^+$	411.117	$C_{33}H_{15}^+$
29.039	$C_2H_5^+$	86.016	$C_7H_2^+$	178.078	$C_{14}H_{10}^+$	303.117	$C_{24}H_{15}^+$	412.125	$C_{33}H_{16}^+$
31.018	CH_{3O}^+	87.023	$C_7H_3^+$	179.086	$C_{14}H_{11}^+$	309.033	$C_{22}H_3N_3^+$	413.133	$C_{33}H_{17}^+$
36	C_3^+	88.031	$C_7H_4^+$	184.035	$C_{12}H_8S^+$	311.086	$C_{25}H_{11}^+$	420.094	$C_{34}H_{12}^+$
37.008	C_3H^+	89.039	$C_7H_5^+$	187.055	$C_{15}H_7^+$	313.102	$C_{25}H_{13}^+$	422.11	$C_{34}H_{14}^+$
38.016	$C_3H_2^+$	91.055	$C_7H_7^+$	189.07	$C_{15}H_9^+$	314.11	$C_{25}H_{14}^+$	423.117	$C_{34}H_{15}^+$
39.023	$C_3H_3^+$	92.063	$C_7H_8^+$	200.063	$C_{16}H_8^+$	315.117	$C_{25}H_{15}^+$	424.125	$C_{34}H_{16}^+$
40.031	$C_3H_4^+$	93.07	$C_7H_9^+$	202.078	$C_{16}H_{10}^+$	322.078	$C_{26}H_{10}^+$	425.133	$C_{34}H_{17}^+$
41.039	$C_3H_5^+$	98.016	$C_8H_2^+$	203.086	$C_{16}H_{11}^+$	324.094	$C_{26}H_{12}^+$	431.086	$C_{35}H_{11}^+$
43.018	C_2H3O^+	99.023	$C_8H_3^+$	211.055	$C_{17}H_7^+$	325.102	$C_{26}H_{13}^+$	433.102	$C_{35}H_{13}^+$
43.055	$C_3H_7^+$	100.031	$C_8H_4^+$	213.07	$C_{17}H_9^+$	326.11	$C_{26}H_{14}^+$	435.117	$C_{35}H_{15}^+$
49.008	C_4H^+	100.987	$C_3HO_4^+$	215.086	$C_{17}H_{11}^+$	327.117	$C_{26}H_{15}^+$	436.125	$C_{35}H_{16}^+$
50.016	$C_4H_2^+$	101.039	$C_8H_5^+$	216.094	$C_{17}H_{12}^+$	333.07	$C_{27}H_9^+$	437.133	$C_{35}H_{17}^+$
51.023	$C_4H_3^+$	102.047	$C_8H_6^+$	224.063	$C_{18}H_8^+$	335.086	$C_{27}H_{11}^+$	444.094	$C_{36}H_{12}^+$
52.031	$C_4H_4^+$	103.055	$C_8H_7^+$	226.078	$C_{18}H_{10}^+$	337.102	$C_{27}H_{13}^+$	446.11	$C_{36}H_{14}^+$
53.039	$C_4H_5^+$	105.07	$C_8H_9^+$	227.086	$C_{18}H_{11}^+$	338.11	$C_{27}H_{14}^+$	448.125	$C_{36}H_{16}^+$
55.018	$C_3H_3O^+$	109.008	C_9H^+	228.094	$C_{18}H_{12}^+$	339.117	$C_{27}H_{15}^+$	449.133	$C_{36}H_{17}^+$
57.034	C_3H5O^+	110.019	C_6H6S^+	229.102	$C_{18}H_{13}^+$	346.078	$C_{28}H_{10}^+$	450.141	$C_{36}H_{18}^+$
57.07	$C_4H_9^+$	111.023	$C_9H_3^+$	237.07	$C_{19}H_9^+$	348.094	$C_{28}H_{12}^+$	457.102	$C_{37}H_{13}^+$
58.066	$C_3H_8N^+$	113.039	$C_9H_5^+$	239.086	$C_{19}H_{11}^+$	350.11	$C_{28}H_{14}^+$	459.117	$C_{37}H_{15}^+$
59.05	$C_3H_7O^+$	115.055	$C_9H_7^+$	240.094	$C_{19}H_{12}^+$	351.117	$C_{28}H_{15}^+$	461.133	$C_{37}H_{17}^+$
60.021	$C_2H_4O_2^+$	120.974	$C_5H_5Fe^+$	248.063	$C_{20}H_8^+$	352.125	$C_{28}H_{16}^+$	468.094	$C_{38}H_{12}^+$
61.008	C_5H^+	122.016	$C_{10}H_2^+$	250.078	$C_{20}H_{10}^+$	357.07	$C_{29}H_9^+$	470.11	$C_{38}H_{14}^+$
62.016	$C_5H_2^+$	123.023	$C_{10}H_3^+$	251.086	$C_{20}H_{11}^+$	359.086	$C_{29}H_{11}^+$	472.125	$C_{38}H_{16}^+$
63.023	$C_5H_3^+$	126.047	$C_{10}H_6^+$	252.094	$C_{20}H_{12}^+$	361.102	$C_{29}H_{13}^+$	473.133	$C_{38}H_{17}^+$
64.031	$C_5H_4^+$	127.055	$C_{10}H_7^+$	253.102	$C_{20}H_{13}^+$	363.117	$C_{29}H_{15}^+$	474.141	$C_{38}H_{18}^+$
65.039	$C_5H_5^+$	128.063	$C_{10}H_8^+$	261.07	$C_{21}H_9^+$	370.078	$C_{30}H_{10}^+$	481.102	$C_{39}H_{13}^+$
66.047	$C_5H_6^+$	139.055	$C_{11}H_7^+$	263.086	$C_{21}H_{11}^+$	372.094	$C_{30}H_{12}^+$	483.117	$C_{39}H_{15}^+$
67.055	$C_5H_7^+$	141.07	$C_{11}H_9^+$	264.094	$C_{21}H_{12}^+$	374.11	$C_{30}H_{14}^+$	485.133	$C_{39}H_{17}^+$
69.07	$C_5H_9^+$	142.078	$C_{11}H_{10}^+$	265.102	$C_{21}H_{13}^+$	375.117	$C_{30}H_{15}^+$	487.149	$C_{39}H_{19}^+$
70.066	$C_4H_8N^+$	146.016	$C_{12}H_2^+$	44.026	$C_2H_4O^+$	376.125	$C_{30}H_{16}^+$	494.11	$C_{40}H_{14}^+$
73.053	$C_3H_7NO^+$	150.047	$C_{12}H_6^+$	274.078	$C_{22}H_{10}^+$	377.133	$C_{30}H_{17}^+$	496.125	$C_{40}H_{16}^+$
74.016	$C_6H_2^+$	151.055	$C_{12}H_7^+$	276.094	$C_{22}H_{12}^+$	383.086	$C_{31}H_{11}^+$	498.141	$C_{40}H_{18}^+$
75.023	$C_6H_3^+$	152.063	$C_{12}H_8^+$	277.102	$C_{22}H_{13}^+$	385.102	$C_{31}H_{13}^+$		
76.031	$C_6H_4^+$	153.07	$C_{12}H_9^+$	278.11	$C_{22}H_{14}^+$	387.117	$C_{31}H_{15}^+$		
76.987	CHO_4^+	155.086	$C_{12}H_{11}^+$	285.043	$C_{18}H_7NO_3^+$	388.125	$C_{31}H_{16}^+$		

© 2020 Tous droits réservés.

lilliad.univ-lille.fr

Thèse de Dumitru Duca, Université de Lille, 2020

Table 3.4 *List of molecular and atomic species, with their exact mass, detected with SIMS in negative polarity. The mass assignment accuracy is better than 20 ppm for all listed peaks. Peaks that have been associated with the substrate are not shown.*

m_{exact}	Formula	m_{exact}	Formula	m_{exact}	Formula	m_{exact}	Formula	m_{exact}	Formula
12	C^-	44.998	CHO_2^-	78.959	$PO3^-$	110.016	$C_9H_2^-$	168	C_{14}^-
13.008	CH^-	45.993	NO_2^-	79.957	SO_3^-	118.941	$NaSO_4^-$	169.008	$C_{14}H^-$
15.995	O^-	48	C_4^-	80.965	HSO_3^-	120	C_10^-	170.016	$C_{14}H_2^-$
17.003	OH^-	49.008	C_4H^-	84	C_7^-	121.008	$C_{10}H^-$	180	C_{15}^-
24	C_2^-	50.003	C_3N^-	85.008	C_7H^-	122.016	$C_{10}H_2^-$	181.008	$C_{15}H^-$
25.008	C_2H^-	55.018	$C_3H_3O^-$	86.016	$C_7H_2^-$	132	C_{11}^-	182.016	$C_{15}H_2^-$
26.003	CN^-	56.026	$C_3H_4O^-$	94.953	PO_4^-	134.016	$C_{11}H_2^-$	193.008	$C_{16}H^-$
31.018	CH_3O^-	57.034	$C_3H_5O^-$	95.952	SO_4^-	135.023	$C_{11}H_3^-$	204	C_{17}^-
31.972	S^-	60	C_5^-	96	C_8^-	144	C_{12}^-	205.008	$C_{17}H^-$
36	C_3^-	61.008	C_5H^-	96.96	HSO_4^-	145.008	$C_{12}H^-$	206.016	$C_{17}H_2^-$
37.008	C_3H^-	61.988	NO_3^-	97.008	C_8H^-	146.016	$C_{12}H_2^-$	217.008	$C_{18}H^-$
38.016	$C_3H_2^-$	62.016	$C_5H_2^-$	98.016	$C_8H_2^-$	156	C_{13}^-		
40.019	$C_2H_2N^-$	62.996	HNO_3^-	99.023	$C_8H_3^-$	157.008	$C_{13}H^-$		
41.003	C_2HO^-	72	C_6^-	108	C_9^-	158.016	$C_{13}H_2^-$		
42.011	$C_2H_{2O}^-$	73.008	C_6H^-	109.008	C_9H^-	159.023	$C_{13}H_3^-$		

All spectra obtained in the positive polarity are dominated by hydrocarbon fragments $C_nH_m^+$. Masses between m/z 128 and 300 can be mostly attributed to PAHs. Additional minor signals correspond to NH_4^+ and oxygenated species such as CH_3O^+ (m/z 31), $C_2H_4O_2^+$ (m/z 60) and CHO_4^+ (m/z 77). CH_3O^+ can be associated with methyl esters or ethers. Alternatively, it can correspond to primary alcohols or methyl-carbinols. The oxygenated positive ions, CH_3O^+ and $C_2H_4O_2^+$ present the highest correlation (pearson coefficeint r = 0.98) between the integrated areas of their peaks (normalized to the total ion count, TIC), thus indicating a common source. For instance, isopropanol, which is used as a gas dryer additive in gasoline for fuel system protection [159], could be a common source for these two ions. Ferrocene ($Fe(C_5H_5)_2$) is believed to be present in the fuel, since its fragment ($FeC_5H_5^+$) was detected. Ferrocene is sometimes used as a fuel additive that acts as an antiknock agent. Hopanes and n-alkanes (C_{26} – C_{36}) were also detected, they are believed to be linked to unburnt lubricant oil [160]. The high correlation between these peaks (r = 0.85 – 0.98) also suggests a common source. The correlation between PAHs and hopanes is almost non-existent, therefore we can conclude that PAHs are formed during the combustion process and are not remnants of oil/fuel.

Negative polarity SIMS spectra, as presented in Figure 3.15, are dominated by H^-, O^-, and OH^- fragments. Additional strong features correspond to the C_n^- and C_nH^- (n = 1 – 9) series with the hydrogenated carbon cluster C_nH^- being more intense compared to C_n^- when n is an even number (except in the case of n = 1). C_n^- (n = 2 – 4) fragments are considered to be a marker for elemental carbon (EC) in aerosol mass spectrometry (AMS) data [161]. The fact that detected carbon clusters have the same source is confirmed by the high positive correlation factors between C_2^-, C_3^-, and C_4^-. The correlation between C_3^- and C_4^- is the highest (r_{max} = 0.95), while the lowest is between C_2^- and C_4^- (r_{min} = 0.74).

All samples can be easily separated by size using PCA, Figure 3.16. The first two principal components account for 92% and 95% of the total variation within

© 2020 Tous droits réservés.

lilliad.univ-lille.fr

the data obtained in the positive and negative polarity, respectively. The loadings plots (Figure 3.17) indicate that for positive polarity, the first principal component receives a high negative contribution from $C_nH^+_{2n-1}$ and $C_nH^+_{2n+1}$ compounds (negative PC1), while other aliphatic species show a positive contribution. PC2 can be seen as the partitioning of aliphatic species (positive PC2) and aromatic compounds, such as PAHs and their fragments (negative PC2 value). For the negative polarity, PC1 is related to the partitioning between oxygenated species and the C_n^-, C_nH^- family (with a positive PC1 contribution linked to a high fraction of oxygenated species, while a negative PC1 value indicates a high amount of C_n^-, C_nH^-, *i.e.* a high EC). PC2 is linked to oxygenated species (positive for hydrocarbon-based compounds and negative for oxygenated species containing S, P and N).

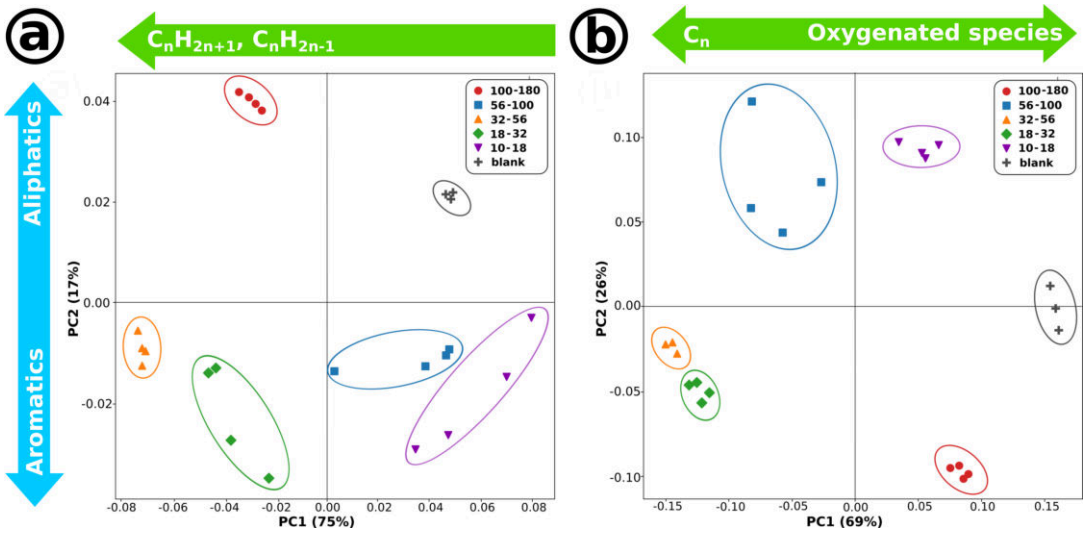

Figure 3.16 *Size discrimination of FM2000 particles based on the PCA of positive (a) and negative (b) SIMS spectra. The blue and green arrows indicate the main trends in various classes of compounds extracted from the loadings plots (Figure 3.17).*

The PCA score plots displayed in Figure 3.16 clearly show an evolution of the particle chemical composition with the size in the FM2000 regime. From the above observations, we can say that aliphatic species are concentrated predominantly on samples $FM2000_{100-180}$, $FM2000_{32-56}$, and $FM2000_{18-32}$ and that aromatic compounds are present in comparable amounts on the lower four stages, 10 – 100 nm particle size ($FM2000_{56-100}$, $FM2000_{32-56}$, $FM2000_{18-32}$ and $FM2000_{10-18}$). Samples $FM2000_{56-100}$, $FM2000_{32-56}$, and $FM2000_{18-32}$ (18 – 100 nm size range) exhibit the highest amount of C_n^- and C_nH^- ions, and therefore have a high EC content. Sample $FM2000_{100-180}$ has the highest contribution from oxygenated compounds that contain elements other than carbon and hydrogen (*e.g.* PO_3^-, SO_3^-, SO_4^-, PO_4^-, $NaSO_4^-$), while samples $FM2000_{56-100}$ and $FM2000_{10-18}$ have the lowest contribution from these compounds.

To summarize, negative polarity SIMS data extracted from FM2000 samples and transformed by PCA (Figure 3.16b) can be divided into three main groups according to the amount and nature of oxygenated species present on the samples. Specifically, the first group encompasses the two samples which exhibit the most oxygenated hydrocarbons, *i.e.* $FM2000_{56-100}$ and $FM2000_{10-18}$. The second one gathers the two samples which bear much less oxygenated hydrocarbons compared to the others, along with more elemental carbon, *i.e.* $FM2000_{32-56}$ and $FM2000_{18-32}$.

© 2020 Tous droits réservés.

lilliad.univ-lille.fr

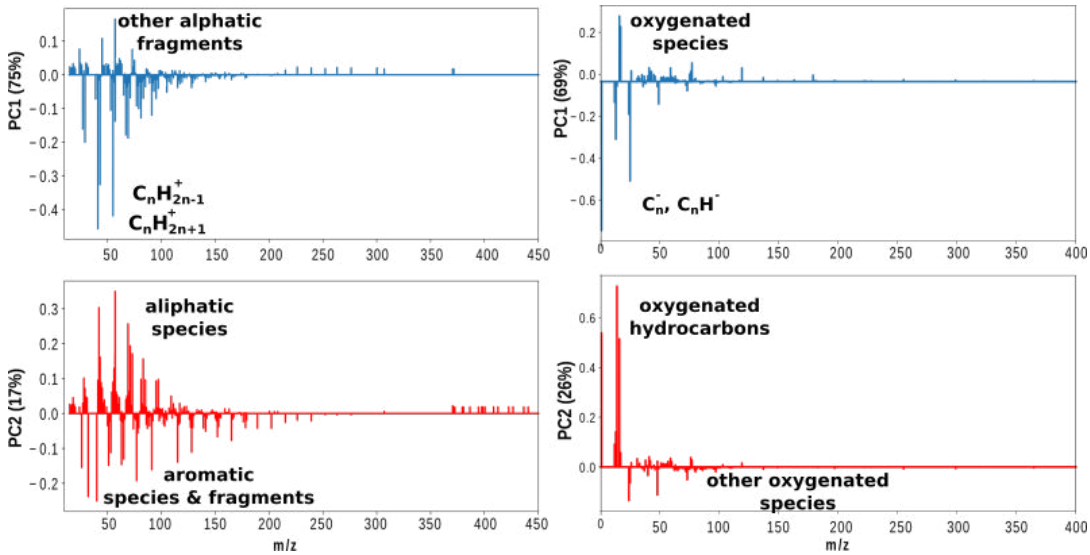

Figure 3.17 *Contribution of different species to PC1 and PC2 for size-selected particles collected in the FM2000 engine regime. Left panel - positive SIMS polarity, right panel - negative SIMS polarity.*

Lastly, the third group contains data points of $FM2000_{10-18}$ sample, which bears the most inorganic oxygenated compounds of all samples.

The clustering of samples in the multidimensional space (*i.e.* on data not transformed by PCA) was performed with hierarchical clustering analysis (HCA, Section 2.3.2.2). The distances between the samples are represented in form of a dendogram, Figure 3.18. We can see that samples $FM2000_{100-180}$, $FM2000_{32-56}$, and $FM2000_{18-32}$ form a relatively compact cluster (small distance between data-points), thus indicating their similarity. Likewise, $FM2000_{56-100}$ and $FM2000_{10-18}$ samples are grouped together hence forming a second cluster, well separated from the first one. Samples in these two clusters are thus very different, primarily due to the high contribution of $C_nH^+_{2n-1}$ and $C_nH^+_{2n+1}$ ions to $FM2000_{56-100}$ and $FM2000_{10-18}$ (as already shown by PCA). The distance between the blank sample and the second cluster ($FM2000_{56-100}$ and $FM2000_{10-18}$ samples) is relatively small, which can be explained by the lower coverage of these samples.

A detailed chemical characterization of particulate matter is desirable and can elucidate the soot formation, growth, ageing, and reactivity. However, to facilitate the comparison of mass spectrometry results with other experimental measurements and also support the interaction with modelers that use the data as inputs for various scale simulations, individual compounds are often grouped into classes. Compounds are grouped based on their chemical family (aromatics$^+$, $C_nH^+_{2n-1}$, $C_nH^+_{2n-3}$, hopanes$^+$, n-alkanes$^+$ – species related to OC [77, 161]), as well as their connection to the elemental carbon content (C_n^-) [162, 163]. These chemical families/groups have been chosen as they have different sources and roles in the formation and ageing mechanism of combustion-generated particles (*e.g.* PAHs are associated with the combustion of gasoline, while hopanoid compounds are seen as markers of unburnt lubricating oil). The contribution of a group to a mass spectrum is equal to its normalized (to TIC) intensity. As an example, trends in the chemical composition for the FM2000 engine regime are illustrated in Figure 3.19, where the error bars correspond to the standard deviation associated with the signal recorded in multi-

© 2020 Tous droits réservés.

lilliad.univ-lille.fr

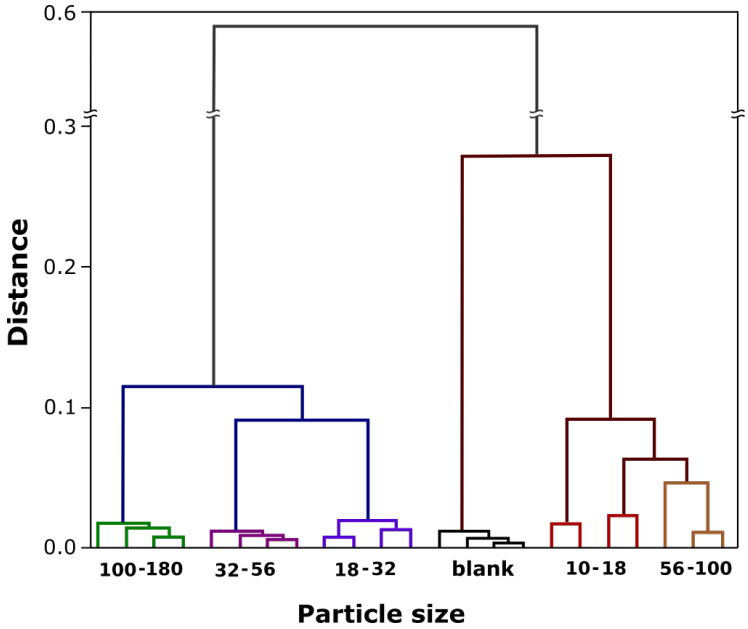

Figure 3.18 *Separation of size-selected particulates obtained in the FM2000 (fuel system malfunction) engine regime by the hierarchical clustering analysis based on positive polarity SIMS spectra.*

ple zones of each sample. The normalized signals obtained for the blank filter are given for comparison. For most chemical species, relative intensities of the blank filter are negligible. The total contribution of aromatic compounds and the C_n^- family increases toward sample $FM2000_{18-32}$; a similar variation was also found for other engine regimes such as NM2000 and NH2000 which will be discussed further on. Aliphatic families ($C_nH_{2n-1}^+$ and $C_nH_{2n-3}^+$) are the most abundant on samples $FM2000_{100-180}$, $FM2000_{32-56}$ and $FM2000_{18-32}$, when only a small contribution is observed for the other two samples (peak intensities comparable to those of the blank aluminum foil). Hopanes and n-alkanes are mostly present on sample $FM_{100-180}$ and since they are attributed to the lubricating oil, one can conclude that the unburnt oil is found predominantly on bigger particles. This is slightly different compared to the OM2000 engine regime where the oil contribution is the highest on sample $OM2000_{56-100}$. This difference might be linked to the state of the oil in the combustion chamber: for the FM2000 regime, the oil originates from an oil film present on the cylinder liner while for OM2000 regime, an excess of oil was deliberately added to the combustion chamber which is atomized by the fast moving piston and forms a mist.

The relative abundance of the C_n^- species (markers of the elemental carbon) in the negative polarity SIMS spectra is shown in Figure 3.19. The relative proportion of these species increases from the sample made of the largest particles (100-180 nm) to that holding the smallest ones, reaching its maximum for sample $FM2000_{18-32}$ and then dropping significantly for $FM2000_{10-18}$. Figure 3.19 shows, once again, that the chemical composition of emitted particles changes with their size due to a size-dependent contribution from different sources of particle emission (*e.g.* fuel/oil combustion, unburnt oil). These trends represent essential information for the development of a precise and reliable model for the formation of particles in an internal combustion engine [61, 103].

© 2020 Tous droits réservés.

lilliad.univ-lille.fr

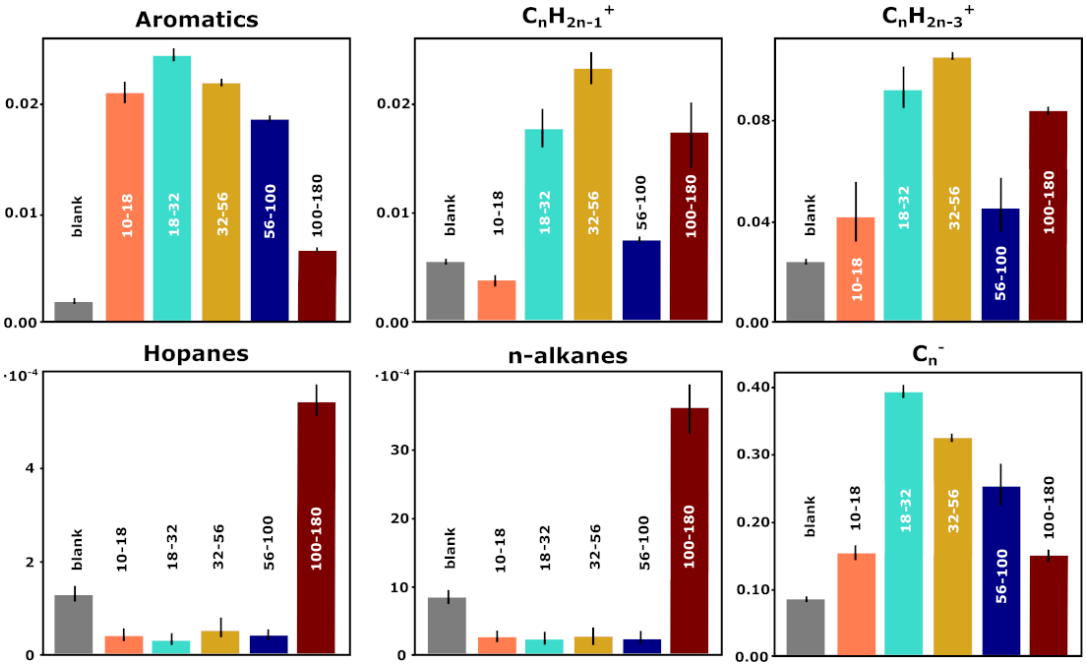

Figure 3.19 *Integrated peak areas of positive and negative SIMS fragment ions of interest normalized to the total ion count (TIC) for particles produced in the FM2000 engine regime (low air/fuel ratio). The error bars represent the standard deviation among all analyzed zones of the same sample.*

3.3.2 Evolution of the chemical composition with engine regime

In the previous section it was shown that some chemical compounds of different provenience are preferentially found on particles featuring a distinct size range. It is now possible to determine the contribution of major sources to the formation and chemical composition of particulates. On that basis, samples obtained in engine operation regimes (OM2000, FM2000, NM2000, and NH2000) with different contribution from fuel and oil (main sources of combustion generated particles) were analyzed with SIMS and then compared using PCA. Before applying PCA, chemical formulas were assigned through mass defect analysis to the majority of detected mass peaks. An example of mass defect plot is given in Figure 3.20 for the OM2000 positive polarity mass spectrum. Homologous series of peaks line up and important patterns are apparent even for complex mass spectra. It was possible to associate classes of molecules to the identified species: for instance aliphatic compounds exhibit a stiffer slope (due to the higher number of hydrogen atoms present in the molecule) than that of aromatic compounds, which appear in this representation with a lower slope (smaller number of hydrogen atoms) [30]. The sequence of low-mass defect compounds was attributed to oxygenated peaks ions ($C_mH_nO_p^+$), whose mass defect decreases with the number of oxygen atoms in the molecule. A group of high-mass defect species was also identified and associated with hopanoid compounds and n-alkanes (Figure 3.20a).

The first two PCA components, PC1 and PC2 (∼98%) are presented in Figure 3.21. It is clear that particles produced in an optimized engine regime (medium and high load) are chemically very different from the ones produced in engine regimes associated with a malfunction and therefore can be easily separated by the value of their principal components (Figure 3.21a). PC1 alone (∼91%) allows the separation

© 2020 Tous droits réservés.

lilliad.univ-lille.fr

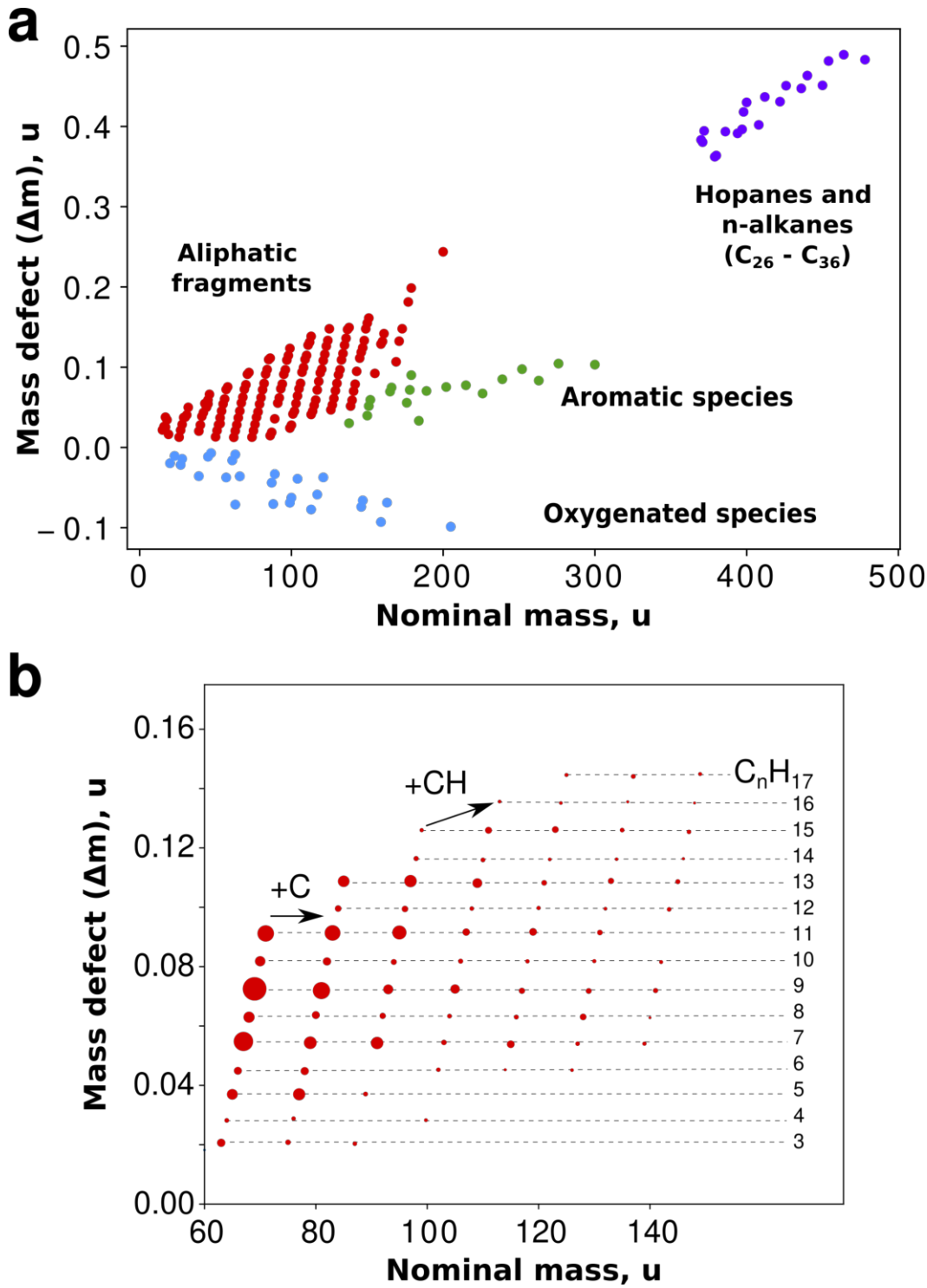

Figure 3.20 *(a) Mass defect plot obtained from positive polarity SIMS mass spectrum of the $OM2000_{100-180}$ sample (addition of oil, medium load, 2000RPM). Four different chemical classes are highlighted: oxygenated species (blue), aliphatic fragment (red), aromatic species (green), and hopanes/n-alkanes (purple). To improve the readability, the marker size was kept constant. (b) A zoomed in portion of the mass defect plot showing the alignment of homologous chemical compounds. The size of the markers is proportional to the corresponding peak integrated area. Molecular formulas of homologous species are displayed.*

© 2020 Tous droits réservés.

lilliad.univ-lille.fr

of regimes, based on the abundance of aliphatic fragments (positive contribution to PC1, Figure 3.22). Consequently, samples produced in non-optimal regimes are characterized by a higher relative contribution from aliphatic fragment ions compared to optimized engine regimes. PC2 is linked to the aliphatic fragment ions and aromatic species (positive PC2 value), however some aliphatic fragment ions ($C_5H_7^+$, $C_5H_9^+$, $C_3H_7^+$, $C_4H_7^+$) contribute to the negative value of PC2. Data points corresponding to optimal engine regimes form a smaller cluster, implying that particles produced in non-optimal conditions exhibit a much larger variability in their chemical composition.

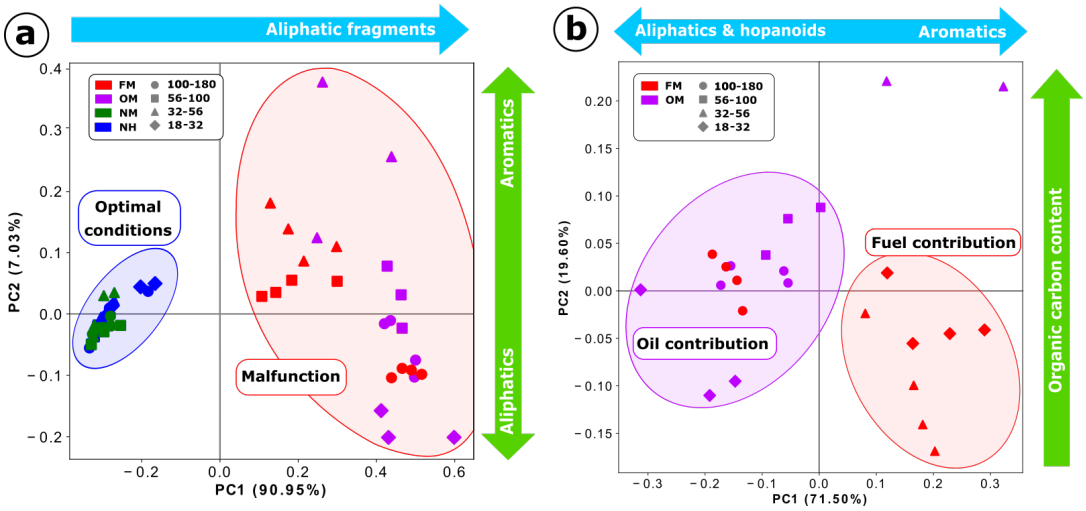

Figure 3.21 *Score plots of PCA performed on SIMS data (positive polarity) revealing sample separation according to (a) engine regime and (b) main source of particles. The blue and green arrows indicate the main trends in various classes of compounds extracted from the loadings plots (Figure 3.22).*

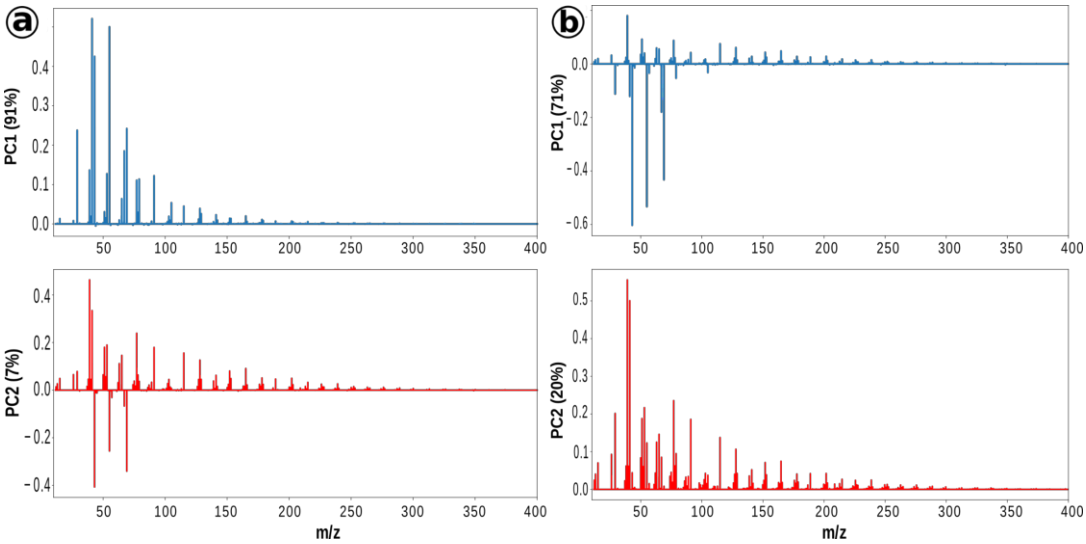

Figure 3.22 *Loading plots of PC1 and PC2 components corresponding to the PCA analysis displayed in Figure 3.21. (a) Separation of engine regimes. (b) Separation of main source of particles.*

The two engine regimes associated with a malfunction have been compared using the same statistical method, which further enables the distinction between the two

© 2020 Tous droits réservés.

Thèse de Dumitru Duca, Université de Lille, 2020

main contributors to particulate emissions from the internal combustion engine: fuel and oil, Figure 3.21b. PC1 (∼71%), which is accountable for the separation of the two regimes (and consequently sources), is linked to the contribution of hydrogen-rich hydrocarbons on the one hand (negative contribution) and to fragment ions and aromatic species on the other hand (positive contribution, Figure 3.22). This reveals that oil-related particles feature more hydrogen-rich hydrocarbons, while an excess of gasoline leads to the production of more aromatic species. The increase in the contribution of fragment ions in the latter is probably linked to the increase in the aromatic contribution, since the majority of fragments can be associated to the fragmentation of PAHs [154]. PC2 (∼20%) is associated with the presence of aromatic hydrocarbons, thus confirming that the presence of aromatic species can be seen as a marker of fuel combustion. Two data-points, corresponding to $OM2000_{32-56}$, show a rather high contribution from OC, and aromatic compounds in particular, unlike other OM samples. Since these compounds are linked to the contribution of fuel, we can infer that, for the OM2000 regime, the surface organic fraction found on particles in this size (32 – 56 nm) is linked to the combustion of fuel.

3.3.3 Influence of the catalytic stripper on the chemical composition

The previous results, gathered from the analysis of particles collected from the "raw exhaust", revealed the presence of a multitude of organic species, with various degrees of volatility. For comparison purposes with the current regulations limiting the number of non-volatile particles, "raw exhaust" particles have been further subjected to a catalytic stripper (CS), whose action was to remove the volatile fraction of the particles. The chemical characterization of such stripped particles is important as it also helped assess the efficiency of the CS that was implemented in the PEMS prototype. The volatile removal efficiency of the CS should be in accordance with European Union regulations, *i.e.* >99% removal of ≥ 30 nm tetracontane (CH_3–$(CH_2)_{38}$–CH_3) particles with an inlet concentration of ≥10000 cm^{-3} at the minimum dilution [164]. However, supplementary efforts are currently being made to better understand how the CS that complies with these regulations affects other individual organic compounds that are commonly present on the surface of combustion generated particles (such as PAHs), representing important information for modeling the non-volatile fraction leaving the CS and entering the counting stage of the instrument. To study the influence of the CS as well as its efficiency on different chemical species, two sets of combustion byproducts (*i.e.* both particles and gas phase) are collected and subsequently analyzed. One set was sampled with and one without the CS. Additionally, the performance of the CS was tested in different regimes that produce particles with a substantially different chemical composition as previously shown. The overall efficiency of the CS with regard to engine combustion byproducts was first investigated on polydisperse particles and gas phase. The study of the latter enabled the evaluation of CS efficiency in stripping gaseous organic compounds, representing an important measure in minimizing their potential condensation in the sampling line. The study of CS efficiency in removing the organic fraction from size-selected particles followed. All the analyses presented in this section were performed with the high resolution two-step laser mass spectrome-

© 2020 Tous droits réservés.

lilliad.univ-lille.fr

Thèse de Dumitru Duca, Université de Lille, 2020

ter (HR-L2MS, Section 2.2.2.3). The higher mass resolution enabled the distinction between chemical species with the same nominal mass (*e.g.* $m(C_{19})$=228.0000 u and $m(C_{18}H_{12})$=228.0939 u), and thus, since chemical species exhibit different responses to the catalytic oxidation, the efficiency of the CS could be better evaluated.

3.3.3.1 Polydisperse particles

Polydisperse particles and their corresponding gas phase were collected using the double-filter sampling system described in Section 2.1.1.2. For each engine regime, the collection was performed twice: once without the catalytic stripper, and once with it in place. Mass spectra of polydisperse particles and their associated gas phase sampled in the NH2000 engine regime (optimal operation conditions, high load) are presented in Figure 3.23. To test the homogeneity of the surface and also to gather data for the subsequent statistical analysis, the measurement was performed on 4 different zones of the same sample.

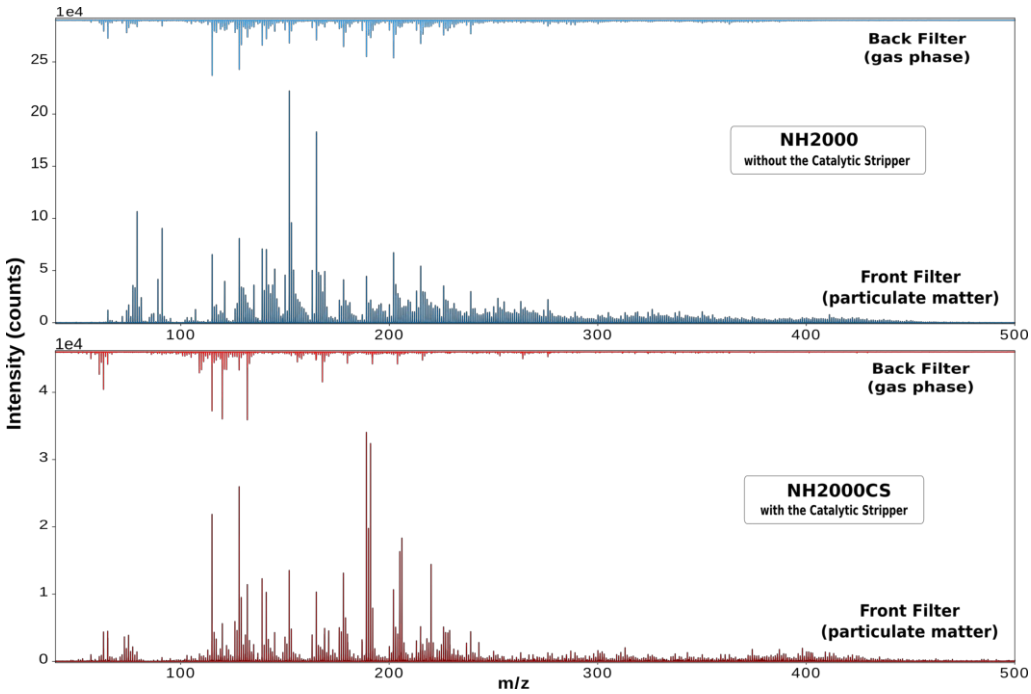

Figure 3.23 *Mass spectra of NH2000$_{FF/BF}$ and NH2000CS$_{FF/BF}$ samples (polydisperse particles and gas phase collected with and without the catalytic stripper) obtained with HR-L2MS (λ_d = 532 nm, λ_i = 266 nm). The desorption and ionization fluences were optimized for a maximum signal of unfragmented molecules. The displayed mass spectra correspond to an average of four spectra obtained in different zones of the same sample.*

Mass spectra of all samples but NH2000CS$_{BF}$ contain predominantly aromatic species and their fragments. In addition, the absolute signal intensities recorded for aromatic species is approximately 7 times smaller on particles that have been sampled from the catalytic stripper. This indicates that the latter was able to significantly reduce the overall content of organic compounds. Note that the decrease in the organic content is observed for both particulate and gas phase. The mass spectrum of the NH2000CS$_{BF}$ sample contains mostly carbon clusters and resembles the blank *back filter* sample. The presence of carbon clusters on back filters, regardless of the sampling conditions (*i.e.* with or without the catalytic stripper), is due to the

© 2020 Tous droits réservés.

lilliad.univ-lille.fr

Thèse de Dumitru Duca, Université de Lille, 2020

layer of activated carbon particles. Therefore, a mass spectrum with only carbon clusters (C_n^+) signifies that after the catalytic treatment few if any organic species have remained in the gas phase and subsequently adsorbed on the back filter.

Once chemical formulas have been assigned to all detected mass peaks with the mass defect analysis (Section 2.3) the contribution of each compound, or group of highly correlated species, can be determined with PCA. For the polydisperse particles, the first two principal components account for $\sim$ 68% of the variance and are enough to discriminate between all samples, Figure 3.24a. The fact that all samples are well separated (forming clearly defined and tight groups) implies that they have a distinct chemical composition. The meaning of each component (reported in Figure 3.24a) can be inferred from their corresponding loadings plot shown in Figure 3.25 (PC1 – blue line, PC2 – red line).

The first principal component ($\sim$59.4%) is linked to the contribution of carbon clusters and oxygenated species (positive PC1 value), and aromatic species with their corresponding fragments (negative PC1 value). Since aromatic species can be considered as good indicators of the organic carbon content in soot samples [77, 85] while carbon clusters (C_n^+) are commonly used as markers for the elemental carbon [102, 153, 161], the first principal component can be seen as the partitioning between the organic and elemental carbon content. The second principal component receives a very small contribution from carbon clusters and oxygenated species unlike that originating from aromatic compounds which clearly dominate PC2 loadings. The positive value of PC2 is determined by the contribution of aromatic compounds with at least 4 aromatic rings as well as some fragments, whereas its negative value is associated with aromatic compounds with less than 4 aromatic rings. As the former can be considered as non-volatile species and the latter as volatile and semi-volatile compounds [85, 152], PC2 ($\sim$8.8%) can be linked to the volatility of the surface organic layer.

The first principal component is able, on its own, to separate all the samples, even though it accounts for only 59.4% of the variance. Figure 3.24 shows that the contribution from organic compounds to the gas phase (back filter) is smaller than to the particulate phase sampled in the same regime (front filter). Moreover, the contribution from organic species to both gas and particulate phases significantly decreases when filters are collected after the CS, as indicated by the PC1 values they show compared to their unstriped counterparts. We can, therefore, conclude that the catalytic stripper is successful in removing the organic fraction from both particulate and gas phases. However, as the sign of PC1 changes for the back filter (gas phase) obtained with the catalytic stripper, the contribution of carbon clusters is much more important for this sample. It is worth noting that this sample is situated very close to the blank filter (black carbon on quartz fiber filter) on the PC1 axis. Carbon clusters, C_n^+, detected on both these samples are linked to the elemental carbon content (EC) which for back filters is determined by the layer of activated carbon and is not linked to the gas phase. Therefore, the catalytic stripper was able to remove the majority of organic species from the gas phase, to the extent that no significant amount of organic species is left to be absorbed by the back filter during sampling. On the PC2 axis, the samples can still be separated based on the volatility of the detected species. As a reminder, the particulate phase is characterized by a high contribution of non-volatile compounds while the gas phase is mostly dominated by volatile species [85, 152]. At the same time, the contribution of non-volatile species

© 2020 Tous droits réservés.

lilliad.univ-lille.fr

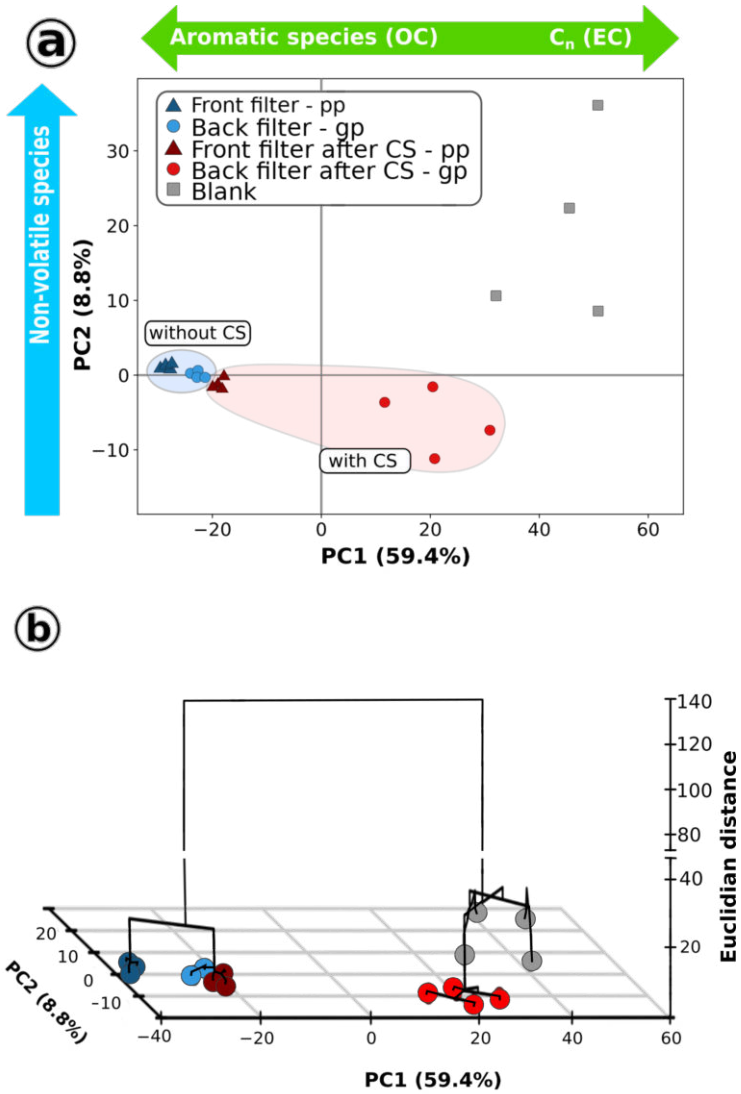

Figure 3.24 *(a) Score plot of the first two principal components for polydisperse soot (**pp**) and gas phase (**gp**) samples ($NH2000_{FF/BF}$ and $NH2000CS_{FF/BF}$). Ellipses highlight different sampling regimes (with and without the CS) and are for visual purposes only. The meaning of each principal component, derived from its loadings plot (Figure 3.25), is illustrated with arrows. (b) Hierarchical clustering analysis performed on the results of PCA (first five components, HCPC). The obtained clusters are displayed on the score plot of the first two principal components. The same color code as in (a) is used here.*

decreases after the catalytic treatment, implying that the catalytic stripper has a higher removal efficiency for the high-mass compounds. The high PC2 value of the control sample is determined mostly by some low-mass hydrocarbon fragments that were detected primarily on the blank filter and, therefore, are not connected to the gas phase.

The majority of the variance within the data set is explained by only a few principal components (compared to hundreds of initial variables), in this case the first 5 principal components explain 90% of the variance. Even though the dimensionality of the data is much smaller after the PCA, it can still be challenging to visualise different clusters in the multidimensional space. In this context, HCPC was used to evidence the clusters that form in the component space formed with the first 5

© 2020 Tous droits réservés.

lilliad.univ-lille.fr

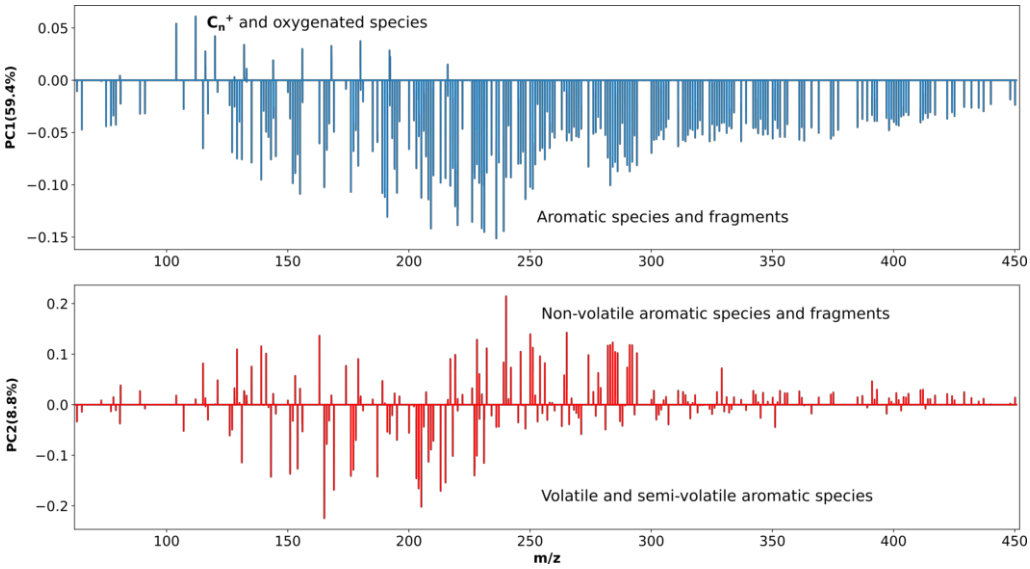

Figure 3.25 *Loadings plots for the first two principal components obtained from the mass spectra of polydisperse particles and gas phase sampled with and without the catalytic stripper (NH2000$_{FF/BF}$ and NH2000CS$_{FF/BF}$): PC1 - upper panel, PC2 - lower panel.*

principal components, Figure 3.24b. On the dendogram, Figure 3.24b, two main clusters are defined: i) two front filters along with the back filter sampled without the CS, and ii) the back filter sampled with the CS and the blank sample. This implies that the gas phase (back filter) sampled with the catalytic stripper exhibits chemical composition akin to that of black carbon and therefore proves, once again, that the catalytic stripper removed the majority of organic compounds from the gas phase.

A one-way clustering analysis is very useful to identify similar samples, but is unable to explain the clustering criterion. The explanation should be drawn from the results of other statistical methods, such as PCA. Another way of visualization of the strong correlations within the data set is a two-way hierarchical clustering heat-map, Figure 3.26. It is obtained by combining hierarchical clustering analyses performed on both samples and detected species, that group the most similar samples and species, with the numerical value for inter-sample correlation, Section 2.3.2.2. On the heatmap obtained for the NH2000$_{FF}$ and NH2000CS$_{FF}$, HCA groups the samples into two major clusters (C^+_{1-3} and C^+_4) – structure that is similar to the one obtained by the HCPC. At the same time, the mass peaks are separated into the following groups: carbon clusters, fragments, volatile, semi-volatile, and non-volatile species. Having the clustering applied to both species and samples allows us to easily identify the main contributors to a certain sample/group of samples. For instance, the control sample and the back filter obtained with the catalytic stripper receive a high contribution from carbon clusters while not being affected by non-volatile species, Figure 3.26. The chemical composition of these samples is very similar, making this technique unable to reliably distinguish between them. This means that very few compounds have been adsorbed from the gas phase, probably, due to their removal by the catalytic stripper. Front filters are characterized by a high correlation with semi- and non-volatile species while the back filter collected without the catalytic stripper is more correlated with volatile species. The correlation between carbon clusters (C_n, marker of EC) detected on front filters increases significantly once the

© 2020 Tous droits réservés.

lilliad.univ-lille.fr

Thèse de Dumitru Duca, Université de Lille, 2020

particles pass through the stripper. It should be noted that the color of each tile is linked to the correlation between species, therefore it cannot be directly used to compare the contribution of a species to several samples.

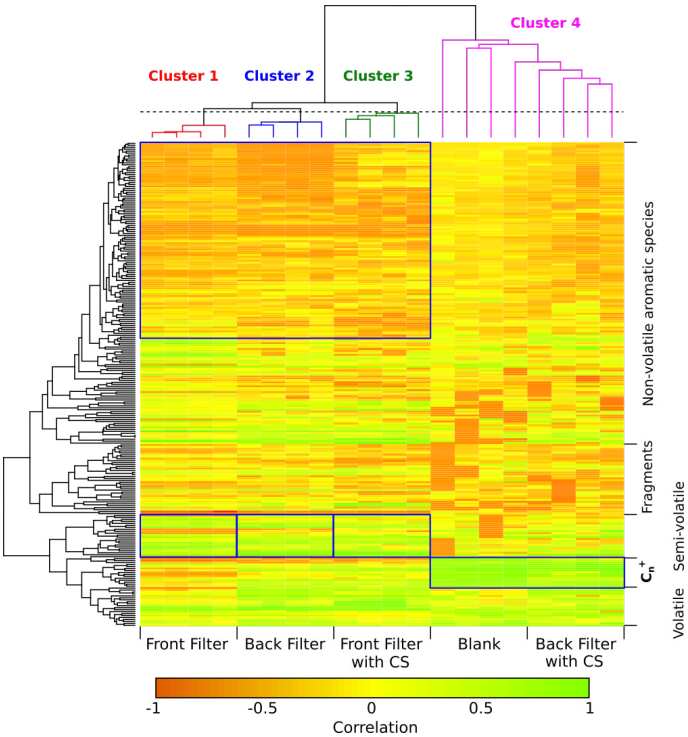

Figure 3.26 *Two-way hierarchical clustering heat-map for ions of $NH2000_{FF}$ and $NH2000CS_{FF}$ samples. The correlation between masses in individual samples is expressed as relative value and represented by the cell color. Several zones on the heatmap that determine the separation between samples are highlighted. For instance, the separation between cluster 4 (magenta) and the rest of the samples (cluster 1 (red), 2 (blue), and 3 (green)) is primarily determined by the different contribution of OC-related (e.g. aromatic species) and EC-related (C_n^+) species.*

When comparing only two samples, known to be different, it is useful to determine what chemical species contribute to this diversity, *i.e.* species that exhibit a "differential expression" on the compared samples. This can be done with a volcano plot – a way of displaying the fold change (a measure describing how much the relative signal changes between samples) of detected species along with their statistical significance (likelihood that the relationship is not a result of a pure chance), Section 2.3.2.3. The differences between the chemical composition of the particulate and gas phases can be clearly seen when the front (particulate phase) and the back (gas phase) filters sampled without the catalytic stripper are compared, Figure 3.27a. The front filter receives a high contribution from higher-mass aromatic species, with at least 4 aromatic rings. As previously mentioned, these species are usually considered to be non-volatile and are typically only present on the particulate phase [85, 152]. It should be noted that all the peaks corresponding to carbon clusters (C_n^+) have been excluded from this analysis since, in this case, they have a different source. Carbon clusters detected on back filters are coming from the layer of black carbon and not from the gas phase, therefore their consideration can skew the result of the analysis. However, this is only true for this particular case (for the comparison between front and back filters – particulate and gas phase), for instance,

© 2020 Tous droits réservés.

lilliad.univ-lille.fr

Thèse de Dumitru Duca, Université de Lille, 2020

when comparing only front filters, carbon clusters provide important information about the elemental carbon content of the collected particles (Figure 3.27b) and the impact of the catalytic stripper on the particulate phase can be identified. One can see that once the particles pass through the catalytic stripper, the contribution of aromatic compounds drastically decreases. Particles that are sampled with the catalytic stripper are characterized by a high elemental carbon content (high contribution from carbon clusters) implying, once again, that the organic carbon content decreased. Moreover, these particles feature a high contribution from oxygen- and nitrogen-bearing species which can be linked to the oxidation processes occuring in the stripper. A similar trend is also observed for the two samples corresponding to the gas phase ($NH2000_{BF}$ and $NH2000CS_{BF}$), Figure 3.27c. The sample obtained without the CS presents a high content of aromatic compounds (mostly low-mass, up to 4 aromatic rings), while the one sampled after the stripper is characterized only by carbon clusters. The fact that no organic species contribute in a significant way to the $NH2000CS_{BF}$ sample implies that the catalytic stripper removed the majority of these species from the gas phase and therefore only an insignificant amount of organics was adsorbed onto the activated carbon layer. It is worth noting that the aforementioned conclusions were obtained with a combination of several statistical techniques that not only provide complementary information but also enables cross validation of all findings. Moreover, using different statistical techniques (PCA, HCPC) enables us to uncover general trends in large data sets as well as subtle variations between only a couple of samples (smaller data sets, volcano plots).

The chemical composition of emitted particles strongly depends on combustion conditions (*i.e.* engine operation regime) which is determined by a plethora of different parameters, for instance engine speed and applied load. The variation in the chemical composition of particles generated in different engine regimes can be an issue for measurement techniques required to remain reliable and precise in a wide range of engine operation conditions (*e.g.* under real driving conditions). The reliability of a particle measuring instrument can be improved by removing the majority of organic compounds from the exhaust, including the ones responsible for the variation in the chemical composition, with a catalytic stripper. To assess whether the catalytic stripper is able to remove the organic fraction to the extent that the variations between the chemical composition of particles produced in different engine regimes is much smaller and would not cause any measurement artifacts, the particulate and gas phase sampled with and without the catalytic stripper in two different engine regimes (NH1200 and NH2000, Table 2.3) were compared using principal component analysis. The first two principal components account for ∼72% of the variance and are able to separate well the samples. The meaning of the components is once again determined from their loadings, Figure 3.28. The positive value of the first principal component (∼63.9%) can be associated primarily with the contribution of carbon clusters (C_n) – marker species for the elemental carbon content (EC). Its negative value is linked to the contribution of organic species (aromatic compounds). Therefore, the first principal component can be seen as the partitioning between EC and OC content. The second principal component (∼8.2%) is influenced by non-volatile aromatic species (compounds with at least 4 aromatic rings) with the mass smaller than m/z = 363 (positive PC2 value). The negative value of PC2 is associated with volatile, semi-volatile species, and some high mass aromatic compounds (m/z > 363). On the score plot, Figure 3.29, three major regions can

© 2020 Tous droits réservés.

lilliad.univ-lille.fr

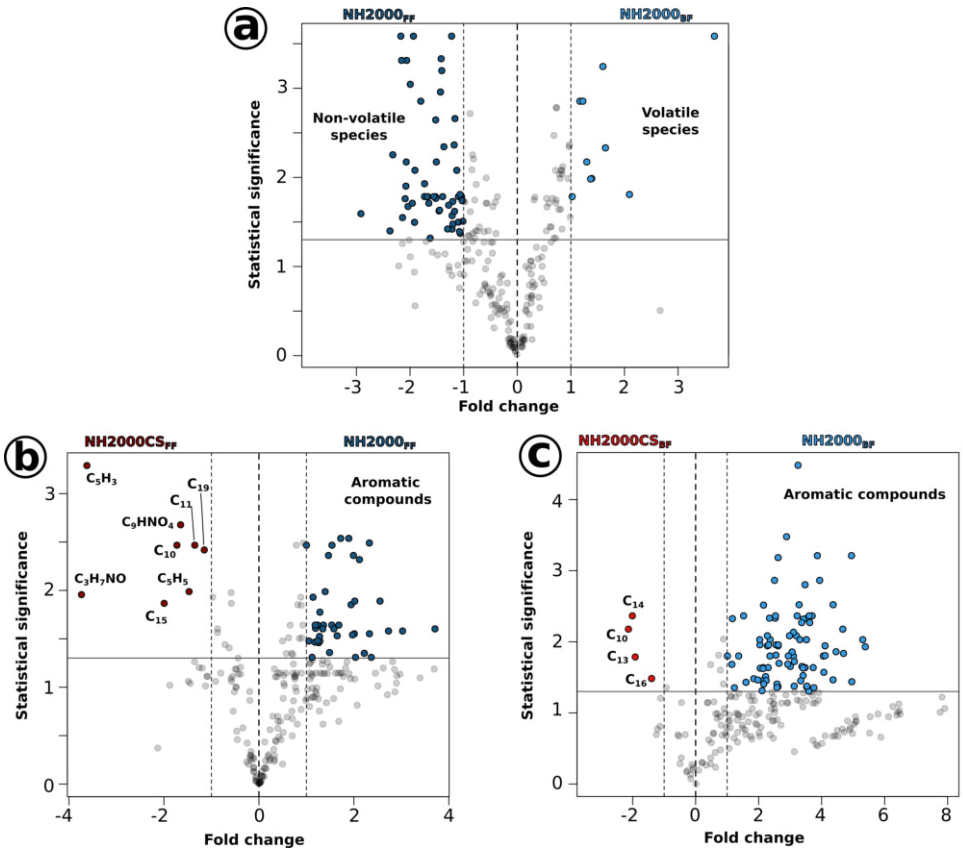

Figure 3.27 *Volcano plots showing the "differential expression" of detected chemical species on different samples. Coloured markers are associated with compounds that have, at the same time, a high statistical significance and fold change, while grey points correspond to chemical species that have either a low statistical significance or fold change, and thus do not contribute to the separation between two spectra. (a) Comparison between the particulate and gas phase sampled without the catalytic stripper ($NH2000_{FF}$ and $NH2000_{BF}$), (b) Comparison between the chemical composition of the particulate phase sampled with and without the catalytic stripper ($NH2000_{FF}$ and $NH2000CS_{FF}$), (c) Influence of the catalytic stripper on the chemical composition of the gas phase ($NH2000_{BF}$ and $NH2000CS_{BF}$).*

be seen: i) particulate phase sampled without the catalytic stripper, ii) particulate phase sampled after the catalytic stripper along with the gas phase sampled without the stripper, and iii) the gas phase collected after the catalytic stripper. It's worth noting that even though the particulate phases sampled without the stripper are located fairly close to each other and can be grouped together, their chemical composition is still different. The PC1 score for the front filter (particulate phase) of the $NH1200_{FF}$ sample is lower, thus indicating a higher contribution from organic compounds. However, after the catalytic treatment, particles emitted in different engine regimes (NH1200 and NH2000) appear to have a more comparable chemical composition, depicted by their almost identical PC1 score. The gas phase contains a much smaller initial amount of organic species (PC1 value is close to zero) which are almost completely removed by the stripper (the PC1 changes its sign). It is worth noting that the sign of the PC2 value for the particulate phase changes after the catalytic treatment, thus indicating the removal of the vast majority of the high mass organic species. The fact that the PC2 value for the gas phase samples is close to zero indicates that these samples are not influenced in a significant way by the

© 2020 Tous droits réservés.

lilliad.univ-lille.fr

explained factor (PC2) and therefore cannot be separated with it.

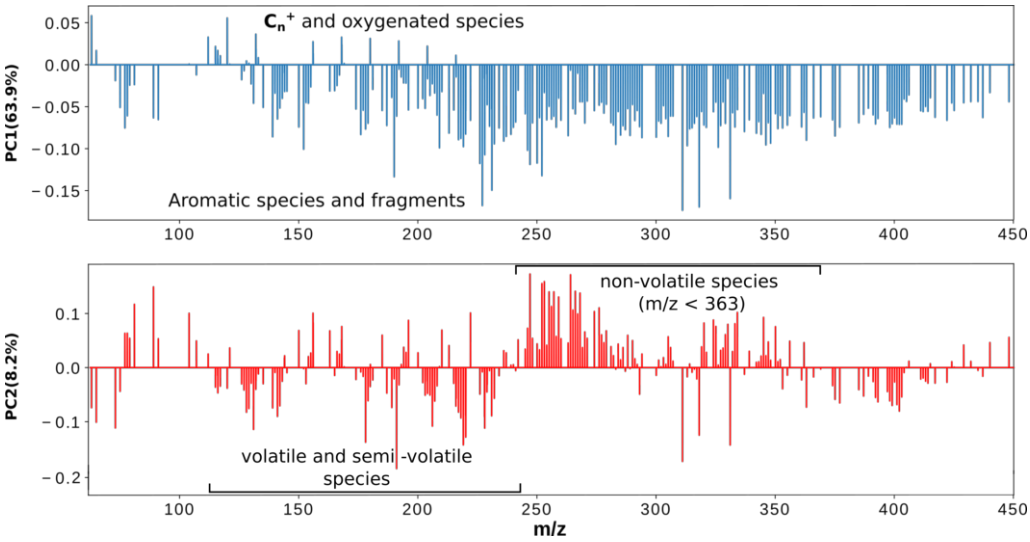

Figure 3.28 *Loadings plots for the first two principal components obtained from the mass spectra of polydisperse particles and gas phase samples collected with and without the catalytic stripper in two different engine regimes (NH1200 and NH2000, Table 2.3): PC1 – upper panel, PC2 – lower panel.*

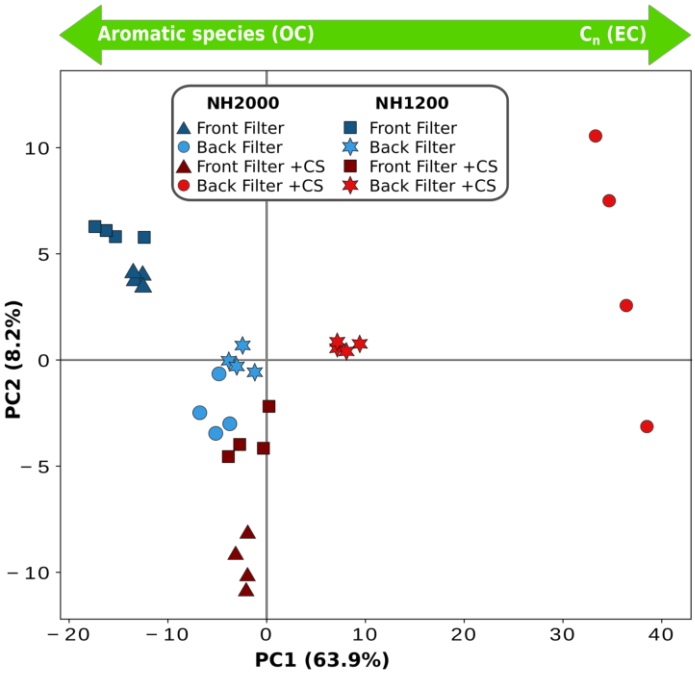

Figure 3.29 *Score plot of the first two principal components for the polydisperse soot particles and gas phase samples obtained with and without the catalytic stripper in two different engine regimes (NH1200 and NH2000, Table 2.3). The arrow indicate the meaning of the principal component derived from the corresponding loadings plot (Figure 3.28a).*

A volcano plot was used to compare the particulate phase collected in different engine regimes with and without the catalytic stripper. This allows the identification of species that discriminate the samples and then determine whether the dissimilarity is statistically significant or not. Figure 3.30 shows the comparison between

© 2020 Tous droits réservés.

lilliad.univ-lille.fr

Thèse de Dumitru Duca, Université de Lille, 2020

the particulate phase (front filters) obtained in different engine regimes and sampled with and without the catalytic stripper. When comparing untreated particles, Figure 3.30a, we can see that while both samples contain a large amount of aromatic compounds, the one obtained at a lower speed (NH1200$_{FF}$) contains more high-mass species. These particles have a significantly different chemical composition, demonstrated by the 55 compounds that contribute, in a statistically significant way, to the separation between the two samples. On the other hand, particles that have passed through the catalytic stripper appear to be very similar, Figure 3.30b. Only a few species contribute to the separation between the particulate phase generated in two different engine regimes and that passed through CS (NH1200CS$_{FF}$ and NH2000CS$_{FF}$). However, the majority of these species are carbon clusters (C_n) – markers of the elemental carbon content, meaning that the organic fraction of the catalytically treated particles is very similar. Even though data points with a small fold change or statistical significance (shown in grey) cannot be used for data interpretation, the change in the shape of their overall distribution can be also of use. For the particles collected after the catalytic stripper, the majority of data points have, at the same time, a very small statistical significance (linked to the p-value) and a small fold change. This implies that the similarity in the chemical composition is due to the removal of the majority of compounds.

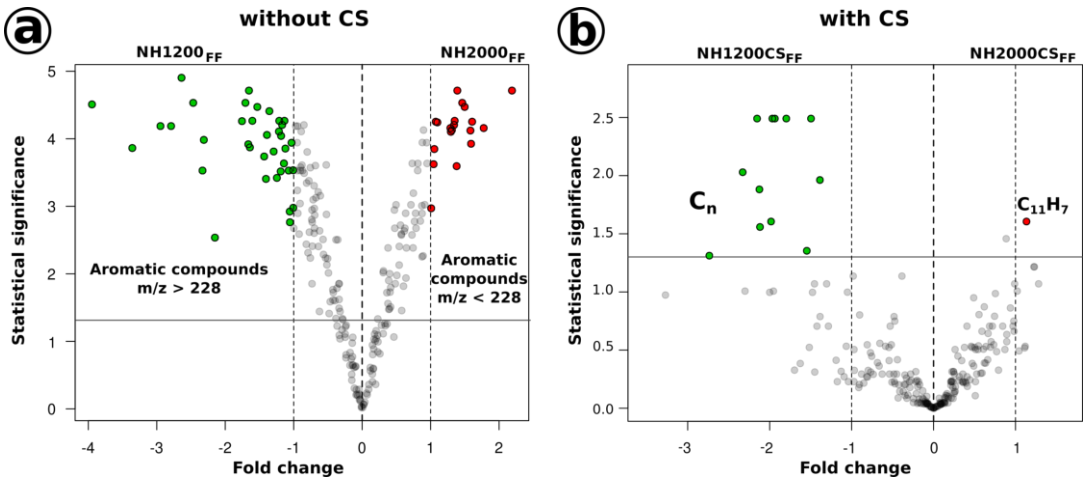

Figure 3.30 *Volcano plots showing the "differential expression" of chemical species between: (a) the particulate phase (front filters) collected in different engine regimes without the catalytic stripper (NH2000$_{FF}$ and NH1200$_{FF}$), (b) the particulate phase collected in different engine regimes with the catalytic stripper (NH2000CS$_{FF}$ and NH1200CS$_{FF}$). Coloured markers are associated with compounds that have, at the same time, a high statistical significance and fold change, while grey points correspond to chemical species that have either a low statistical significance or fold change, and thus do not contribute to the separation between two spectra.*

3.3.3.2 Size-selected particles

Chemical characterization of polydisperse particles can shed light on the composition of engine emissions and the overall efficiency of the catalytic stripper in removing the organic fraction. However, since the size distribution of emitted particles can be rather broad, the chemical composition determined for the particles sampled on quartz fiber filters (polydisperse particles) can be only seen as a weighted average

© 2020 Tous droits réservés.

lilliad.univ-lille.fr

Thèse de Dumitru Duca, Université de Lille, 2020

composition of size selected particles. Considering that the size distribution of particles for all studied engine regimes has a maximum at 70–80 nm, the contribution of the smallest nanopaticles is relatively small (mainly because of their low mass). For that reason, the size dependent chemical composition should be studied. The information about the size dependency of the particle chemical composition can not only help better understand the fuel combustion process in the engine but also deepen our understanding of the effects of the CS on the ICE particles (size- and composition-wise). With that in mind, size-selected particles produced in the same engine conditions as studied in the previous section and sampled with and without the catalytic stripper were chemically characterized and compared. Since the particles were separated into 13 distinct size-bins by the NanoMOUDI cascade impactor, the sampling time required to obtain an adequate coverage of the substrate was significantly longer compared to the time used to collect polydisperse particles, see Section 2.1.1.3.

Particles produced in the NH2000 engine regime and sampled with and without the catalytic stripper were collected in sufficient quantities for chemical characterization on the last 7 stages of the NanoMOUDI. These stages covered a quite extended size-range: from 10 nm up to 560 nm (samples referred to as $NH2000_{10-18}$ – $NH2000_{320-560}$). It's worth noting that the filter installed at the exit of the last impaction stage of NanoMOUDI (aerodynamic particle diameter < 10nm) was also tested, however, its mass spectrum was nearly identical to that of a blank filter and therefore it will not be considered in the following analysis. Mass spectra of size-selected particles obtained with HR-L2MS ($\lambda_d = 532\,nm$ and $\lambda_i = 266\,nm$) are presented in Figure 3.31. One can see that mass spectra of particles collected without the catalytic stripper (all sizes) show a high contribution from heavy-mass PAHs (also hopanoid compounds). The majority of these species, however, are successfully removed by the stripper – illustrated by the significant decrease in the absolute signal intensity. At the same time the contribution of carbon clusters (C_n) increases, indirectly indicating the reduction in the organic carbon content. In contrast to *Back Filters* that were described in the previous section, carbon clusters detected on samples with size selected particles can be entirely associated with the collected material as no black carbon layer was applied to the substrates (in this case, Al foils) prior to sampling. Size wise, the relative contribution of low-mass PAHs and their fragments increases toward smaller particles.

PCA was applied to, once again, reduce the dimensionality of the data set and uncover hidden trends. The first two principal components account for ∼60% of the variance in the data set and are able to discriminate between different samples (with particles of different size and collected with or without the catalytic stripper), Figure 3.32. The meaning of each component was derived using the contribution it receives from each detected species, Figure 3.33.

The first principal component separates samples based on the contribution of aromatic species (marker of the organic carbon) – positive PC1 values and carbon clusters (markers of the elemental carbon) – negative PC1 scores. This component enables the separation of particles collected with and without the catalytic stripper (NH2000 and NH2000CS). Since the NH2000 samples have mainly positive PC1 scores, while the NH2000CS ones exhibit mainly negative scores, we can conclude that a significant amount of the organic fraction present on the particles was successfully removed by the catalytic stripper. Moreover, the smallest analyzed particles

© 2020 Tous droits réservés.

lilliad.univ-lille.fr

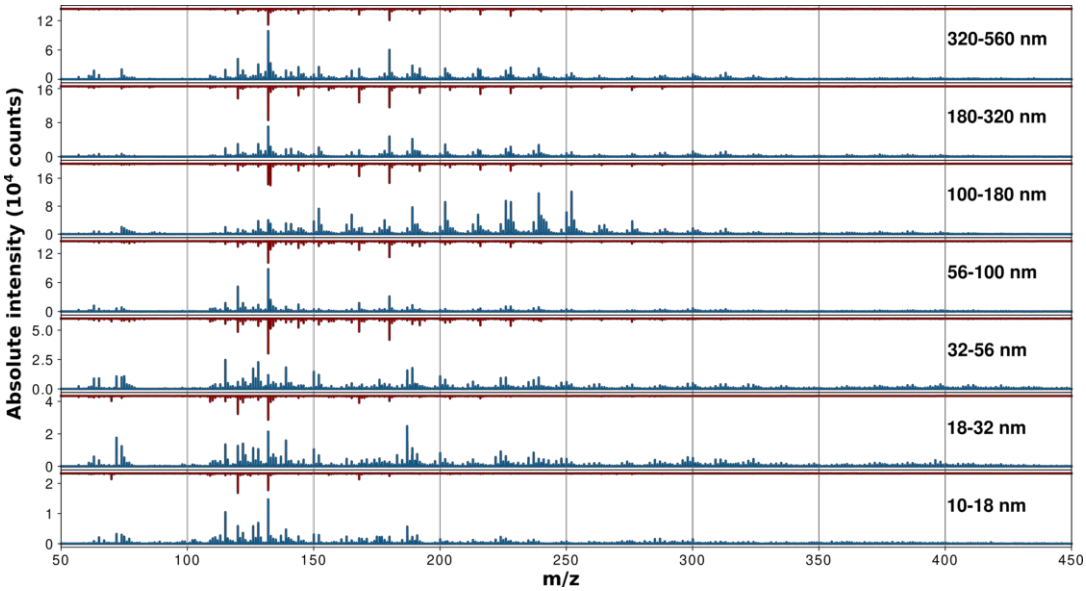

Figure 3.31 *Mass spectra of size-selected particles produced in the NH2000 engine regime and sampled with (red line – NH2000CS) and without (blue line – NH2000) the catalytic stripper. The labels indicate the NanoMOUDI size-bin that was used to collect the size-selected particles. All displayed spectra have been obtained by averaging the signal recorded in 4 different zones of each sample.*

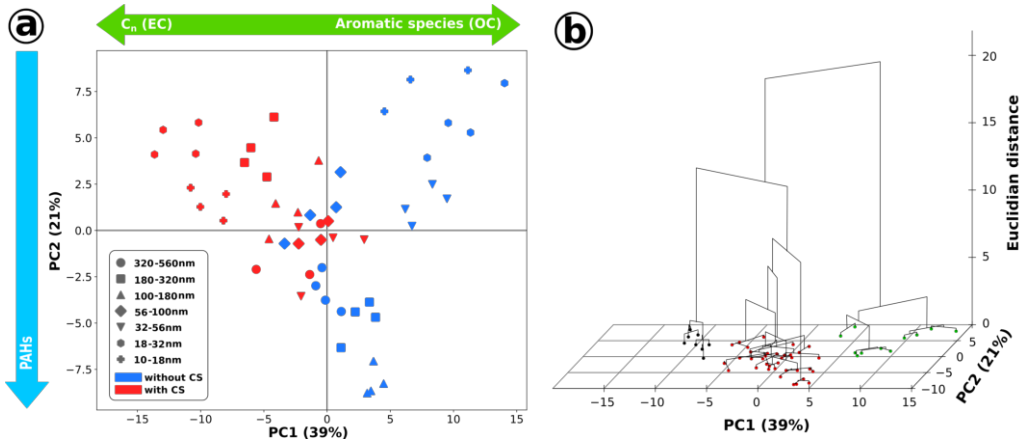

Figure 3.32 *(a) Score plot of the first two principal components obtained from mass spectra of size-selected particles collected with and without catalytic stripper (NH2000 and NH2000CS, Table 2.3). The arrows show the meaning of the principal components derived from their loadings. (b) HCPC performed on the first five principal components (explaining more than 82% of the variance). The biggest clusters correspond to: small particles collected with the catalytic stripper (NH2000CS$_{10-18}$ and NH2000CS$_{18-32}$) – black markers, small particles collected without the catalytic stripper (NH2000$_{10-18}$, NH2000$_{18-32}$, and NH2000$_{32-56}$) – green markers, and bigger particles collected in both regimes – red markers.*

(NH2000$_{10-18}$ and NH2000$_{18-32}$) seem to be the most affected by this treatment. This might be associated with the high relative content of organic species that are nearly completely removed, thus leading to a significant change in the PC1 score. Once the organic fraction is removed, the signal related to the elemental carbon (EC) becomes more important (C_n ions) – decreasing PC1 score. This conclusion is

© 2020 Tous droits réservés.

lilliad.univ-lille.fr

Thèse de Dumitru Duca, Université de Lille, 2020

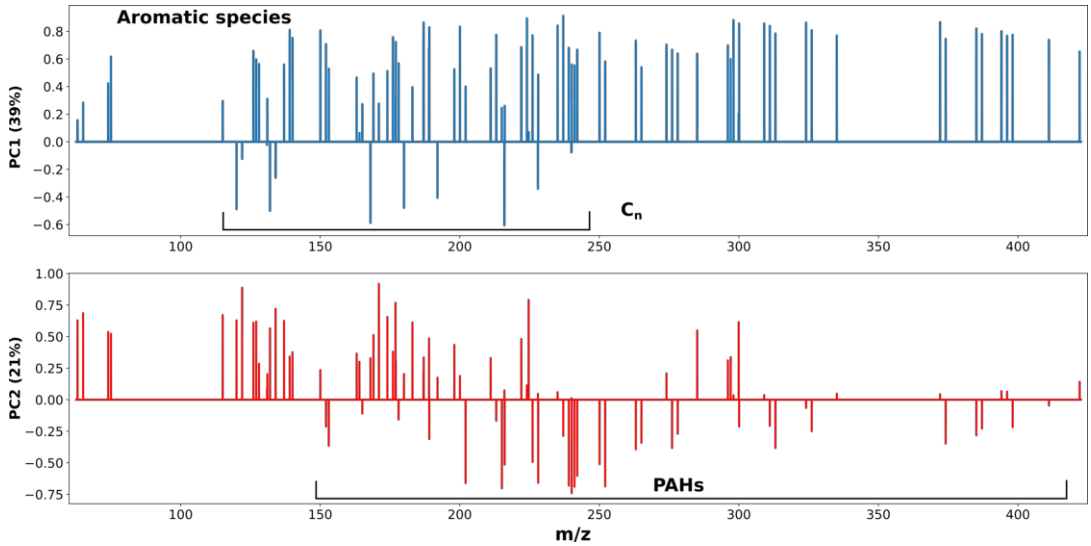

Figure 3.33 *Loadings plots of the first two principal components obtained from the mass spectra of size-selected particles collected with and without the catalytic stripper (NH2000 and NH2000CS).*

supported by volatile mass fraction measurements conducted by a group from University of Cambridge (A. Boies) in parallel with size-selective sampling. The volatile mass fraction was determined with a combination of an Aerodynamic Aerosol Classifier (AAC, Cambustion Ltd.), a Differential Mobility Analyser (3080 DMA, TSI Inc.), and a Centrifugal Particle Mass Analyser (CPMA, Cambustion Ltd.), Figure 3.34. Online measurements showed that the volatile mass fraction increases for smaller particles which would make them more susceptible to a catalytic treatment, Figure 3.35.

The contribution of PAHs (*i.e.* stabilomers [165]) can be derived from the second principal component (negative PC2 score). Bigger particles (100 – 560 nm) receive a higher contribution from PAHs which disappears once they pass through the catalytic stripper (PC2 score changes from being negative to positive or almost zero). It is worth noting that the spread between data points across the second dimension (PC2) is much smaller for particles collected with the catalytic stripper (NH2000CS) indicating that, when it comes to the organic fraction, the chemical composition of stripped size-selected particles is not very different.

HCPC was performed on the first five principal components, accounting for more than 82% of the variance within the data set, Figure 3.32b. For the analyzed samples, we can distinguish three separate clusters: small particles collected with the catalytic stripper ($NH2000CS_{10-18}$ and $NH2000CS_{18-32}$) – black markers, small particles collected without the catalytic stripper ($NH2000_{10-18}$, $NH2000_{18-32}$, and $NH2000_{32-56}$) – green markers, and bigger particles collected in both regimes – red markers. This shows, once again, that the catalytic stripper has a very high impact on the smallest particles, thus suggesting that they contain a higher surface organic fraction.

The compounds that are efficiently removed from the smallest particles by the stripper can be identified with a volcano plot, Figure 3.36. We can see that the catalytic stripper removes, as expected, the organic fraction from these particles. This leads to a relative increase in the signal from carbon clusters. It is worth noting that, for this particular size-bin, the stripper effectively removes PAHs from

© 2020 Tous droits réservés.

lilliad.univ-lille.fr

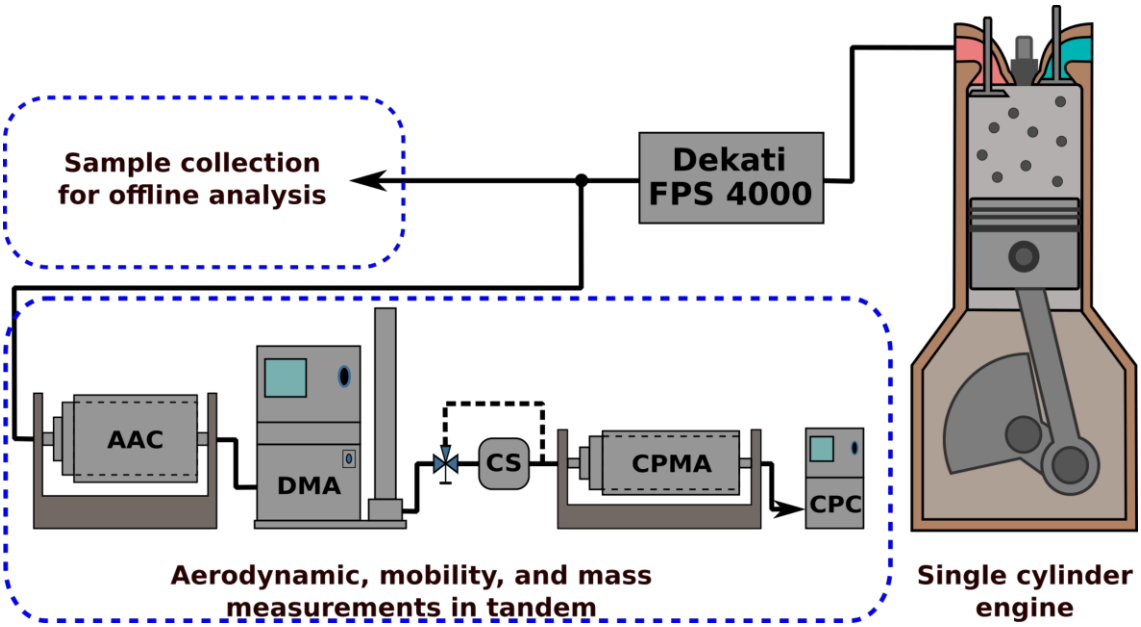

Figure 3.34 *Schematic representation of the experimental setup used for simultaneous online volatile mass fraction measurements and particle sampling. The on-line particle characterization was performed with a series of Aerodynamic Aerosol Classifier (AAC), differential mobility analyser (DMA), optional catalytic stripper (CS) and subsequent centrifugal particle mass analyser (CPMA) followed by a condensation particle counter (CPC).*

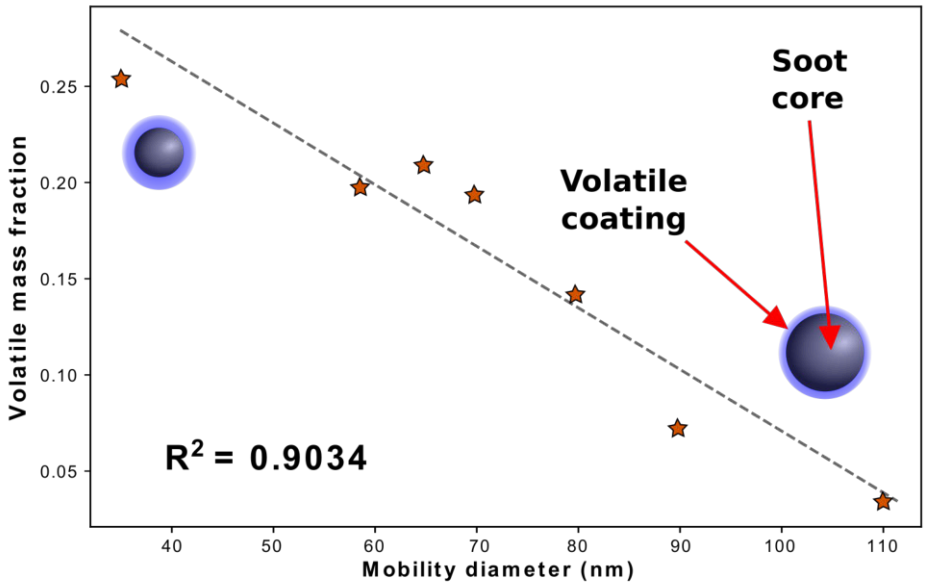

Figure 3.35 *Variation of the volatile mass fraction with the particle size obtained from online aerodynamic-mass-mobility measurements (A. Boies, University of Cambridge).*

the entire mass-range. After the treatment ($NH2000_{10-18}$ sample), particles show a negligible contribution from organic species and the only detected peaks correspond to carbon clusters (data points with a negative fold change in Figure 3.36).

As already discussed in the previous section, chemical composition of emitted particles strongly depends on the engine regime and can significantly affect the accuracy of particle measurement systems. This also gives an opportunity to test

© 2020 Tous droits réservés.

lilliad.univ-lille.fr

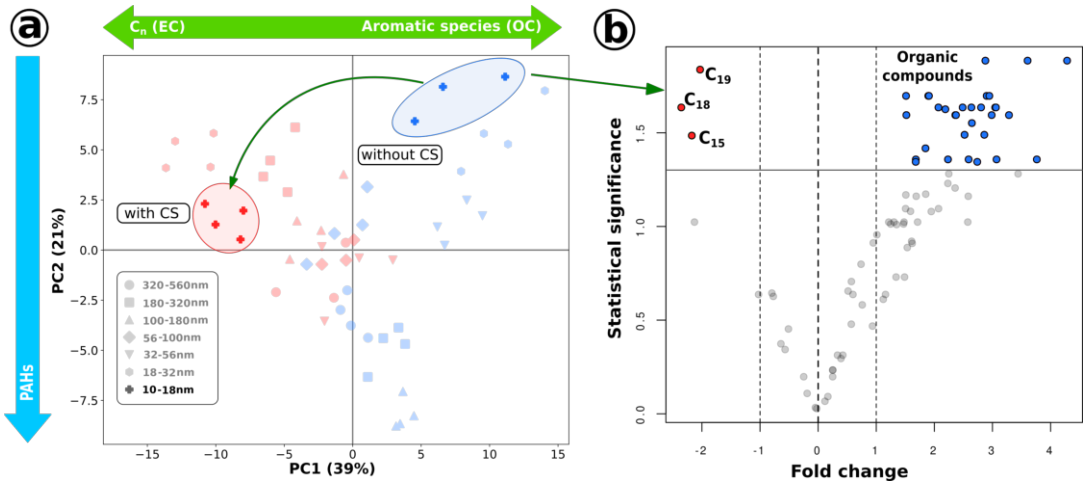

Figure 3.36 *(a) Score plot of the first two principal components obtained from mass spectra of size-selected particles collected with and without catalytic stripper (NH2000 and NH2000CS) with datapoints corresponding to the smallest particles (10 – 18 nm) highlighted. (b) Volcano plot for the smallest analyzed particles ($NH2000_{10-18}$ and $NH2000CS_{10-18}$) showing the "differentially expressed" species that result in the separation by PCA of the two samples, Figure 3.32. Coloured markers are associated with compounds that have, at the same time, a high statistical significance and fold change, while grey points correspond to chemical species that have either a low statistical significance or fold change, and thus do not contribute to the separation between two spectra.*

whether the catalytic stripper maintains its high efficiency, observed with NH2000 particles, in other regimes (generating significantly more organic compounds). Size-selected particles obtained in the NH2000 and NH1200 engine regime were chosen to study the influence of the stripper on particles of the same size but different chemical composition. Polydisperse particles produced in the same engine regimes were analyzed in the previous section where it was determined that the exhaust produced in the NH1200 regime has an overall higher organic content, Section 3.3.3.1. Size-selected samples obtained in the NH1200 regime were analyzed using HR-L2MS ($\lambda_d = 532\,nm$, $\lambda_i = 266\,nm$) and then compared with particles produced in the NH2000 regime. As expected, mass spectra of all unstripped particles, Figure 3.37, are dominated by aromatic compounds, present in the higher amount for the low speed engine regime compared to the high speed one (*i.e.* $OC_{NH1200} > OC_{NH2000}$), for all size bins. The same trend is observed after passing in the CS (*i.e.* $OC_{NH1200CS} > OC_{NH2000CS}$), although the OC content is much reduced for both engine regimes.

First of all, the differences between the chemical composition of size-selected particles produced in the NH1200 and NH2000 engine regimes must be identified (size-selected particles collected without catalytic stripper). This will later allow the interpretation of the results for NH1200CS samples. PCA was used to compare two sets of samples (NH1200 and NH1200CS). The first two principal components, accounting for 61% of the variation in the data set, are located before the "elbow" on the eigenvalue plot (Section 2.3.2.1) and are therefore used to explain the differences in the chemical composition. A positive PC1 value can be linked to a high contribution from PAHs while a negative score is indicative of fragment or C_n presence. The samples can be separated based on the contribution they receive from marker species of OC and EC with the help of the second principal component. For

© 2020 Tous droits réservés.

lilliad.univ-lille.fr

Thèse de Dumitru Duca, Université de Lille, 2020

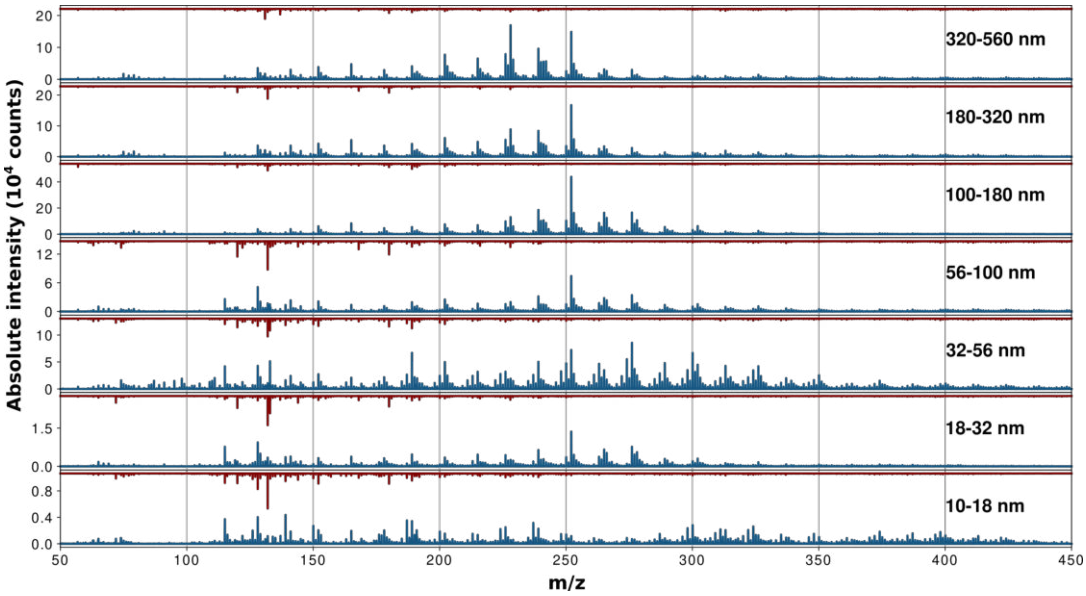

Figure 3.37 *Mass spectra of size-selected particles produced in the NH1200 engine regime and sampled with (red line – NH1200CS) and without (blue line – NH1200) the catalytic stripper.*

instance, samples with a high signal related to EC have a negative PC2 score, while the ones with a high amount of organic species (*i.e.* OC) exhibit a positive PC2 value.

On the score plot, Figure 3.38a, it can be seen that data points corresponding to different engine regimes are well separated by the first principal component. It is then possible to distinguish between these two engine regimes based only on the contribution from PAHs, fragments, and carbon clusters. On that account, the NH1200 engine regime feature a much higher contribution from PAHs, with particles from all size-bins having a negative PC1 score, with the sole exception being $NH1200_{10-18}$. In contrast, particles emitted in the NH2000 engine regime seem to have a high signal coming from fragments and carbon clusters. It is worth recalling that PCA is emphasizing the differences and similarities between samples and, therefore, the interpretation of the data should be only done by comparing several samples. As a result, the fact that NH2000 samples show a positive PC1 score cannot be seen as an indicator of the missing organic fraction and only that the relative contribution of peaks attributed to organic species is smaller compared to NH1200 samples. The second principal component shows that in the NH1200 regime, the smallest particles have the highest OC/EC ratio, higher than on the corresponding NH2000 sample. Putting the two components together, we can see that bigger particles (56 – 560 nm) produced in the NH2000 regime have the highest contribution from carbon clusters, *i.e.* high relative EC content. In addition, small particles from the NH2000 regime (10 – 100 nm) are influenced the most by organic species. It is worth noting that particles in the size range of 100 – 320 nm have a similar PC2 score, implying that they are the least affected by the change in the engine regime (NH1200 and NH2000 regimes).

After the differences between the chemical composition of particles produced in different engine regimes have been identified, the effect of the catalytic stripper onto these particles can be studied. PCA was applied to mass spectra of NH1200CS and

© 2020 Tous droits réservés.

lilliad.univ-lille.fr

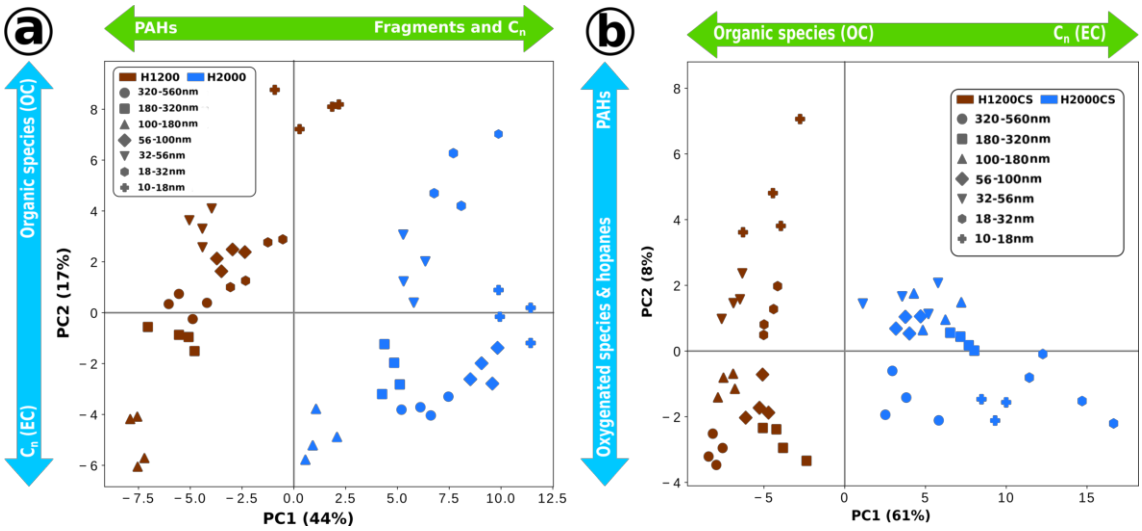

Figure 3.38 *Score plot of the first two principal components obtained from the mass spectra of size-selected particles collected in the NH1200 and NH2000 engine regimes without (a) and with (b) catalytic stripper. The arrows indicate the meaning of principal components obtained from their corresponding loadings.*

NH2000CS samples. The first two principal components explain 69% of the observed variance and are able to distinguish between particles generated in different engine regimes, even after they passed through the catalytic stripper. The loadings plot for PC1 and PC2 is presented in the Figure 3.39 and is used to determine the physical meaning of the separation between samples.

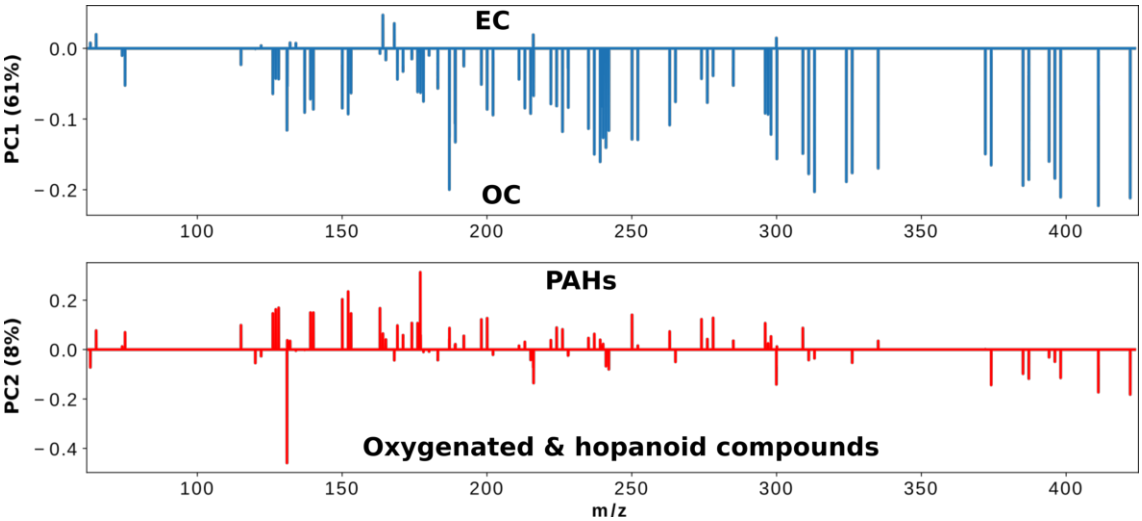

Figure 3.39 *Loadings plots of the first two principal components obtained from mass spectra of size-selected particles collected in the NH1200 and NH2000 regimes with the catalytic stripper.*

The samples can be grouped based on their OC/EC ratio inferred from the first principal component (61%). Accordingly, the samples produced in the NH1200 regime and that passed through a catalytic stripper have a higher OC content compared to the NH2000CS samples, Figure 3.38b. This is likely caused by the larger initial organic fraction present on the particles. The amount of PAHs (positive PC2 score), oxygenated species, and hopanoid compounds (negative PC2 score)

© 2020 Tous droits réservés.

lilliad.univ-lille.fr

Thèse de Dumitru Duca, Université de Lille, 2020

can be inferred from the second principal component. Bigger NH1200CS particles (100 – 560 nm) are characterized by an increased contribution from hopanoid compounds, which seem to be removed from smaller particles by the catalytic stripper. NH2000CS samples do not seem to have a high hopanoid content, the negative PC2 score observed for three size-bins ($NH2000CS_{320-560}$, $NH2000CS_{18-32}$, $NH2000CS_{10-18}$) are determined by oxygenated species. The NH2000CS cluster in located very close to the PC2 axis, suggesting, once again, that these particles contain a very small amount of organic fraction.

3.3.4 Conclusion

In this chapter the exhaust of a single-cylinder engine operated in various regimes was characterized, providing extensive information relative to the structure, morphology and chemical composition of the emitted particulate matter. Detailed molecular-level characterization of particulate matter in conjunction with statistical procedures demonstrated that the chemical composition depends on particle size. Moreover, the identification of chemical markers allowed the definitive discrimination of particles generated from different sources, as well as engine regimes, even for samples where all particle sizes were collected simultaneously (*i.e.* polydisperse particles). For size-selected particles (collected with the NanoMoudi), particle characterization allowed for a detailed description of the size-dependent chemical composition, including attribution of particle sources and a direct link to fuel and lubricant raw composition or combustion products. Moreover, it was possible to discriminate particles of different sizes and collected in various regimes from their specific chemical composition. Atomic force and electronic microscopy (SEM and TEM) were employed to monitor the morphology of collected soot particles while TERS was used for the first time to probe the nanostructure of sub-10 nm soot particles. It was shown that ultra fine particles that are produced in the same engine regime and sampled in the same size-bin can be still very different.

The impact of the catalytic stripper on the chemical composition of size-selected, polydisperse particles and the corresponding gas phase was also studied. It was shown that the CS is able to remove the majority of particle-bound organic species as well as most of organic compounds present in the gas phase. Polydisperse particles generated in different engine regimes and having significantly different chemical composition become similar after going through the stripper.

When polydisperse particles are studied, a weighted average composition of particles in different size ranges is obtained. Individual weights are related to the initial particle size distribution which can significantly change depending on the engine operation regime. Further, the size dependent chemical composition, makes the direct comparison between polydisperse particles sampled in different engine regimes more difficult. This illustrates how important it is to sample and characterize size-selected particulate matter, especially since the chemical composition of smaller particles (with a relative low particle mass) cannot be otherwise inferred. It was discovered that small particles (< 32 nm) are more affected by the catalytic stripper, implying that they hold a larger surface volatile fraction. This conclusion is also supported by online aerodynamic-mass-mobility measurements indicating that the volatile mass fraction decreases for larger particles. A multitude of chemical species (*e.g.* PAHs) are present in the surface organic layer, therefore, a higher volatile fraction could

© 2020 Tous droits réservés.

lilliad.univ-lille.fr

Thèse de Dumitru Duca, Université de Lille, 2020

be potentially linked to a higher overall toxicity. Consequently, ultra-fine particles matter generated by gasoline engines can possibly present a double risk – due to their small size they penetrate deeper in the respiratory system while also carrying a larger amount of potentially toxic compounds. This illustrates the importance of characterizing size-selected particles. Such measurements enable the study of different particle sources, and their physico-chemical evolution throughout the exhaust system – including interaction with the catalytic stripper, and thus allow to interpret the measured PN at the exhaust out using the new measurement system under real road conditions.

© 2020 Tous droits réservés.

lilliad.univ-lille.fr

Chapter 4

A novel laser-based method to measure the adsorption energy on carbonaceous surfaces

4.1 Introduction

Carbon is the second most abundant element in the biosphere and carbonaceous materials are used in a wide range of applications including aerospace and defense, automotive, energy, construction, electronics, and sports. The extensive use of carbon-based materials in their multiple forms (*e.g.* carbon fibers, carbon nanotubes, graphene) is determined by their superior properties including excellent stiffness, high tensile strength, low thermal expansion, and good temperature tolerance [166, 167]. Carbon-based materials can also be turned into metal-free catalysts and serve as a promising alternative to transform sustainable biomass into renewable energy systems [168].

Due to their excellent adsorption capacities, carbonaceous materials are widely employed as filtration media. Carbon nanotubes (CNT) show great potential at revolutionizing water and gas treatment technologies [169] as they provide much higher surface areas, adsorption capacities, and faster kinetics than activated carbon – the currently prevailing filtration agent. The utility of the adsorptive fixation of organics in the gas and liquid phases for treating wastewaters and emission gasses is already showcased for a number of harmful compounds [72–75]. Another considerable advantage of carbon nanostructures is that their properties can be tailored to target certain chemical species (*e.g.* toxins, heavy metal ions) [72, 170, 171].

For carbonaceous materials, the downside of exhibiting high adsorptive capacities is the potential to act as surface carriers for a variety of chemical compounds. This can lead to a long-range transport of toxic species adsorbed on the surface of these materials. This effect is commonly observed with combustion generated aerosols (soot), which consist of a carbonaceous matrix often coated with a plethora of organic species [21, 78, 153], many of them exhibiting a proven carcinogenic potential [11–13]. This considerably increases the impact of combustion generated particles on human health, especially since their inhalation can result in health problems beyond the lungs [14]. In fact, the presence of combustion derived nanoparticles has been detected in the frontal cortex of autopsy brain samples [15], urine of healthy children [16], and even in the fetal side of the placenta [17]. If transported to the fetus, these

© 2020 Tous droits réservés.

lilliad.univ-lille.fr

Thèse de Dumitru Duca, Université de Lille, 2020

particles – as surface carriers for potentially toxic species – could significantly affect fetal health and development [17].

In this context, the benefit of identifying the adsorption mechanism on carbonaceous surfaces and its associated adsorption energy is threefold. It can provide necessary information to better understand, and potentially minimize, the health impact of carbonaceous aerosols. It can help design better carbon-based materials for industrial use. And finally, it can offer some insights into the complex and still only partially understood soot formation mechanism since adsorption energies define whether the surface species (adsorbates) are chemisorbed or physisorbed, and therefore if the surface molecular compounds result from surface chemistry (remnants of the soot formation) or physical condensation [76]. Adsorption performances are governed by physical and chemical parameters that greatly vary across adsorbate/adsorbent systems. Thus, a systematic study needs to be undertaken in order to determine i) to what extent the adsorption energy depends on the nature and the size of the adsorbate, and ii) the type of interactions established between adsorbate and adsorbent. Depending upon the nature of the adsorbate (gas or liquid) and adsorbent (*e.g.* polycrystalline film, single-crystal, oxides, or nanoparticle surfaces, powders suspended in a liquid or loose powders) [172], various microcalorimetry techniques, such as single-crystal adsorption calorimetry (SCAC), isothermal titration calorimetry (ITC), and differential scanning calorimetry (DSC) [173, 174], or temperature-programmed desorption (TPD) [175, 176] are commonly used to either measure directly the heat of adsorption (microcalorimetry) [177–179], or evaluate the activation energy of desorption (TPD). Despite their advantages, the application of these conventional techniques to systems exhibiting meso or macro scale (micrometer- or sub-millimeter sized) inhomogeneities or field-collected samples exhibiting small quantities of matter and complex compositions (*i.e.* with a multitude of co-adsorbed species) becomes at best arduous and at worst impossible.

In this chapter, a novel method of determining the adsorption energy of chemical species is presented. The proposed method relies on laser-induced thermal desorption (LITD). One of the unique characteristics of the method is its ability to be applied to systems exhibiting sub-millimeter range heterogeneities. Specifically, it can be utilized to recover the mean adsorption energy of analytes present in distinct areas of a sample with a lateral resolution defined by the diameter of the utilized laser spot. The method requires no sample preparation prior to analysis (*e.g.* extraction of material) and necessitates only micrograms of materials to operate. Therefore, it can be directly applied to field-collected and natural samples, for which collecting as much as micrograms of material can be challenging (*e.g.* sampling of aircraft engine [77] or on-road vehicle internal combustion engine emissions [153]). This is especially important when the focus is on size-select particles [102, 103] as small as 10 nm with an average particle mass of only several attograms. The method also enables the simultaneous study of one or several analytes co-adsorbed on the same surface, which is particularly adapted to real-world complex mixtures. These characteristics, in conjunction with the very low limit of detection (sub-femtomole), make this method a valuable solution when more conventional techniques cannot be utilized.

The chapter is divided into several sections. First, an overview of previous works is presented, describing earlier studies that first linked the desorption behaviour with the analyte-surface interaction. Several experimental considerations are then

© 2020 Tous droits réservés.

lilliad.univ-lille.fr

Thèse de Dumitru Duca, Université de Lille, 2020

provided, detailing different approaches used here to gather experimental data. The following section is dedicated to the development of the theoretical part of the method, where two different models describing the laser-induced thermal desorption of chemical species from a surface are derived, along with the mathematical apparatus needed to fit the models to experimental data. Finally, the results of the analysis performed with the developed method on a variety of samples are presented. The method was applied to several samples containing either a single or several co-adsorbed species (both organic and inorganic compounds were tested). Moreover, the performance of the proposed technique was evaluated for a number of carbonaceous surfaces (porous and non-porous) featuring a variable number of surface defects. The potential application of the method to the analysis of complex, field-collected samples is also discussed.

4.2 Previous works

Laser-induced desorption, phenomenon the described method is based on, is largely used in the field of interface preparation and in the study of processes occurring at the surface level. The effectiveness of this technique was demonstrated for cleaning and annealing surfaces [180, 181], analyzing adsorbed compounds [182, 183], and desorbing large organic molecules [78, 98, 153, 184]. This technique was previously used to study surface diffusion [185], probe surface reactions [186], and even attempted to investigate adsorption/desorption kinetics [187–189].

In spite of multiple studies, the laser-induced desorption mechanism is not completely understood. Moreover, multiple models are used to explain the experimentally obtained desorption signal and subsequently extract important information about the desorbed species. Early studies showed that H, CO, and CO_2 molecules were desorbed from a variety of surfaces when hit by high energy laser beams [187], phenomenon interpreted as a purely thermal effect. This effect was later used to study the adsorption and desorption kinetics of these gases by means of relaxation methods [190]. LITD was also used to examine the desorption of Na and Cs atoms with a sub-monolayer surface concentration from Ge (100) substrates [191]. The authors postulated that the adsorption energy of these metals decreases with analyte coverage due to the higher contribution of the adsorbate-adsorbent interaction. The adsorption energy, however, was not determined in that study and, instead, the conclusion was drawn from the measured variation of Na or Cs coverages. A more detailed study of desorption from metal surfaces was performed by Christmann et al. [190] (desorption of H_2 from Ni (100), (110) and (111) surfaces), Wedler and Ruhmann [192] (desorption of CO from Fe surfaces), Arnolds et al. [193] (desorption of benzene from Pt (111) surfaces) where LITD was used to determine the adsorption kinetics and even compare the results with the values obtained with other methods.

The majority of these previous studies used a single high-fluence laser pulse to desorb all the adsorbed species from the surface, thereby "cleaning" the irradiated spot of the sample with only one laser pulse. However, when a lower desorption laser fluence is used, not all the molecules can be desorbed by a single laser pulse. In this case, multiple, consecutive laser pulses can be used to desorb all the compounds present on the surface [194]. Since after each desorption pulse the surface concentration of molecules reduces, the amount of desorbed compounds decreases after each subsequent laser pulse, thus resulting in a pseudo-exponential (Arrhenius-

© 2020 Tous droits réservés.

lilliad.univ-lille.fr

Thèse de Dumitru Duca, Université de Lille, 2020

type) variation of both surface coverage and desorbed amount. The shape of such a variation was first linked to the energetics of the adsorbate-adsorbent interaction by Specht and Blades [76]. The authors postulated that the decay obtained for pyrene desorbing from charcoal corresponds to molecules that are weakly bound to the surface, while the relatively constant signal that followed was associated with molecules that have a stronger interaction with the carbonaceous surface. The observed decay, however, was not used to evaluate the strength of the pyrene-surface interaction. A similar decay, observed by Faccinetto and coworkers [78], was used to determine the limit of detection of the L2MS technique in our laboratory. Although the energetics of the analyte-surface bond was not studied, the authors demonstrated that a single form of interaction between the analyte and the carbonaceous surface (in this case physisorption) can be achieved on surrogate soot samples (since no constant background was observed). A different approach was proposed by Dreisewerd et al. [195] to derive the activation energy of desorption from sinapic acid and bovine insulin thick layers deposited on stainless steel, based on the evolution of the desorbed amount of molecules with the irradiation laser fluence. These studies motivated us to go further and utilize the previously mentioned signal decay and fluence dependency to retrieve the desorption energy of organic and inorganic compounds adsorbed (at low, sub-monolayer coverage) on carbonaceous surfaces. Moreover, by developing a theoretical model of laser-induced thermal desorption, an extra step was taken toward better understanding fast processes occurring at the sample surface.

4.3 Experimental considerations

This section provides a summary of the experimental approaches used to acquire data for adsorption energy determination. Moreover, several experimental considerations required for the development of the theoretical model are discussed. The development and validation of the method required well characterized samples and was performed with "surrogate soot" samples described in Section 2.1.2. Briefly, several chemical species were chosen as adsorbates: polycyclic aromatic hydrocarbons, as they are known to be present on the surface of soot particles collected from real combustors, and a heavy metal (Pb) since carbonaceous materials are often used to remove heavy metals from aqueous solutions. They were adsorbed in controlled concentration on three types of adsorbents: activated carbon nanoparticles (60 – 80 nm average particle size, 80 – 150 m^2g^{-1} specific surface area), graphite sheets, and highly-oriented pyrolitic graphite (HOPG). The synthesized samples used in the following are summarized in Table 2.4. Considering the low coverages and the preparation protocol, we can assume that no lateral interaction between adsorbate molecules is present, and that the coverage is homogeneous across the surface.

4.3.1 Experimental approaches

The experimental setup used to obtain the characteristic signal decay or fluence curve is based on the L2MS technique described in detail in Section 2.2.2.2. During measurements, the desorption fluence was carefully adjusted to be in the low, pre-ablation regime [78, 98], which ensures the desorption of neutral species from the surface of the sample without affecting the underlying carbonaceous substrate. Two

© 2020 Tous droits réservés.

lilliad.univ-lille.fr

Thèse de Dumitru Duca, Université de Lille, 2020

distinct approaches were followed to collect experimental data used for adsorption energy determination: "signal decay" and "fluence curve".

"Signal decay" experimental approach

The first experimental approach is presented in Figure 4.1a-c: A region of the sample (delimited by the laser spot on the surface) is irradiated with successive nano-second, constant low-fluence laser pulses (10 Hz repetition rate). For each pulse, a fraction of desorbed molecules is ionized by the second ns laser and detected by the mass spectrometer. Mass spectra are so recorded for successive laser pulses and the signal corresponding to the adsorbate of interest (integrated area, including the peaks associated with its isotopic distribution) is plotted as a function of applied laser pulses (Figure 4.1c). The pseudo-exponential decay observed simply illustrates a gradual "cleaning" of the irradiated spot by the successive desorption pulses. If this decay is "slow" (*i.e.* a high number of laser pulses is needed to "clean" the surface) then one can infer a strong interaction between the adsorbate and the surface. Conversely, a faster decay (in the same irradiation conditions) will be indicative of looser bonding of the adsorbate to the surface.

To account for possible experimental fluctuations (mainly due to desorption and ionization lasers), several equivalent measurements are performed in different spots of the same sample. For this first experimental approach, four signal decays are recorded for the same laser set-point, each one in a pristine zone of the sample.

"Fluence curve" experimental approach

The second approach (called "fluence curve", Figure 4.1d-e) relies on the variation of the adsorbate signal intensity with the desorption laser fluence. In this case, multiple spots on the sample surface are irradiated with nanosecond laser pulses delivering distinct laser fluences (typically in the range 20–140 $mJ\,cm^{-2}$), each resulting in desorption of distinct amounts of adsorbate from the surface (the higher the fluence, the higher the number of desorbed molecules). For this approach, the signal corresponding only to the first desorption laser pulse is recorded for different fluences from distinct sample spots (Figure 4.1d). Recording each signal from a pristine surface spot (*i.e.* which was not irradiated before) ensures the same initial coverage for each desorption pulse.

For this second approach, four experimental data points per desorption fluence value were acquired on four distinct (pristine) zones of the sample (*e.g.* for pyrene, seven desorption fluence values were utilized resulting in 28 experimental datapoints / irradiated spots in total). As all measurements are performed in different spots on the sample, each datapoint can be considered as fully independent. Therefore, different combinations of these points can be made to build distinct "fluence curves". Among all possible combinations, a total of 10 distinct fluence curves are constructed by randomly combining experimental datapoints.

4.3.2 Detected molecules

The signal recorded by the mass spectrometer is proportional to the number of molecules desorbing from the sample surface (only a fraction of them being ionized

© 2020 Tous droits réservés.

lilliad.univ-lille.fr

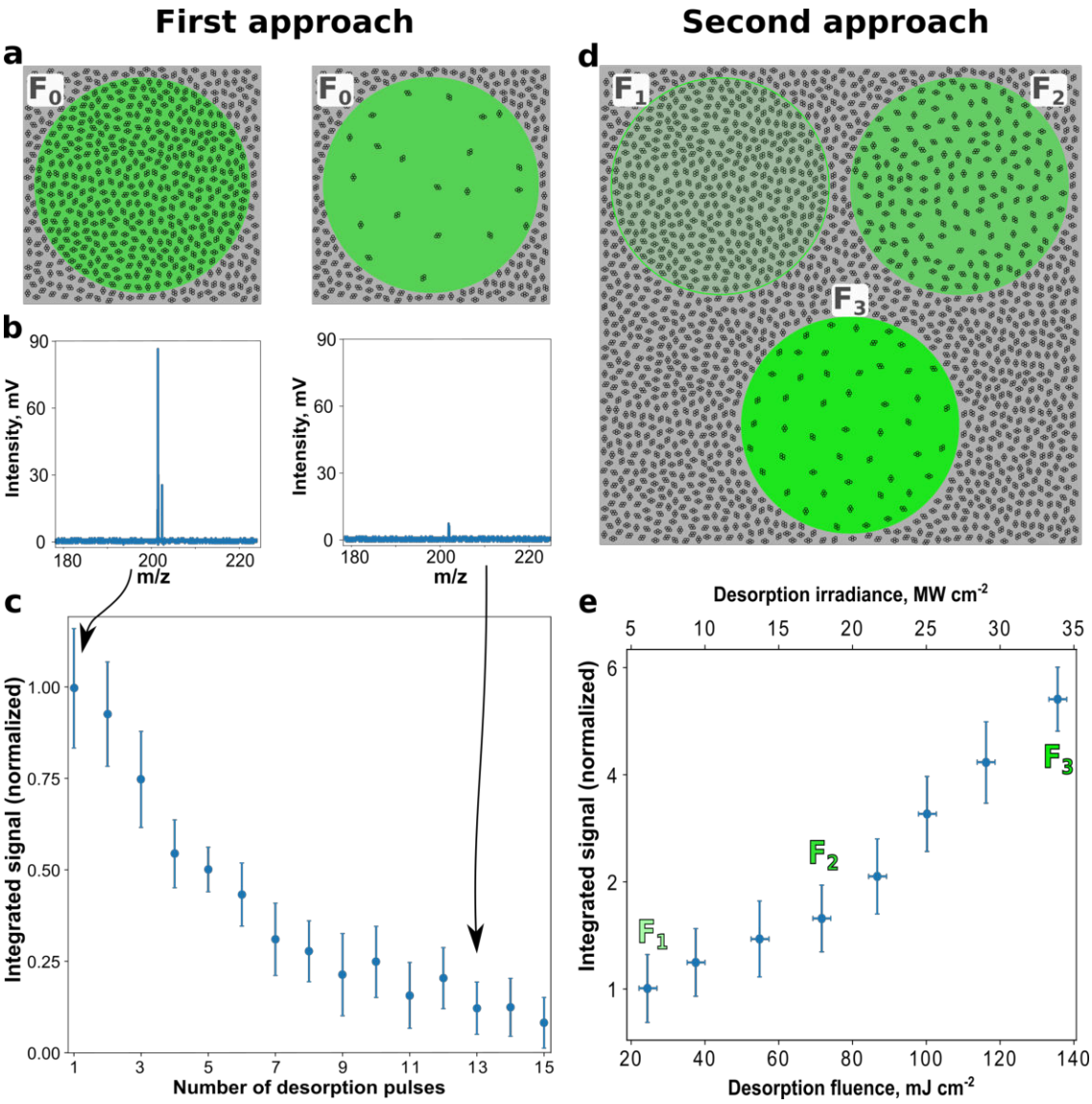

Figure 4.1 *(a) Schematic representation of the "signal decay" approach: adsorbate coverage evolution upon successive laser irradiation (at constant fluence, F_0) of the same spot on the sample surface. (b) Recorded mass spectra corresponding to two distinct desorption laser pulses (left – 1st pulse, right – 13th pulse). (c) Signal (pyrene) recorded by the mass spectrometer for the first 15 laser pulses successively applied on the same spot of a pyrene / activated carbon sample. (d) Schematic representation of the "fluence curve" approach – different zones of the sample irradiated with single laser pulses of various fluences. (e) Recorded "fluence curve".*

by the ionization laser). For nanoporous samples (as those synthesized using activated carbon as adsorbent), one can raise the question of detecting molecules which come from underneath the "geometrical" ($z = 0$) surface of the sample. In fact, for our experimental arrangement, the ratio between the ionization beam radius and the distance to the sample surface (Figure 4.2) implies that only desorbed molecules having a lateral velocity component close to zero will get a chance to be ionized and detected, *i.e.* this considerably reduces the probability for a molecule possibly desorbing from underneath the $z = 0$ sample surface (in the case of porous adsorbents) to be ionized. Moreover, the time delay between the desorption and ionization

© 2020 Tous droits réservés.

lilliad.univ-lille.fr

Thèse de Dumitru Duca, Université de Lille, 2020

pulses (4 ns pulse duration each) is set to 100 μs by a digital delay/pulse generator, Section 2.2.2.2. This value is optimized to match the maximum of the velocity distribution of the molecules originating from the sample surface. All the species that are potentially desorbing from the "volume" of the material and manage to reach the surface and "escape" the (porous) sample (*i.e.* without being re-adsorbed on the pore walls), will not only exhibit much lower axial velocities (with relatively higher lateral velocities), but also will leave the surface of the sample at a later time as they have to travel within the pore network first. A time delay of even a few nanoseconds or a trajectory deviating from the normal to the surface by more than 1° will make these molecules miss the ionization beam pulse. Therefore, the unique configuration of the experimental setup allows us to specifically target molecules that originate from the sample surface, and thus only surface desorption will be considered for the theoretical model.

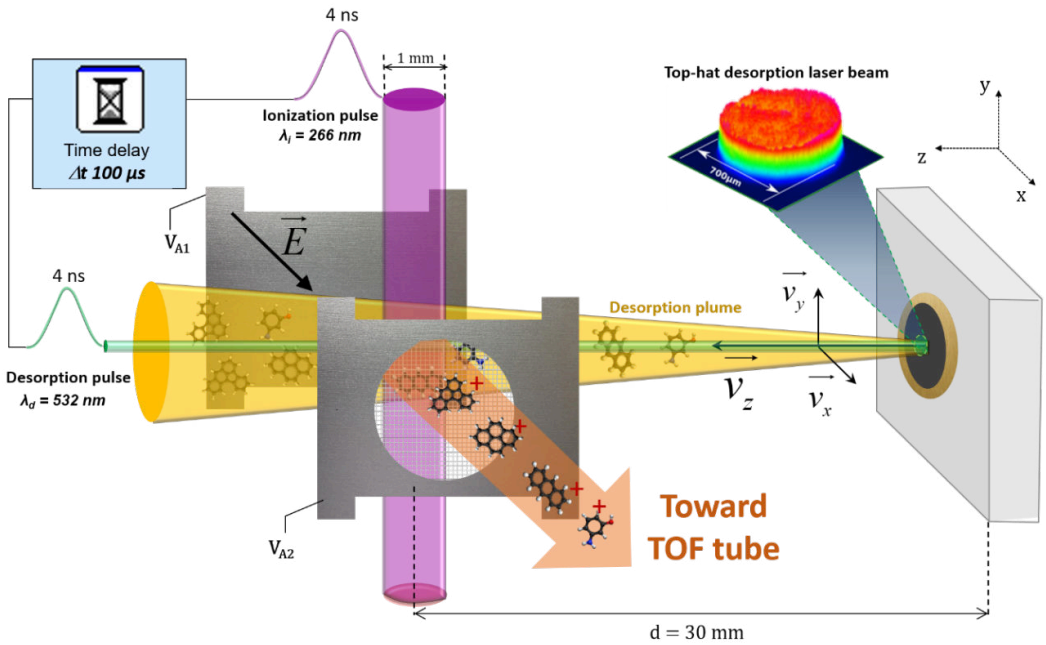

Figure 4.2 *Schematic representation of the laser desorption / laser ionization / ToF-MS experimental arrangement. The desorption laser beam (green) with a top-hat transverse beam profile forms a 700µm spot on the sample surface. The desorbed neutral molecules form a "plume" (dark yellow) which propagates from the sample surface (z axis) toward the ionization region situated in between the extraction electrodes of the Time-Of-Flight (TOF) mass spectrometer. A pulsed UV ionization laser beam (purple, y axis) intersects the desorption plume 100 µs after the desorption beam hits the surface. The obtained ions are then extracted and accelerated (x axis) toward a 1-meter long reflectron TOF mass spectrometer (see Section 2.2.2.2).*

4.3.3 Sample (surface) evolution upon irradiation

Based on the previous work performed in our laboratory [78], the desorption fluences used here were carefully adjusted to avoid damaging (*i.e.* ablating) the carbon matrix of the adsorbent. This was confirmed by the absence of atomic carbon or carbon clusters signal (representative of the ablation of the carbonaceous substrate) in the

© 2020 Tous droits réservés.

lilliad.univ-lille.fr

Thèse de Dumitru Duca, Université de Lille, 2020

mass spectra. Moreover, the "gentle" desorption of the adsorbates was confirmed by the absence of any fragmentation process in the mass spectra (i.e. only intact, unfragmented adsorbate molecules were detected).

However, when considering the high peak power provided by the desorption laser to the sample (irradiance in the range of $\mathrm{MW\,cm^{-2}}$), one can raise the question of possible structural modification of the irradiated sample after application of each laser pulse on its surface. Previous experimental [196] and simulation [78] works revealed fast transient (nanosecond range) surface temperature increase as high as 2000 K, followed by a slower (microsecond range) cooling toward its initial temperature. However, despite this high surface temperatures (reached for only nanoseconds) it was demonstrated that such a fast transient process generated with low-fluence pulses as the ones used here does not result in adsorbent nanostructure rearrangement. Previous works on amorphous carbon films [197] or black carbon nanoparticles [196] irradiated by nanosecond Nd:YAG laser pulses showed that no significant change in the sample structure was induced in the low fluence regime (typically <50 $\mathrm{mJ{\cdot}cm^{-2}}$). In the work of Abrahamson and coworkers [196], multi-wavelength pyrometry was used to measure transient surface temperatures of more than 2000°C, while no notable difference in carbon nanostructure (*i.e.* no rearrangement) was observed by transmission electron microscopy.

For the first experimental approach (*i.e.* signal decay, when a single region of the surface is irradiated with successive nanosecond laser pulses resulting in the gradual desorption of the adsorbate), it is worth noting that the changing adsorbate surface concentration upon subsequent irradiations does not affect the thermal and optical properties of the system as long as the adsorbed chemical species are transparent to the desorption pulse ($\lambda_d = 532$ nm) and as the system exhibits a very low surface coverage (both conditions are met in this work). As the L2MS technique involves the fast removal of species from the vicinity of the sample [198, 199], re-adsorption of desorbed species is negligible. Additionally, any lateral diffusion of molecules across the surface that could potentially replenish the laser spot in between two consecutive desorption laser pulses (100 ms) can be neglected. For instance, it would take minutes for a pyrene molecule to travel a distance of 1μm on a carbon surface [200]. Therefore, the physical characteristics of the sample will not change with the increasing number of desorption pulses and thus not influence the desorption process.

4.4 Theoretical framework

While discussing the fundamentals of adsorption processes it is useful to distinguish between different types of adsorption that can occur on the surface. Depending on the origin and the value of the attractive force between the adsorbent and adsorbate and whether it perturbs the electronic structure, the phenomenon of adsorption can be categorised into two types: physisorption and chemisorption [201, 202].

The term physisorption refers to the case when the adsorbate-adsorbent interaction is based on weak forces. The forces involved in physical adsorption include both Van-der-Waals forces and electrostatic interactions (*i.e.* polarization, dipole and quadrupole interactions). The Van-der-Waals forces are always present while the contribution of electrostatic forces is only significant in the case of adsorbents with an ionic structure, such as zeolites [202]. Since the interaction is weak, the

© 2020 Tous droits réservés.

lilliad.univ-lille.fr

Thèse de Dumitru Duca, Université de Lille, 2020

physisorbed atom or molecule does not disturb the structural environment near the adsorption site (*i.e.* there is no significant redistribution of electron density) [203]. A typical example of physisorption is the low-temperature adsorption of noble-gas atoms on metal surfaces.

Chemisorption corresponds to the case when a strong chemical bond is formed between the adsorbate and the substrate atoms. The nature of the bond can lie anywhere between a complete ionic (with an electronic charge transfer) and a complete covalent (with sharing electrons) bond. The strong interaction changes the chemical state of adsorbed molecules and can even cause their dissociation with formation of new species. The state of the substrate can also change. This involves modifications ranging from a simple relaxation of the interlayer spacing of the top layer to a complete rearrangement in the atomic structure of the surface layer [203]. A typical example of chemisorption is adsorption of metal atoms on metal or semiconductor surfaces at high temperatures.

Even though this classification is useful, many intermediary cases exist, where adsorbate–adsorbant systems do not fit straightforwardly into one of the two categories. The general features that help distinguish between physi- and chemisorption are presented in Table 4.1. The focus of this study is the physical adsorption and therefore several assumptions will be used henceforth:

- The adsorption is non-specific (*i.e.* there is a homogeneous coverage of adsorbate at the macroscopic scale);
- No dissociation occurs during adsorption/desorption;
- The process of adsorption is non-activated;

Table 4.1 *Typical characteristics of adsorption processes.*

Physisorption	**Chemisorption**
Low heat of adsorption (on the same order of magnitude as the energy of condensation)	High heat of adsorption (on same order of magnitude as the energy change in a chemical reaction between a solid and a fluid)
Non specific	Highly specific
Monolayer or multilayer	Monolayer only
No dissociation of adsorbed species	May involve dissociation
Only significant at relatively low temperatures (decreases with temperature)	Can occur in a wide range of temperatures (increases with temperature)
Rapid, non-activated and reversible	May be slow, activated and irreversible
No electron transfer (polarization of adsorbate can occur)	Electron transfer leading to bond formation

The desorption of adsorbed species from the surface is considered the reverse process of adsorption. Therefore, the rate of desorption can be used to determine the energetics of the process. Moreover, since only physisorbed molecules are considered here, the desorption energy obtained in this way is equal to the adsorption energy and therefore can be used to characterize the adsorption process.

© 2020 Tous droits réservés.

lilliad.univ-lille.fr

Thèse de Dumitru Duca, Université de Lille, 2020

4.4.1 Thermal desorption of physisorbed species

In a macroscopic physisorption model, the surface concentration of the adsorbate is modeled as a function of equilibrium gas pressure. For a simple physisorption system, the relation between the adsorbate surface coverage θ (in monolayers) and the gas pressure p is given by the Langmuir adsorption isotherm [203]:

$$\theta = \frac{bp}{1 + bp} \tag{4.1}$$

where b is a temperature dependent constant given by:

$$b = \frac{s_0}{\nu\sqrt{2\pi m k_B T}} \exp\left(\frac{E_{des}}{k_B T}\right) \tag{4.2}$$

with s_0 the sticking probability ($0 \leq s_0 \leq 1$), m the mass of the adsorbate molecule, ν the pre-exponential frequency factor for desorption and E_{des} the activation energy for desorption. The relationship (4.1) is only true when there is no interaction between neighbouring adsorbate molecules. This assumption, however, is not valid for all physisorption systems. In many systems, the interaction between adsorbates becomes significant at high surface coverages. Furthermore, depending on the magnitude of adsorbate-adsorbate and adsorbate-surface interactions, mono- or multi-layer adsorbate systems can be formed. However, at low adsorbate coverages ($10^{-3} - 10^{-2}$ monolayers) any effects of interaction between neighbouring adsorbed molecules can be neglected [202] and therefore equation (4.1) is valid for samples that have been studied in this work (Section 4.3).

In the kinetic approach, the desorption is described in terms of the desorption rate – the number of molecules that desorb from a unit of surface per unit of time. Assuming that all adsorbed atoms or molecules occupy identical sites, the desorption rate can be expressed by the Polanyi-Wigner equation [203]:

$$r_{des} = -\frac{d\theta}{dt} = \nu\theta^n \exp\left(-\frac{E_{des}}{k_B T}\right) \tag{4.3}$$

where n is the order of the desorption kinetics (usually $n = 1$ for physisorption). The first-order pre-exponential factor ν (measured in s^{-1}) is also called *attempt frequency* and is on the order of the atomic frequency of the crystal lattice ($\sim 10^{13} s^{-1}$) [204]. For the atom or molecule to leave the surface it needs to overcome the activation barrier for desorption – *desorption energy*. Since physisorption is a non-activated process, the activation energy of desorption is equal to the adsorption energy: $E_{ads} = E_{des}$, and therefore these two terms will be used interchangeably hereafter.

As seen in (4.3), the driving force of desorption is the surface temperature (*i.e.* the adsorbed species gain enough energy from the thermal vibrations of surface atoms to escape the adsorption well and leave the surface). Therefore, one of the most common methods of determining the energetics of the adsorbate-adsorbant interaction involves the manipulation of the sample temperature. Traditional methods are based on either monitoring the desorption process at fixed temperature values (isothermal method) or during a slow and monotonous increase in the temperature of the adsorbate-covered sample (temperature-programmed desorption) [203]. These methods are built around conventional heat sources (*e.g.* resistive heating) capable of heating the entire sample at relatively low rates. In desorption studies, atoms

© 2020 Tous droits réservés.

lilliad.univ-lille.fr

Thèse de Dumitru Duca, Université de Lille, 2020

and molecules that originate from the surface of the sample are the most important since they participate in the surface driven chemical reactions and therefore can be used to interpret the macroscopic behavior of the studied system. In this case, heating of the whole sample is not required and a heating source that targets only the surface can be used. Such localized sample heating can be achieved with a pulsed laser. Moreover, a much higher heating rate (up to $10^{11} K/s$ with a nanosecond pulsed laser) can be obtained, unattainable with conventional heating sources. A high heating rate is essential for the desorption of large molecules without their fragmentation [205]. Laser-based heating is used here to induce the desorption of species from the sample. In the following sections the process of laser-induced heating will be described and two different models of laser-induced thermal desorption will be derived. The described models will be subsequently used to determine the adsorption energy of several chemical compounds from experimental data.

4.4.1.1 "Effective temperature" desorption model

As an initial step, a steady-state approach was used to simplify the real physical process. Within this approximation, an "effective temperature" model is utilized to calculate the desorption rate of the adsorbates. While this model constitutes only a crude approximation of the physical process at play, its simplicity makes it quite advantageous for situations where computational speed is important. In addition, as this model was used in the past to describe single desorption events [195], its adaptation to our experimental conditions provides a proper basis for comparison.

In this simplified model, the number of desorbed molecules N for short-pulse (nanoseconds and below) laser excitations can be described by [195]:

$$N \approx A \cdot \exp\left(\frac{-E_{ads}}{k_B\,(T_0 + BF)}\right) \tag{4.4}$$

where E_{ads} is the adsorption energy, B is a factor that describes the conversion of deposited energy into surface temperature increase, T_0 the initial temperature, F the desorption laser fluence at the surface, and k_B the Boltzmann constant. The term $(T_0 + BF)$ can be interpreted as an "effective" steady-state temperature reached by the surface upon laser irradiation. The factor A can be expressed as $A = p\,Q$, where p reflects the probability of a molecule to be desorbed. Q, the surface adsorbate concentration in the irradiated spot, changes after each successive desorption laser pulse.

The energy deposited into the sample unit volume is determined by the incident laser fluence, and accounts for the reflection R and the optical absorption coefficient α of the sample. The fluence used here is relatively low, therefore nonlinear absorption can be neglected. Taking all into account, the B parameter can be calculated as follows [195]:

$$B = (1 - R)\frac{\alpha(\lambda_0)}{\rho c} \tag{4.5}$$

where c is the specific heat capacity of the sample, λ_0 is the desorption laser wavelength and ρ is the sample density. The value of the B parameter can considerably change depending on the actual sample characteristics; however, a good approximation can be obtained with values reported in the literature. B can also be determined

© 2020 Tous droits réservés.

lilliad.univ-lille.fr

Thèse de Dumitru Duca, Université de Lille, 2020

Table 4.2 *B parameters calculated from (Equation 4.5) for activated carbon particles and graphite, along with physical parameters sourced from the literature (references in brackets) and used in the calculation.*

Parameter	**Carbonaceous surface**	
	Activated carbon particles	**Graphite**
R	0.2 [206]	0.1 [207]
α, $10^7 m^{-1}$	1.0951 [78, 208]	3.4385 [207]
ρ, $10^3 kg\, m^{-3}$	0.4 [78]	1.9 [208]
c, $J\, K^{-1}\, kg^{-1}$	840 [78]	970 [208, 209]
B, $J^{-1}\, K\, m^2$	26.0	16.2

using the measured physical parameters of the sample (*e.g.* α, ρ) prior to the adsorption energy determination. Such measurements, depending on the sample, are not always possible since characterizing several micrograms of material can be challenging and adds extra preparation steps that can potentially damage and/or contaminate the sample (often being very expensive to obtain and/or unique). Therefore, the developed model should be able to determine the adsorption energy based on only an "initial guess" for the B parameter obtained with values sourced from the literature. The B parameter values calculated for two different adsorbent materials used in this work (nano-porous soot and graphite surfaces, see Section 4.3), along with the physical constants used in their calculation, are presented in Table 4.2. The values for the B parameter calculated in such a way can be only seen as estimates, sufficiently close to the real B value and only intended to be used as an "initial guess" by the fitting algorithm.

Because the surface concentration of adsorbed species decreases after each desorption pulse, the pre-exponential factor A in (4.4) decreases with each subsequent laser pulse. The first laser pulse will yield N_1 desorbed molecules:

$$N_1 = p \cdot Q_0 \cdot \exp\left(-\frac{E_{ads}}{k_B(T_0 + BF)}\right) \tag{4.6}$$

where Q_0 is the initial number of adsorbed molecules in the irradiated spot. The number of molecules that remain on the irradiated surface after the first desorption pulse is:

$$Q_1 = Q_0 - N_1 = Q_0\left(1 - p \cdot \exp\left(-\frac{E_{ads}}{k_B(T_0 + BF)}\right)\right) \tag{4.7}$$

The second laser pulse will result in the desorption of N_2 molecules from the surface:

$$N_2 = p \cdot Q_0\left(1 - p \cdot \exp\left(-\frac{E_{ads}}{k_B(T_0 + BF)}\right)\right)\exp\left(-\frac{E_{ads}}{k_B(T_0 + BF)}\right) \tag{4.8}$$

Assuming that E_{ads} does not change with the surface concentration, N_j molecules will be desorbed on the jth desorption pulse:

© 2020 Tous droits réservés.

lilliad.univ-lille.fr

Thèse de Dumitru Duca, Université de Lille, 2020

$$N_j = p \cdot Q_0 \left(1 - p \cdot \exp\left(-\frac{E_{ads}}{k_B(T_0 + BF)}\right)\right)^{j-1} \cdot \exp\left(-\frac{E_{ads}}{k_B(T_0 + BF)}\right) \tag{4.9}$$

The total number of molecules desorbed in j laser shots is:

$$N(j) = \sum_{1}^{j} \left(p \cdot Q_0 \left(1 - p \cdot \exp\left(-\frac{E_{ads}}{k_B(T_0 + BF)}\right)\right)^{j-1} \cdot \exp\left(-\frac{E_{ads}}{k_B(T_0 + BF)}\right)\right) \tag{4.10}$$

In order to correlate the number of desorbed molecules with the signal recorded at the detector, another factor is introduced:

$$S_j = m \cdot N_j = m \cdot p \cdot Q_0 \left(1 - p \cdot \exp\left(-\frac{E_{ads}}{k_B(T_0 + BF)}\right)\right)^{j-1} \cdot \exp\left(-\frac{E_{ads}}{k_B(T_0 + BF)}\right) \tag{4.11}$$

where S_j is the signal recorded at the detector and m is the proportionality factor.

The sample will reach different temperatures for different desorption fluences which will effectively change the desorption rate. Therefore, the adsorption energy can also be retrieved from the "fluence curve" – variation of the recorded signal with the desorption laser fluence. In this case, the initial surface concentration of the adsorbate, Q_0 should be always the same, *i.e.* the desorption laser pulse must always irradiate a pristine surface (previously not irradiated by the laser). The "fluence curve" can thus be expressed as follows:

$$S(F) = m \cdot p \cdot Q_0 \cdot exp\left(-\frac{E_{ads}}{k_B(T_0 + BF)}\right) \tag{4.12}$$

Fitting the signal decay and fluence curves with equations (4.11)) and (4.12), respectively, can be challenging as they contain two highly correlated parameters. Since the "effective" temperature reached by the surface upon laser irradiation is significantly higher than its initial temperature (*i.e.* $BF >> T_0$), the adsorption energy E_{ads} and the "nuisance parameter" [170, 171] B are highly correlated. This renders the use of the regular least-squares fitting technique very difficult. Therefore, Bayesian statistics methods were used instead to retrieve the value for the adsorption energy (see Section 4.4.2).

4.4.1.2 Transient laser-induced heating

The model described in the previous section, while greatly simplifying the calculations, approximates the desorption process to a steady-state phenomenon. However, to better represent the physical reality, the fast variation of the surface temperature during desorption must be taken into account. This sections provides details on the process of determining the temporal and spatial temperature profiles of the sample, required to better model the laser-induced thermal desorption process.

© 2020 Tous droits réservés.

lilliad.univ-lille.fr

Thèse de Dumitru Duca, Université de Lille, 2020

When a pulsed laser beam hits a sample surface, a part of its energy is passed on to the sample. The physical properties of the sample material determine the portion of laser energy that is transferred to the material. This energy transfer induces a temperature jump that, depending on its magnitude, may trigger the desorption of adsorbates that are present on the surface, alter the surface (nanostructure changes), or even ablate micro-volumes of sample. The latter only occurs at higher laser fluences that were not used here and therefore are out of the scope of this work.

A variety of studies addressed the fast heating of solid samples exposed to lasers, describing the processes occurring at different wavelengths, laser irradiances, pulse lengths and on various target materials [78, 194, 210–214]. The common approach used to describe laser-solid interactions at a macroscopic scale is by using the thermal heat conduction equation. For low-fluence nanosecond laser pulses, the energy passed on to the sample does not lead to its melting nor its evaporation, therefore no phase transition terms are needed in the equations [212]. Most of the studies focus on the temperature variation in the sample volume (*i.e.* along the z depth axis) without considering the radial temperature variation on the surface. Moreover, the laser pulse is often considered as a surface heat source ($z = 0$), which does not take into account its propagation into the sample volume as described by the Beer-Lambert law [78]. In this study, a model for laser-induced heating similar to the one presented by Faccinetto et al. [78] was adapted and extended to all three dimensions of the sample. To be able to calculate the temperature variation upon laser irradiation, the analyzed sample must be considered as a medium characterized by continuous specific heat capacity c_p, thermal conductivity k and density ρ. This consideration is justified if the dimensions of the affected zone is much larger than the scale of surface heterogeneities which is the case for this study (see Section 4.3). In case of laser desorption with a low enough fluence, which will not trigger a phase explosion, the surface temperature will rise and, ultimately, decrease due to the thermal relaxation. Heat propagation in all three dimensions was calculated with the following equation:

$$\rho(T) \cdot c_p(T) \frac{\partial T(x,y,z,t)}{\partial t} = k(T) \left(\frac{\partial^2 T(x,y,z,t)}{\partial x^2} + \frac{\partial^2 T(x,y,z,t)}{\partial y^2} + \right. \\ \left. + \frac{\partial^2 T(x,y,z,t)}{\partial z^2} \right) + q_H(x,y,z,t) \tag{4.13}$$

where T is the local surface temperature of the sample as a function of the time t and position on the surface (x, y, z). ρ, c_p and k are the density, specific heat capacity and thermal conductivity of the sample, all being functions of the temperature. The term $q_H(x, y, z, t)$ describes the heat source which, in this case, is the desorption laser pulse. To match the characteristics of the laser pulse used in the experiments (Section 2.2.2.2), the heat source is represented as a flat space profile (equivalent to a top-hat laser profile) in the calculations. In the temporal domain, the laser beam is represented as a Gaussian pulse. The intensity of the laser pulse is absorbed by the sample according to the Beer-Lambert law:

$$q_H(x,y,z,t) = \alpha\, I_0\, (1 - R) \cdot f(x,y) \cdot g(t) \cdot e^{-\alpha z}$$

© 2020 Tous droits réservés.

lilliad.univ-lille.fr

Thèse de Dumitru Duca, Université de Lille, 2020

$$f(x,y) = \begin{cases} 1, & \sqrt{x^2+y^2} \leq r_{des} \\ 0, & \text{otherwise} \end{cases} \tag{4.14}$$

$$g(t) = \frac{1}{\sigma\sqrt{2\pi}} \cdot \exp\left[-\frac{1}{2}\left(\frac{t-t_0}{\sigma}\right)^2\right], \text{ where } \sigma = \frac{\tau_{des}}{2\sqrt{2\ln 2}}$$

where R is the sample surface reflectivity, α is the adsorption coefficient at the desorption wavelength (532 nm), I_0 is the pulse peak irradiance. The $f(x,y)$ and $g(t)$ functions define the space and time profiles of the pulsed laser beam of radius r_{des} (top-hat) and duration τ_{des} (full width at half maximum, Gaussian profile). Previous studies conducted by multi-wavelength pyrometry [196] showed no change in the structural or optical properties of carbonaceous surfaces (similar to the ones used here, Section 4.3) for a laser-induced transient temperature increase of more than 2000°C, which is above the maximum temperatures reached here. Accordingly, the R and α parameters were kept constant in the calculations. This approach is also commonly adopted in the laser-induced incandescence (LII) community, where even higher temperatures (4000 K) are reached [215]. The boundary conditions required to solve Equation (4.13) are:

$$\begin{cases} T(x \to \infty, y \to \infty, z \to \infty, t) = T_i \\ T(x, y, x, t = 0) = T_i \end{cases} \tag{4.15}$$

where T_i is the initial temperature of the sample. The thermal conductivity of graphite samples can be found in the literature [208]. For porous materials, such as activated carbon (ac), the thermal conductivity k_{ac} strongly depends on the porosity as the efficiency of phonon propagation is related to the number of contact points between the nanoparticles forming the sample. In this case, the thermal conductivity of the ac layer can be expressed as [216]:

$$k_{ac}(T) = k_{graph}(T)\left[(1-\xi)^{3/2} + \xi^{1/4}\frac{k_{air}(T)}{k_{graph}(T)}\right] \tag{4.16}$$

where k_{ac} is the calculated thermal conductivity of the activated carbon layer, k_{graph} is the thermal conductivity of bulk graphite [208] and k_{air} is the conductivity of the air filling the pores. The layer porosity ξ is given by:

$$\xi = 1 - \frac{\rho_{ac}}{\rho_{graph}} \tag{4.17}$$

where ρ_{ac} and ρ_{graph} are the densities of activated carbon and graphite, respectively.

The parameters required to calculate the temperature profile of the studied sample were either taken from the literature or calculated from the values for graphite while accounting for the porosity of the sample, Equation (4.16) [78, 208, 209, 216–218]. The temperature variations of all parameters required for solving Equation (4.13) are presented in Figure 4.3. Physical parameters for the graphite and HOPG samples used in this work (see Section 4.3) are identical which allows the use of the same physical characteristics for these two sets of samples.

Equation (4.13) was solved using the COMSOL Multiphysics simulation platform with finite element methods. The temporal and spatial temperature evolutions calculated for activated carbon and graphite (Figure 4.4) show a fast increase with

© 2020 Tous droits réservés.

lilliad.univ-lille.fr

Thèse de Dumitru Duca, Université de Lille, 2020

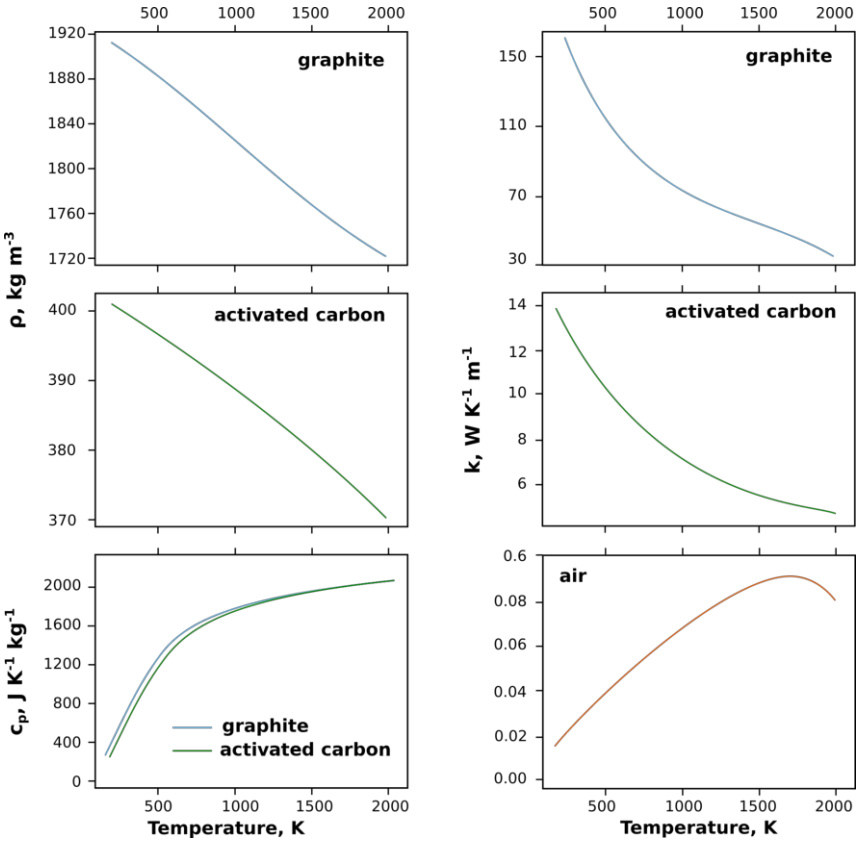

Figure 4.3 *Temperature variation of physical parameters used for temperature profile calculations sourced from the literature: the density of graphite [208] and activated carbon (ac) [78], specific heat capacity of graphite [208, 211] and ac [217], and thermal conductivity of graphite [208] and air [176]. The thermal conductivity of activated carbon was calculated using Equation (4.16).*

a maximum value reached at t=5.5 ns in the center of the irradiated surface, followed by a slower cooling toward the initial sample temperature (on a microsecond timescale). The heat-affected sample depth is in the range of 100 μm (Figure 4.4b), which is significantly lower than the thickness of the samples used in this study (Section 2.1.2). Even though the obtained depth and temporal profiles follow a similar trend to the ones previously reported [194, 211, 212], a direct, quantitative comparison is not possible, as the temperature profiles reported in the literature were computed for different substrates and desorption laser characteristics (*e.g.* wavelength, pulse duration, fluence).

Once the temperature profile is known, it is possible to calculate the time dependence of the desorption rate and the number of molecules desorbed from each unit of surface. Moreover, the total number of molecules desorbed after a single desorption laser pulse can be also determined.

4.4.1.3 Transient temperature desorption model

The temperature profile calculated in the previous section can now be used to model the desorption of species present on the sample surface. Since chemical species examined here (see Section 4.3) are transparent to the desorption pulse ($\lambda_d = 532\,nm$) and also have a very low surface coverage, their thermal and optical properties can

© 2020 Tous droits réservés.

lilliad.univ-lille.fr

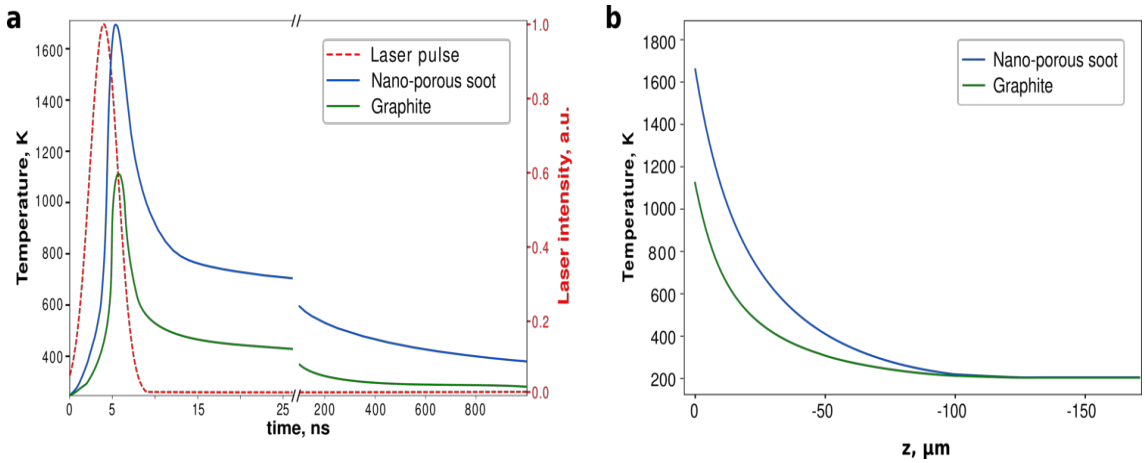

Figure 4.4 *Temperature profiles calculated for activated carbon (blue lines) and graphite (green lines) obtained for F_{des} = 32 mJ cm^{-2}: (a) temporal variation of the temperature in the center of the irradiated spot T(x=0, y=0, z=0, t), (b) temperature depth profile in the center of the sample at t=5.5 ns, T(x=0, y=0, z, t=5.5 ns). The temporal profile of the desorption laser is plotted for comparison (red dashed line).*

be neglected [78]. Therefore, the temperature variation at the surface will be the same throughout a multitude of desorption pulses, regardless of the change in the adsorbate surface coverage. Although the temperature variation model returns 3D and temporal variations of the temperature, only data at z=0 (*i.e.* surface temperature profiles) are needed here, as the experimental setup used in this work probes only molecules desorbing from the sample surface (z=0, see Section 4.3.2).

If the sample is irradiated with a low fluence laser pulse, it will promote the desorption of only a portion of adsorbed species. The number of molecules desorbing from the surface of the sample after the first desorption laser pulse can be expressed as follows:

$$N_1 = \iint_{-\infty}^{+\infty} Q_0(x,y) \cdot \left(1 - \exp\left(-\nu \int_0^{\frac{1}{f}} \exp\left(-\frac{E_{ads}}{k_B T(x,y,z=0,t)}\right) dt\right)\right) dxdy \tag{4.18}$$

where Q_0 is the initial adsorbate surface concentration and f is the repetition rate of the desorption laser. If the same spot on the sample surface continues to be irradiated with equivalent desorption pulses, the number of molecules left on the surface will progressively decrease after each subsequent laser pulse. Assuming that the adsorption energy, E_{ads}, does not change with the surface concentration, N_j, the total number of molecules desorbed on the jth desorption pulse can be determined with the following relationship:

$$N_j = \iint_{-\infty}^{+\infty} Q_{j-1}(x,y) \cdot \left(1 - \exp\left(-\nu \int_0^{\frac{1}{f}} \exp\left(-\frac{E_{ads}}{k_B T(x,y,z=0,t)}\right) dt\right)\right) dxdy \tag{4.19}$$

$Q_{j-1}(x,y)$ represents the analyte surface concentration after the $(j-1)^{th}$ desorption pulse (*i.e.* before the jth desorption pulse). Figure 4.5 presents simulation examples for the temporal evolution of the desorption rate of pyrene adsorbed on activated

© 2020 Tous droits réservés.

lilliad.univ-lille.fr

carbon and graphite (initial coverage $\theta_0 = 10^{-3}$ ML) and for successive laser pulses applied on the same spot.

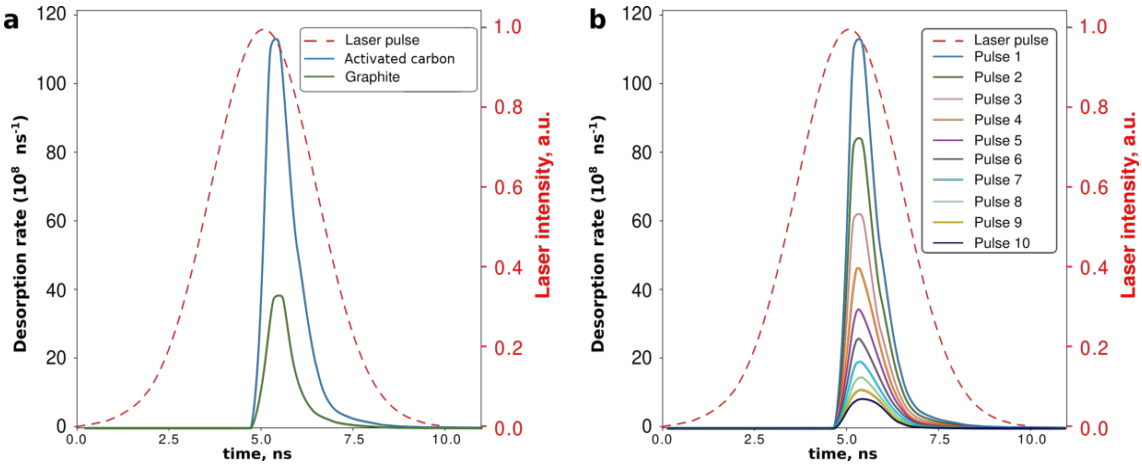

Figure 4.5 *(a) Comparison between temporal evolution of the desorption rate for pyrene molecules desorbing from activated carbon and graphite (with an initial surface coverage of 10^{-3} monolayers) induced by adsorption of an identical laser pulse. (b) Temporal evolution of the desorption rate of pyrene from activated carbon for successive laser pulses. The temporal laser profile is shown for comparison (red dashed line).*

The assumption of a non-varying adsorption energy is only correct for very low coverages (sub-monolayer), when the interaction between adsorbed molecules is minimal (the case studied here, see Section 4.3). A low coverage also reduces the possibility of adsorbates forming islands of stacked molecules [219] and thus ensures that the only interaction probed is between adsorbates and the adsorbent surface. Moreover, under these experimental conditions any lateral diffusion of molecules across the surface that could potentially replenish the laser spot between desorption laser pulses can also be neglected [200].

A two-step laser mass spectrometer is used to obtain experimental data necessary for a proof of concept study (Section 4.3), therefore the model must take into consideration all the losses that can occur during experimental data collection. To account for the ionization efficiency, transfer function of the mass spectrometer as well as for the efficiency of the detector, a proportionality factor m is introduced.

$$S_j = m \cdot N_j = m \cdot \iint_{-\infty}^{+\infty} Q_{j-1}(x,y) \cdot \left(1 - \exp\left(-\nu \cdot \cdot \int_0^{\frac{1}{f}} \exp\left(-\frac{E_{ads}}{k_B T(x,y,z=0,t)}\right) dt\right)\right) dxdy \tag{4.20}$$

where S_j is the signal recorded by the detector. The only unknowns in this equation are the pre-exponential factor ν, the adsorption energy E_{ads}, and the proportionality factor m. Equation (4.20) models the variation of the signal recorded by the mass spectrometer upon irradiation of the sample with a number of consecutive laser pulses (*i.e.* signal decay curve). The adsorption energy of an analyte can be retrieved by fitting experimental data with Equation (4.20). The fitting algorithm, described in Section 4.4.2, requires an "initial guess" – a starting point relatively close to

© 2020 Tous droits réservés.

lilliad.univ-lille.fr

Thèse de Dumitru Duca, Université de Lille, 2020

the actual values. The initial values for the adsorption energy and pre-exponential parameter were taken in accordance with literature data (*e.g.* E_{ads} = 0.98 eV [220, 221] and $\nu = 10^{12}$ s^{-1} [204, 219, 222] for pyrene).

4.4.2 Data fitting process

Fitting the experimental data (*i.e.* signal decay and fluence curves) with the developed models for laser-induced thermal desorption with the intention of retrieving the adsorption energy can be challenging as some of the unknown parameters are highly correlated. Fitting experimental data with functions that contain highly correlated parameters and/or multiple exponential functions using a regular least-squares fitting technique can be difficult and, more importantly, very unstable, especially when dealing with a small number of potentially "noisy" data points. In such cases, the outcome of the fit highly depends on the provided initial guess, making the result unreliable. To overcome this issue, the *search method* [223] can be used – an implementation of the least-squares fitting algorithm believed to be more stable when it comes to highly correlated models. This method is fitting the experimental data multiple times, each time with different initial values (in user-defined ranges), each resulting in a unique set of values for the fitted parameters. The most probable value for the fitted parameters (*e.g.* E_{ads}) is then taken as the "true" value along with the standard deviation of the distribution obtained from multiple fits. Since a large number of initial values combinations is tested, this method is characterized by a rather slow rate of convergence, especially for functions with a large number of parameters ($n > 2$). Moreover, the obtained distribution for fitted parameters is determined by the choice of initial values (*i.e.* widths of the user-defined ranges), which means that the returned parameter values can potentially be biased and that another fitting technique should be used instead.

4.4.2.1 Markov chains Monte Carlo fitting

Statistical Bayesian inference framework [224–226] provides powerful tools for estimating complex models where the maximum likelihood-based estimation methods fail. A commonly used method for numerical approximation of the inference that converges at a much faster rate is the Markov chains Monte Carlo (MCMC). The MCMC method is designed to estimate the joint posterior distribution of a parameter of interest by random sampling in the probability space. Many problems described by models containing a large number of free parameters, making them expensive to compute with regular methods (*e.g.* problems in cosmology and astrophysics that deal with low signal-to-noise measurements [224–226]), have benefited from MCMC. One of the most important benefits of Bayesian data analysis is the ability to minimize the impact of nuisance parameters [226] – parameters that are required to model the studied process but otherwise are not the main objective of the fit. Most uses of the MCMC are based on the Metropolis-Hastings (M-H) method [224–226] or its derivatives and consist of three main parts:

- Monte Carlo simulations generating random numbers to model complex systems.
- Markov chains - sequences of events that are probabilistically related to one

© 2020 Tous droits réservés.

lilliad.univ-lille.fr

another. Each event comes from a set of outcomes and each outcome determines the next one, in accordance with a fixed set of probabilities.

- The acceptance-rejection sampling is an iterative algorithm that generates parameter values from their unknown theoretical posterior distribution.

MCMC allows to generate a data subset covering many possible outcomes of a given system in order to obtain an estimate of the theoretical posterior distribution that can be used to extract statistical measures as mean, median or standard deviation. The simulation process is based on a Markov behavior of the iterative algorithm [225, 226]. An example of a model that can benefit from the use of the MCMC algorithm is the laser induced thermal desorption, Section 4.4.1.1. In case of the steady-state approximation, Equation 4.11 contains two exponential functions that make the fitting of the experimental data with a regular least-squares technique [224] very difficult. Additionally, the parameter of interest E_{ads} is highly correlated with the nuisance parameter B, making the retrieval of the former even more complicated. The MCMC method can be used to fit the experimental data and retrieve the E_{ads} value with a significantly narrower credibility interval. The performance of the M-H sampler can be very sensitive to the initial choice of parameters. The result of the MCMC fit will be more reliable for longer chains. For this reason, the first values of the Markov chain are usually dropped. Thus, to determine optimal parameters in a data-driven way, a lengthy "burn-in" period must be used. The burn-in allows to start the MCMC procedure with parameters chosen for convenience that might be located in low probability regions, Figure 4.6a. Once the chain has entered the high-probability region, the states of the Markov chain become more representative of the correct distribution (the convergence is achieved). All the values after the convergence are then used to retrieve the distributions and mode values of all parameters, Figure 4.6.

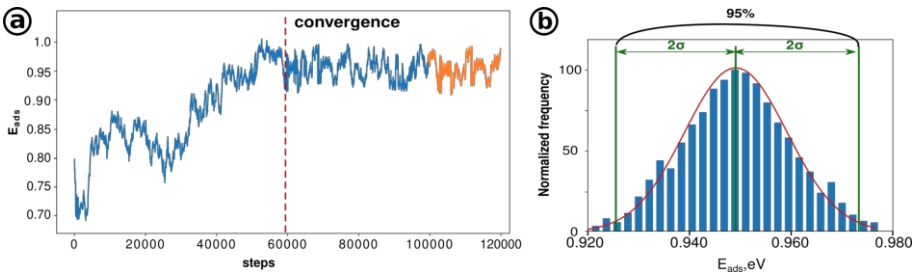

Figure 4.6 *(a) Example of a Markov chain obtained during fitting of experimental data with equation (4.11). The convergence of the fit is depicted with a red dashed line. The last portion of the chain (orange line) is used to determine the posterior distribution of the fitted parameter (b). The distribution is then used to identify the most probable value and variance of the determined parameter.*

4.4.2.2 Retrieving the average values and error bars of fitted parameters

The posterior distribution associated with the fit of the models on a given set of data only reflects the "mathematical" fitting error and does not fully reflect experimental measurement sources of variability such as stability of the desorption and ionization lasers. The latter can be determined by considering several equivalent measurements

© 2020 Tous droits réservés.

lilliad.univ-lille.fr

Thèse de Dumitru Duca, Université de Lille, 2020

performed in distinct zones of the same sample (with the same adsorbate coverage). Therefore, for each experimental set-point (*i.e.* same (time-averaged) desorption and ionization laser fluences) four measurements were performed in distinct zones of the sample (A, B, C, and D). The analyzed regions do not overlap and therefore all measurements can be considered as being independent. For the first experimental approach (*i.e.* signal decay), four signal decays (one per each zone) were recorded, while for the second one (*i.e.* fluence curve), four data points were recorded for each desorption fluence value, see Section 4.3. The recorded experimental data points, obtained with multiple values for the desorption fluence, were then combined to generate 10 distinct fluence curves. Signal decays and fluence curves obtained in this way were then fitted with the proposed mathematical model.

The individual fits (*i.e.* of individual signal decays or fluence curves) provide the estimated values and associated with them variances for all the parameters of interest (*e.g.* E_{ads}, B) throughout the posterior distributions (*i.e.* credibility intervals, Figure 4.6b). Figure 4.7 illustrates the individual fits of four signal decays recorded in the same experimental conditions (the solid lines represent the "most probable fit" (mode) of the Bayesian posterior distribution for each dataset). The variation of the recorded signal displayed in Figure 4.7 is determined by measurement variability (*e.g.* fluctuations in the desorption/ionization laser fluence). In order to account for the measurement variability and determine "physically-significant" average values and error bars associated with the fitted parameters (called "estimators" henceforth), the "internal"' (*i.e.* inside one individual dataset) and "external" (*i.e.* between different datasets, such as A, B, C, D zones in the signal decay approach) variances must be combined. A methodology proposed by Buckland et al. [227] and Slud et al. [228] was used to combine the estimators – "estimator aggregation" methodology. For a given parameter $\hat{\beta}$, let $\hat{\beta}_i$ be the estimators obtained from data collected in the zone i, $i \in A, B, C, D$. Then, the best linear-combination estimator for the $\hat{\beta}$ parameter with respect to the mean squared error will be:

$$\hat{\beta} = \sum_{i=1}^{n} \omega_i \hat{\beta}_i \tag{4.21}$$

where $\omega_i = \frac{Var^{-1}(\hat{\beta}_i)}{\sum_j Var^{-1}(\hat{\beta}_j)}$ is the weight associated with each estimator, retrieved from fitting individual datasets (either signal decays or fluence curves). Assuming the independence of data recorded in different zones of the sample, the standard deviation of the $\hat{\beta}$ parameter is given by:

$$\sigma(\hat{\beta}) = \sqrt{Var(\hat{\beta})} = \sqrt{\sum_i \omega_i^2 (Var(\hat{\beta}_i) + (\hat{\beta}_i - \hat{\beta})^2)} \tag{4.22}$$

The first term in Equation (4.22) represents the "internal" variance of each dataset, while the second term represents the "external" variance (*i.e.* between datasets).

The average values and error bars were calculated for the parameters of interest with the described method and reported in Section 4.5 in the form $\hat{\beta} \pm \sigma(\hat{\beta})$. The validity of the method can be verified with the "average" fitting curve (*i.e.* average for all datasets) calculated with the average values for the required parameters. An example of such a curve obtained with the "effective temperature" model is presented in Figure 4.7 (dashed line).

© 2020 Tous droits réservés.

lilliad.univ-lille.fr

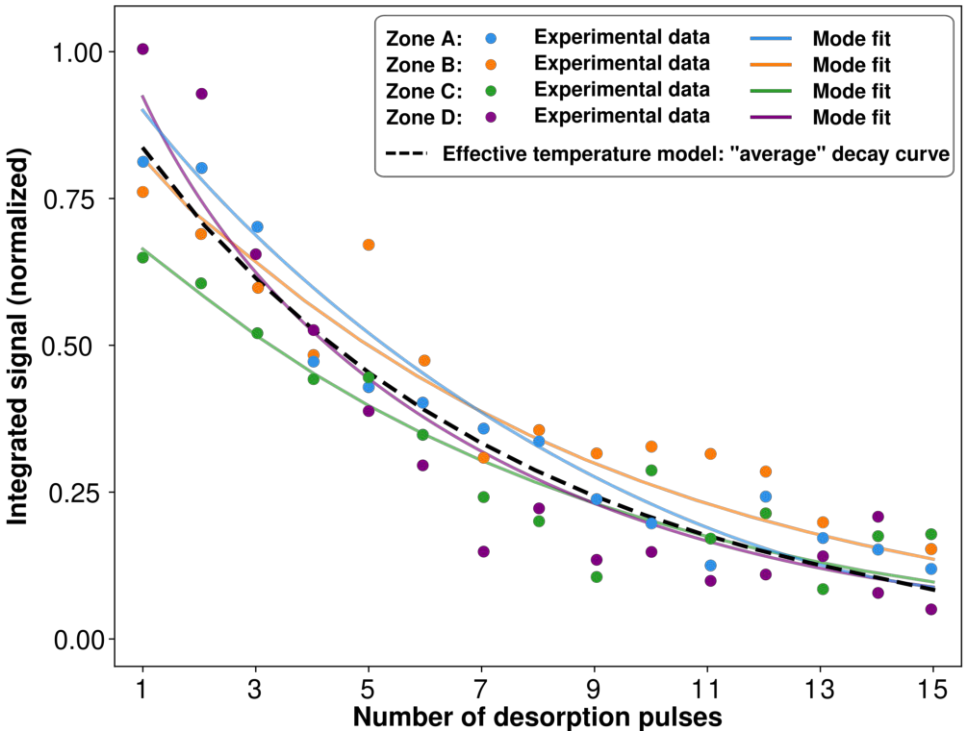

Figure 4.7 *Symbols: pyrene molecule signal recorded in the same experimental conditions (F_{des} = 32 mJ cm^{-2}) from four different zones (A, B, C, D) of the same pyrene / activated carbon sample (homogeneous coverage). Solid lines: most probable (mode) fits returned by the Bayesian posterior distribution for each individual dataset. Dashed line: effective temperature model decay curve generated with average parameter values.*

4.5 Results on various systems

In order to validate the proposed method of adsorption energy determination (Section 4.4), adsorbant-adsorbate systems featuring different energetics must be studied. In this manner, the method is tested for a wide range of adsorption energies thus ensuring its validity and reliability. Different adsorption energies can be achieved by either using different chemical species that are adsorbed on the same substrate or by studying the same compound adsorbed on different surfaces. In this section, the results of adsorption energy measurements performed on a set of different samples (Table 2.4) is reported. The measurements were performed with surrogate soot samples containing organic species, such as PAHs, designed to mimic combustion-generated soot particles, as well as lead (Pb) – heavy metal often removed from waste waters with porous carbonaceous materials [170, 171]. Further, the performance of the method is tested with more ordered surfaces such as graphite and HOPG. This not only illustrates the impact of the adsorbent structure on the energetics of the system but also showcases the performance and versatility of the described method. Finally, the extension of the method toward the analysis of field collected samples is discussed. Two different experimental approaches have been used to obtain the data necessary for adsorption energy measurements, namely “signal decay” and “fluence curve” that were described in Section 4.3.

© 2020 Tous droits réservés.

lilliad.univ-lille.fr

4.5.1 Adsorption energy measurements on surrogate soot systems

4.5.1.1 Pyrene/activated carbon system

The described method was first tested with a surrogate soot system composed of pyrene adsorbed on activated carbon particles (Table 2.4), forming a system structurally resembling the real-world soot particles [21, 101, 153] but having a predefined chemical composition ($2 \cdot 10^{-3}$ monolayers of pyrene). For the "signal decay" approach, four zones on the same surface (of homogeneous adsorbate concentration) were probed (at constant fluence, 32 $mJ\,cm^{-2}$) in order to test the experimental reproducibility. The signals recorded and averaged over the 4 zones along with the associated experimental error bars (2σ) are displayed in Figure 4.8a. The averaged experimental data were then fitted with both the "effective" and transient temperature models to determine the adsorption energy of pyrene. The correlations between the fitted parameters (*e.g.* between E_{ads} and B, Section 4.4) prevented the use of traditional least-squares fitting algorithms and a Bayesian fitting approach was required for a reliable and repeatable fitting, in particular the Markov chain Monte Carlo algorithm (Section 4.4.2). From the obtained fit it was then possible to retrieve the most probable value of the adsorption energy along with its posterior distribution (or credibility interval) [224, 226], while also minimizing the impact of nuisance parameters [225].

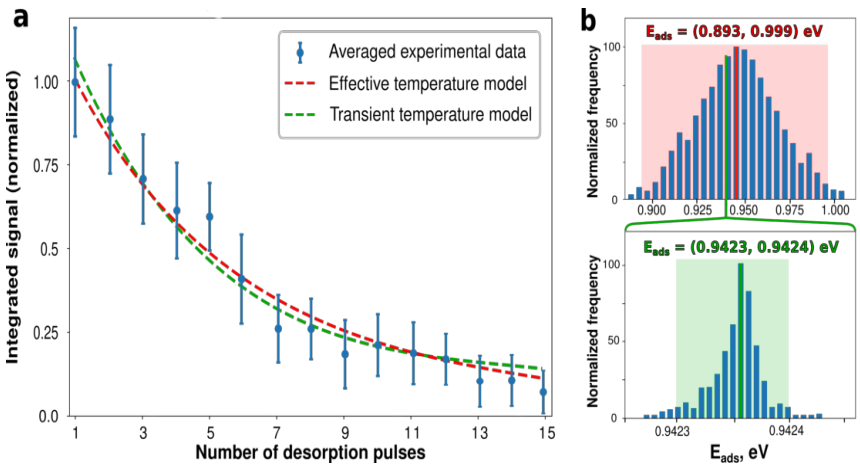

Figure 4.8 *(a) Experimental signal decay recorded for pyrene desorbing from activated carbon (F_{des} = 32 $mJ\,cm^{-2}$, four zone average data points) along with the fits with the "effective temperature" (red dashed line) and transient (green dashed line) models. The fits correspond to the mode of the Bayesian posterior distribution of E_{ads}. (b) Bayesian posterior distribution retrieved with the "effective temperature" (top) and transient temperature model (bottom). Shaded areas represent the 95% credibility intervals of E_{ads}.*

Figure 4.8b displays the normalized posterior distributions of the fitted adsorption energy E_{ads}, along with its 95% credibility intervals (shaded areas). The distribution returned by the transient model fit is much narrower (two orders of magnitude narrower) compared to the one obtained with the "effective temperature" model. This difference is determined by the lower correlation between the fitted parameters present in the transient temperature model. The modes of the posterior distributions displayed in Figure 4.8b for E_{ads} are associated with the most proba-

© 2020 Tous droits réservés.

lilliad.univ-lille.fr

Thèse de Dumitru Duca, Université de Lille, 2020

ble fits within the batch performed for each model. These fits are represented by the red ("effective temperature" model) and green (transient temperature model) dashed lines in Figure 4.8a. It should be noted that even though the two curves fit the experimental data equally well, they represent two fundamentally different concepts. The first one results from an approximation that the desorption process occurs at a constant ("effective") surface temperature, while the second one better represents the physical reality by taking into account the fast variation of the surface temperature during the desorption process. The credibility intervals displayed in Figure 4.8b are a measure of the "goodness" of the mathematical fit applied to the average experimental data, and therefore do not define on its own the experimental dispersion (induced by the detection scheme) of individual datasets recorded from different zones on the same homogeneous sample (see Section 4.3). To derive the experimentally-related error bars of the calculated adsorption energies, the data obtained in different zones of the sample are individually fitted and then combined with the help of the "aggregation of estimators" technique (Section 4.4.2). The derived average adsorption energies and their associated error bars are listed in Table 4.3 for both models.

Table 4.3 *Main parameters derived with the "signal decay" experimental approach with the steady-state and transient models. Mean values and error bars are computed using the procedure described in Section 4.4.2.*

Monitored compound	**Adsorbate/Adsorbent system**	**Steady-state model**		**Transient model**	
		E_{ads}, eV	**B, $J^{-1}K\,m^2$**	**E_{ads}, eV**	**ν, $10^{12}\,s^{-1}$**
Pyrene	Pyrene / activated carbon	0.949±0.049	23.9±3.4	0.965±0.014	1.56±0.21
	(Pyrene + coronene) / activated carbon	0.961±0.054	20.4±2.8	0.958±0.018	1.31±0.34
	Pyrene / graphite sheet	0.681±0.019	14.1±1.9	0.696±0.010	1.24±0.18
	Pyrene / HOPG	0.476±0.021	13.5±1.9	0.508±0.011	1.38±0.13
Coronene	(Pyrene + coronene) / activated carbon	1.519±0.022	22.8±2.4	1.513±0.013	2.46±0.15
Pb	Pb / activated carbon	0.226±0.024	20.6±2.3	0.243±0.011	7.46±0.26

Both models provide similar adsorption energies ($E_{ads}^{steady-state} = 0.949\,eV$, $E_{ads}^{transient} = 0.965\,eV$), which are also well in line with the literature value measured for pyrene adsorbed on soot particles using thermal desorption kinetics ($0.986\,eV$) [220]. Similar to the "signal decay" experimental approach, the "fluence curve" method (Figure 4.9) returns a mean value of $0.968\,eV$ for the adsorption energy, when applied to the same sample (Table 4.4). Moreover, the values of the B parameter returned by the two approaches ($B^{decay} = 23.9 \pm 3.4\,J^{-1} \cdot K \cdot m^2$ and $B^{fluence} = 21.3 \pm 2.1\,J^{-1} \cdot K \cdot m^2$) are in good agreement with each other and slightly smaller than the initial estimation calculated using literature values. The retrieved pre-exponential factor ν ($1.56 \cdot 10^{12}\,s^{-1}$) is also close to the initial guess. The good agreement with previous works not only validates the analytical method but also confirms that the analyzed samples (surrogate soot) mimic well soot samples collected from real combustors that are thoroughly described in the literature.

© 2020 Tous droits réservés.

lilliad.univ-lille.fr

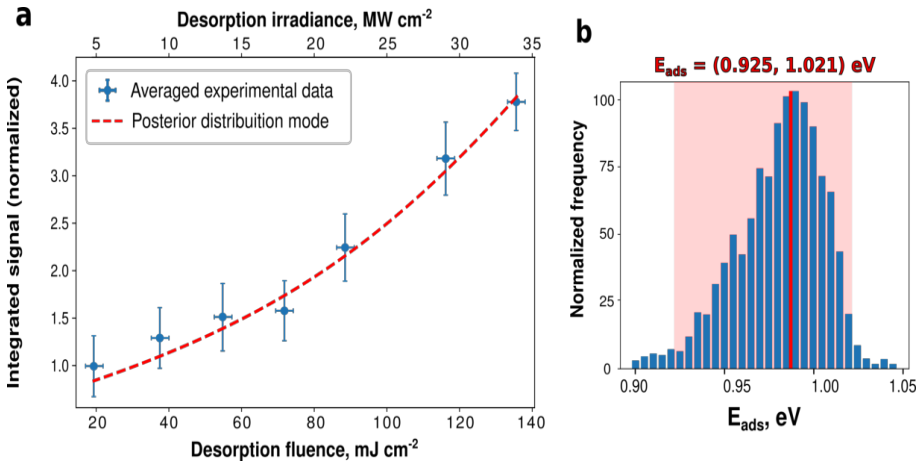

Figure 4.9 *(a) Steady-state model fitted to the "fluence curve" recorded for pyrene desorbing from activated carbon. Each data-point is the average of the signal obtained in four different zones of the same sample, irradiated with the same fluence. (b) Posterior distribution of adsorption energy retrieved with the "effective temperature" model. The most probable fit (mode of the distribution) is plotted (dashed line) in (a).*

Table 4.4 *Estimated adsorption energy (E_{ads}) and B parameter for 3 species desorbing from distinct environments. Values of E_{ads} were retrieved using the fluence curve experimental approach, mathematically described by the "effective temperature" model. The reported values represent the average parameters computed with the procedure described in Section 4.4.2.*

Monitored compound	**Adsorbate/Adsorbent system**	**Fluence curve**	
		E_{ads}, eV	**B, $J^{-1}K\,m^2$**
Pyrene	Pyrene / activated carbon	0.968 ± 0.041	21.3 ± 2.1
	(Pyrene + coronene) / activated carbon	0.983 ± 0.038	22.4 ± 2.5
	Pyrene / graphite sheet	0.662 ± 0.015	15.1 ± 1.4
Coronene	(Pyrene + coronene) / activated carbon	1.508 ± 0.024	23.1 ± 1.1
Pb	Pb / activated carbon	0.206 ± 0.015	21.1 ± 2.1

4.5.1.2 Binary system: Pyrene and Coronene adsorbed on activated carbon

After demonstrating the capability of the method with a single chemical compound (pyrene) adsorbed onto activated carbon, the proposed method is tested with a system consisting of two different polycyclic aromatic compounds (pyrene – $C_{16}H_{10}$ and coronene – $C_{24}H_{12}$) adsorbed onto the same substrate. The adsorbed amount for each compound is low enough (10^{-3} – 10^{-2} monolayer) to exclude any lateral interactions between the adsorbed molecules. Pyrene and coronene were chosen since they both are known to be present on combustion generated soot samples [78, 101, 103, 153] and, at the same time, exhibit significantly different adsorption energies, which makes them perfect candidates to test the E_{ads} determination method. Since

© 2020 Tous droits réservés.

lilliad.univ-lille.fr

Thèse de Dumitru Duca, Université de Lille, 2020

the signal of multiple mass peaks could be monitored at the same time by time-of-flight mass spectrometry, the adsorption energy of several species can be studied concurrently.

Signal decays recorded for the two adsorbates (pyrene and coronene) are fitted with the two temperature models (steady-state and transient). The values obtained for pyrene with both models are very close to each other ($E_{ads}^{steady-state} = 0.961\,eV$ and $E_{ads}^{transient} = 0.958\,eV$, Table 4.3) and to the values previously determined when pyrene was the only analyte adsorbed onto activated carbon ($E_{ads}^{steady-state} = 0.949\,eV$ and $E_{ads}^{transient} = 0.965\,eV$). For coronene, the fits of the signal decay curves yield adsorption energies of $1.519\,eV$ and $1.513\,eV$ with the "effective" (steady-state) and transient temperature models, respectively (Table 4.3, Figure 4.10a). The obtained values for the adsorption energy are in line with those experimentally determined with temperature programmed desorption measurements for coronene adsorbed on carbon nanofibers ($1.31-1.50\,eV$) [219]. The adsorption energies of the two analytes are also retrieved from their "fluence curves" (Table 4.4, Figure 4.10b), with values very close to those previously determined from the signal decay.

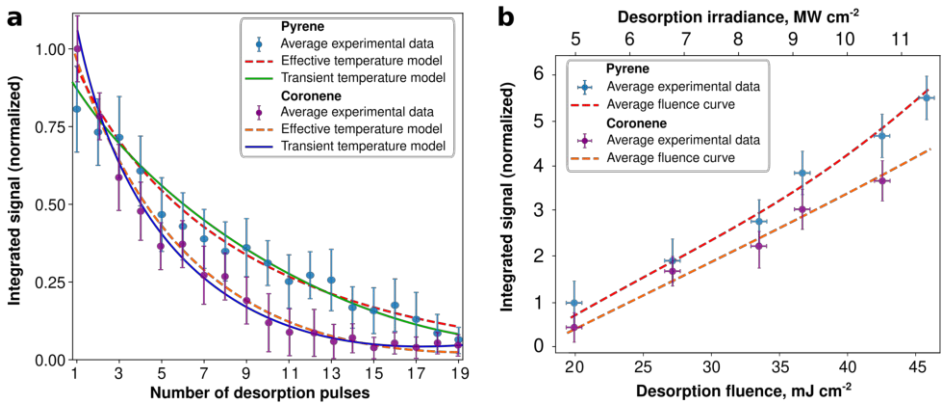

Figure 4.10 *(a) Symbols: four-zone averaged experimental data for pyrene (blue) and coronene (purple) desorbed in the same experimental conditions ($F_{des} = 43\,mJ\,cm^{-2}$) from the same (pyrene+coronene) / activated carbon sample (homogeneous coverage). Dashed lines: effective temperature model decay curves calculated with average parameter values from Table 4.3. Solid lines: transient temperature model decay curves calculated with average parameter values from Table 4.3. (b) Symbols: average experimental data for pyrene (blue) and coronene (purple) desorbed from multiple zones of the same (pyrene+coronene) / activated carbon sample (homogeneous coverage) for a range of desorption fluence values. Dashed lines: effective temperature model fluence curves calculated with average parameter values from Table 4.4.*

The B parameters determined from the two fits of the binary adsorbate system (*i.e.* pyrene and coronene adsorbed onto activated carbon) are in good agreement with each other and also with the ones retrieved for the previous single adsorbate system (pyrene / activated carbon). Similarly, the ν parameter for pyrene agrees well between the two systems. Coronene shows a higher ν value (with respect to pyrene), as expected from theoretical calculations [204, 222]. These results demonstrate the robustness of the adsorption energy calculation method from laser-induced thermal desorption experiments and allow us to conceive its extension to other adsorbate/adsorbent systems.

© 2020 Tous droits réservés.

lilliad.univ-lille.fr

Thèse de Dumitru Duca, Université de Lille, 2020

4.5.1.3 Desorption of heavy metals: Pb / activated carbon

Heavy metals (*e.g.* Pb) are common contaminants of industrial wastewater and are usually removed using various carbonaceous materials [170, 171, 229]. Therefore, the study of the interaction between heavy metals, proven to be carcinogenic even at low concentration, and materials used for their removal from water, such as activated carbon, is of great importance. Detection of lead on soot particles (presumably coming from combustion of leaded gasoline) was already shown to be possible with laser-based mass spectrometry (*e.g.* Particle Analysis by Laser Mass Spectrometry, PALMS) employing UV ionization of desorbed species [230, 231].

$PbCl_2$ salt was dissolved in deionized water and the resulting solution was used as a source of lead (see Section 4.3). Mass spectra recorded upon sample irradiation with the 532 nm laser and ejecta ionization with the 266 nm laser exhibited the characteristic isotopic distribution of Pb^+ in the m/z 204–208 range, as shown in Figure 4.11. No signal for Pb^{2+} or other lead derivatives was present in the mass spectra. Moreover, experiments performed with the ionization laser switched off gave no signal in the mass spectra, *i.e.* the ionized lead is not directly sampled from the surface. The absence of Pb^{2+} ions can be explained by a relatively low desorption fluence used in the experiments (limited by the carbonaceous surface ablation threshold) that might be too low for desorbing these ions from the surface. Moreover, the formation of Pb^{2+} in the aqueous solution is only one of many other possibilities, as $Pb - Cl$ is not a "pure" ionic bond ($\Delta\chi_{Pb-Cl} < 1.7$). Furthermore, in aqueous solution the formation of an array of (partially) solvated ions is to be expected. All these ions can then adsorb onto activated carbon via different mechanisms (*e.g.* adsorption, surface precipitation, ion exchange, sorption) [171, 232–236] and participate to further acid/base, redox or coordination reaction at the particle surface. A thorough investigation of such a complex surface chemistry is well beyond the scope of the present work.

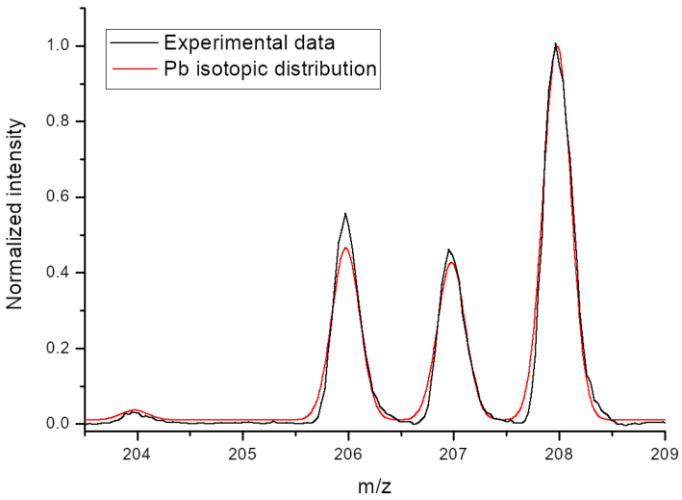

Figure 4.11 *Pb^+ isotopes (m/z 204–208) detected by 532 nm laser desorption of the lead/activated carbon prepared sample / 266 nm laser ionization of the ejecta / time-of-flight mass spectrometry. Comparison with the natural isotopic abundance of Pb [237].*

The signal recorded for Pb vanishes in fewer desorption pulses than in case of aromatic species when using the same desorption fluence, Figure 4.12a. As a result, the obtained signal decay curve contains fewer data points which results in a higher

© 2020 Tous droits réservés.

lilliad.univ-lille.fr

Thèse de Dumitru Duca, Université de Lille, 2020

fitting error for all parameters. Nonetheless, fitting both models to the experimental data, Figure 4.12a, resulted in values for the adsorption energy ($E_{ads}^{steady-state} = 0.226\,eV$ and $E_{ads}^{transient} = 0.243\,eV$, Table 4.3) close to that found in the literature (0.21 eV for Pb adsorbed on carbon particles obtained from bio waste [171]). A similar value ($E_{ads}^{fluence} = 0.206\,eV$) was also determined from the fluence curve (Figure 4.12b, Table 4.4). The adsorption energy of Pb to carbonaceous surfaces is therefore much lower compared to that of aromatic species [171]. The B parameter (which is only related to the adsorbent material) is in good agreement (within the limits of the error bars) with the values returned by the "effective temperature" model fits on the other samples involving activated carbon (see Table 4.3). The pre-exponential factor determined from the transient model fit ($\nu = 7.5 \cdot 10^{12}\,s^{-1}$) is in line with its theoretical value, estimated from pre-exponential factors reported for small adsorbates [204]. To the best of our knowledge, no ν experimental value for this system was reported in the literature.

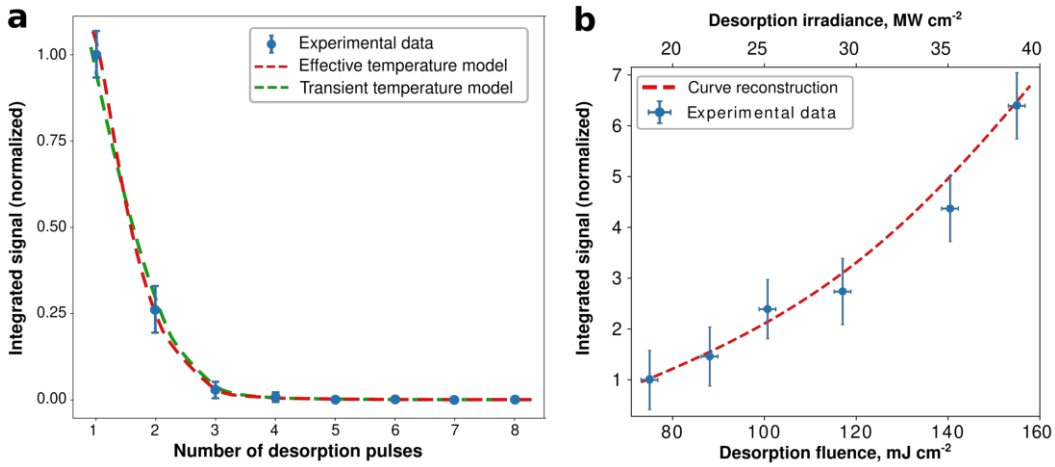

Figure 4.12 *(a) Symbols: four-zone averaged experimental data for lead desorbed in the same experimental conditions ($F_{des} = 104\,mJ \cdot cm^{-2}$) from the same lead/activated carbon sample (homogeneous coverage). Dashed lines: decay curves calculated with average parameter values from Table 4.3. (b) Symbols: average experimental data for lead desorbed in the same experimental conditions from multiple zones of the same lead/activated carbon sample (homogeneous coverage). Dashed line: effective temperature model fluence curve calculated with average parameter values from Table 4.4.*

4.5.2 Effect of the adsorbent: from activated carbon to graphite surfaces

To further explore the capabilities of the proposed method, systems exhibiting significantly different adsorption energies need to be explored. This can be realized by testing either distinct adsorbates on the same adsorbent or, conversely, the same adsorbate on distinct adsorbents, the latter being studied here. The adsorption energy retrieved by the proposed method corresponds to the average energy of all desorbed molecules. If the irradiated surface contains n different adsorption sites, each one characterized by a different adsorption energy, then the measured E_{ads} can be expressed as an average of all adsorption energy values (*i.e.* energies that correspond to all existing sites).

© 2020 Tous droits réservés.

lilliad.univ-lille.fr

Thèse de Dumitru Duca, Université de Lille, 2020

Various surface defects can act as adsorption sites (*e.g.* vacancies, impurities) and most of them are present and abundant on the surface of surrogate (and combustion-generated) soot particles. The adsorption energy of aromatic compounds on adsorbents exhibiting defect-rich surfaces is higher than that expected when the same compounds are adsorbed on a defect-free carbon lattice [238–240]. Since the surfaces of materials such as graphite and highly oriented pyrolytic graphite (HOPG) contain a much smaller number of defects compared to activated carbon, the adsorption energy of pyrene (as well as other chemical species) on such substrates is expected to be substantially lower.

As predicted, the shape of the signal decay curve and the adsorption energy of pyrene desorbed from a graphite sheet and HOPG are noticeably different, Figure 4.13. Since the adsorption energy is lower, a smaller number of laser pulses are required to desorb all molecules present on the irradiated spot, hence a shorter signal decay curve is observed. The adsorption energies obtained from the fits performed with the two models (steady-state and transient) are, yet again, very similar. Adsorption energies obtained for pyrene adsorbed on HOPG (Table 4.3) are in line with values resulting from ab initio calculations ($0.42 - 0.5\,eV$) [238–240]. A spread in the values reported in the literature is determined by the use of different computational methods. To the best of our knowledge, no experimental measurement for either system (pyrene/HOPG or pyrene/graphite sheet) was reported in the literature.

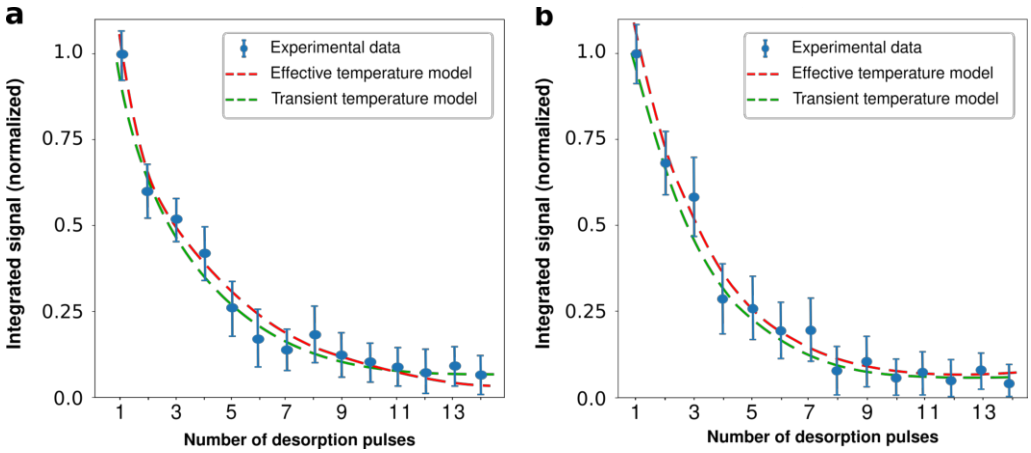

Figure 4.13 *Experimental datapoints (four-zone average) recorded with the "signal decay" approach for pyrene desorbing from (a) graphite sheet ($F_{des} = 50\,mJ\,cm^{-2}$) and (b) HOPG ($F_{des} = 61 mJ\,cm^{-2}$). Steady-state (red dashed line) and transient (green dashed line) decay curves calculated with parameters from Table 4.3.*

It is also possible to obtain "fluence curves" for pyrene desorbing from graphite and retrieve the adsorption energy and B parameter, Table 4.4. The values for E_{ads} and B ($0.662\,eV$ and $15.1\,J^{-1} \cdot K \cdot m^2$, respectively) are also in line with the values previously obtained from the signal decay ($0.681\,eV$ and $14.1\,J^{-1} \cdot K \cdot m^2$, respectively). Moreover, the obtained B values are close to the one calculated with values sourced from the literature ($16.2\,J^{-1} \cdot K \cdot m^2$).

The adsorption energy value obtained for pyrene desorbing from the graphite sheet ranges between the ones retrieved for activated carbon and HOPG, which is expected since this substrate contains an intermediate number of defects compared to HOPG (fewer surface defects) and activated carbon (more surface defects). This assumption can be verified using Raman spectroscopy [21]. Raman spectra,

© 2020 Tous droits réservés.

lilliad.univ-lille.fr

Thèse de Dumitru Duca, Université de Lille, 2020

obtained with a Renishaw spectrometer (514 nm excitation wavelength, see Section 2.2.1.3), of the analyzed samples (activated carbon, graphite sheet and HOPG) were deconvoluted into two bands - D (associated with the disordered structure, centered at $1350\,cm^{-1}$) and G (arising from the stretching of the $C-C$ bond, centered at $1580\,cm^{-1}$) [146, 241], Figure 4.14. Even though Raman spectra of soot particles are usually deconvoluted into five or even six different bands [21, 85], D and G bands by themselves are able to provide useful information about the presence of structural defects and allow to make a qualitative comparison of the studied samples. It can be clearly seen that for the activated carbon sample both bands exhibit comparable intensities while for the other substrates the D band has a much smaller intensity and completely vanishes for the HOPG sample. This indicates that for the graphite sheet and HOPG the contribution of surface defects is significantly reduced, effectively lowering the number of adsorption sites related to them. As a result, a higher percentage of desorbed molecules will originate from adsorption sites associated with the ideal graphitic lattice, which, for carbonaceous substrates, are characterized by a lower adsorption energy [239, 242, 243]. It is worth noting that the D band provides information only about the disordered graphitic lattice (*e.g.* graphene layer edges) and cannot be used to study the contribution of other defects, for instance impurities. Nevertheless, this information is extremely useful and explains the observed decrease in the adsorption energy of pyrene.

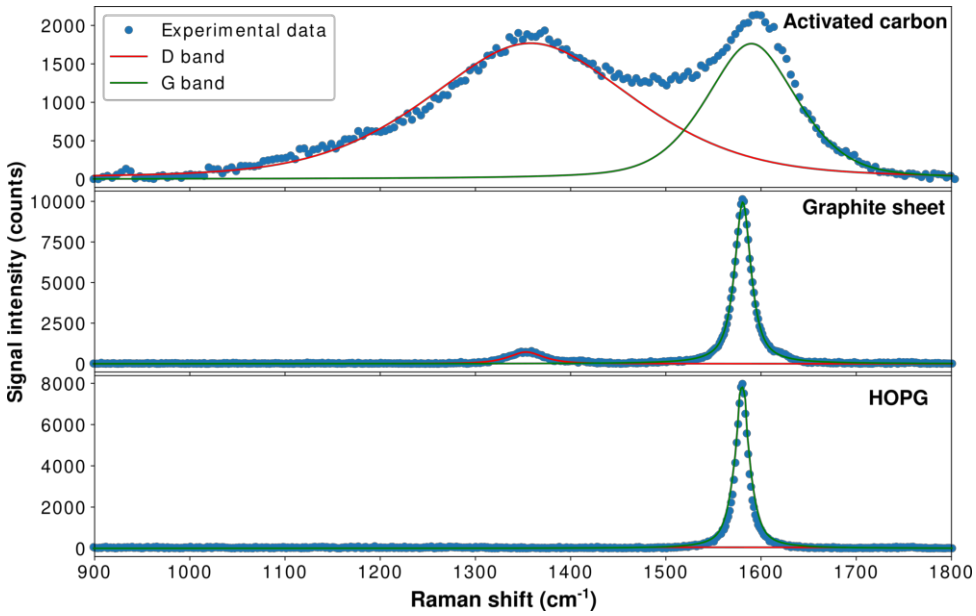

Figure 4.14 *Comparison between Raman spectra of three different carbonaceous samples used in adsorption energy studies: activated carbon, graphite sheet, and HOPG. Spectra were deconvoluted into two bands: D and G.*

4.6 Toward studying complex soot samples

In the previous subsection it was shown that the structure of the substrate impacts the mean adsorption energy of a compound. When it comes to combustion generated soot particles, the structure of emitted particles highly depends on the fuel and combustion conditions. Therefore, the adsorption energy obtained with the

© 2020 Tous droits réservés.

lilliad.univ-lille.fr

Thèse de Dumitru Duca, Université de Lille, 2020

proposed method would change in accordance with the combustion regime. Further, chemical species generated during the combustion process can be found at the same time in two phases: adsorbed on the surface of soot particles and in the gas phase [85, 152]. Chemical compounds that are present in the gas phase can adsorb on different surfaces, including soot particles, during the transport or collection of combustion by-products. The ability to differentiate between species that have been adsorbed on the surface of soot particles during soot formation and the ones that adsorbed at a later stage (chemi- or physisorbed, respectively) can potentially reveal the key species that are present in the combustion region during soot inception period. This separation between the two groups of compounds (adsorbed during and after combustion) can be achieved by measuring their adsorption energy. As a first step in developing a reliable detection and classification method, a soot sample was analyzed, Figure 4.15. The sample was obtained (A. Faccinetto) by collecting combustion generated byproducts (both particulate and gas phase) from a laboratory methane flame using an impactor centered onto a *Ti* wafer. This sampling system, developed by A. Faccinetto and C. Irimiea and described in more detail in [30, 120], spatially separates the particulate and gas phase. The separation between phases enables the study of the same compound (combustion generated) adsorbed to either bare *Ti* wafer (during collection) or soot particles. Three different concentric regions are seen on the sample: the first (center) corresponds to soot particles, the second one (first light circle) is associated with the condensed gas phase adsorbed on the *Ti* surface, and the third (grey circle) is a mixture of the two phases, Figure 4.15. The third region forms due to bouncing of soot particles from the center of the sample during the collection process. The association between the zone on the sample and its composition was confirmed by Raman spectroscopy performed on each of the three zones, Figure 4.15. A strong soot signature (D and G bands) was identified in the center of the sample (soot particles) superimposed on a high fluorescence background. The observed fluorescence background can be attributed to surface organic content [244] (*i.e.* organic species such as PAHs adsorbed on the surface of soot particles). Only the fluorescence background was detected in the second zone of the sample, suggesting that this zone is associated with species condensed from the gas phase on the Ti surface. A much weaker soot signature, compared to the center of the sample, was detected in the third zone, indicating the small amount of present soot particles.

The signal decay curve for m/z 202 was recorded for each of the aforementioned regions and then compared, Figure 4.16. The signal decays obtained for the three zones clearly show a different behavior determined by the mean adsorption energy of the $C_{16}H_{10}$ compound. It seems that the adsorption energy is the smallest for compounds desorbing from the *Ti* wafer (associated with the condensed gas phase) as the signal vanishes after fewer desorption pulses. For the central region (soot particles), the decay resembles the one observed for surrogate soot. The decay from the third region (mixture of particulate and gas phase), as expected, appears to be a combination of the other two, so that the analyte is desorbing from both soot particles and *Ti* wafer. It is clear that only by following the signal decay it was possible to discriminate between different zones of the sample containing the same chemical compound adsorbed on different surfaces, and thus having different desorption energies. This shows the potential of the proposed method in the study of samples exhibiting sub-millimeter range heterogeneities.

© 2020 Tous droits réservés.

lilliad.univ-lille.fr

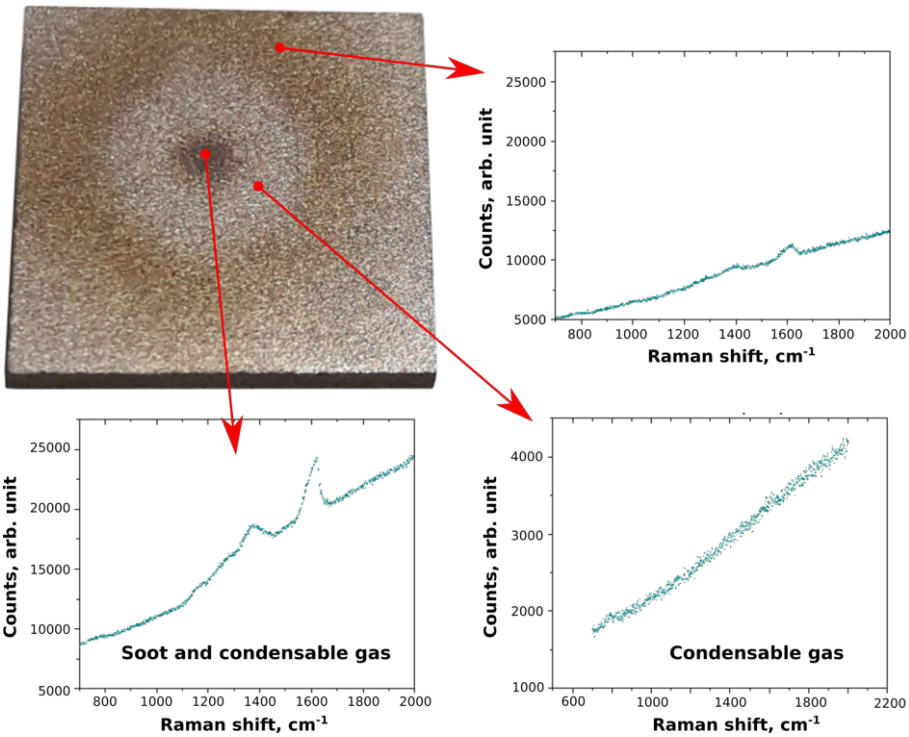

Figure 4.15 *Laboratory flame byproducts deposited on a Ti wafer with a home-built impactor (top left) and Raman/fluorescence spectra recorded on various zones of the sample. The sampling technique enables the separation of the two phases present in combustion byproducts: particulate and gas phase. The sample contains three different concentric regions: center – corresponds to soot particles and gas phase condensed on their surface, first light circle – gas phase (condensable gas) adsorbed on Ti wafer, and the second, darker circle – a mixture of the two phases containing a lower amount of soot particles. Raman spectra of each zone of the sample (bottom panel) illustrate a significantly different response.*

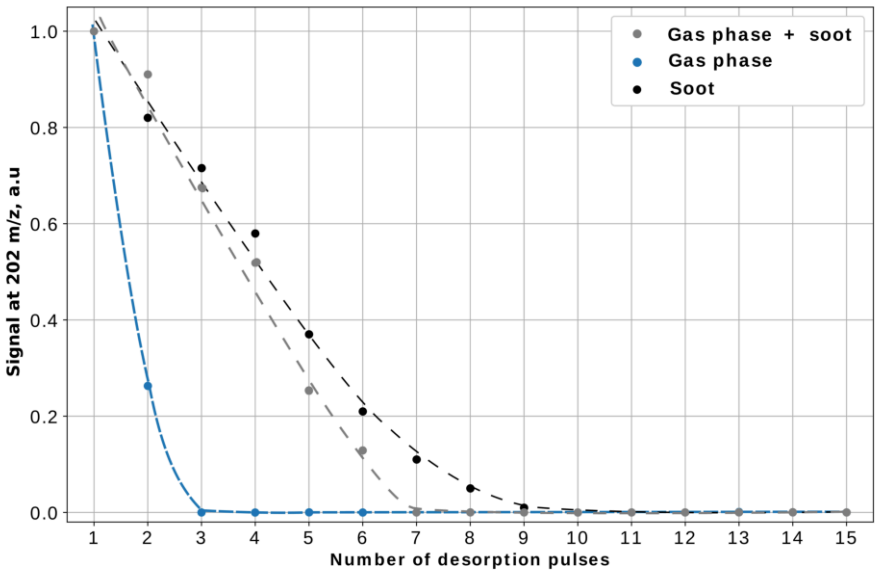

Figure 4.16 *Signal decays corresponding to different zones (soot, condensed gas phase, and soot+gas phase) of the sample shown in Figure 4.15.*

© 2020 Tous droits réservés.

lilliad.univ-lille.fr

Thèse de Dumitru Duca, Université de Lille, 2020

4.7 Conclusion

In this section, a new method of adsorption energy determination based on laser induced thermal desorption was formulated and experimentally validated. Two different mathematical equations modeling the desorption phenomena were derived. The "effective temperature" model approximates the desorption process to a steady state phenomenon. This model, while greatly simplifying the calculations, also only constitutes a rough approximation of the physical process. The higher computational speed allows it to be used in conjunction with real-time chemical mapping to better characterize the zone of interest (shown to be possible for a sample with spatially separated particulate and gas phase). The more elaborated transient temperature model accounts for the fast variation of the surface temperature triggered by the absorption of the laser pulse. This model implies increased complexity, but it describes a scenario much closer to the physical reality. Additionally, this model features very little correlation between the variables. Both models fit well the experimental data and provide results close to the values reported in the literature that were determined from temperature programmed desorption measurements and ab initio calculations. The adsorption energy was determined for two organic molecules (pyrene and coronene) as well as for an inorganic adsorbate (lead). This approach was also able to retrieve the adsorption energy of different compounds co-adsorbed on the same sample (from the same measurements). This serves as a good "proof of concept" for the method, proving that laser induced desorption combined with the mathematical formulations presented here can be used to study adsorption mechanisms.

The presented method is sensitive enough to show how the structure of the adsorbent (*e.g.* number of surface defects) can significantly change the mean adsorption energy. As expected, the adsorption energies derived from the experiments increase with the number of surface defects. As a result, this method can be used to probe and monitor defect densities of various adsorbate/adsorbent systems, complementing the sample characterization obtained with other surface sensitive techniques, for instance, micro-Raman spectroscopy. While currently limited to sub-millimeter scale heterogeneities, the lateral resolution could be improved by reducing the diameter of the desorption laser spot size. The high sensitivity of the technique (ensured by the mass spectrometric detection) can be used to finely map spatial variations of physi- and chemisorption interactions across heterogeneous samples, possibly containing small surface inclusions (regions with a distinct composition).

The capabilities of the proposed method open perspectives of application in various fields. First, it can serve as a benchmark for adsorbate/adsorbent systems against which other methods (*e.g.* ab initio calculations) can be compared. On a technological level, it can also encourage the development of advanced materials specially designed to selectively target and capture dangerous compounds such as toxins or heavy metals [245]. This method can be used to characterize catalytic and energy storage materials [246] as well as thin films grown by physical or chemical deposition methods [247, 248], which can (depending on the deposition geometry, substrate etc.) exhibit quite large heterogeneities [249, 250] in their adhesion/adsorption properties. The local character of the proposed technique (defined by the laser beam diameter) in conjunction with a fast mathematical treatment (in the form of the simplified "effective temperature" model) can help in implement-

© 2020 Tous droits réservés.

lilliad.univ-lille.fr

Thèse de Dumitru Duca, Université de Lille, 2020

ing a real-time, spatially-resolved probe directly in the technological process line. Finally, in the combustion field, the proposed method can help shed light on the formation process of soot particles [30, 99] by identifying the origin of the aromatic species present on their surface (*i.e.* remnants of the nucleation/growth process or condensation from the gas phase).

© 2020 Tous droits réservés.

lilliad.univ-lille.fr

Chapter 5

Conclusions and perspectives

The main objectives of my PhD work was the study of the physico-chemical characteristics of size-selected particles emitted by a gasoline direct injection engine, and the development of a new analytical approach for measuring the adsorption energy of chemical species on carbonaceous surfaces. Therefore, this research is structured into two main topics. The first topic is related to the collection of size-selected soot particles from an ICE engine and their subsequent analysis. The combination of multiple analytical techniques employed in this study resulted in a comprehensive physico-chemical characterization of ICE emissions. As the reactivity and toxicity of combustion-generated particles, such as soot emissions of an ICE, are mainly determined by their surface chemical composition, it is also important to study the interaction of adsorbed chemical compounds with the particle surface, in order to truly understand and predict their impact on climate and human health . For that reason, the second part of the thesis is dedicated to fundamental adsorption studies, involving various chemical species (adsorbate) and carbonaceous surfaces (adsorbent), with the ultimate goal being the development and validation of a novel laser-based method for determining the adsorption energy of adsorbates.

As already mentioned, the first part of the thesis focused on the physico-chemical characterization of engine emissions, study performed in the framework of the H2020 PEMS4Nano project with the objective to develop a robust, reliable and reproducible particle emission monitoring system for particles as small as 10 nm thus contributing to possible future automobile regulations. In this project, a bottom-up approach was selected for the development of such a system, involving a theoretical framework meant to model particle formation and evolution in the engine and exhaust system [61]. Training and validation of such a model requires extensive information about the physico-chemical properties of the emitted particles – a database that was obtained in this study. Furthermore, both polydisperse and size-selected particles were analyzed as to gain insight into the size variation of soot properties, and offer a higher level of data granularity. A single-cylinder test engine was used as a particle generator. Engine emissions obtained in several regimes were studied, encompassing a number of operating conditions encountered during real driving conditions as well as some associated with common mechanical malfunctions (*e.g.* engine wear, fuel system failure).

Particles were sampled from the engine exhaust and separated into different size-bins for subsequent analysis. Additionally, an original two-filter system [85, 86] was employed to sample simultaneously the gas phase and the particulate matter

© 2020 Tous droits réservés.

lilliad.univ-lille.fr

Thèse de Dumitru Duca, Université de Lille, 2020

(without size-selection) from the exhaust of the engine on separate substrates. A multitechnique offline analysis was then employed to acquire extensive information about the structure, morphology and chemical composition of collected samples. The morphology and nanostructure of individual particles were studied by means of scanning or transmission electron microscopy (TEM) and atomic force microscopy / tip-enhanced Raman spectrometry (AFM/TERS). These measurements demonstrate the ability to study individual solid particles as small as 6 nm that were explicitly identified as being soot based on their unique Raman signatures (D and G bands obtained with TERS) and turbostratic nanostructure (TEM). These TERS measurements were performed, to the best of our knowledge, for the first time on ultra-fine combustion-generated particulate matter and show how diverse the soot particles are (at least in terms of nanostructure), even when they are generated by the same engine, operating in the same conditions, and collected in the same size bin [103]. This finding is very important for interpreting the off-line chemical composition measurements that followed and were carried out by mass spectrometry techniques that rather than probing individual particles, deal with many of them at the same time (the number is determined by the laser or ion beam diameter). Therefore, the properties and trends derived from the subsequent chemical composition analyses are averaged over many (different) particles, and thus are statistically significant. Such trends offer valuable input for the theoretical model, also operating with statistical approaches on particles ensembles [61].

Detailed molecular-level characterization of particulate matter was obtained with ex-situ techniques such as Time-of-Flight Secondary Ion Mass Spectrometry and Two-Step Laser Mass Spectrometry. The latter has been developed by the ANATRAC group for more than 15 years to study the surface chemical composition of combustion-generated particles [30, 78, 97–99, 102, 103, 184, 198, 251, 252]. The obtained information in conjunction with statistical procedures [30, 102, 103] showed decisive evidence that the chemical composition depends on particle size. Moreover, such a molecular-level characterization allowed the identification of key chemical markers (*e.g.* aromatic compounds, hopanoid species) that helped us identify the main particle production source (*e.g.* fuel, lubricant, engine wear). In addition, the specific chemical composition was used to discriminate particles that were produced in different engine regimes, including the ones associated with mechanical failures. Such a separation was also possible for samples containing gaseous emissions (*i.e.* the gas phase) and even where all particle sizes were collected simultaneously (*i.e.* polydisperse particles). A clear relationship was observed between the elemental carbon (EC) content and carbon clusters, as well as an excellent correlation between the organic carbon (OC) content, the volatility, and the presence of aromatic species. The aromatic compounds proved to be the main chemical species associated with the volatile organic fraction. The OC/EC partitioning was additionally shown to vary with particle size and engine regime [103].

The particle measurement programme [46] specifies that only solid (non-volatile) particles (*i.e.* particles that do not evaporate below 350°C) must be measured, and thus requires the addition of a volatile particle removal (VPR) system to the particle measurement device. Current PMP compliant systems use an evaporative tube (ET) to remove the volatile particles, which proved to be a robust and reliable solution for measurements of particulates larger than 23 nm. When it comes to smaller ones, specifically smaller than 23 nm, the use of ET may lead to a significant increase in the

© 2020 Tous droits réservés.

lilliad.univ-lille.fr

Thèse de Dumitru Duca, Université de Lille, 2020

number of artifact ultrafine particles formed by renucleation of semivolatiles [253]. Therefore, the use of the a catalytic stripper (CS) seem to be more effective in preventing the formation of non-solid artifacts [253], which may considerably increase the robustness of the PMP system for ultra-fine particles. Moreover, the measurements performed with both a CS and an ET showed that the differences between the results obtained for different VPR systems only become significant for smaller particles [253], and thus a CS-equipped PMP system will be backward compatible with previous regulations (*i.e.* measurements obtained with a CS-equipped PMP system for particles larger than 23 nm will be equivalent to the ones obtained with an ET). In order to evaluate the efficiency of a PMP compliant CS, measurements of the volatile organic fraction were performed on different phases collected from the ICE exhaust (*i.e.* particulate and gas phase) as well as on size-selected particles. Mass spectrometry analyses showed that the catalytic stripper effectively removed the organic content regardless of the phase (gas or particles), as demonstrated by a drastic reduction (more than one order of magnitude) of the corresponding partial ion count. Regarding size-selected particles, it was discovered that the smallest ones (10–32 nm) hold a larger volatile fraction, and thus are the most affected by the removal of organic compounds by the catalytic stripper. A similar conclusion (*i.e.* that smallest nanoparticles have the most important surface-organic fraction) was obtained with online aerodynamic-mass-mobility measurements* performed in parallel with the collection of samples analyzed here [254]. Moreover, there is an excellent agreement between the theoretical predictions [61] and independently performed chemical and physical characterizations. These findings highlight that the volatile fraction covering the solid carbonaceous core of particulates present in the raw engine exhaust may represent a significant fraction of the overall particle mass. These results evidence the importance of stripping the volatile fraction from the sampled exhaust (with a CS) as to obtain reliable and repeatable measurements for particles as small as 10 nm in a variety of engine regimes. Ultimately, a PMP system that includes a CS, designed to have both a high catalytic function efficiency and low particle losses, and calibrated with the theoretical model trained on experimental data presented in this work represents a robust technology that can serve as a basis for regulating sub-23 nm particles.

The presented work and conclusions give the motivation for the second part of this PhD which focuses on fundamental studies of the adsorption process of various chemical species on carbonaceous surfaces. Adsorption studies can help identify the adsorption mechanism of chemical compounds present on a surface (physisorption or chemisorption) which is beneficial for a number of reasons. First, since the behavior of carbonaceous particles, such as soot, in the atmosphere is determined by the processes occurring at the surface, information on the adsorption energy (*i.e.* interaction strength between an atom/molecule and the surface) can provide necessary information to better understand, predict, and potentially minimize the health and climate impact of carbonaceous particle emissions. For one, the adsorption energy of condensed species is closely related to the volatility of the surface organic layer present on soot particles, and thus can help predict the impact of various VPR systems. Ultimately, such information can be used to design a VPR system well adapted for the treatment of particles emitted by a given source. Another reason

*Measurements performed by a research group from University of Cambridge led by Dr. Adam Boies.

© 2020 Tous droits réservés.

lilliad.univ-lille.fr

Thèse de Dumitru Duca, Université de Lille, 2020

to study the adsorption mechanism on carbonaceous particles is the potential to gain insights into the complex and still only partially understood soot formation process [30, 99] by identifying the origin of the aromatic species present on their surface. This is possible since adsorption energies define whether the surface species (adsorbates) are chemisorbed or physisorbed, and therefore if the surface molecular compounds result from surface chemistry (remnants of the soot formation) or physical condensation [76]. Finally, since carbonaceous materials are ubiquitous, such studies can help design better carbon-based advanced materials for industrial use, for instance materials designed for adsorptive fixation of organics/toxins in the gas and liquid phases for treating wastewaters and emission gasses [72–75, 245].

Within the adsorption studies, a new method of adsorption energy determination based on laser-induced thermal desorption was formulated and experimentally validated. The development of this method included derivation of two different mathematical models describing laser-induced desorption phenomena. The "effective temperature" model approximates the desorption process to a steady state phenomenon. While only representing a rough approximation of the physical process, this method greatly simplifies the calculations, and thus can be used in conjunction with real-time and spatially-resolved chemical mapping as to better characterize the surface of heterogeneous samples, for instance, directly in the technological process line for advanced materials. The validity of such an approach was demonstrated for a sample with spatially separated particulate and gas phase, each characterized by a different adsorption energy. The more elaborate transient temperature model accounts for the fast variation of surface temperature triggered by the absorption of the laser pulse. This transient temperature model, while being more complex and computation intensive, describes a scenario much closer to physical reality. In addition, it features very little correlation between the variables. The method was validated by determining the adsorption energy for two organic molecules (pyrene and coronene) as well as for an inorganic adsorbate (lead). Both mathematical models fit well the experimental data and provide results close to the values reported in the literature that were determined from temperature programmed desorption measurements and ab initio calculations. The developed approach was also able to retrieve the adsorption energy of different compounds co-adsorbed on the same sample (from the same measurements). These measurements serve as a good "proof of concept" for the method, proving that laser-induced desorption combined with the derived mathematical formulations can be used to study adsorption mechanisms.

The developed method has high enough sensitivity to show how the structure of the adsorbent (*e.g.* number of surface defects) impacts the mean adsorption energy characterizing the adsorbate-adsorbent system. Specifically, the measured mean adsorption energy increases with the number of surface defects. As a result, the proposed method can be used to probe and monitor adsorbent defect densities, complementing the sample characterization obtained with other surface sensitive techniques, for instance, micro-Raman spectroscopy. The high sensitivity of the technique, on account of the low detection limit of the mass spectrometric setup, can be used to finely map spatial variations of physi- and chemisorption interactions across heterogeneous samples.

The results obtained during this thesis point out that the analysis of combustion-generated aerosols can be very complex, and can require further optimization of the methodology in place. Therefore, this work brings new research opportunities

© 2020 Tous droits réservés.

lilliad.univ-lille.fr

Thèse de Dumitru Duca, Université de Lille, 2020

for improving both the instrumentation and data-treatment methodology. First, the spatial resolution of the HR-L2MS instrument is significantly improved with the addition of a new ion source that combines laser desorption/ionization with an optical microscope, Figure 5.1. The new source** was installed and tested during this work with some preliminary optimizations applied during several pilot experiments. In the new configuration, transmission and reflection images of the sample can be obtained simultaneously with the desorption, and subsequent ionization of adsorbed species, Figure 5.1. The lateral resolution of the setup is considerably improved by decreasing the laser-irradiated sample area to only $\sim 300\,\mu m^2$. The new source features a fully motorized sample holder with a nm-range positioning resolution, which in conjunction with a reduced laser desorption spot enables the high-resolution chemical mapping of the analyzed sample. The obtained chemical image can be later superimposed on the optical picture of the sample, and thus considerably facilitating the analysis of heterogeneous surfaces. The optimization of the new source along with the development of the real-time chemical mapping methodology, well adapted for the analysis of highly heterogeneous samples, is undertaken by another PhD student (Siveen Thlaijeh).

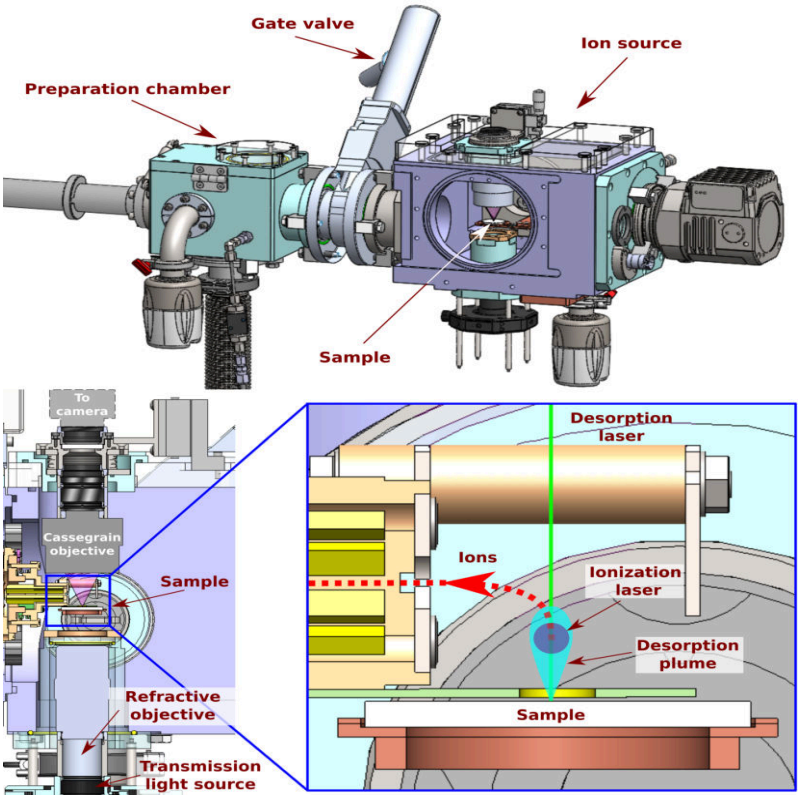

Figure 5.1 *Top panel – 3D representation of the new ion source installed on the HR-L2MS instrument that combines laser desorption and laser ionization with optical microscopy. Bottom panel – Internal layout of the new ion source illustrating the relative position of optical microscopy elements. The sample, positioned horizontally on a motorized platform, is irradiated at normal incidence by a desorption laser beam, focused on its surface with the Cassegrain objective (the same objective as used for microscopy). The ionization laser intercepts the expanding plume in an orthogonal direction. The ions are then guided into the inlet of the ion source, described in Section 2.2.2.3.*

**The new ion source was manufactured by Fasmatech S&T.

© 2020 Tous droits réservés.

lilliad.univ-lille.fr

Thèse de Dumitru Duca, Université de Lille, 2020

The new desorption/ionization source, once well characterized and optimized, will significantly contribute to the further development of various research axes. First and foremost, a much smaller desorption spot (∼10 µm diameter instead of currently 700 μm) will allow the refinement of the adsorption energy values determined in this work with a much smaller mapping scale. With this in mind, a new PhD thesis (Joelle Al Aseel) will start (Oct. 2020) in collaboration with the theoretical physico-chemistry group of the PhLAM laboratory. Systematic adsorption studies of species present on a variety of substrates, not only carbonaceous, will be continued and refined at experimental and theoretical levels. The new source will be also beneficial for targeting micrometer-range heterogeneities, a great asset in, e.g., the search for organic matter in fossil inclusions for paleontological purposes (quest for early-life molecular markers, thesis of S. Thlaijeh in collaboration with Dr. K. Lepot, LOG laboratory). From the combustion perspective, a smaller desorption laser spot translates into fewer irradiated particles, and thus can help highlight the variability between particles produced in the same regime and sampled in the same conditions (which was already observed here with microscopy techniques, Chapter 3). The new source will enable the analysis of sub-picogram amounts of field- or lab-collected samples, which represents a significant improvement for the adsorption energy studies and for the chemical analysis itself.

Furthermore, the analysis of some samples can be quite challenging (or impossible) under vacuum conditions. One example is given by the analysis of in vivo biological tissues to, *e.g.* detect molecular markers of cancers. The collaboration started by the ANATRAC group with the PRISM laboratory (Prof. I. Fournier, Prof. M. Salzet) led to the development of an atmospheric pressure IR laser desorption approach dedicated to medical/biological purposes [255–261]. Efforts to generalize this to all types of samples, by changing the desorption/ablation mechanism with the use of other wavelengths, and by adjoining various and complementary highly-effective post-ionization sources (photonic, plasma, electron attachment etc.) are starting, especially in the frame of the new France-Bayern funded project with the Technical University of Münich (Prof. C. Haisch). The final goal of these efforts is to propose a versatile multi-diagnostic experimental arrangement combining atmospheric pressure mass spectrometry, Raman spectroscopy, and Laser Induced Breakdown Spectroscopy (LIBS) in a unique instrument. A PhD thesis co-funded by Horiba Scientific (Dr. S. Legendre) will start on this subject in October 2020 (Vikas Madhur). As said above, the experimental developments performed in this work could be helpful for these future endeavors.

At the theoretical/computational level, the new tools developed in this thesis will serve further works (for instance, those related to the control and data processing of the new HR-L2MS spectrometer) and open some interesting perspectives. As previously mentioned, the physico-chemical characterization of combustion-generated soot particles obtained in this work was used by the University of Cambridge and CMCL Innovations for the development of a theoretical model to simulate the formation and evolution of soot particles in the engine. Information on the chemical composition of emitted particles, clustered by unsupervised machine learning algorithms into several groups, was later linked to specific sources (i.e. fuel, lubricant, engine wear) or engine regimes. Therefore, such a comprehensive database can also be used to help interpret mass spectrometry data obtained from other soot particles or even other types of samples. This can be achieved by utilizing supervised

© 2020 Tous droits réservés.

lilliad.univ-lille.fr

Thèse de Dumitru Duca, Université de Lille, 2020

machine learning algorithms trained and validated on the available, already labeled data. Such a model, based either on decision trees, combination of PCA, clustering and k-nearest neighbors algorithm or even neural networks [262], has the potential of determining the provenience (*e.g.* in terms of engine regime and size-bin) of soot particles only from the obtained mass spectrum in a fully automated manner. Moreover, such a model will also be able to assign chemical formulas to unknown mass peaks and perform cross-validation to ensure a high assignment confidence. A model built with the data presented in this work will only be able to make accurate predictions for particulate matter emitted by a gasoline engine. However, as a large number of combustion-generated aerosols collected from a variety of sources were analyzed during the development of the L2MS instrument by the ANATRAC group, a great amount of mass spectrometry data was generated and can be used to extend the capabilities of the prediction model. Training a model on such a large dataset will allow the algorithm to differentiate between, *e.g.* soot particles produced by different combustors operating on different fuels. This automatization can potentially enable the on-site real-time identification of major particle producers (source apportionment) in polluted areas, at a molecular level of description beyond the current performances of aerosol mass spectrometers and associated data processing. The development of such a model represents an exciting perspective for the work started here.

© 2020 Tous droits réservés.

lilliad.univ-lille.fr

This page is intentionally left blank

© 2020 Tous droits réservés.

lilliad.univ-lille.fr

Bibliography

[1] T. F. Stocker, D. Qin, G. K. Plattner, M. Tignor, S. K. Allen, J. Boschung, A. Nauels, Y. Xia, V. Bex, P. M. Midgley, et al., Climate change 2013: The physical science basis – Contribution of working group I to the fifth assessment report of the intergovernmental panel on climate change, https://www.ipcc.ch/report/ar5/wg1/ (2013).

[2] W. C. Hinds, Aerosol technology: properties, behavior, and measurement of airborne particles, John Wiley and Sons, New York, 1999.

[3] T. C. Bond, S. J. Doherty, D. W. Fahey, P. M. Forster, T. Berntsen, B. J. DeAngelo, M. G. Flanner, S. Ghan, B. Kärcher, D. Koch, et al., Bounding the role of black carbon in the climate system: A scientific assessment, Journal of Geophysical Research: Atmospheres 118 (2013) 5380–5552. doi:10.1002/jgrd.50171.

[4] L. D. Rotstayn, Indirect forcing by anthropogenic aerosols: A global climate model calculation of the effective-radius and cloud-lifetime effects, Journal of Geophysical Research 104 (1999) 9369–9380. doi:10.1029/1998JD900009.

[5] N. Pidgeon, K. Parkhill, A. Corner, N. Vaughan, Deliberating stratospheric aerosols for climate geoengineering and the spice project, Nature Climate Change 3 (2013) 451–457. doi:10.1038/nclimate1807.

[6] World Health Organization, Burden of disease from the joint effects of household and ambient air pollution for 2012, http://www.who.int/phe/health_topics/outdoorair/databases/AP_jointeffect_BoD_results_March2014.pdf?ua=1 (2014).

[7] World Health Organization, Air quality guidelines: global update 2005: particulate matter, ozone, nitrogen dioxide, and sulfur dioxide, https://www.who.int/phe/health_topics/outdoorair/outdoorair_aqg/en/ (2006).

[8] T. C. Carvalho, J. I. Peters, R. O. Williams III, Influence of particle size on regional lung deposition–what evidence is there?, International Journal of Pharmaceutics 406 (2011) 1–10. doi:10.1016/j.ijpharm.2010.12.040.

[9] K. Sankhe, T. Khan, C. Bhavsar, M. Momin, A. Omri, Selective drug deposition in lungs through pulmonary drug delivery system for effective management of drug-resistant TB, Expert Opinion on Drug Delivery 16 (2019) 525–538. doi:10.1080/17425247.2019.1609937.

© 2020 Tous droits réservés.

lilliad.univ-lille.fr

[10] S. Fuzzi, U. Baltensperger, K. Carslaw, S. Decesari, H. Denier van der Gon, M. C. Facchini, D. Fowler, I. Koren, B. Langford, U. Lohmann, et al., Particulate matter, air quality and climate: lessons learned and future needs, Atmospheric Chemistry and Physics 15 (2015) 8217–8299. doi:10.3929/ethz-b-000103253.

[11] D. L. Diggs, K. L. Harris, P. V. Rekhadevi, A. Ramesh, Tumor microsomal metabolism of the food toxicant, benzo(a)pyrene, in ApcMin mouse model of colon cancer, Tumour biology : the journal of the International Society for Oncodevelopmental Biology and Medicine 33 (2012) 1255–1260. doi:10.1007/s13277-012-0375-6.

[12] K. H. Kim, S. A. Jahan, E. Kabir, R. J. C. Brown, A review of airborne polycyclic aromatic hydrocarbons (PAHs) and their human health effects, Environment International 60 (2013) 71–80. doi:10.1016/j.envint.2013.07.019.

[13] G. Grimmer, Environmental carcinogens: Polycyclic aromatic hydrocarbons: Chemistry, occurrence, biochemistry, carcinogenicity, CRC Press, Boca Ratov, 2018. doi:10.1201/9781351071758.

[14] C. A. Pope, D. W. Dockery, Health effects of fine particulate air pollution: Lines that connect, Journal of the Air and Waste Management Association 56 (2006) 709–742. doi:10.1080/10473289.2006.10464485.

[15] B. A. Maher, I. A. Ahmed, V. Karloukovski, D. A. MacLaren, P. G. Foulds, D. Allsop, D. M. Mann, R. Torres-Jardón, L. Calderon-Garciduenas, Magnetite pollution nanoparticles in the human brain, Proceedings of the National Academy of Sciences of the United States of America 113 (2016) 10797–10801. doi:10.1073/pnas.1605941113.

[16] N. D. Saenen, H. Bové, C. Steuwe, M. B. Roeffaers, E. B. Provost, W. Lefebvre, C. Vanpoucke, M. Ameloot, T. S. Nawrot, Children's urinary environmental carbon load: A novel marker reflecting residential ambient air pollution exposure?, American Journal of Respiratory and Critical Care Medicine 196 (2017) 873–881. doi:10.1164/rccm.201704-0797OC.

[17] H. Bové, E. Bongaerts, E. Slenders, E. M. Bijnens, N. D. Saenen, W. Gyselaers, P. V. Eyken, M. Plusquin, M. B. J. Roeffaers, M. Ameloot, T. S. Nawrot, Ambient black carbon particles reach the fetal side of human placenta, Nature Communications 10 (2019) 3866. doi:10.1038/s41467-019-11654-3.

[18] H. Bladh, N.-E. Olofsson, T. Mouton, J. Simonsson, X. Mercier, A. Faccinetto, P.-E. Bengtsson, P. Desgroux, Probing the smallest soot particles in low-sooting premixed flames using laser-induced incandescence, Proceedings of the Combustion Institute 35 (2015) 1843–1850. doi:10.1016/j.proci.2014.06.001.

[19] K. Dewa, K. Ono, A. Watanabe, K. Takahashi, Y. Matsukawa, Y. Saito, Y. Matsushita, H. Aoki, K. Era, T. Aoki, et al., Evolution of size distribution and morphology of carbon nanoparticles during ethylene pyrolysis, Combustion and Flame 163 (2016) 115–121. doi:10.1016/j.combustflame.2015.09.007.

© 2020 Tous droits réservés.

lilliad.univ-lille.fr

[20] T. Ishiguro, Y. Takatori, K. Akihama, Microstructure of diesel soot particles probed by electron microscopy: first observation of inner core and outer shell, Combustion and Flame 108 (1997) 231–234. doi:10.1016/S0010-2180(96)00206-4.

[21] P. Parent, C. Laffon, I. Marhaba, D. Ferry, T. Z. Regier, I. K. Ortega, B. Chazallon, Y. Carpentier, C. Focsa, Nanoscale characterization of aircraft soot: A high-resolution transmission electron microscopy, Raman spectroscopy, X-ray photoelectron and near-edge X-ray absorption spectroscopy study, Carbon 101 (2016) 86–100. doi:10.1016/j.carbon.2016.01.040.

[22] R. L. Vander Wal, A. Yezerets, N. W. Currier, D. H. Kim, C. M. Wang, Hrtem study of diesel soot collected from diesel particulate filters, Carbon 45 (2007) 70–77. doi:10.1016/j.carbon.2006.08.005.

[23] M. L. Botero, Y. Sheng, J. Akroyd, J. Martin, J. A. Dreyer, W. Yang, M. Kraft, Internal structure of soot particles in a diffusion flame, Carbon 141 (2019) 635–642. doi:10.1016/j.carbon.2018.09.063.

[24] S. Di Stasio, Electron microscopy evidence of aggregation under three different size scales for soot nanoparticles in flame, Carbon 39 (2001) 109–118. doi:10.1016/S0008-6223(00)00099-3.

[25] M. Frenklach, Reaction mechanism of soot formation in flames, Physical Chemistry Chemical Physics 4 (2002) 2028–2037. doi:10.1039/b110045a.

[26] J.-O. Müller, D. S. Su, R. E. Jentoft, J. Kröhnert, F. C. Jentoft, R. Schlögl, Morphology-controlled reactivity of carbonaceous materials towards oxidation, Catalysis Today 102 (2005) 259–265. doi:10.1016/j.cattod.2005.02.025.

[27] K. Hayashida, S. Nagaoka, H. Ishitani, Growth and oxidation of graphitic crystallites in soot particles within a laminar diffusion flame, Fuel 128 (2014) 148–154. doi:10.1016/j.fuel.2014.03.008.

[28] T. S. Totton, D. Chakrabarti, A. J. Misquitta, M. Sander, D. J. Wales, M. Kraft, Modelling the internal structure of nascent soot particles, Combustion and Flame 157 (2010) 909–914. doi:10.1016/j.combustflame.2009.11.013.

[29] M. R. Kholghy, A. Veshkini, M. J. Thomson, The core–shell internal nanostructure of soot–a criterion to model soot maturity, Carbon 100 (2016) 508–536. doi:10.1016/j.carbon.2016.01.022.

[30] C. Irimiea, A. Faccinetto, X. Mercier, I. K. Ortega, N. Nuns, E. Therssen, P. Desgroux, C. Focsa, Unveiling trends in soot nucleation and growth: When secondary ion mass spectrometry meets statistical analysis, Carbon 144 (2019) 815–830. doi:10.1016/j.carbon.2018.12.015.

[31] P. Desgroux, A. Faccinetto, X. Mercier, T. Mouton, D. A. Karkar, A. El Bakali, Comparative study of the soot formation process in a "nucleation" and a "sooting" low pressure premixed methane flame, Combustion and Flame 184 (2017) 153–166. doi:10.1016/j.combustflame.2017.05.034.

© 2020 Tous droits réservés.

lilliad.univ-lille.fr

[32] M. Frenklach, A. M. Mebel, On the mechanism of soot nucleation, Physical Chemistry Chemical Physics 22 (9) (2020) 5314–5331. doi:10.1039/D0CP00116C.

[33] H. Wang, Formation of nascent soot and other condensed-phase materials in flames, Proceedings of the Combustion Institute 33 (2011) 41–67. doi:10.1016/j.proci.2010.09.009.

[34] S. Krishnan, K.-C. Lin, G. Faeth, Optical properties in the visible of overfire soot in large buoyant turbulent diffusion flames, Journal of Heat Transfer 122 (2000) 517–524. doi:10.1115/1.1288025.

[35] D. R. Snelling, F. Liu, G. J. Smallwood, Ö. L. Gülder, Determination of the soot absorption function and thermal accommodation coefficient using low-fluence lii in a laminar coflow ethylene diffusion flame, Combustion and Flame 136 (2004) 180–190. doi:10.1016/j.combustflame.2003.09.013.

[36] J. Yon, A. Bescond, F.-X. Ouf, A simple semi-empirical model for effective density measurements of fractal aggregates, Journal of Aerosol Science 87 (2015) 28–37. doi:10.1016/j.jaerosci.2015.05.00.

[37] R. W. Atkinson, G. W. Fuller, H. R. Anderson, R. M. Harrison, B. Armstrong, Urban ambient particle metrics and health: a time-series analysis, Epidemiology 21 (2010) 501–511. doi:10.1097/EDE.0b013e3181debc88.

[38] J. E. Dec, Advanced compression-ignition engines—understanding the in-cylinder processes, Proceedings of the Combustion Institute 32 (2009) 2727–2742. doi:10.1016/j.proci.2008.08.008.

[39] J. B. Heywood, Internal Combustion Engine Fundamentals, McGraw-Hill Education, New York, 2018.

[40] R. Stone, Introduction to Internal Combustion Engines, Macmillan, New York, 2012.

[41] S. Kook, L. M. Pickett, Soot volume fraction and morphology of conventional and surrogate jet fuel sprays at 1000 K and 6.7 MPa ambient conditions, Proceedings of the Combustion Institute 33 (2011) 2911–2918. doi:10.1016/j.proci.2010.05.073.

[42] P. Greening, European vehicle emission legislation—present and future, Topics in Catalysis 16 (2001) 5–13. doi:10.1023/A:1016629326634.

[43] H. Minoura, K. Takahashi, J. C. Chow, J. G. Watson, Multi-year trend in fine and coarse particle mass, carbon, and ions in downtown tokyo, japan, Atmospheric Environment 40 (2006) 2478–2487. doi:10.1016/j.atmosenv.2005.12.029.

[44] M. Williams, R. Minjares, A technical summary of Euro 6/VI vehicle emission standards, https://theicct.org/publications/technical-summary-euro-6vi-vehicle-emission-standards (2016).

© 2020 Tous droits réservés.

lilliad.univ-lille.fr

[45] G. Martini, B. Giechaskiel, P. Dilara, Future european emission standards for vehicles: the importance of the un-ece particle measurement programme, Biomarkers 14 (2009) 29–33. doi:10.1080/13547500902965393.

[46] B. Giechaskiel, P. Dilara, E. Sandbach, J. Andersson, Particle measurement programme (pmp) light-duty inter-laboratory exercise: comparison of different particle number measurement systems, Measurement Science and Technology 19 (2008) 095401. doi:10.1088/0957-0233/19/9/095401.

[47] J. Andersson, A. Mamakos, B. Giechaskiel, M. Carriero, G. Martini, Particle Measurement Programme (PMP) heavy-duty inter-laboratory correlation exercise (ILCE_HD), Scientific and Technical Research Reports, Publication Office of the European Union (2010). doi:10.2788/31407.

[48] B. Hassler, B. C. McDonald, G. J. Frost, A. Borbon, D. C. Carslaw, K. Civerolo, C. Granier, P. S. Monks, S. Monks, D. D. Parrish, et al., Analysis of long-term observations of nox and co in megacities and application to constraining emissions inventories, Geophysical Research Letters 43 (18) (2016) 9920–9930. doi:10.1002/2016GL069894.

[49] M. Raza, L. Chen, F. Leach, S. Ding, A review of particulate number (PN) emissions from gasoline direct injection (GDI) engines and their control techniques, Energies 11 (2018) 1417–1443. doi:10.3390/en11061417.

[50] P. Karjalainen, L. Pirjola, J. Heikkila, T. Lahde, T. Tzamkiozis, L. Ntziachristos, J. Keskinen, T. Ronkko, Exhaust particles of modern gasoline vehicles: A laboratory and an on-road study, Atmospheric Environment 97 (2014) 262–270. doi:10.1016/j.atmosenv.2014.08.025.

[51] A. Manke, L. Wang, Y. Rojanasakul, Mechanisms of nanoparticle-induced oxidative stress and toxicity, BioMed Research International 2013 (2013) 15 pp. doi:10.1155/2013/942916.

[52] T. Sager, V. Castranova, Surface area of particle administered versus mass in determining the pulmonary toxicity of ultrafine and fine carbon black: Comparison to ultrafine titanium dioxide, Particle and fibre toxicology 6 (2009) 15 pp. doi:10.1186/1743-8977-6-15.

[53] A. Seaton, L. Tran, R. Aitken, K. Donaldson, Surface area of particle administered versus mass in determining the pulmonary toxicity of ultrafine and fine carbon black: Comparison to ultrafine titanium dioxide, Journal of the Royal Society Interface 7 (2009) S119–S129. doi:10.1186/1743-8977-6-15.

[54] Environmental Protection Agency, Integrated science assessment for particulate matter, https://cfpub.epa.gov/ncea/isa/recordisplay.cfm?deid=216546 (2009).

[55] B. Giechaskiel, U. Manfredi, G. Martini, Engine exhaust solid sub-23 nm particles: I. literature survey, SAE International Journal of Fuels and Lubricants 7 (2014) 950–964. doi:10.4271/2014-01-2834.

© 2020 Tous droits réservés.

lilliad.univ-lille.fr

[56] K. Donaldson, X. Li, W. MacNee, Ultrafine (nanometre) particle mediated lung injury, SIAM Journal of Scientific Computing 29 (1998) 553–560. doi:10.1016/S0021-8502(97)00464-3.

[57] G. Oberdorster, Significance of particle parameters in the evaluation of exposure-dose relationships of inhaled particles, Inhalation Toxicology 8 (1996) 73–90. doi:10.1155/2013/942916.

[58] B. Giechaskiel, J. Vanhanen, M. Vakeva, G. Martini, Investigation of vehicle exhaust sub-23 nm particle emissions, Aerosol Science and Technology 51 (2017) 626–641. doi:10.4271/2014-01-2834.

[59] A. Kontses, G. Triantafyllopoulos, L. Ntziachristos, Z. Samaras, Particle number (PN) emissions from gasoline, diesel, LPG, CNG and hybrid-electric light-duty vehicles under real-world driving conditions, Atmospheric Environment 222 (2020) 117–126. doi:10.1016/j.atmosenv.2019.117126.

[60] L. Chasapidis, A. D. Melas, A. Tsakis, D. Zarvalis, A. Konstandopoulos, A sampling and conditioning particle system for solid particle measurements down to 10 nm, SAE International Journal of Advances and Current Practices in Mobility 2 (2019) 702–709. doi:10.4271/2019-24-0154.

[61] K. F. Lee, N. Eaves, S. Mosbach, D. Ooi, J. Lai, A. Bhave, A. Manz, J. N. Geiler, J. A. Noble, D. Duca, C. Focsa, Model guided application for investigating particle number (pn) emissions in gdi spark ignition engines, SAE International Journal of Advances and Current Practices in Mobility 1 (2019) 76–88. doi:10.4271/2019-26-0062.

[62] P. Simonen, J. Kalliokoski, P. Karjalainen, T. Rönkkö, H. Timonen, S. Saarikoski, M. Aurela, M. Bloss, G. Triantafyllopoulos, A. Kontses, et al., Characterization of laboratory and real driving emissions of individual euro 6 light-duty vehicles–fresh particles and secondary aerosol formation, Environmental Pollution 255 (2019) 113175. doi:10.1016/j.envpol.2019.113175.

[63] B. Giechaskiel, A. Zardini, G. Martini, Particle emission measurements from L-category vehicles, SAE International Journal of Engines 8 (2015) 2322–2337. doi:10.4271/2015-24-2512.

[64] S. Bekki, On the possible role of aircraft-generated soot in the middle latitude ozone depletion, Journal of Geophysical Research: Atmospheres 102 (1997) 10751–10758. doi:10.1029/97JD00134.

[65] R. Gao, B. Kärcher, E. Keim, D. Fahey, Constraining the heterogeneous loss of o3 on soot particles with observations in jet engine exhaust plumes, Geophysical research letters 25 (1998) 3323–3326. doi:10.1029/98GL02505.

[66] S. Kamm, O. Mohler, K.-H. Naumann, H. Saathoff, U. Schurath, The heterogeneous reaction of ozone with soot aerosol, Atmospheric Environment 33 (1999) 4651–4661. doi:10.1016/s1352-2310(99)00235-6.

© 2020 Tous droits réservés.

lilliad.univ-lille.fr

[67] D. Hauglustaine, B. Ridley, S. Solomon, P. Hess, S. Madronich, Hno3/nox ratio in the remote troposphere during mlopex 2: Evidence for nitric acid reduction on carbonaceous aerosols?, Geophysical Research Letters 23 (1996) 2609–2612. doi:10.1029/96GL02474.

[68] C. Longfellow, A. Ravishankara, D. Hanson, Reactive and nonreactive uptake on hydrocarbon soot: HNO_3, 0_3, and N_2O_5, Journal of Geophysical Research 105 (2000) 24345–24350. doi:10.1029/2000JD900297.

[69] B. Aumont, S. Madronich, M. Ammann, M. Kalberer, U. Baltensperger, D. Hauglustaine, F. Brocheton, On the NO_2^+ soot reaction in the atmosphere, Journal of Geophysical Research: Atmospheres 104 (1999) 1729–1736. doi:10.1029/1998JD100023.

[70] Y. Zhang, B. Yang, J. Gan, C. Liu, X. Shu, J. Shu, Nitration of particle-associated PAHs and their derivatives (nitro-, oxy-, and hydroxy-PAHs) with NO_3 radicals, Atmospheric Environment 45 (2011) 2515–2521. doi:10.1016/j.atmosenv.2011.02.034.

[71] D. U. Pedersen, J. L. Durant, K. Taghizadeh, H. F. Hemond, A. L. Lafleur, G. R. Cass, Human cell mutagens in respirable airborne particles from the northeastern United States. 2. Quantification of mutagens and other organic compounds, Environmental Science and Technology 39 (2005) 9547–9560. doi:10.1021/es050886c.

[72] M. R. Elamin, B. Y. Abdulkhair, A. O. Elzupir, Insight to aspirin sorption behavior on carbon nanotubes from aqueous solution: Thermodynamics, kinetics, influence of functionalization and solution parameters, Scientific Reports 9 (2019) 12795. doi:10.1038/s41598-019-49331-6.

[73] M. Ahmaruzzaman, D. Mohanta, A. Nath, Environmentally benign fabrication of SnO_2-CNT nanohybrids and their multifunctional efficiency as an adsorbent, catalyst and antimicrobial agent for water decontamination, Scientific Reports 9 (2019) 12795. doi:10.1038/s41598-019-49181-2.

[74] S. T. Lim, J. H. Kim, C. Y. Lee, S. Koo, D. Jerng, S. Wongwises, H. S. Ahn, Mesoporous graphene adsorbents for the removal of toluene and xylene at various concentrations and its reusability, Scientific Reports 9 (2019) 10922. doi:10.1038/s41598-019-47100-z.

[75] M. Darvish Ganji, H. Kiyani, Molecular simulation of efficient removal of H2S pollutant by cyclodextrine functionalized CNTs, Scientific Reports 9 (2019) 10605. doi:10.1038/s41598-019-46816-2.

[76] A. A. Specht, M. W. Blades, Direct determination of polycyclic aromatic hydrocarbons in solid matrices using laser desorption/laser photoionization ion trap mass spectrometry, Journal of the American Society for Mass Spectrometry 14 (2003) 562–570. doi:10.1016/S1044-0305(03)00143-0.

[77] D. Delhaye, F. X. Ouf, D. Ferry, I. K. Ortega, O. Penanhoat, S. Peillon, F. Salm, X. Vancassel, C. Focsa, C. Irimiea, N. Harivel, B. Perez, E. Quinton,

© 2020 Tous droits réservés.

lilliad.univ-lille.fr

J. Yon, D. Gaffie, The mermose project: Characterization of particulate matter emissions of a commercial aircraft engine, Journal of Aerosol Science 105 (2017) 48–63. doi:10.1016/j.jaerosci.2016.11.018.

[78] A. Faccinetto, C. Focsa, P. Desgroux, M. Ziskind, Progress toward the Quantitative Analysis of PAHs Adsorbed on Soot by Laser Desorption/Laser Ionization/Time-of-Flight Mass Spectrometry, Environmental Science and Technology 49 (2015) 10510–10520. doi:10.1021/acs.est.5b02703.

[79] J. Moldanová, E. Fridell, O. Popovicheva, B. Demirdjian, V. Tishkova, A. Faccinetto, C. Focsa, Characterisation of particulate matter and gaseous emissions from a large ship diesel engine, Atmospheric Environment 43 (2009) 2632–2641. doi:10.1016/j.atmosenv.2009.02.008.

[80] J. Swanson, D. Kittelson, M. Twigg, A Miniature Catalytic Stripper for Particles Less Than 23 Nanometers, SAE International 1570 (2013) 542–551. doi:10.4271/2013-01-1570.

[81] J. Ko, K. Kim, C. Chung, W.and Myung, S. Park, Characteristics of on-road particle number (PN) emissions from a GDI vehicle depending on a catalytic stripper (CS) and a metal-foam gasoline particulate filter (GPF), Fuel 238 (2019) 363–374. doi:10.1016/j.fuel.2018.10.091.

[82] R. Douglas, Closed-cycle studies of a two-stroke-cycle spark ignition engine, Ph.D. thesis, Queen's University, Belfast, Northern Ireland (UK) (1981).

[83] Y. Okada, S. Miyashita, Y. Izumi, Y. Hayakawa, Study of low-speed pre-ignition in boosted spark ignition engine, SAE International Journal of Engines 7 (2014) 584–594. doi:10.4271/2014-01-1218.

[84] C. Elliott, V. Vijayakumar, W. Zink, R. Hansen, National Instruments LabVIEW: A Programming Environment for Laboratory Automation and Measurement, Journal of Laboratory Automation 12 (2007) 17–24. doi:10.1016/j.jala.2006.07.012.

[85] L. D. Ngo, D. Duca, J. A. Noble, A. R. Ikhenazene, M. Vojkovic, Y. Carpentier, C. Irimiea, Chemical discrimination of the particulate and gas phases of miniCAST exhausts using a two-filter collection method, Atmospheric Measurement Techniques 13 (2020) 951–967. doi:10.5194/amt-13-951-2020.

[86] L. D. Ngo, Characterization of soot particles and their precursors produced during the combustion of conventional and alternative fuels: an in-situ laser diagnostics and ex-situ mass spectrometry investigation, Ph.D. thesis, University of Lille, Lille, France (2019).
URL http://www.theses.fr/2019LIL1R040

[87] V. A. Marple, K. L. Rubow, S. M. Behm, A microorifice uniform deposit impactor (MOUDI): Description, calibration, and use, Aerosol Science and Technology 14 (1991) 434–436. doi:10.1002/pssc.201600009.

[88] MSP Corporation (A TSI Company), NANO MOUDI – II User Guide (2015).

© 2020 Tous droits réservés.

lilliad.univ-lille.fr

[89] F. Tuinstra, J. L. Koenig, Raman Spectrum of Graphite, The Journal of Chemical Physics 53 (1970) 1126–1130. doi:10.1063/1.1674108.

[90] R. Saito, T. Takeya, T. Kimura, G. Dresselhaus, M. Dresselhaus, Raman intensity of single-wall carbon nanotubes, Physical Review B - Condensed Matter and Materials Physics 57 (1998) 4145–4153. doi:10.1103/PhysRevB.57.4145.

[91] L. Gao, W. Ren, B. Liu, R. Saito, Z. S. Wu, S. Li, C. Jiang, F. Li, H. M. Cheng, Surface and interference coenhanced Raman scattering of graphene, ACS Nano 3 (2009) 933–939. doi:10.1021/nn8008799.

[92] J. L. Holmes, C. Aubry, P. M. Mayer, Assigning Structures to Ions in Mass Spectrometry, CRC Press, New York, 2007.

[93] Y. J. Shi, R. H. Lipson, An overview of organic molecule soft ionization using vacuum ultraviolet laser radiation, Canadian Journal of Chemistry 83 (2005) 1891–1902. doi:10.1139/v05-193.

[94] S. A. Getty, W. B. Brinckerhoff, X. Li, J. Elsila, T. Cornish, S. Ecelberger, Q. Wu, R. Zare, A compact tandem two-step laser time-of-flight mass spectrometer for in situ analysis of non-volatile organics on planetary surfaces, IEEE Aerospace Conference Proceedings (2014) 2786–2790doi:10.1109/AERO.2014.6836334.

[95] J. C. Vickerman, D. Briggs, TOF-SIMS: Materials Analysis by Mass Spectrometry, IM Publications LLP, 2013.

[96] C. Focsa, C. Mihesan, M. Ziskind, B. Chazallon, E. Therssen, P. Desgroux, J. Destombes, Wavelength-selective vibrationally excited photodesorption with tunable ir sources, Journal of Physics: Condensed Matter 18 (2006) S1357–S1387. doi:10.1088/0953-8984/18/30/S02.

[97] K. Thomson, M. Ziskind, C. Mihesan, E. Therssen, P. Desgroux, C. Focsa, Influence of the photoionization process on the fragmentation of laser desorbed polycyclic aromatic hydrocarbons, Applied Surface Science 253 (2007) 6435–6441. doi:10.1016/j.apsusc.2007.01.050.

[98] A. Faccinetto, P. Desgroux, M. Ziskind, E. Therssen, C. Focsa, High-sensitivity detection of polycyclic aromatic hydrocarbons adsorbed onto soot particles using laser desorption/laser ionization/time-of-flight mass spectrometry: An approach to studying the soot inception process in low-pressure flames, Combustion and Flame 158 (2011) 227–239. doi:10.1016/j.combustflame.2010.08.012.

[99] C. Irimiea, A. Faccinetto, Y. Carpentier, I. K. Ortega, N. Nuns, E. Therssen, P. Desgroux, C. Focsa, A comprehensive protocol for chemical analysis of flame combustion emissions by secondary ion mass spectrometry, Rapid Communications in Mass Spectrometry 32 (2018) 1015–1025. doi:10.1002/rcm.8133.

© 2020 Tous droits réservés.

lilliad.univ-lille.fr

[100] J. Delhay, P. Desgroux, E. Therssen, H. Bladh, P. E. Bengtsson, H. Hönen, J. D. Black, I. Vallet, Soot volume fraction measurements in aero-engine exhausts using extinction-calibrated backward laser-induced incandescence, Applied Physics B: Lasers and Optics 95 (2009) 825–838. doi:10.1007/s00340-009-3534-8.

[101] R. Lemaire, A. Faccinetto, E. Therssen, M. Ziskind, C. Focsa, P. Desgroux, Experimental comparison of soot formation in turbulent flames of Diesel and surrogate Diesel fuels, Proceedings of the Combustion Institute 32 (2009) 737–744. doi:10.1016/j.proci.2008.05.019.

[102] D. Duca, C. Irimiea, A. Faccinetto, J. A. Noble, M. Vojkovic, Y. Carpentier, I. K. Ortega, C. Pirim, C. Focsa, On the benefits of using multivariate analysis in mass spectrometric studies of combustion-generated aerosols, Faraday Discussions 218 (2019) 115–137. doi:10.1039/C8FD00238J.

[103] C. Focsa, D. Duca, J. A. Noble, M. Vojkovic, Y. Carpentier, C. Pirim, C. Betrancourt, P. Desgroux, T. Trischer, J. Spielvogel, M. Rahman, A. Boies, K. F. Lee, A. N. Bhave, S. Legendre, O. Lancry, P. Kreutziger, M. Rieker, Multi-technique physico-chemical characterization of particles generated by a gasoline engine: towards measuring tailpipe emissions below 23 nm, Atmospheric Environment 235 (2020) 117642. doi:10.1016/j.atmosenv.2020.117642.

[104] R. F. Haglund Jr, Microscopic and mesoscopic aspects of laser-induced desorption and ablation, Applied surface science 96 (1996) 13pp. doi:10.1016/0169-4332(95)00371-1.

[105] A. Faccinetto, High sensitivity detection of Polycyclic Aromatic Hydrocarbons desorbed from soot particles using Laser Desorption/Laser Ionisation/Time-Of-Flight Mass Spectrometry : an approach for studying the soot growth process in flames, Ph.D. thesis, University of Lille, Lille, France (2009).

[106] L. V. Zhigilei, E. Leveugle, B. J. Garrison, Y. G. Yingling, M. I. Zeifman, Computer simulations of laser ablation of molecular substrates, Chemical reviews 103 (2003) 321–348. doi:10.1021/cr010459r.

[107] R. Kelly, A. Miotello, Comments on explosive mechanisms of laser sputtering, Applied Surface Science 96 (1996) 205–215. doi:10.1016/0169-4332(95)00481-5.

[108] C. Mihesan, N. Lebrun, M. Ziskind, B. Chazallon, C. Focsa, J. Destombes, Ir laser resonant desorption of formaldehyde–H_2O ices: hydrated cluster formation and velocity distribution, Surface science 566 (2004) 650–658. doi:10.1016/j.susc.2004.06.128.

[109] P. Desgroux, X. Mercier, K. A. Thomson, Study of the formation of soot and its precursors in flames using optical diagnostics, Proceedings of the Combustion Institute 34 (2013) 1713–1738. doi:10.1016/j.proci.2012.09.004.

[110] O. P. Haefliger, R. Zenobi, Laser mass spectrometric analysis of polycyclic aromatic hydrocarbons with wide wavelength range laser multiphoton ionization spectroscopy., Analytical chemistry 70 (1998) 2660–2665. doi:10.1021/ac971264f.

© 2020 Tous droits réservés.

lilliad.univ-lille.fr

[111] R. Hilbig, R. Wallenstein, Narrow-band tunable VUV radiation generated by nonresonant sum- and difference-frequency mixing in xenon and krypton, Applied optics 21 (1982) 913–917. doi:10.1364/AO.21.000913.

[112] B. A. Mamyrin, Time-of-flight mass spectrometry (concepts, achievements, and prospects), International Journal of Mass Spectrometry 206 (2001) 251–266. doi:10.1016/S1387-3806(00)00392-4.

[113] H. Sabbah, A. Bonnamy, D. Papanastasiou, J. Cernicharo, J.-A. Martín-Gago, C. Joblin, Identification of pah isomeric structure in cosmic dust analogs: the aroma setup, The Astrophysical Journal 843 (1) (2017) 34. doi:10.3847/1538-4357/aa73dd.

[114] L. Martínez, G. Santoro, P. Merino, M. Accolla, K. Lauwaet, J. Sobrado, H. Sabbah, R. J. Pelaez, V. J. Herrero, I. Tanarro, et al., Prevalence of non-aromatic carbonaceous molecules in the inner regions of circumstellar envelopes, Nature astronomy 4 (2019) 97–105. doi:10.1038/s41550-019-0899-4.

[115] D. Papanastasiou, L. Ding, E. Raptakis, I. Brookhouse, J. Cunningham, M. Robinson, Dynamic pressure measurements during pulsed gas injection in a quadrupole ion trap, Vacuum 81 (2006) 446–452. doi:10.1016/j.vacuum.2006.06.013.

[116] D. Papanastasiou, O. Belgacem, M. Sudakov, E. Raptakis, Ion thermalization using pressure transients in a quadrupole ion trap coupled to a vacuum matrix-assisted laser desorption ionization source and a reflectron time-of-flight mass analyzer, Review of Scientific Instruments 79 (2008) 055103. doi:10.1063/1.2919881.

[117] A. A. Shvartsburg, R. D. Smith, Fundamentals of traveling wave ion mobility spectrometry, Analytical chemistry 80 (2008) 9689–9699. doi:10.1021/ac8016295.

[118] L. Sleno, The use of mass defect in modern mass spectrometry, Journal of Mass Spectrometry 47 (2012) 226–236. doi:10.1002/jms.2953.

[119] C. A. Hughey, C. L. Hendrickson, R. P. Rodgers, A. G. Marshall, K. Qian, Kendrick mass defect spectrum: a compact visual analysis for ultrahigh-resolution broadband mass spectra, Analytical Chemistry 73 (19) (2001) 4676–4681. doi:10.1021/ac010560w.

[120] C. Irimiea, A. Faccinetto, Y. Carpentier, I. K. Ortega, N. Nuns, E. Therssen, P. Desgroux, C. Focsa, A comprehensive protocol for chemical analysis of flame combustion emissions by secondary ion mass spectrometry, Rapid Communications in Mass Spectrometry 32 (2018) 1015–1025. doi:10.1002/rcm.8133.

[121] A. G. Brenton, A. R. Godfrey, Accurate mass measurement: Terminology and treatment of data, Journal of the American Society for Mass Spectrometry 21 (2010) 1821–1835. doi:10.1016/j.jasms.2010.06.006.

© 2020 Tous droits réservés.

lilliad.univ-lille.fr

[122] A. Kassambara, Practical Guide To Principal Component Methods in R: PCA, M (CA), FAMD, MFA, HCPC, factoextra., Vol. 2, STHDA, 2017.

[123] H. Abdi, L. Williams, Principal component analysis, Wiley interdisciplinary reviews: computational statistics 2 (2010) 433–470. doi:10.1002/wics.101.

[124] T. Adam, R. R. Baker, R. Zimmermann, Characterization of puff-by-puff resolved cigarette mainstream smoke by single photon ionization-time-of-flight mass spectrometry and principal component analysis, Journal of Agricultural and Food Chemistry 55 (2007) 2055–2061. doi:10.1021/jf062360x.

[125] P. Cejnar, S. Kuckova, A. Prochazka, L. Karamonova, B. Svobodova, Principal component analysis of normalized full spectrum mass spectrometry data in multiMS-toolbox: An effective tool to identify important factors for classification of different metabolic patterns and bacterial strains, Rapid Communications in Mass Spectrometry 32 (2018) 871–881. doi:10.1002/rcm.8110.

[126] T. Alexandrov, MALDI imaging mass spectrometry: statistical data analysis and current computational challenges, BMC Bioinformatics 13 (2012) S11. doi:10.1186/1471-2105-13-S16-S11.

[127] J. V. Bradley, The insidious L-shaped distribution, Bulletin of the Psychonomic Society 20 (1982) 85–88. doi:10.3758/BF03330089.

[128] A. F. Vermeulen, Industrial Machine Learning. Using Artificial Intelligence as a Transformational Disruptor, 2020. doi:10.1007/978-1-4842-5316-8.

[129] L. I. Smith, A Principal Components Analysis Introduction, Statistics 51 (2002) 52. doi:10.1080/03610928808829796.

[130] P. R. Peres-Neto, D. A. Jackson, K. M. Somers, How many principal components? stopping rules for determining the number of non-trivial axes revisited, Computational Statistics and Data Analysis 49 (2005) 974–997. doi:10.1016/j.csda.2004.06.015.

[131] L. Pei, G. Jiang, B. J. Tyler, L. L. Baxter, M. R. Linford, Time-of-flight secondary ion mass spectrometry of a range of coal samples: A chemometrics (PCA, cluster, and PLS) analysis, Energy and Fuels 22 (2008) 1059–1072. doi:10.1021/ef7003199.

[132] R. Alvin C, Methods of multivariate analysis, Vol. 59, Wiley, 2000. doi:10.1016/S0378-3758(96)00098-5.

[133] P. Reitz, S. R. Zorn, S. H. Trimborn, A. M. Trimborn, A new, powerful technique to analyze single particle aerosol mass spectra using a combination of OPTICS and the fuzzy c-means algorithm, Journal of Aerosol Science 98 (2016) 1–14. doi:10.1016/j.jaerosci.2016.04.003.

[134] W. Li, Volcano plots in analyzing differential expressions with mRNA microarrays, Journal of Bioinformatics and Computational Biology 10 (2012) 1231003. doi:10.1142/S0219720012310038.

© 2020 Tous droits réservés.

lilliad.univ-lille.fr

[135] P. Baldi, A. D. Long, A Bayesian framework for the analysis of microarray expression data : regularized t-test, Bioinformatics 17 (2001) 509–519. doi:10.1093/bioinformatics/17.6.509.

[136] L. Shi, W. Tong, H. Fang, U. Scherf, J. Han, R. K. Puri, F. W. Frueh, F. M. Goodsaid, L. Guo, Z. Su, T. Han, J. C. Fuscoe, Z. A. Xu, T. A. Patterson, H. Hong, Q. Xie, R. G. Perkins, J. J. Chen, D. A. Casciano, Cross-platform comparability of microarray technology: Intra-platform consistency and appropriate data analysis procedures are essential, BMC Bioinformatics 6 (2005) S12–S26. doi:10.1186/1471-2105-6-S2-S12.

[137] J. Stolcpartova, M. Pechout, L. Dittrich, M. Mazac, M. Fenkl, K. Vrbova, J. Ondracek, M. Vojtisek-Lom, Internal combustion engines as the main source of ultrafine particles in residential neighborhoods: Field measurements in the czech republic, Atmosphere 6 (2015) 1714–1735. doi:10.3390/atmos6111714.

[138] C. K. Gaddam, R. L. Wal, Physical and chemical characterization of SIDI engine particulates, Combustion and Flame 160 (2013) 2517–2528. doi:10.1016/j.combustflame.2013.05.025.

[139] P. Price, R. Stone, D. Oudenijeweme, X. Chen, Cold Start Particulate Emissions from a Second Generation DI Gasoline Engine, SAE International 1931 (2007) 1738–1752. doi:10.4271/2007-01-1931.

[140] C. D. Lagally, C. C. O. Reynolds, A. P. Grieshop, M. Kandlikar, S. N. Rogak, Carbon nanotube and fullerene emissions from spark-ignited engines, Aerosol Science and Technology 46 (2012) 156–164. doi:10.1080/02786826.2011.617399.

[141] J. J. Swanson, R. Febo, A. M. Boies, D. B. Kittelson, Fuel Sulfur and Iron Additives Contribute to the Formation of Carbon Nanotube-like Structures in an Internal Combustion Engine, Environmental Science and Technology Letters 3 (2016) 364–368. doi:10.1021/acs.estlett.6b00313.

[142] V. B. Malmborg, A. C. Eriksson, S. Török, Y. Zhang, K. Kling, J. Martinsson, E. C. Fortner, L. Gren, S. Kook, T. B. Onasch, P. E. Bengtsson, J. Pagels, Relating aerosol mass spectra to composition and nanostructure of soot particles, Carbon 142 (2019) 535–546. doi:10.1016/j.carbon.2018.10.072.

[143] Z. Li, C. Song, J. Song, G. Lv, S. Dong, Z. Zhao, Evolution of the nanostructure, fractal dimension and size of in-cylinder soot during diesel combustion process, Combustion and Flame 158 (2011) 1624–1630. doi:10.1016/j.combustflame.2010.12.006.

[144] C. Messaoudil, T. Boudier, C. O. S. Sorzano, S. Marco, TomoJ: Tomography software for three-dimensional reconstruction in transmission electron microscopy, BMC Bioinformatics 8 (2007) 288. doi:10.1186/1471-2105-8-288.

[145] G. T. Herman, A. Lent, S. W. Rowland, Mathematics and Applications, Journal of Theoretical Biology 42 (1973) 1–32. doi:10.1142/9789812567130_0038.

© 2020 Tous droits réservés.

lilliad.univ-lille.fr

[146] A. Sadezky, H. Muckenhuber, H. Grothe, R. Niessner, U. Pöschl, Raman microspectroscopy of soot and related carbonaceous materials: Spectral analysis and structural information, Carbon 43 (2005) 1731–1742. doi:10.1016/j.carbon.2005.02.018.

[147] Y. Carpentier, G. Féraud, E. Dartois, R. Brunetto, E. Charon, A. Cao, L. D'Hendecourt, P. Bréchignac, J. Rouzaud, T. Pino, Nanostructuration of carbonaceous dust as seen through the positions of the 6.2 and 7.7 μm AIBs, Astronomy and Astrophysics 548 (2012) A40. doi:10.1051/0004-6361/201118700.

[148] X. Huang, I. O. Olmez, N. K. Aras, G. E. Gordon, Emissions of trace elements from motor vehicules: Potential marker elements and source composition, Atmospheric Environment 28 (1994) 1385–1391. doi:10.1016/1352-2310(94)90201-1.

[149] S. H. Cadle, P. a. Mulawa, J. Ball, C. Donase, a. Weibel, J. C. Sagebiel, K. T. Knapp, R. Snow, Particulate emission rates from in use high emitting vehicles recruited in Orange County, California, Environmental Science and Technology 31 (1997) 3405–3412. doi:10.1021/es9700257.

[150] E. S. Cross, A. Sappok, E. C. Fortner, J. F. Hunter, J. T. Jayne, W. A. Brooks, T. B. Onasch, V. W. Wong, A. Trimborn, D. R. Worsnop, J. H. Kroll, Real-Time Measurements of Engine-Out Trace Elements: Application of a Novel Soot Particle Aerosol Mass Spectrometer for Emissions Characterization, Journal of Engineering for Gas Turbines and Power 134 (2012) 72801. doi:10.1115/1.4005992.

[151] T. R. Dallmann, T. B. Onasch, T. W. Kirchstetter, D. R. Worton, E. C. Fortner, S. C. Herndon, E. C. Wood, J. P. Franklin, D. R. Worsnop, A. H. Goldstein, R. A. Harley, Characterization of particulate matter emissions from on-road gasoline and diesel vehicles using a soot particle aerosol mass spectrometer, Atmospheric Chemistry and Physics 14 (2014) 7585–7599. doi:10.5194/acp-14-7585-2014.

[152] M. A. Bari, G. Baumbach, B. Kuch, G. Scheffknecht, Particle-phase concentrations of polycyclic aromatic hydrocarbons in ambient air of rural residential areas in southern Germany, Air Quality, Atmosphere and Health 3 (2010) 103–116. doi:10.1007/s11869-009-0057-8.

[153] O. B. Popovicheva, C. Irimiea, Y. Carpentier, I. K. Ortega, E. D. Kireeva, N. K. Shonija, J. Schwarz, M. Vojtíšek-Lom, C. Focsa, Chemical composition of diesel/biodiesel particulate exhaust by FTIR spectroscopy and mass spectrometry: Impact of fuel and driving cycle, Aerosol and Air Quality Research 17 (2017) 1717–1734. doi:10.4209/aaqr.2017.04.0127.

[154] F. T. Fred W. McLafferty, F. McLafferty, F. Tureek, Interpretation of Mass Spectra, University Science Books, Mill Valley, CA, 1993.

[155] H. J. Tobias, D. E. Beving, P. J. Ziemann, H. Sakurai, M. Zuk, P. H. McMurry, D. Zarling, R. Waytulonis, D. B. Kittelson, Chemical analysis of diesel engine nanoparticles using a nano-DMA/thermal desorption particle beam mass

© 2020 Tous droits réservés.

lilliad.univ-lille.fr

spectrometer, Environmental Science and Technology 35 (2001) 2233–2243. doi:10.1021/es0016654.

[156] H. Sakurai, H. J. Tobias, K. Park, D. Zarling, K. S. Docherty, D. B. Kittelson, P. H. McMurry, P. J. Ziemann, On-line measurements of diesel nanoparticle composition and volatility, Atmospheric Environment 37 (2003) 1199–1210. doi:10.1016/S1352-2310(02)01017-8.

[157] N. Hansen, S. J. S. S. J. Klippenstein, P. R. P. Westmoreland, T. Kasper, K. Kohse-Höinghaus, J. Wang, T. A. T. Cool, T. Kohse-Höinghaus, J. Wang, T. A. T. Cool, K. Kohse-Höinghaus, J. Wang, T. A. T. Cool, A combined ab initio and photoionization mass spectrometric study of polyynes in fuel-rich flames., Physical Chemistry Chemical Physics 10 (2008) 366–374. doi:10.1039/b711578d.

[158] Y. Li, L. Zhang, Z. Tian, T. Yuan, K. Zhang, B. Yang, F. Qi, Investigation of the rich premixed laminar acetylene/oxygen/argon flame: Comprehensive flame structure and special concerns of polyynes, Proceedings of the Combustion Institute 32 (2009) 1293–1300. doi:10.1016/j.proci.2008.07.009.

[159] N. Patil, A. Poul, A. Patil, R. N. Yerrawat, Literature Review on Effect of Oxygenated Additives on S.I. Engine Performance and Emissions, International Journal of Engineering, Business and Enterprise Applications 10 (2014) 73–76.

[160] G. Wang, K. Kawamura, M. Xie, S. Hu, S. Gao, J. Cao, Z. An, Z. Wang, Size-distributions of n-alkanes, PAHs and hopanes and their sources in the urban, mountain and marine atmospheres over East Asia, Atmospheric Chemistry and Physics 9 (2009) 8869–8882. doi:10.5194/acp-9-8869-2009.

[161] J. Pagels, D. D. Dutcher, M. R. Stolzenburg, P. H. Mcmurry, M. E. Gälli, D. S. Gross, Fine-particle emissions from solid biofuel combustion studied with single-particle mass spectrometry: Identification of markers for organics, soot, and ash components, Journal of Geophysical Research Atmospheres 118 (2013) 859–870. doi:10.1029/2012JD018389.

[162] S. Gilardoni, L. M. Russell, A. Sorooshian, R. C. Flagan, J. H. Seinfeld, T. S. Bates, P. K. Quinn, J. D. Allan, B. Williams, A. H. Goldstein, T. B. Onasch, D. R. Worsnop, Regional variation of organic functional groups in aerosol particles on four U.S. east coast platforms during the International Consortium for Atmospheric Research on Transport and Transformation 2004 campaign, Journal of Geophysical Research Atmospheres 112 (2007) D10S27. doi:10.1029/2006JD007737.

[163] U. Kirchner, R. Vogt, C. Natzeck, J. Goschnick, Single particle MS, SNMS, SIMS, XPS, and FTIR spectroscopic analysis of soot particles during the AIDA campaign, Journal of Aerosol Science 34 (2003) 1323–1346. doi:10.1016/S0021-8502(03)00362-8.

[164] European Commission, Commission regulation (EU) 2017/1154, Official Journal of the European Union 1154 (2017) 708–732. doi:10.1016/j.proci.2010.07.039.

© 2020 Tous droits réservés.

lilliad.univ-lille.fr

[165] S. E. Stein, A. Fahr, High-temperature stabilities of hydrocarbons, Journal of Physical Chemistry 89 (1985) 3714–3725. doi:10.1021/j100263a027.

[166] T. D. Burchell, Carbon Materials for Advanced Technologies, Elsevier Science Ltd, 1999. doi:10.1016/B978-008042683-9/50002-9.

[167] A. Jorio, G. Dresselhaus, M. S. Dresselhaus, Carbon Nanotubes. Advanced Topics in the Synthesis, Structure, Properties and Applications, Springer, 2007. doi:10.1071/978-3-540-72865-8.

[168] Z. Zhang, S. Yang, H. Li, Y. Zan, X. Li, Y. Zhu, M. Dou, F. Wang, Sustainable Carbonaceous Materials Derived from Biomass as Metal-Free Electrocatalysts, Advanced Materials 31 (2019) 1805718. doi:10.1002/adma.201805718.

[169] M. Inagaki, F. Kang, M. Toyoda, H. Konno, Carbon Materials for Adsorption of Molecules and Ions, Advanced Materials Science and Engineering of Carbon 5 (2014) 335–361. doi:10.1016/b978-0-12-407789-8.00015-6.

[170] A. A. Abia, E. D. Asuquo, Lead (II) and nickel (II) adsorption kinetics from aqueous metal solutions using chemically modified and unmodified agricultural adsorbents, African Journal of Biotechnology 5 (2006) 1475–1482.

[171] R. Ahmad, S. Haseeb, Adsorption of Pb(II) on Mentha piperita carbon (MTC) in single and quaternary systems, Arabian Journal of Chemistry 10 (2017) S412–S421. doi:10.1016/j.arabjc.2012.09.013.

[172] L. Basta, S. Veronesi, Y. Murata, Z. Dubois, N. Mishra, F. Fabbri, C. Coletti, S. Heun, A sensitive calorimetric technique to study energy (heat) exchange at the nano-scale, Nanoscale 10 (2018) 10079–10086. doi:10.1039/C8NR00747K.

[173] C. T. Campbell, J. R. Sellers, Enthalpies and entropies of adsorption on well-defined oxide surfaces: Experimental measurements, Chemical Reviews 113 (2013) 4106–4135. doi:10.1021/cr300329s.

[174] A. Saha, A simultaneous volumetric adsorption–isothermal titration calorimetry study of small molecules on supported metallic nanoparticles, Journal of Thermal Analysis and Calorimetry 124 (2016) 1623–1634. doi:10.1007/s10973-016-5262-8.

[175] J. L. Falconer, J. A. Schwarz, Temperature-programmed desorption and reaction: applications to supported catalysts, Catalysis Reviews Science and Engineering 25 (1983) 141–227. doi:10.1080/01614948308079666.

[176] R. A. Ketola, J. T. Kiuru, V. Tarkiainen, J. T. Kokkonen, J. Räsänen, T. Kotiaho, Detection of volatile organic compounds by temperature-programmed desorption combined with mass spectrometry and fourier transform infrared spectroscopy, Analytica chimica acta 562 (2006) 245–251. doi:10.1016/j.aca.2006.01.069.

[177] J. T. Stuckless, D. E. Starr, D. J. Bald, C. T. Campbell, J. T. Stuckless, D. E. Starr, D. J. Bald, C. T. Campbell, Metal adsorption calorimetry and adhesion energies on clean single-crystal surfaces Metal adsorption calorimetry

© 2020 Tous droits réservés.

lilliad.univ-lille.fr

and adhesion energies on clean single-crystal surfaces, Journal of Chemical Physics 107 (1997) 5547–5553. doi:10.1063/1.474230.

[178] W. A. Brown, R. Kose, D. A. King, Femtomole Adsorption Calorimetry on Single-Crystal Surfaces, Chemical Reviews 98 (1998) 797–831. doi:10.1021/cr9700890.

[179] J.-H. Fischer-Wolfarth, J. A. Farmer, J. M. Flores-Camacho, A. Genest, I. V. Yudanov, N. Rösch, C. T. Campbell, S. Schauermann, H.-J. Freund, Particle-size dependent heats of adsorption of CO on supported Pd nanoparticles as measured with a single-crystal microcalorimeter, Physical Review B 81 (2010) 241416. doi:10.1103/PhysRevB.81.241416.

[180] S. M. Bedair, H. P. Smith, Atomically clean surfaces by pulsed laser bombardment, Journal of Applied Physics 40 (1969) 4776–4781. doi:10.1063/1.1657288.

[181] D. H. Auston, J. A. Golovchenko, A. L. Simons, C. M. Surko, T. N. C. Venkatesan, Dynamics of Q-switched laser annealing, Applied Physics Letters 34 (1979) 777–779. doi:10.1063/1.90670.

[182] A. Pospieszczyk, P. Bogen, H. Hartwig, Y. T. Lie, Determination of low surface coverages of H_2 and CO by vacuum UV-resonance fluorescence spectroscopy of laser desorbed particles, Journal of Nuclear Materials 94 (1980) 368–376. doi:10.1016/0022-3115(80)90350-5.

[183] F. Schwirzke, L. Oren, S. Talmadge, R. J. Taylor, Laser-induced desorption of impurities from the macrotor tokamak walls, Physical Review Letters 40 (1978) 1181–1184. doi:10.1103/PhysRevLett.40.1181.

[184] A. Faccinetto, K. Thomson, M. Ziskind, C. Focsa, Coupling of desorption and photoionization processes in two-step laser mass spectrometry of polycyclic aromatic hydrocarbons, Applied Physics A: Materials Science and Processing 92 (2008) 969–974. doi:10.1007/s00339-008-4605-0.

[185] S. M. George, A. M. DeSantolo, R. B. Hall, Surface diffusion of Hydrogen on Ni(100) studied using lase-induced thermal desorption, Surface Science 159 (1985) L425–L432. doi:10.1016/0039-6028(85)90097-4.

[186] R. B. Hall, A. M. Desantolo, Pulsed Laser Induced excitation of metal surfaces: Application as a probe of surface reaction kinetics of methanol on Ni, Surface Science 137 (1984) 421–441. doi:10.1016/0039-6028(84)90521-1.

[187] L. P. Levine, J. F. Ready, E. Bernal, Gas desorption produced by a giant pulse laser, Journal of Applied Physics 38 (1967) 331–336. doi:10.1063/1.1708977.

[188] R. R. Lucchese, J. C. Tully, Laser induced thermal desorption from surfaces, The Journal of Chemical Physics 81 (1984) 6313–6319. doi:10.1063/1.447540.

[189] A. Pospieszczyk, J. A. Tagle, Adsorption behaviour of H_2 and CO on inconel 600 surfaces under laser-induced thermal desorption, Journal of Nuclear Materials 105 (1982) 14–22. doi:10.1016/0022-3115(82)90447-0.

© 2020 Tous droits réservés.

lilliad.univ-lille.fr

[190] K. Christmann, O. Schober, G. Ertl, M. Neumann, Adsorption of hydrogen on nickel single crystal surfaces, The Journal of Chemical Physics 4528 (1974) 4528–4540. doi:10.1063/1.1680935.

[191] J. M. Chen, C. C. Chang, Laser desorption of submonolayers of Na and Cs from Ge substrates, Journal of Applied Physics 43 (1972) 3884–3886. doi:10.1063/1.1661832.

[192] G. Wedler, H. Ruhmann, Laser induced thermal desorption of carbon monoxide from Fe(110) surfaces, Surface science 121 (1982) 464–486. doi:10.1016/0039-6028(82)90255-2.

[193] H. Arnolds, C. Rehbein, G. Roberts, R. J. Levis, D. A. King, Femtosecond Near-Infrared Laser Desorption of Multilayer Benzene on Pt(111): A Molecular Newton's Cradle?, Journal of Physical Chemistry B 104 (2002) 3375–3382. doi:10.1021/jp993688e.

[194] J. L. Brand, S. M. George, Effects of laser pulse characteristics and thermal desorption parameters on laser induced thermal desorption, Surface Science 167 (1986) 341–362. doi:10.1016/0039-6028(86)90709-0.

[195] K. Dreisewerd, M. Schürenberg, M. Karas, F. Hillenkamp, Influence of the laser intensity and spot size on the desorption of molecules and ions in matrix-assisted laser desorption/ionization with a uniform beam profile, International Journal of Mass Spectrometry and Ion Processes 141 (1995) 127–148. doi:10.1016/0168-1176(94)04108-J.

[196] J. P. Abrahamson, M. Singh, J. P. Mathews, R. L. Vander Wal, Pulsed laser annealing of carbon black, Carbon 124 (2017) 380–390. doi:10.1016/j.carbon.2017.08.080.

[197] E. Cappelli, C. Scilletta, S. Orlando, V. Valentini, M. Servidori, Laser annealing of amorphous carbon films, Applied Surface Science 255 (2009) 5620–5625. doi:10.1016/j.apsusc.2008.10.062.

[198] C. Mihesan, M. Ziskind, E. Therssen, P. Desgroux, C. Focsa, IR laser resonant desorption of polycyclic aromatic hydrocarbons, Chemical Physics Letters 423 (2006) 407–412. doi:10.1016/j.cplett.2006.04.032.

[199] A. Puretzky, D. Geohegan, G. Hurst, M. Buchanan, B. Luk'yanchuk, Imaging of vapor plumes produced by matrix assisted laser desorption: a plume sharpening effect, Physical Review Letters 83 (1999) 444. doi:10.1103/PhysRevLett.83.444.

[200] S. Ahn, D. Werner, H. K. Karapanagioti, D. R. McGlothlin, R. N. Zare, R. G. Luthy, Phenanthrene and pyrene sorption and intraparticle diffusion in polyoxymethylene, coke, and activated carbon, Environmental Science and Technology 39 (2005) 6516–6526. doi:10.1021/es050113o.

[201] A. P. G. Arthur W. Adamson, Physical chemistry of surfaces, Wiley-Interscience publication, New York, 1982.

© 2020 Tous droits réservés.

lilliad.univ-lille.fr

[202] R. M. Bouglas, Principles of adsorption and adsorption processes, Wiley-Interscience publication, New York, 1984.

[203] K. Oure, V. G. Lifshits, A. A. Saranin, A. V. Zotov, M. Katayama, Surface Science: An Introduction, Springer, Berlin, 2003.

[204] K. Christmann, Introduction to Surface Physical Chemistry, Springer, Heidelberg, 1991.

[205] R. J. Beuhler, E. Flanigan, L. J. Greene, L. Friedman, Proton transfer mass spectrometry of peptides. rapid heating technique for underivatized peptides containing arginine, Journal of the American Chemical Society 96 (1974) 3990–3999. doi:10.1021/ja00819a043.

[206] W. H. Dalzell, a. F. Sarofim, Optical Constants of Soot and Their Application to Heat-Flux Calculations, Journal of Heat Transfer 91 (1969) 100. doi:10.1115/1.3580063.

[207] A. B. Djurišić, E. H. Li, Optical properties of graphite, Journal of Applied Physics 85 (1999) 7404–7410. doi:10.1063/1.369370.

[208] R. J. M. Konings, Comprehensive Nuclear Materials, Material Properties - Oxide Fuels for Light Water Reactors and Fast Neutron Reactors, Elsevier, 2012. doi:10.1016/B978-0-08-056033-5.90001-6.

[209] A. Butland, R. Maddison, The specific heat of graphite: an evaluation of measurements, Journal of Nuclear Materials 49 (1973) 45–56. doi:10.1016/0022-3115(73)90060-3.

[210] A. Bogaerts, Z. Chen, R. Gijbels, A. Vertes, Laser ablation for analytical sampling: what can we learn from modeling?, Spectrochimica Acta Part B: Atomic Spectroscopy 58 (2003) 1867–1893. doi:10.1016/j.sab.2003.08.004.

[211] D. Burgess Jr., P. C. Stair, E. Weitz, Calculations of the surface temperature rise and desorption temperature in laser-induced thermal desorption, Journal of Vacuum Science and Technology A 4 (1986) 1362 – 1366. doi:10.1116/1.573571.

[212] P. C. Stair, E. Weitz, Pulsed-laser-induced desorption from metal surfaces, Journal of the Optical Society of America B 4 (1987) 255–260. doi:10.1364/JOSAB.4.000255.

[213] J. Ho, C. Grigoropoulos, J. Humphrey, Computational study of heat transfer and gas dynamics in the pulsed laser evaporation of metals, Journal of Applied Physics 78 (1995) 4696–4709. doi:10.1063/1.359817.

[214] J. Bechtel, Heating of solid targets with laser pulses, Journal of Applied Physics 46 (1975) 1585–1593. doi:10.1063/1.321760.

[215] E. V. Gurentsov, A review on determining the refractive index function, thermal accommodation coefficient and evaporation temperature of light-absorbing nanoparticles suspended in the gas phase using the laser-induced

© 2020 Tous droits réservés.

lilliad.univ-lille.fr

incandescence, Nanotechnology Reviews 7 (2018) 583–604. doi:10.1515/ntrev-2018-0080.

[216] W. D. Ciro, E. G. Eddings, A. F. Sarofim, Experimental and numerical investigation of transient soot buildup on a cylindrical container immersed in a jet fuel pool fire, Combustion Science and Technology 178 (2006) 2199–2218. doi:10.1080/00102200600626108.

[217] C. Pradère, J.-C. Batsale, J.-M. Goyhénèche, R. Pailler, S. Dilhaire, Thermal properties of carbon fibers at very high temperature, Carbon 47 (2009) 737–743. doi:10.1016/j.carbon.2008.11.015.

[218] Engineering ToolBox, Air – Thermal Conductivity (2009), https://www.engineeringtoolbox.com/air-properties-viscosity-conductivity-heat-capacity-d_1509.html, accessed: 25-04-2020 (2009).

[219] R. Zacharia, H. Ulbricht, T. Hertel, Interlayer cohesive energy of graphite from thermal desorption of polyaromatic hydrocarbons, Physical Review B 69 (2004) 155406. doi:10.1103/PhysRevB.69.155406.

[220] A. Guilloteau, M. L. Nguyen, Y. Bedjanian, G. Le Bras, Desorption of polycyclic aromatic hydrocarbons from soot surface: Pyrene and fluoranthene, Journal of Physical Chemistry A 112 (2008) 10552–10559. doi:10.1021/jp803043s.

[221] Y. Bedjanian, M. L. Nguyen, A. Guilloteau, Desorption of polycyclic aromatic hydrocarbons from soot surface: five- and six-ring PAHs., Journal of Physical Chemistry 114 (2010) 3533–3539. doi:10.1021/jp912110b.

[222] K. A. Fichthorn, R. A. Miron, Thermal desorption of large molecules from solid surfaces, Physical Review Letters 89 (2002) 196103. doi:10.1103/PhysRevLett.89.196103.

[223] X. L. Han, Monte Carlo Least-Squares Fitting of Experimental Signal Waveforms Random Walk Method Testing the Fitting Algorithm, Journal of Information and Computational Science 4 (2006) 1548–1555, URL: https://digitalcommons.butler.edu/facsch_papers/750.

[224] J. Dunkley, M. Bucher, P. G. Ferreira, K. Moodley, C. Skordis, Fast and reliable Markov chain Monte Carlo technique for cosmological parameter estimation, Monthly Notices of the Royal Astronomical Society 356 (2005) 925–936. doi:10.1111/j.1365-2966.2004.08464.x.

[225] J. Akeret, S. Seehars, A. Amara, A. Refregier, A. Csillaghy, CosmoHammer: Cosmological parameter estimation with the MCMC Hammer, Astronomy and Computing 2 (2013) 27–39. doi:10.1016/j.ascom.2013.06.003.

[226] D. Foreman-Mackey, D. W. Hogg, D. Lang, J. Goodman, EMCEE: The MCMC Hammer, Publications of the Astronomical Society of the Pacific 125 (2012) 306–312. doi:10.1086/670067.

© 2020 Tous droits réservés.

lilliad.univ-lille.fr

[227] S. T. Buckland, K. P. Burnham, N. H. Augustin, Model selection: an integral part of inference, Biometrics 53 (1997) 603–618. doi:10.2307/2533961.

[228] E. Slud, I. Vonta, A. Kagan, Combining estimators of a common parameter across samples, Statistical Theory and Related Fields 2 (2018) 158–171. doi:10.1080/24754269.2018.1530903.

[229] T. Wajima, K. Murakami, T. Kato, K. Sugawara, Heavy metal removal from aqueous solution using carbonaceous K_2S-impregnated adsorbent, Journal of Environmental Sciences 21 (2009) 1730–1734. doi:10.1016/S1001-0742(08)62480-8.

[230] S. H. Lee, D. M. Murphy, D. S. Thomson, A. M. Middlebrook, Chemical components of single particles measured with particle analysis by laser mass spectrometry (PALMS) during the Atlanta supersite project: Focus on organic/sulfate, lead, soot, and mineral particles, Journal of Geophysical Research: Atmospheres 107 (2002) AAC1–13. doi:10.1029/2000JD000011.

[231] Y. Zhang, X. Wang, H. Chen, X. Yang, J. Chen, J. O. Allen, Source apportionment of lead-containing aerosol particles in shanghai using single particle mass spectrometry, Chemosphere 74 (2009) 501–507. doi:10.1016/j.chemosphere.2008.10.004.

[232] M. Sekar, V. Sakthi, S. Rengaraj, Kinetics and equilibrium adsorption study of lead (II) onto activated carbon prepared from coconut shell, Journal of Colloid and Interface Science 279 (2004) 307–313. doi:10.1016/j.jcis.2004.06.042.

[233] T. A. Saleh, Nanocomposite of carbon nanotubes/silica nanoparticles and their use for adsorption of Pb(II): from surface properties to sorption mechanism, Desalination and Water Treatment 57 (2016) 10730–10744. doi:10.1080/19443994.2015.1036784.

[234] E. Bottani, J. M. Tascon, Adsorption of Inorganic Species from Aqueous Solutions. Adsorption by Carbon, Elsevier, Amsterdam, 2008. doi:10.1016/B978-0-08-056033-5.90001-6.

[235] J. P. Chen, X. Wang, Removing copper, zinc, and lead ion by granular activated carbon in pretreated fixed-bed columns, Separation and Purification Technology 19 (2000) 157–167. doi:10.1016/S1383-5866(99)00069-6.

[236] K. Kadirvelu, C. Faur-Brasquet, P. L. Cloirec, Removal of Cu(II), Pb(II), and Ni(II) by adsorption onto activated carbon cloths, Langmuir 16 (2000) 8404–8409. doi:10.1021/la0004810.

[237] M. Berglund, M. E. Wieser, Isotopic compositions of the elements 2009 (iupac technical report), Pure and Applied Chemistry 83 (2011) 397–410. doi:10.1351/PAC-REP-10-06-02.

[238] Y. Zhang, C. Liu, W. Shi, Z. Wang, L. Dai, X. Zhang, Direct measurements of the interaction between pyrene and graphite in aqueous media by single molecule force spectroscopy: Understanding the π-π interactions, Langmuir 23 (2007) 7911–7915. doi:10.1021/la700876d.

© 2020 Tous droits réservés.

lilliad.univ-lille.fr

[239] C. Ehli, N. Jux, D. Balbinot, G. M. A. Rahman, D. M. Guldi, F. Paolucci, M. Marcaccio, D. Paolucci, M. Melle-Franco, F. Zerbetto, S. Campidelli, M. Prato, Interactions in Single Wall Carbon Nanotubes/Pyrene/Porphyrin Nanohybrids, Journal of the American Chemical Society 128 (2006) 11222–11231. doi:10.1021/ja0624974.

[240] T. L. Sordo, J. A. Sordo, R. Flórez, Theoretical study of adsorption of hydrocarbons on graphite, Journal of Computational Chemistry 11 (1990) 291–296. doi:10.1002/jcc.540110303.

[241] A. C. Ferrari, J. Robertson, Interpretation of Raman spectra of disordered and amorphous carbon, Phys. Rev. B 61 (2000) 14095–14107. doi:10.1103/PhysRevB.61.14095.

[242] F. Tournus, S. Latil, M. I. Heggie, J. C. Charlier, Π-Stacking Interaction Between Carbon Nanotubes and Organic Molecules, Physical Review B - Condensed Matter and Materials Physics 72 (2005) 75431. doi:10.1103/PhysRevB.72.075431.

[243] J. T. Dickinson, J. J. Shin, S. C. Langford, The role of defects in laser induced positive ion emission from ionic crystals, Applied Surface Science 96-98 (1996) 316–320. doi:10.1016/0169-4332(95)00436-X.

[244] E. Cloutis, P. Szymanski, D. Applin, D. Goltz, Identification and discrimination of polycyclic aromatic hydrocarbons using raman spectroscopy, Icarus 274 (2016) 211–230. doi:10.1016/j.icarus.2016.03.023.

[245] P. A. Turhanen, J. J. Vepsäläinen, S. Peräniemi, Advanced material and approach for metal ions removal from aqueous solutions, Scientific Reports 5 (2015) 8992. doi:10.1038/srep08992.

[246] S. Cao, B. Li, R. Zhu, H. Pang, Design and synthesis of covalent organic frameworks towards energy and environment fields, Chemical Engineering Journal 355 (2019) 602–623. doi:10.1016/j.cej.2018.08.184.

[247] D. Benetti, R. Nouar, R. Nechache, H. Pepin, A. Sarkissian, F. Rosei, J. MacLeod, Combined magnetron sputtering and pulsed laser deposition of TiO_2 and $BFCO$ thin films, Scientific Reports 7 (2017) 2503–2512. doi:10.1038/s41598-017-02284-0.

[248] H. Matsumura, H. Umemoto, K. K. Gleason, R. Schropp, Catalytic Chemical Vapor Deposition: Technology and Applications of Cat-CVD, Wiley, Germany, 2019.

[249] J. Perrière, C. Hebert, N. Jedrecy, W. Seiler, O. Zanellato, X. Portier, R. Perez-Casero, E. Millon, M. Nistor, On the relevance of large scale pulsed-laser deposition: Evidence of structural heterogeneities in ZnO thin films, Journal of Applied Physics 116 (2014) 123502. doi:10.1063/1.4896379.

[250] F. Chiarella, C. A. Perroni, F. Chianese, M. Barra, G. M. De Luca, V. Cataudella, A. Cassinese, Post-Deposition Wetting and Instabilities in Organic Thin Films by Supersonic Molecular Beam Deposition, Scientific Reports 8 (2018) 12015. doi:10.1038/s41598-018-30567-7.

© 2020 Tous droits réservés.

lilliad.univ-lille.fr

[251] Y. Bouvier, C. Mihesan, M. Ziskind, E. Therssen, C. Focsa, J. F. Pauwels, P. Desgroux, Molecular species adsorbed on soot particles issued from low sooting methane and acetylene laminar flames: A laser-based experiment, Proceedings of the Combustion Institute 31 (2007) 841–849. doi:10.1016/j.proci.2006.08.036.

[252] C. Irimiea, Characterization of soot particles and their precursors by coupling laser-based techniques, Ph.D. thesis, University of Lille, Lille, France (2017). URL http://www.theses.fr/2017LIL10066

[253] Z. Zheng, K. C. Johnson, T. D. Durbin, S. Hu, T. Huai, D. B. Kittelson, H. S. Jung, Investigation of solid particle number measurement: Existence and nature of sub 23 nm particles under PMP methodology, Fall Technical Meeting of the Western States Section of the Combustion Institute 2011, WSS/CI 2011 Fall Meeting 42 (2011) 455–461. doi:10.1016/j.jaerosci.2011.08.003.

[254] M. Kazemimanesh, M. Rahman, D. Duca, T. Johnson, A. Adad, G. Giannopoulos, C. Focsa, A. M. Boies, Morphology, effective density, and volatility of particulate emissions from gasoline direct injection engine using aerodynamic diameter, mobility diameter, and mass measurements in tandem, to be submitted to the Journal of Aerosol Science (2020).

[255] B. Fatou, M. Wisztorski, C. Focsa, M. Salzet, M. Ziskind, I. Fournier, Substrate-mediated laser ablation under ambient conditions for spatially-resolved tissue proteomics, Scientific Reports 5 (2015) 18135. doi:10.1038/srep18135.

[256] T. Maulouet, B. Fatou, C. Focsa, M. Salzet, I. Fournier, M. Ziskind, Optimizing the substrate-mediated laser ablation of biological tissues: Quest for the best substrate material, Applied Surface Science 473 (2019) 486–492. doi:10.1016/j.apsusc.2018.12.173.

[257] M. Salzet, I. Fournier, C. Focsa, M. Ziskind, B. Fatou, M. Wisztorski, Device for real-time in vivo molecular analysis, US Patent 10,254,275 (2019).

[258] B. Fatou, P. Saudemont, E. Leblanc, D. Vinatier, V. Mesdag, M. Wisztorski, C. Focsa, M. Salzet, M. Ziskind, I. Fournier, In vivo real-time mass spectrometry for guided surgery application, Scientific Reports 6 (2016) 25919. doi:10.1038/srep25919.

[259] B. Fatou, M. Ziskind, P. Saudemont, J. Quanico, C. Focsa, M. Salzet, I. Fournier, Remote atmospheric pressure infrared matrix-assisted laser desorption-ionization mass spectrometry (remote ir-maldi ms) of proteins, Molecular and Cellular Proteomics 17 (8) (2018) 1637–1649. doi:10.1074/mcp.TIR117.000582.

[260] P. Saudemont, J. Quanico, Y.-M. Robin, A. Baud, J. Balog, B. Fatou, D. Tierny, Q. Pascal, K. Minier, M. Pottier, et al., Real-time molecular diagnosis of tumors using water-assisted laser desorption/ionization mass spectrometry technology, Cancer Cell 34 (5) (2018) 840–851. doi:10.1016/j.ccell.2018.09.009.

© 2020 Tous droits réservés.

lilliad.univ-lille.fr

[261] B. Fatou, P. Saudemont, M. Duhamel, M. Ziskind, C. Focsa, M. Salzet, I. Fournier, Real time and in vivo pharmaceutical and environmental studies with spidermass instrument, Journal of Biotechnology 281 (2018) 61–66. doi:10.1016/j.jbiotec.2018.06.339.

[262] F. Pereira, T. Mitchell, M. Botvinick, Machine learning classifiers and fmri: a tutorial overview, Neuroimage 45 (1) (2009) S199–S209. doi:10.1016/j.neuroimage.2008.11.007.

© 2020 Tous droits réservés.

lilliad.univ-lille.fr

This page is intentionally left blank

© 2020 Tous droits réservés.

Caractérisation physico-chimique de nanoparticules sélectionnées en taille émises par moteur à combustion interne et méthode originale pour la mesure des énergies d'adsorption sur surfaces carbonées par spectrométrie de masse laser

Résumé

Les émissions à l'échelle mondiale de particules carbonées fines et ultra-fines présentent un risque bien connu pour la santé et soulèvent des préoccupations environnementales importantes. Bien que les niveaux ambiants de particules carbonées aient été considérablement réduits au cours des dernières décennies par les restrictions successives des normes d'émission, leurs rejets dans l'atmosphère continuent de représenter l'une des principales sources de particules dans les zones urbaines. Les émissions de particules ultra-fines (suie) générées par les moteurs essence à combustion interne modernes sont au centre des préoccupations puisque les plus petites d'entre elles ne sont actuellement pas concernées par les règlementations sur les émissions automobiles qui se limitent aux particules de taille supérieure à 23 nm. Les effets potentiels sur l'environnement et la santé de ces émissions ultra-fines ne sont pas encore complètement compris en raison de l'absence de caractérisation expérimentale de ces nanoparticules carbonées.

La caractérisation physico-chimique détaillée de particules sélectionnées en taille émises par un moteur essence à combustion interne a été réalisée dans ce travail pour fournir des informations cruciales au bon développement de nouvelles technologies pour la détection et la mesure des particules de taille inférieure à 23 nm. Ces analyses ont été réalisées dans le cadre du projet H2020 PEMS4Nano qui vise à développer une technologie de mesure robuste, fiable et reproductible de particules ultrafines atteignant une taille aussi petite que 10 nm émises sur banc de test et en conditions réelles de conduite. Les caractérisations chimiques de ces particules sélectionnées en taille ont été réalisées par spectrométrie de masse (par exemple de type désorption ionisation laser, L2MS), qui révèle au niveau moléculaire des informations essentielles sur les classes chimiques des composés les constituant telles que les organosulfates, les hydrocarbures oxygénés, les hydrocarbures azotés, les métaux ou les hydrocarbures aromatiques polycycliques. La morphologie des particules émises a été sondée avec des techniques de microscopie à force atomique, microscopie électronique en transmission et à balayage. La spectroscopie Raman exaltée par effet de pointe a été également appliquée pour la première fois à des particules de combustion inférieures à 10 nm pour recueillir des informations sur leur nanostructure.

La composition chimique de suface et la nature de l'interaction entre les adsorbats et la surface (chimi/physi-sorption) régissent la réactivité des particules dans l'environnement et leurs effets nocifs sur la santé humaine. Afin de mieux comprendre ces interactions et prédire leurs impacts, il est nécessaire de pouvoir déterminer les énergies d'adsorption des composés chimiques présents à la surface des particules. Dans ce but a été développée et validée dans ce travail une nouvelle méthode basée sur le phénomène de désorption induite par laser pour déduire l'énergie d'adsorption d'espèces chimiques sur différents types de surfaces carbonées à partir de spectres de masse L2MS. Cette procédure expérimentale a été développée pour être rapide, résolue spatialement, sensible aux molécules de surface, et, supplémentée par un modèle théorique décrivant le phénomène de désorption, permet de déterminer l'énergie d'adsorption sur une grande variété d'échantillons. La preuve de concept de la méthode a été fournie par son application à des systèmes chimiques de complexité grandissante, montrant son énorme potentiel pour l'étude d'échantillons de terrain complexes.

Mots-clés: spectrométrie de masse laser, caractérisation physico-chimique, aérosols générés par la combustion, moteur à combustion interne, surfaces carbonées, nanoparticules

© 2020 Tous droits réservés.

Physico-chemical characterization of size-selected internal combustion engine nanoparticles and original method for measuring adsorption energies on carbonaceous surfaces by laser mass spectrometry

Abstract

The extensive global emissions of fine and ultra-fine carbon-based particulates present a well-known health risk and raise significant environmental concern. Although the ambient particulate matter levels have been significantly reduced in the past decades by the successive tightening of emission standards, transport emission of carbonaceous particles continues to represent one of the main sources of particulates in urban areas. A major concern is now raised by the ultra-fine particle (soot) emissions of modern internal combustion engines. A large portion of these emissions are not covered by existing vehicle emission regulations that only limit the number of particles larger than 23 nm. The potential environmental and health effects of ultra-fine vehicle emissions are still not entirely understood due to the lack of experimental characterization of such carbonaceous nanoparticles.

Detailed physico-chemical characterizations of size-selected particulate matter emitted by an internal combustion gasoline engine (ICE) were carried out in this work to support the development process of measurement technologies for sub-23 nm particles. These analyses were performed in the framework of the H2020 PEMS4Nano project which aims to develop robust, reliable, and reproducible measurement technology for particles down to 10 nm for both chassis dyno and real driving emissions. Chemical characterizations of the ICE size-selected particles were performed using mass spectrometry, such as laser desorption/ionization mass spectrometry, L2MS, which gives access to detailed molecular information on the chemical classes of critical interest such as organosulphates, oxygenated hydrocarbons, nitrogenated hydrocarbons, metals, or polycyclic aromatic hydrocarbons. The morphology of the emitted particles was probed with atomic force microscopy and transmission and scanning electron microscopies. Tip-Enhanced Raman Spectroscopy was applied for the first time to sub-10 nm combustion-generated particles to gather information on their nanostructure.

The reactivity of particles is mainly driven by the surface chemical composition and by the strength of the interaction between the adsorbates and the surface (physi- /chemisorption), therefore, to truly understand and predict the impact of soot emissions, the adsorption energies of chemical compounds present on their surface must be also determined. In this regard, a novel laser-based method for determining the adsorption energy of chemical species on various carbonaceous surfaces was developed and validated. This involved the development of a fast, spatially resolved, surface-sensitive experimental procedure and a theoretical model that allows us to determine the adsorption energy of chemical species adsorbed on a wide variety of samples. The proof of concept of this method has been demonstrated on several surrogate carbonaceous systems of varying complexity which demonstrated the great potential of the method for the future analyses of field collected samples.

Keywords: laser mass spectrometry, physico-chemical characterization, combustion-generated aerosols, internal combustion engine, carbonaceous surface, nanoparticles

© 2020 Tous droits réservés.